A Field and Petrological Study of Oxide-Facies Algoma-Type Banded Iron Formation, Sherman Mine, Temagami

Stephen Ginley

A thesis submitted to the

Faculty of Graduate and Postdoctoral Studies

In partial fulfillment of the requirements for the

Master of Science Degree in Earth Sciences

Department of Earth and Environmental Science

Faculty of Science

University of Ottawa

Abstract

Banded iron formation (BIF) is the most commonly mined source of iron ore, but the details of its genesis are poorly defined. Algoma-Type BIF is a predominantly chemical sedimentary rock comprising iron-rich phases (hematite, magnetite, chlorite) and chert as distinct laminae associated with deep marine lithologies, especially volcanic rocks and black shales. The iron minerals are thought to be direct chemical precipitates from Fe-enriched bottom waters or formation waters, most probably related to proximal volcanic activity. Key questions examined in this study are the paragenetic relationships and origins of mineralogically distinct layers in the Temagami BIF and the possible mechanism of replacement of primary hematitic layers by magnetite. The latter is a fundamental process in generating ore-grade BIF. The mineralogical and geochemical fingerprints of the different components of the BIF are also examined as clues to their likely sources (i.e., from upflowing hydrothermal fluids, contemporaneous volcaniclastic material, or precipitation from the local bottom water). Field observations indicate three separate depositional horizons for BIF in the area and exclude previous suggestions of fold repetition. Documented relationships between different types of layers and different facies of BIF in outcrop and in samples of the ore material, including petrographic features and aspects of the mineral chemistry and whole rock geochemistry, were used to construct a detailed paragenesis of the Temagami BIF. Two paragenetically distinct types of hematite and three types of magnetite are distinguished by different habits, grain size, cross-cutting relationships and growth features. Whole rock geochemical data confirm that the different facies of BIF were mainly products of redox-driven precipitation, combined with local hydrothermal and clastic input.

Résumé

Les formations de fer rubanées (BIF) sont la source principale de minerai de fer, cependant leur origine reste peu définie. Les BIF de Type Algoma sont formées de roches sédimentaires comprenant des laminations distinctes riches en fer qui sont associées à des lithologies de fond marin, particulièrement des roches volcaniques et des shale noirs. Les minéraux de fer seraient directement précipités à partir d'eaux enrichies en fer, se trouvant dans les fonds marins à proximité d'activité volcanique. Les points clés étudiés dans cette étude sont la relation paragénétique et l'origine des laminations minéralogiquement distinctes dans le BIF de Temagami, ainsi que le remplacement apparent de couches hématitique par la magnétite. Ce dernier est un processus fondamental dans la formation de BIF économiques. Une autre question étudiée lors de cette étude est la signature minéralogique et géochimique des différentes sources de fer, ainsi que plusieurs autres constituants du BIF (e.g. fluides hydrothermaux, matériel syn-volcanique, ou précipitation à partir d'eau de fond à proximité). La documentation des liens entre différentes couches d'un BIF en affleurements et échantillons, la pétrographie des différentes caractéristiques en lames minces, ainsi que la géochimie des différents faciès ont été utilisés sur 63 échantillons afin de construire une paragenèse complète du BIF de Temagami. Les observations de terrain indiquent trois horizons de déposition distincts pour le BIF et excluent certaines propositions suggérant que ces différents horizons représentent des changements de faciès à l'intérieur d'une seule unité plissée. Deux formes distinctes d'hématite et trois formes de magnétite se distinguent par différentes formes de cristaux, taille des grains, relations de recoupement et textures de croissance. Les données géochimiques

suggèrent que les différents faciès du BIF proviennent d’une précipitation menée par des réactions de réduction, de l’activité hydrothermale ainsi que d’un apport clastique.

Table of Contents

List of Tables

List of Figures

Appendices

1. Introduction

Banded iron formation (BIF) is the source of the vast majority of the world's supply of iron. Giant Proterozoic Lake Superior-Type iron formations formed mainly in shallow seas at continental margins (Gross, 1983). Smaller, Archean Algoma-Type BIF are found mainly in greenstone belts, which also host volcanogenic massive sulfide (VMS) deposits (Gross, 1983). The close spatial association of Algoma-Type BIF with many VMS deposits has been particularly useful in mineral exploration (Peter and Goodfellow, 1996). Because of the important role of paleoredox conditions in the formation of BIF, their study is relevant to both economic geology and the Precambrian evolution of the oceans and atmosphere (Holland, 1973; Ohmoto et al., 2006). A major goal of BIF research has been to understand the nature of the Archean ocean chemistry preserved in the sedimentary layers.

Algoma-Type banded iron formation is a chemical sedimentary rock comprising iron-rich phases (hematite, magnetite, chlorite, sulfide, carbonate) as distinct millimeter to centimeter-scale laminae within a cherty matrix deposited with deep marine volcanic rocks, especially extensive pillow lava sequences, and shales (Gross, 1983; James, 1954). The ore minerals are thought to be direct chemical precipitates from reduced bottom waters that are enriched in iron from proximal volcanic sources (James, 1954). However, little is known about the primary phases deposited on the seafloor or the diagenetic transformations that produced the main minerals now present in the ores. Extensive research has shown that iron will precipitate from solution in a variety of static

and non-static redox conditions (e.g., Byrne and Kester, 1976; Taylor and Konhauser, 2011), however, a number of different pathways have been suggested for the precipitation of both iron oxides and silica from the water column (Ohmoto, 2003; Slack et. al, 2007; Bekker, 2011).

Within Algoma-Type BIF, the dominant mineralogy can change abruptly between layers and along layers (e.g., from hematite to magnetite facies, and from chert to chlorite facies), however, the causes of these transitions are poorly understood. Some researchers have argued that the different BIF facies record large-scale changes in the Archean ocean (James, 1954). Others suggest that the fine-scale features of the sediments represent changes in the redox chemistry of local sub-basins and/or postdepositional processes (e.g., diagenetic or metamorphic recrystallization: Gross, 1983). Cataloging these features in the field, followed by detailed petrographic characterization, has revealed a number of paragenetic relationships that shed new light on the mineralogical transformations during BIF formation. In particular, the origins of the fine, sometimes rhythmically banded, Fe-oxide, chert and clastic layers are examined, and complex local deformation features are reinterpreted in terms of synsedimentary and diagenetic processes.

This study examines a number of key features of Algoma-Type BIF in one of its type localities in the Temagami greenstone belt of Ontario. Key questions examined in the study are the paragenetic relationships between the major components of the sediments and the origin of mineralogically distinct layers in the BIF. In particular, the study has

focused on the apparent replacement of hematitic layers by magnetite, a fundamental process in generating ore grade BIF. Like modern metalliferous sediments (e.g., Laurila et al., 2015), Algoma-Type BIF comprise both chemical and clastic components that must be isolated in order to understand the record of deposition related to redox changes in the water column and/or hydrothermal inputs. The study also considers the record of post-depositional effects on the BIF, including diagenesis, synsedimentary deformation, hydrothermal alteration and metamorphic recrystallization. An extensive sample suite is examined from the former Sherman Mine, including ore from the major open pits and a "classic" exposure of the BIF on Highway 11, just outside the mine. This locality has been the focus of extensive research in the past on aspects as diverse as the oxidation state of the Archean atmosphere to the behavior of rare earth elements (REE) in the Archean oceans (e.g., Bau and Alexander 2009), but a detailed accounting of the BIF mineralogy and the paragenesis of the key outcrops has never been carried out. In particular, the world-class exposure on Highway 11 has been sampled by many previous studies but never mapped in detail (Ohmoto et al., 2006). Careful consideration is given to the effects of regional deformation (e.g., whether two BIF "horizons" in the north and south pits represent a break in BIF deposition or large-scale folding) and to differences in the BIF facies between the major occurrences.

This thesis was conducted in parallel with a Ph.D. project focused on high-resolution trace element geochemistry and isotopic systematics (Diekrup et al., in preparation). Field work, mapping and sample collection was carried out jointly by Ginley and Diekrup. Whole rock geochemical and mineral chemical data from samples collected in

the joint study are considered in this thesis and presented in their entirety in Diekrup et al. (in preparation).

2. Algoma-Type BIF: General Features and Previous Work

Algoma-Type BIF are minor but important parts of many Archean greenstone belts. They comprise well-defined and spatially extensive sedimentary successions, from a few meters up to several 100s of meters in thickness and with strike lengths up to 10s of kilometers. They have been recognized as important regional stratigraphic markers in many greenstone belts (e.g., Thurston et al., 2012). They consist of macroscopic to microscopic alternating layers or beds of chert (microcrystalline quartz) and iron-rich minerals, including magnetite and hematite, and less commonly sulphides, carbonates and silicates (James, 1954; Gross, 1996; Bekker et al., 2010). They are closely associated with submarine volcanic rocks and are widely considered to be products of direct chemical precipitation of Fe and Si from local bottom waters enriched by hydrothermal vents. In some cases the iron formation is associated with volcanogenic massive sulfide (VMS) deposits (see Franklin, 1996). By contrast, the larger Superior-Type iron formations (cf., Cloud, 1983; Gross, 1996), which formed at passive margins in sedimentary rock successions, generally lack a direct relationships with volcanic rocks, are regionally extensive (100s of kilometers) and may be 500 m up to 2 km in thickness. Unlike Algoma-Type BIF, in which the Fe-rich layers are typically fine-grained to microcrystalline, Superior-Type BIF are commonly granular (James, 1954; Gross, 1972; James, 1992; Baldwin, 2009, Baldwin et al., 2011).

The first major studies of Algoma-Type BIF in Canada were carried out by Gordon Gross of the Geological Survey of Canada, who mapped and conducted mineralogical and geochemical studies of different deposits in the eastern Superior Province, including the Sherman Mine, Griffith Mine, Adams Mine and BIF in the Kirkland Lake District (Gross, 1980; Gross, 1983). Gross (1970) identified many of the primary sedimentary features of Algoma-Type BIF, from the desiccation cracks in the chert to the alternating millimeter-scale laminations that were interpreted to be the result of precipitation in quiet water. He mapped several of the open pits in the Sherman Mine and characterized the deposit as dominantly oxide facies BIF with minor sulfide facies BIF in the hanging wall. This work included analysis of 50 samples from the mine, now compiled in Gross (2009). However, limited additional field work has been carried out in the area. Bowins (1989) completed a PhD dissertation on the REE chemistry of the Temagami BIF but did not conduct a detailed mineralogical or paragenetic study of the samples as a context for the analysis.

In early models of BIF deposition, the general thinking was that a particular oxide preserved in the rock (hematite or magnetite) simply recorded different redox potential of the water at the time of precipitation (James, 1954; Gross, 1983). However, the different facies of Algoma-Type BIF (oxide, silicate, carbonate and sulfide) must also reflect additional sources of BIF components. In addition to hematite and magnetite, the silicate facies commonly includes minerals such as chlorite, grunerite or other aluminosilicates, the carbonate facies contains ankerite or siderite, and the sulfide facies may be dominantly pyritic or pyrrhotite-rich. The sulfide facies is commonly a

carbon-rich shale with framboidal (diagenetic?) pyrite. James (1954) considered that Fe-oxides, Fe-rich aluminosilicates, Fe-carbonate and Fe-sulfide reflected the redox conditions, in order of decreasing redox potential, but the availability of sulfur, silica, and carbonate must also be a contributing factor. Early workers also considered that redox potential was negatively correlated with depth, so the sulfide-bearing shales were generally thought to have been deposited only in the deepest basins (James, 1954). It is now generally recognized that proximity to marine volcanic centers also influences both local redox conditions and sources of components in the BIF (e.g., Ohmoto, 2003; see also modern examples in Zierenberg and Shanks, 1983).

Most recent models of BIF deposition involve primary precipitation of hydrated amorphous Fe-oxides that are progressively transformed, first to hematite and then eventually magnetite. A number of different mechanisms for the transformation to magnetite have been proposed. The actions of microorganisms have been widely suggested as drivers of changing redox conditions, especially where the reductants (i.e., organic carbon) or microbial byproducts (e.g., phosphates) are present.
In this case magnetite (mt) replaces primary hematite (hm) by:

(1) $3Fe_2O_3$ (hm) + H_2 = $2Fe_3O_4$ (mt) + H_2O

where H_2 is representative of the microbially produced reductant. However, hydrothermal fluids with reduced iron also have been proposed as drivers of the hematite to magnetite conversion (Zierenberg and Shanks, 1983; Ohmoto, 2003), according to the reaction:

(2) Fe_2O_3 (hm) + Fe^{2+} + H_2O = Fe_3O_4 (mt) + $2H^+$

This is potentially relevant where biogenic reduction is unlikely. Ohmoto (2003) addressed the specific question of coexisting magnetite and hematite, and whether this reflects the redox of the Archean ocean during iron precipitation or some secondary process. He suggested that the transition between magnetite and hematite along single layers cannot be due to changes in broad basin-scale redox chemistry but is more likely the result of local hydrothermal activity (i.e., input of reduced iron according to reaction 2).

Different authors also have studied BIF to address the question whether these mineralogical changes could reflect global ocean conditions around the first Global Oxidation Event (GOE) (e.g., Bekker, 2001; Bekker, 2004). A number of different researchers investigating the evolution of the Earth's atmosphere and oceans have sampled the Highway 11 outcrop as a baseline for Archean ocean water chemistry. Ohmoto et al. (2006) and Shimada et al. (2007) reported on two samples from the Highway 11 outcrop in their work on geochemical and isotopic proxies for ocean redox chemistry at 2.72 Ga. Another study of four samples from the Highway 11 outcrop and four samples from the North Pit of the Sherman Mine linked decreasing nickel content in the Neoarchean with the rise of sulfur-reducing bacteria at ~2.7 Ga (Konhauser et. al, 2009). A few studies have examined the REE geochemistry (Bowins, 1989; Bau and Alexander, 2009), and one recent study documented what was considered to be primary

hematite in one sample (Sun et al., 2015). However, no detailed sections have ever been made and none of the published studies examined more than a few samples.

3. Regional Geological Context

The Temagami BIF is part of the Temagami Greenstone Belt of the Superior Province (Figure 3.1). The Superior Province is at the core of the Canadian Shield and consists of deformed and metamorphosed granitic complexes, greenstone belts and metasedimentary sequences formed during the Archean (Card, 1990). The different subterranes are generally east-west trending and young from north to south. The large Abitibi Greenstone Belt in the south became part of the Superior Province between 2.73 and 2.68 Ga (Thurston, 2012). It is one of the best-studied Archean greenstone terranes in the world (Ayer, 2002). The smaller Temagami Greenstone Belt is located immediately to the southeast of the Abitibi Greenstone Belt, about 150 km south of Kirkland Lake, but is considered to be somewhat older and geologically distinct. Regionally, the rocks of the Temagami Greenstone Belt have been metamorphosed to lower greenschist facies, with a quartz-chlorite-albite±epidote assemblage in the mafic volcanic rocks. Metamorphic grade is somewhat higher close to granitic plutons such as the Spawning Lake Stock and Iceland Lake Pluton (Bowins, 1989).

U-Pb dating of the Temagami Greenstone belt has been attempted with inconclusive results. The Iceland Lake granitic pluton and rhyolite flows south of the Temagami BIF have an age of 2736±3 Ma (Bowins and Heaman, 1991). The youngest age in the area is from a rhyolite porphyry dike north of the BIF, dated at 2687±2 Ma (Bowins and Heaman, 1991). However, zircon ages from other volcanic rocks north of the mine range from 2676 to 2717 Ma (Ayer at al., 2007). U-Pb dating of detrital zircon in

sandstone interlayered with the BIF indicate maximum ages of 2724 to 2720 Ma for the formation (Ayer et al., 2007). The locations of the samples dated in these studies are shown in Figure 3.2. However, the U-Pb ages are generally inconsistent with field observations. The Bowins and Heaman (1991) dates suggest stratigraphic younging to the north, with rhyolite flows immediately south of the BIF being ~49 m.y. older than volcanic units immediately to the north, but pillow facing directions in the same rocks clearly indicate younging to the south (Bennett, 1978). Although a regional synform has been proposed to explain the two main BIF horizons, no evidence of folding could be found in the field.

Figure 3.3 shows the world-class exposure of the Temagami BIF in a roadcut along Highway 11 in Temagami, ON.

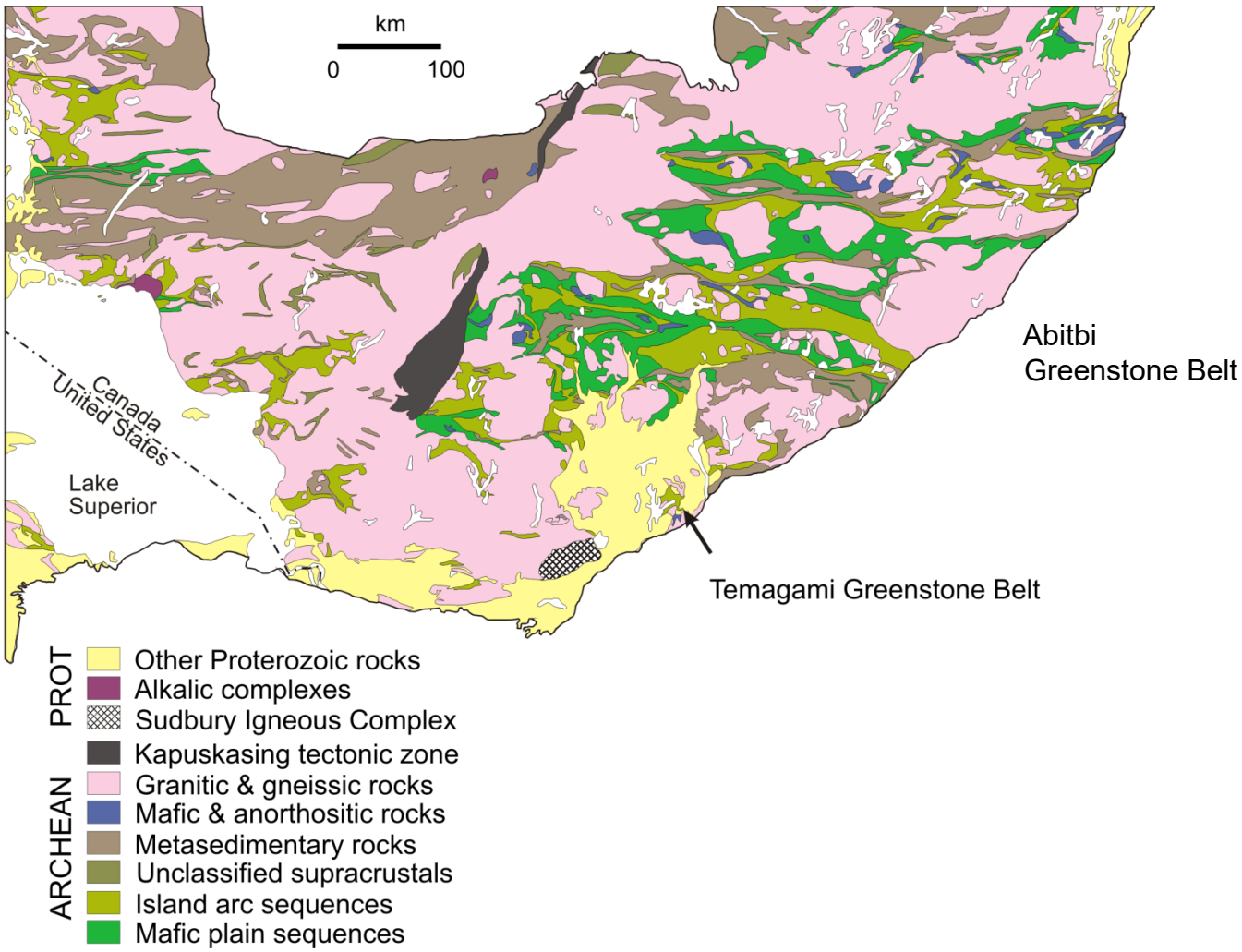

Figure 3.1 Generalized regional geology map of the western Superior Province. The Superior Province comprises a series of volcano-plutonic, metasedimentary belts and gneiss belts formed in the Archean as part of the Canadian craton. The location of the Temagami Greenstone Belt is indicated, exposed in a window within the Proterozoic sediments (Huronian cover in yellow). Modified after Card et al. (1996).

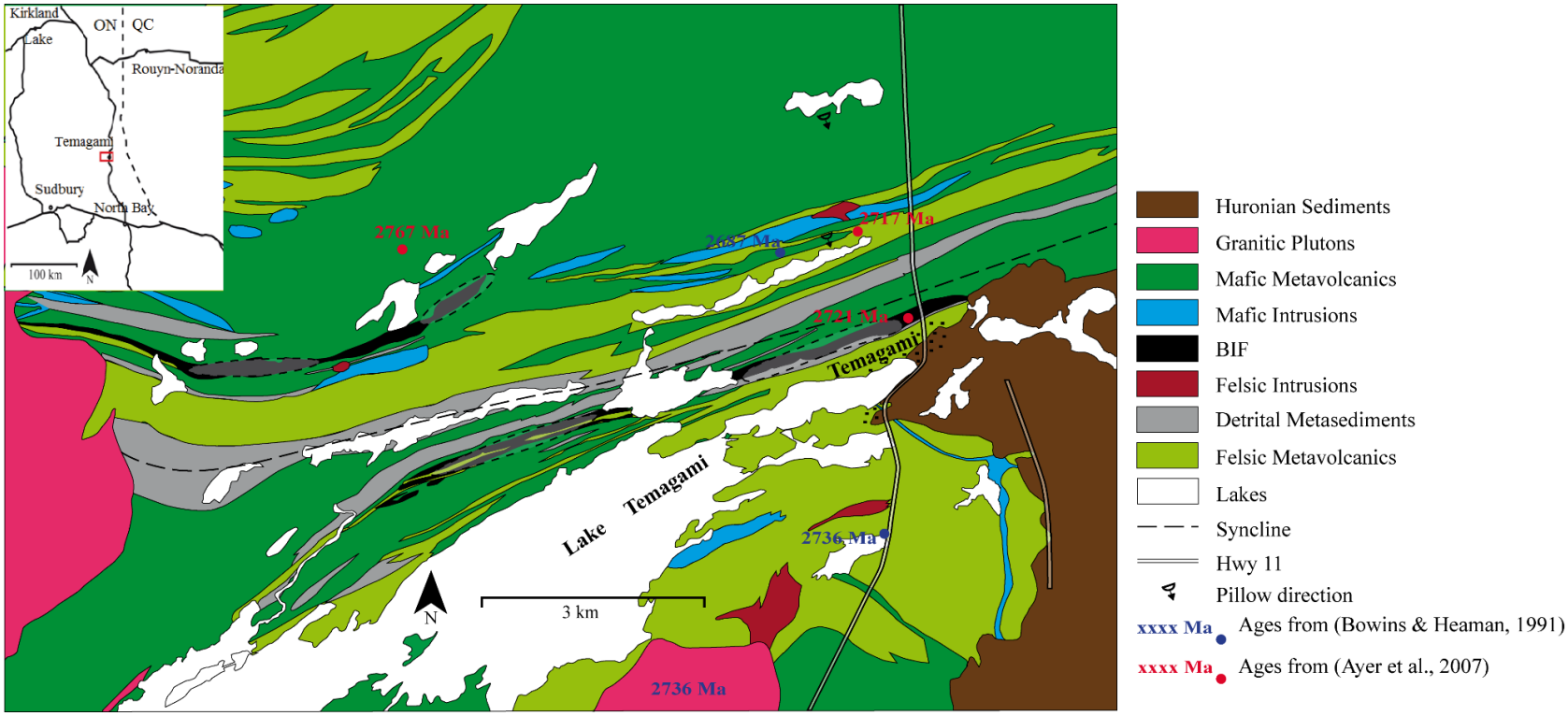

Figure 3.2 Sampling locations and U-Pb age determinations of a number of different units of the Temagami Greenstone Belt (geology area after Bennett, 1978). The granitic pluton and rhyolite flows south of the Temagami BIF have been dated at 2736±3 Ma. North of the BIF, a rhyolite porphyry dike in the Temagami Greenstone Belt has been dated at at 2687 Ma (Bowins and Heaman 1991). U-Pb dating of volcanic flows north of the Temagami BIF revealed ages ranging from 2767-2717 Ma (Ayer, 2007). A sandstone interlayered with the Temagami BIF has U-Pb ages ranging from 2724-

2720 Ma (Ayer, 2007). These data are contradictory and generally inconsistent with pillow-facing directions within the mine area. Displayed on the map are sampling locations for U-Pb ages. The Sherman Mine comprises the north and south open pits (short dashed outlines).

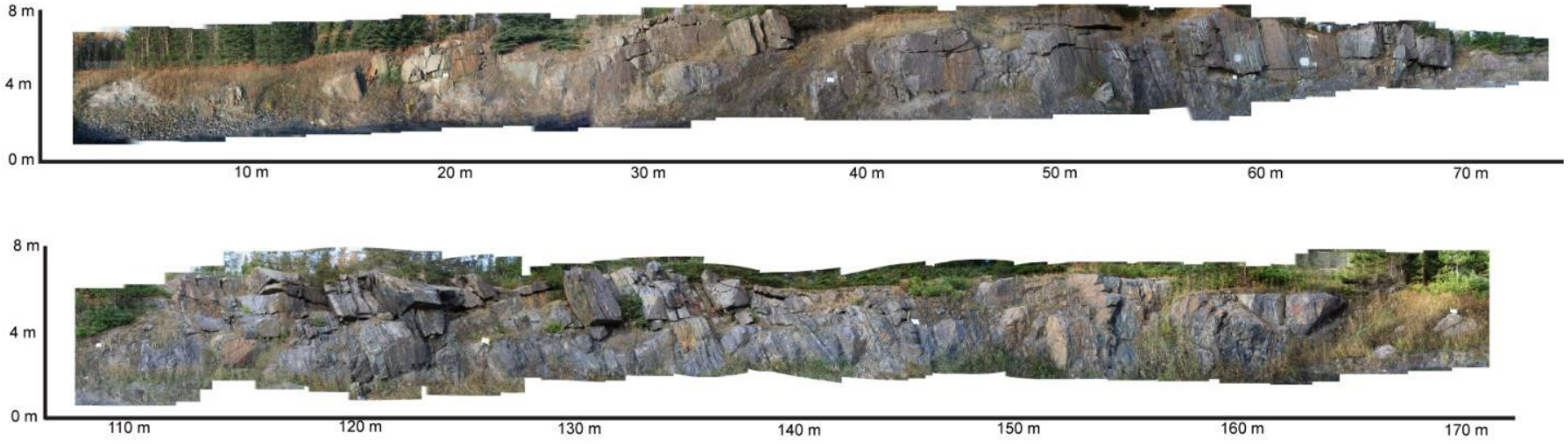

Figure 3.3 Photomosaic of the Highway 11 outcrop, located roughly 500 m north of the center of the town of Temagami, ON. Detailed mapping and sampling of the Highway 11 section was a major component of this study. The exposure of BIF is in two 60-70 m sections (both 5-7 m tall) separated by a 15 m section of mafic flows with pillow forms and sulfide mineralization, partially covered by overburden. The exposure includes more than 500 discrete beds of BIF, bound above and below by well-defined bedding surfaces and other beds of a different facies (see Chapter 6). The bedding is near vertically dipping but shows widespread evidence of synsedimentary folding and faulting.

4. Geology of the Sherman Mine

The Sherman Mine was first developed in the 1960s to extract iron ore from the Temagami BIF. The mine was operated between 1964 and 1990 as a joint venture of DOFASCO (Dominion Foundries and Steel, Limited), with 90% ownership, and Tetapaga Mining Company Limited, owning 10% of the mine. The latest mining was carried out by Cliffs of Canada Limited; both Tetapaga Mining Company and Cliffs of Canada were wholly owned subsidiaries of The Cleveland Cliffs Iron Company. A total of 22,650,000 metric tonnes of iron ore pellets was shipped from the Sherman Mine during its lifetime (Donaldson and Garrett, 1991). Gyratory crushing, milling, concentrating, and pelletizing was conducted on site, and the produced pellets were then transferred to DOFASCO's steel making facilities in Hamilton, ON (Riedel, 1969). The mine exploited iron ore with an average grade of 30 wt% Fe from the North and West pits. Production from the South and East pits, which started in 1980 and 1983, respectively, yielded somewhat lower ore grades (Wilson, 2012). The pits exploited two parallel, east-west trending BIF horizons with a strike length of more than six kilometers. The open pit mines can be clearly seen from an eye elevation of several hundred kilometers in Google Earth (see Figure 5.1).

Mapping in the Temagami area was first done by Moorehouse (1942) and then Bennett (1978) (Figure 4.1). The major lithologies in the mine area are mafic metavolcanic rocks, felsic metavolcanic rocks, detrital metasediments, and banded iron formation. Minor felsic plutons, mafic intrusions and Huronian sediments are also present. Based

on field observations in this study and the mapping of Bennett (1978), the oldest unit in the vicinity of the mine is a package of felsic and mafic flows south of the open pits. Extensively altered felsic volcaniclastic rocks, locally with sulfide clasts, occur in the stratigraphic footwall and indicate that VMS-style hydrothermal activity was ongoing at the time of deposition. The altered volcanic rocks are overlain by a laterally extensive mafic volcaniclastic unit, which includes an outcrop of pyrite-bearing carbonaceous shale, which is well-exposed exposed in the Temagami garbage dump. The first BIF, in the north pit, sits on top of the altered felsic rocks and mafic volcaniclastic units. The second BIF, originally exposed in the south and west pits of the Sherman mine (and in the Highway 11 outcrop) overlies another package of felsic and mafic flows that are cut by mafic dikes and felsic intrusions. The entire mine sequence is overlain by more felsic and mafic flows south of the Highway 11 outcrop. These rocks are overlain unconformably which by Huronian sediments and intruded by the Iceland Lake pluton and associated rhyolite dikes. The Spawning Lake Pluton, to the west of Temagami, intrudes the entire package.

The 1978 map of Bennett showed a steeply dipping east-west trending, isoclinal fold structure between the north and south pits (with the north pit BIF on the north limb and the south pit BIF on the south limb). The interpreted structure was justified by slightly different dip directions on opposite sides in the north and south pits. However, more recent field work during this study has indicated: 1) all pillow facing directions are to the south, including north of the north pit; 2) lithologies observed in the south pit (e.g., black shales at the west end of the BIF) are not repeated at the north pit; 3) no fold closures

have been observed, including on the east side of Highway 11; 4) no other folds have been documented regionally; 5) U-Pb ages around the deposit, while being inconsistent with observed facing directions, also do not support a syncline or repetition of the stratigraphy. The balance of observations in this study suggest that the Temagami mine sequence is a homoclinal succession of mafic flows and altered felsic volcanic rocks in the footwall, with intervening black shale and BIF horizons and an overall younging direction to the south.

Typical sedimentological features of Algoma-Type BIF are well-represented in the Sherman Mine and include syndepositional faults and folds, sediment loading structures and some instances of grain sorting (e.g., see Chapter 5, Figure 5.2). Features that reflect deformation have been variably interpreted as resulting from regional deformation or synsedimentary depositional processes, such as faulting at the seafloor or reflecting paleo-seafloor topography (e.g., slumping and brecciation; thinning and thickening of beds around topographic highs and lows). However, some examples of folding and boudinage may reflect either syndepositional soft-sediment deformation or postdepositional strain. Despite the excellent preservation, there is evidence of late-stage deformation and metamorphism. These include lower greenschist metamorphic mineral assemblages, pervasive quartz veining perpendicular to bedding, and brittle faults. A definite cleavage is observed in the southernmost exposure of the BIF-hosting volcanic rocks in the Highway 11 outcrop.

The dominant BIF facies is chert (black, white and diffusely microbanded), accounting for ~60% of the mapped exposures. Chlorite-rich facies make up ~25% of the BIF, and jasper is the least common at 15%. Slightly different proportions of these facies are found in blocks from different parts of the open pits compared to the Highway 11 outcrop (see below). Sulfide facies, in black shale is present at the west end of the south pit and in the footwall mafic volcanic rocks. These occurrences may represent the proximal, low-temperature discharge of hydrothermal fluids into the local sub-basins that contain the BIF.

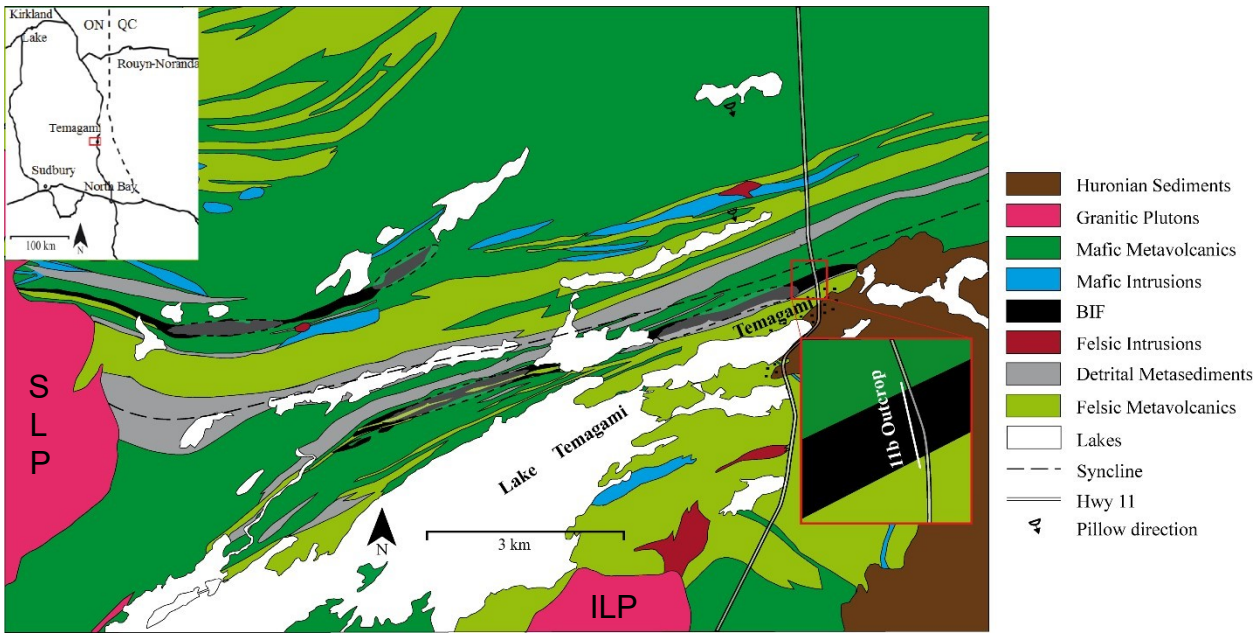

Figure 4.1 Surface geology of the Temagami area after Bennett (1978). The major depositional units in the Sherman Mine area are mafic metavolcanic rocks, felsic metavolcanic rocks, detrital metasedimentary rocks and banded iron formation. Minor felsic plutons and intrusions, mafic intrusions, and Huronian sediments are also present locally. Based on pillow-facing directions, the oldest units are Archean felsic and mafic flows intruded by mafic dikes, north of the mine area, overlain by Archean clastic metasedimentary rocks. These units described above are all intruded by the Spawning Lake Pluton (SLP) to the west of Temagami. The BIF of the Sherman mine area occurs in two main horizons (outlined by the north and south pits) and is overlain by a second sequence of felsic and mafic flows cut by mafic dikes and felsic intrusions. This led Bennett (1978) to infer a large synclinal structure within the mine area. However, consistent pillow-facing directions observed during this study suggest a homoclinal

sequence; no pillows were observed that indicated a younging direction to the north. The Iceland Lake Pluton (ILP) and associated rhyolite dikes cut the succession in the south of the mine area.

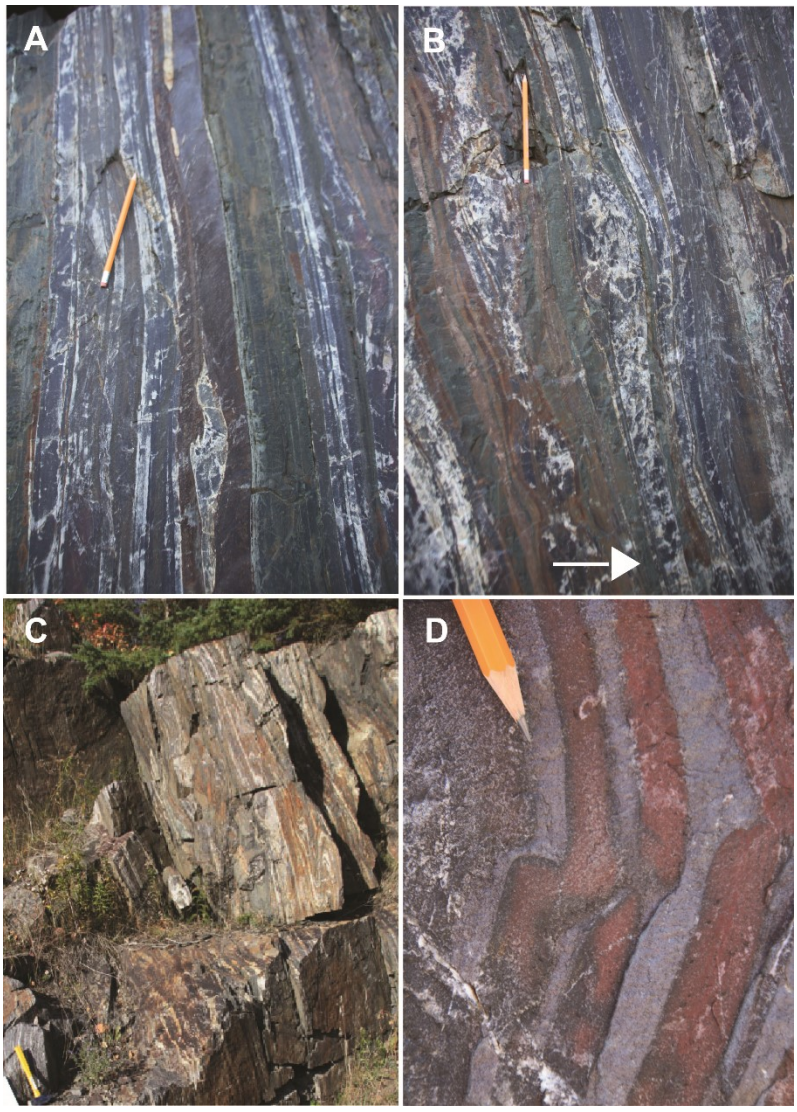

Figure 4.2 Examples of field photographs showing typical features of the Temagami BIF. A) Relatively undisturbed bedding with local internal deformation, common in the Highway 11 outcrop. A folded white chert layer is partly boudinaged. However, adjacent layers and most other white chert layers in this section of the outcrop are not similarly deformed. B) Locally thinned chlorite layer in a thick section of a white chert in the Highway 11 outcrop. The younging direction (arrow) is inferred from pillow-facing directions in nearby outcrops. C) An interpreted synsedimentary fold in white chert. The

folding is seen in 5-7 layers but does not affect adjacent layers. D) Possible sediment loading structures in jasper and magnetite layers of BIF in an ore block from the Sherman Mine. The synsedimentary structures are not penetrative and do not cross all bedding, consistent with soft sediment deformation.

5. Methodology

5.1 Fieldwork

Field work was carried out in 2014 and 2015. In the first season, the field work focused on the type section of the Temagami BIF exposed in the large outcrop on Highway 11, which is an extension of the geology in the South and West Pits. For the first time, this classic outcrop was mapped at 1:100 scale to document the meter- and centimeter-scale layering, the stratigraphic facies relationships, and post-depositional features of the units. The outcrop is the thickest preserved section of BIF exposed in the Temagami area. Despite the extensive studies of the exposure, there is no record that it had ever been mapped in detail.

In 2015, more extensive mapping of local outcrops was carried out at the Sherman Mine, and a large collection of more than 600 massive blocks of ore (1-3 m in size) was documented in and around the North, South and West pits. Figures 5.1 and 5.2 show the locations of the pits, the large blocks located at the edges of the pits, and the Highway 11 outcrop. Figure 5.3 shows the distribution of the ore blocks as seen in a satellite image. The ore blocks were placed at the margins of the open pits at the time of mining, most likely because they were too large to be accommodated by the crusher and would have required additional blasting to reduce their size. Representative ore types from all of the large mined pits are contained in the blocks. Although the blocks are not in place, they provide an unprecedented record of the BIF facies that were

present in the adjacent open pits that have now been largely mined out. A comprehensive inventory of the blocks was carried out, taking stock of the relative abundance of different BIF facies, band thicknesses, and structural and paragenetic relationships. These features were logged and mapped in detail to obtain a broader view of the Temagami BIF, and they provide the first quantitative analysis of the BIF facies in the Sherman mine.

5.2 Sampling and Sample Preparation

50 samples of the Temagami BIF were collected from the Highway 11 outcrop. The samples were spaced approximately 5 m apart and were selected to be representative of the different BIF facies. Samples that exhibited particular paragenetic relationships or sedimentological or metamorphic features of interest were also collected for petrographic examination. 70 samples were also collected from the archive of large ore blocks (on average about one in 5 blocks) with emphasis on specific textural or paragenetic features not represented in the Highway 11 samples. All samples were cut and described in detail. A complete list with the descriptions is provided in Appendix 1. Polished thin sections were prepared to examine specific mineralogical and facies relationships. A list of sections, brief mineralogical descriptions and photomicrographs are provided in Appendix 2.

5.3 Sample Analysis

Whole rock geochemical analyses were obtained on 34 samples from the Highway 11 outcrop and 29 samples from the archive of ore blocks. The emphasis was on high-precision, layer-by-layer variations that could be directly linked to observations in thin section, rather than larger-scale bulk chemical characterization of the ores. The analyzed samples are described in Appendix 1.

Individual facies types were selected from discrete beds in a way to limit cross-bed contamination in the final powdered samples. To do this, layers between 3 and 5 cm thick were cut from the rock samples. Multiple cuts with a rock saw typically were needed to isolate individual layers. The subsampled layers were kept in plastic bags while crushed with a rock hammer to limit metal contamination from steel jaw crushers. Chips of the layers were then pulverized in an agate rock mill to produce ~5 g of fine powder. 65 whole-rock samples were prepared with matching thin sections, and analysed using a combination of research-grade fusion and 4-acid digestion with ICP-OES (optical emission spectrometry) and ICP-MS (mass spectrometry).

An exhaustive investigation of the appropriate methodology for analysis was carried out, to achieve a complete geochemical characterization of the samples at ultra-low detection limits. Accuracy and precision were based on analyses of international rock standards produced from the Temagami BIF when the Sherman mine was in production (cf. Govindaraju, 1994; Dulski, 2001; Bau and Alexander, 2009). The analyses were

conducted by Activation Laboratories in Ancaster Ontario. The methods used for each element are described below and listed in Table 5.2. A detailed discussion of the quality control measures and the complete data set are presented in Diekrup et al. (in preparation).

Major elements, Si, Al, Fe, Mg, Ca, P, and Ti, were determined following a lithium metaborate/lithium tetraborate fusion. In this technique, a 0.2-0.25 g sample is mixed with the flux and then fused to create a homogeneous sample. The fused sample is dissolved in 5% nitric acid and all elements are solubilized. The solutions were then analysed by ICP-OES using the method of internal standardization. By comparison of detection limits and results for reference materials FeR-3 and FeR-4 and published data from Bau and Alexander (2009), Govindarju (1994), and Dulski, 2001), it was determined that Na and K, as well as the minor elements, Mn, Ba, Sr, Rb, Cs, Li, B, Be, V, Cr, Zr, Hf, Sc, and U, were best analyzed by 4-acid dissolution and ICP-MS (near total dissolution, TD-ICP) rather than by metaborate fusion (Diekrup et al., in preparation). For this analysis a 0.25-g sample is treated first with hydrofluoric acid and then by a mixture of nitric and perchloric acids, at each step heated in several ramping and holding cycles which take the samples to dryness. The samples are then brought back into solution using hydrochloric acid and analysed by ICP-MS and the method of internal standardization. The trace elements, As, Sb, Hg, Tl, W, Ag, Zn, Cd, Cu, Pb, Ni, Co, Bi, Ga, In, Mo, Sn, Re, Te, and Se were also determined by TD-ICP. Au was analyzed in select samples by instrumental neutron activation (INAA). The REE, together with Ge, Nb, Ta, Th, Y, were determined by the fusion technique (FUS-ICPMS)

to ensure total dissolution of refractory host minerals. C-total and S-total were determined by combusting a 0.2-g sample in pure oxygen in an induction furnace coupled to infrared detectors (IR-EA). During combustion, carbon-bearing compounds release all carbon in the sample, which binds with the oxygen to form CO_2. Sulfur-bearing compounds release sulfur, which binds with oxygen to form SO_2. Carbon dioxide and SO_2 were determined by absorption of IR energy at different wavelengths. Loss on ignition (LOI) was determined prior to the fusion described above. The LOI, which includes H_2O+, CO_2, S and other volatiles, is determined from the weight loss after roasting the sample at 1050°C for 2 hours.

Detailed mineral chemical data were obtained by scanning electron microscopy (SEM) and electron microprobe analysis (EPMA). Backscattered electron images were produced on a JEOL 6610LV scanning electron microscope (SEM) at the Department of Earth and Environmental Sciences at the University of Ottawa. Chemical analyses of selected minerals were obtained on a JEOL 8230 SuperProbe (EPMA) in the same facility, allowing quantitative chemical analyses of volumes as low as 1 μm^3. Details of the analytical methods are provided in Appendix 5. Cathodoluminescence (CL) imaging of quartz and apatite was conducted using the CL detector on the JEOL 6610LV SEM. The CL effect is hampered by the presence of trace Fe, so the technique could not be used for the other minerals.

Table 5.1. Whole-rock analytical methods used for different elements and limits of detection. The detailed analyses are presented in Diekrup et al. (submitted).

Element		DL	Method
Si	%	0.005	FUS-ICP
Al	%	0.005	FUS-ICP
Fe	%	0.007	FUS-ICP
Ca	%	0.007	FUS-ICP
Mg	%	0.006	FUS-ICP
Na	%	0.002	TD-ICP
K	%	0.002	TD-ICP
P	%	0.004	FUS-ICP
LOI	%	0.01	FUS-ICP
Total C	%	0.01	IR-EA
Total S	%	0.01	IR-EA
Ti	ppm	6	FUS-ICP
Mn	ppm	0.2	TD-ICP
Zn	ppm	0.04	TD-ICP
Cu	ppm	0.04	TD-ICP
Pb	ppm	0.1	TD-ICP
Au	ppb	2	INAA
Ag	ppm	0.01	TD-ICP
As	ppm	0.02	TD-ICP
Sb	ppm	0.02	TD-ICP
Hg	ppm	0.002	TD-ICP
Tl	ppm	0.01	TD-ICP

Cd	ppm	0.02	TD-ICP
Co	ppm	0.02	Td-ICP
Ni	ppm	0.10	TD-ICP
Se	ppm	0.02	TD-ICP
Mo	ppm	0.01	TD-ICP
Te	ppm	0.02	TD-ICP
Sn	ppm	0.2	TD-ICP
Ge	ppm	0.5	FUS-ICP
Bi	ppm	0.004	TD-ICP
In	ppm	0.02	TD-ICP
Re	ppm	0.0002	TD-ICP
W	ppm	0.02	TD-ICP
Cr	ppm	0.1	TD-ICP
V	ppm	0.2	TD-ICP
Ga	ppm	0.02	TD-ICP
Zr	ppm	0.2	TD-ICP
Ba	ppm	0.2	TD-ICP
Cs	ppm	0.01	TD-ICP
Li	ppm	0.1	TD-ICP
Be	ppm	0.02	TD-ICP
B	ppm	0.2	TD-ICP
Hf	ppm	0.1	FUS-ICP
Nb	ppm	0.2	FUS-ICP
Ta	ppm	0.01	FUS-ICP
Rb	ppm	0.04	TD-ICP
Sr	ppm	0.04	TD-ICP
U	ppm	0.01	FUS-ICP

Th	ppm	0.05	FUS-ICP
Y	ppm	0.5	FUS-ICP
La	ppm	0.05	FUS-ICP
Ce	ppm	0.05	FUS-ICP
Pr	ppm	0.01	FUS-ICP
Nd	ppm	0.05	FUS-ICP
Sm	ppm	0.01	FUS-ICP
Eu	ppm	0.005	FUS-ICP
Gd	ppm	0.01	FUS-ICP
Tb	ppm	0.01	FUS-ICP
Dy	ppm	0.01	FUS-ICP
Ho	ppm	0.01	FUS-ICP
Er	ppm	0.01	FUS-ICP
Tm	ppm	0.005	FUS-ICP
Yb	ppm	0.01	FUS-ICP
Lu	ppm	0.002	FUS-ICP
Sc	ppm	1	FUS-ICP

Figure 5.1 Satellite (Google Earth) image of the Temagami area and the Sherman Mine. The North, South, and West pits and the Highway 11 outcrop, where mapping and sampling was conducted, are shown in red letters. The A-series of ore blocks (see Appendix 3) are located near the former mill sites (indicated by the short orange line).

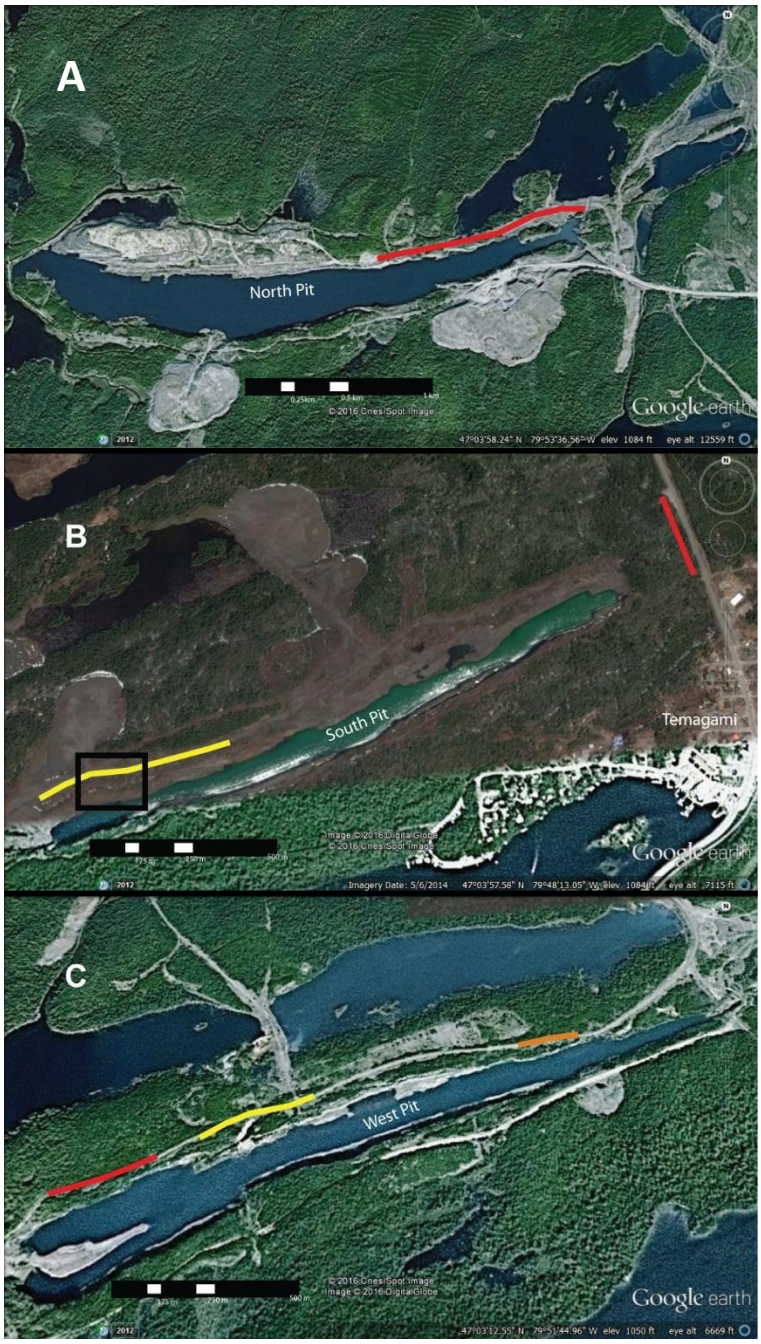

Figure 5.2 Satellite (Google Earth) images of the Sherman Mine showing the locations of mapping and sampling sites. A) North pits of the Sherman Mine showing the location of the C-series blocks (see Appendix 3) along the red line. B) South pit of the Sherman Mine showing the location of the B-series ore blocks (see Appendix 3) along the yellow

line. The box is shown in greater detail in Figure 5.3. The red line corresponds to the Highway 11 outcrop. C) West pit of the Sherman Mine showing the locations of the D-, E- and F-series ore blocks (see Appendix 3) along the yellow, orange and red lines, respectively.

Figure 5.3 A) Typical distribution of ore blocks at the edges of the open pits. Ore blocks, 1-2 m in size, are placed approximately every 2-3 m along almost all roads of the mine site. A total of 301 blocks of this size were documented. Blocks A015, A016 and A017 are pictured. B) A section of B-series ore blocks from Figure 5.2B as seen in Google Earth.

Figure 5.4 Field photographs of representative large ore blocks from the Sherman Mine pits. A) Block A013: black chert-dominated BIF. B) Block B031: white chert-dominated BIF. C) Block C004: magnetite and jasper BIF from the C-series. D) Block D001: chlorite-rich BIF. E) Block E004: magnetite and jasper BIF from the E-series. F) Block F021: mixed chert and chlorite BIF.

6. Field Observations

The major depositional units of the Sherman Mine sequence are mafic metavolcanic rocks, felsic metavolcanic rocks, detrital metasedimentary rocks and banded iron formation. Together they comprise the Formation level elements of the Temagami Greenstone Belt. They can be divided into lower and upper members, corresponding to the footwall and hangingwall units of the mine sequence, respectively (Figure 4.1).

Terms used in this thesis to describe the BIF and its hots rocks are defined as follows:
A formation is a mappable lithology (i.e., traceable from outcrop to outcrop) recognized as having a particular stratigraphic position and usually consisting of more than unit (e.g., Temagami rhyolite formation, which consists of both coherent and clastic units).
A section is used here to describe a number of different BIF units assembled into a contiguous exposure and bound above and below by rocks of a different type. This term has no stratigraphic or depositional significance but, if formally defined and accepted, could be equivalent to a “formation.”
A member is part of a formation that is higher in rank than an individual unit (e.g., volcanic sandstone member of the Temagami rhyolite formation).
A unit is one or more beds of a particular type plus interlayer material (e.g., a mafic flow unit consisting of several flows); if formally defined and accepted, this could be equivalent to a “member” or “formation.”

A bed is a layer of sediments bounded above and below by well-defined depositional surfaces. In the Temagami BIF, beds typically comprise a single facies type but may comprise many sub-layers.

A lamina is the thinnest possible layer of a sedimentary rock that differs from other layers in composition or grain size (e.g., a single layer of white chert). A bed can consist of many individual laminae.

By these definitions, and according to the local structural and stratigraphic interpretation, the BIF exposed in the different pits (and Highway 11 outcrop) represents a “formation” level stratigraphic unit.

The type section of the upper Temagami BIF is exposed in the Highway 11 outcrop, the main features of which are shown in Figure 6.1. The exposure is part of the BIF exploited from the South and West pits, which extend for more than 0.5 km to the west. The BIF layers in the outcrop dip subvertically and are overturned. Their total thickness is 170 m (although a 40-m interval in the middle of the outcrop is not exposed). The same BIF units can be traced 200 m to the east, on the east side of Highway 11, and the BIF has been mapped more than 3 km to the west of the North pit (1978 OGS map). Therefore, the total strike length is at least 6 km.

In the Highway 11 outcrop, the lower contact of the BIF section is broadly conformable with pillowed mafic volcanic rocks. The upper contact is gradational with poorly sorted but locally graded volcanicastic rocks (wacke) that are well exposed in the southernmost

10-m wide section of the outcrop. Minor centimeter- to decimeter-thick units of clastic metasediment are interbedded with the BIF, including black shale, massive sulfide, and mafic volcaniclastic layers. The entire section is cut by small dikes of mafic intrusive rock, which are well exposed at meter 40, 65 and 130 (Figure 6.1 and Figure 6.2a). Most of the dikes are at a low angle to bedding, suggesting that they were intruded after the BIF section weas overturned.

More than 600 discrete beds were counted in the Highway 11 outcrop. Individual beds can exhibit a number of different synsedimentary features within individual layers, including faulting, folding, and load structures (Figure 4.2), as well as internal mineralogical changes (e.g., magnetite-jasper transitions and microbanding: Figure 6.3d and Figure 6.2c). Quartz veinlets, which are generally perpendicular to bedding, are widespread (Figure 6.4b).

The different facies identified in outcrop include chert BIF, magnetite BIF, chlorite BIF, jasper BIF, greywacke, and mafic volcaniclastics (Figure 6.4). The chert BIF occurs in layers that are typically 3-10 cm thick and can appear black, white, or grey with black and white patches; some layers are composed of many ~1 mm alternating black and white microbands. Chert BIF commonly exhibits synsedimentary deformation (Figure 4.2c, Figure 4.2d). Thicker black chert layers locally can be seen to grade into jasper (red chert). In other black chert and magnetite BIF layers, apparent clasts of jasper, ~1 mm in size, can be seen (Figure 6.3a). Jasper BIF generally occurs in thinner, 1-5 cm layers and they also commonly show synsedimentary deformation (Figure 4.2d).

Magnetite BIF occurs in layers that are typically 1-4 cm thick. They range from dark grey to black with a metallic luster. In outcrop, the magnetite can be massive and fine-grained or locally with visible ~1 mm euhedral crystals. Some layers of magnetite BIF show spaced fractures that are confined to the layers and most likely represent extension cracks or dessication cracks (Figure 6.3b). Chlorite BIF occurs as 1-10 cm thick green layers, which are soft and extremely fine grained (Figure 6.4c).

Figure 6.5 is a stratigraphic section of the Highway 11 outcrop showing the distribution of the different BIF facies. The lowermost 25 m of BIF is underlain by pillowed mafic volcanic rocks and mafic volcaniclastics with BIF clasts. Chlorite BIF and jasper BIF are found in these lowermost units, close to the mafic volcanic footwall; the rest of the section is dominated by magnetite and chert BIF. Two mafic dikes and numerous quartz veins cut the BIF layers. This section of BIF is more thickly banded, layer boundaries are straight, and little or no (synsedimentary) folding is evident. The lowermost BIF section is overlain by 10 m of mafic volcaniclastics with BIF clasts (although ~10 m of this section is not exposed). An isolated pod of semi-massive pyrite occurs in the mafic volcaniclastics, which are pervasively altered (and possibly accounts for the erosion of this part of the outcrop). Mafic volcaniclastics with BIF clasts continue for another ~5 m to a second, much thicker upper section of BIF, approximately 40 m thick and containing different layers of jasper, magnetite, chert, and chlorite BIF. The number of jasper layers varies through the outcrop, many layers have irregular or uneven boundaries, and synsedimentary folding is abundant in this section. A visual comparison between the upper and lower section of the Highway 11 outcrop shows the

increased prevalence of jasper in the upper section (Figure 6.6). The uppermost layers of the upper BIF section include chlorite BIF in addition to jasper BIF. The chlorite BIF is mostly undeformed but shows local synsedimentary folding (Figure 6.3c). Two Types of chlorite bands are recognized; one consisting of very fine-grained chlorite that may represent primary Fe-Mg-rich clays, and another associated with lithic clasts that are likely volcaniclastic in origin (see below). Fine-grained chlorite has a preferred orientation parallel to bedding, while chlorite associated with lithic clasts is massive. Above the last jasper layer in the Highway 11 outcrop, chlorite, chert and magnetite layers alternate. The top of the BIF section includes mafic volcaniclastics with BIF clasts and is overlain by greywacke. Locations along the Highway 11 outcrop from which rock samples were taken are indicated in Figure 6.7.

Both synsedimentary and post-depositional deformation features are evident throughout. The synsedimentary folds are most obvious in the thickest layers and are indicated by their nonpenetrative nature in the outcrop; with the intensity of folding varying within layers and between layers (Figure 4.2c). Most faults in the outcrop are also synsedimentary, showing ductile displacement and terminating within layers. Beds are generally displaced by <1 cm (Figure 4.2d). Some late faulting is evident adjacent to quartz veins and mafic dikes.

A smaller BIF outcrop on the east side of the highway extends ~10 m farther south than on the west side of the Highway. This may be due to large-scale block faulting as proposed by Bennett (1978).

Sedimentological features: Different sedimentological features shown in Figures 6.2-6.4 are illustrated schematically in Figure 6.8. Typical interlayering of chert, chlorite, and magnetite facies and undulating boundaries between them are illustrated. Discrete bands of BIF show clear laminations as well as undulating layer boundaries and thickening or thinning, most probably related to the microtopography of the paleoseafloor. Larger-scale scouring features, where one set of BIF layers cuts another set, are also seen on the outcrop, and sediment loading structures are evident locally. All of these features indicate way-up consistent with younging to the south. Even in sections of BIF deformed by synsedimentary folding and faulting, boundaries between the macroscopic layering appear uniformly sharp, although gradations are evident at the microscopic scale (see below).

Facies relationships: The black chert facies is most common (40 % of the BIF); in decreasing order of abundance, magnetite (23 %), chlorite (20 %), white chert (10 %), and jasper (7 %) account for the remainder of the BIF units. Somewhat less magnetite is observed in the archive blocks, and this may partly account for the fact that they were not sent to crusher. Different facies relationships observed in the Highway 11 outcrop, including several key textural relationships between layers are also summarized in Figure 6.8.

The mineralogy of most beds does not change along strike. Exceptions include beds with alternating ~1 mm laminae of both black chert and white chert, or where jasper is

replaced by black chert within the same band (see Figure 6.8). It is not uncommon for hematite-dominated and magnetite-dominated layers to coexist within one bed (Figure 6.3d). Establishing the paragenetic relationship between hematite and magnetite in these different examples was a major goal of this study. In most cases, it appears that hematite is replaced by magnetite, for example where black chert "encroaches" on jasper beds (Figure 6.3e), leaving remnants of jasper along the layer boundaries. Inclusions or jasper "relicts" are also found in magnetite BIF (Figure 6.3a).

Table 6.1- Field characteristics of the Temagami BIF facies.

Facies	Color	Mineral Habit	Magnetism	Thickness (cm)
Black Chert	Black	Massive	Magnetic-strongly magnetic	0.1-10
White Chert	White	Massive	Nonmagnetic	0.1-10
Magnetite	Gray	Aggregate	Strongly magnetic	0.5-5
Chlorite	Green	Aggregate	Magnetic-strongly magnetic	2-10
Jasper	Red	Massive	Nonmagnetic-magnetic	0.1-5

Distinguishing features of the different BIF facies observed in the field are summarized in Table 6.1. In wet conditions, the magnetite and black chert facies often could not be distinguished easily by colour; in this case only magnetism and the mineral habit visible with a hand lens could be used to distinguish one facies from another. The magnetic intensity varies along the outcrop with magnetite content (Figure 6.9), but it is clear that all layers contain some magnetite. The mafic intrusions and clastic metasedimentary units are least magnetic.

More detailed observations of the individual facies were possible in the large ore blocks. These were used to document the variations in the characteristics of the different facies throughout the Sherman mine (thickness of layers, abundance of layers, relationships between layers) and also the distribution of different facies in the pits. These data are compiled in Appendix 3. As an example, a detailed description of a block from the south pit, B013, is given in Figure 6.10. It shows the remarkably fine scale of layering and facies variations at a scale much smaller than the Highway 11 outcrop. However, the relative abundance of the different facies are similar despite the very different scale: 40% chlorite, 20% chert, 20% magnetite and 10% jasper in block B013 and 40% chert, 30% chlorite, 20% magnetite and 10% jasper on average in the Highway 11 outcrop. The locations of the other blocks included in this study are shown in Figure 6.11.

Important differences are seen between the BIF from the North and South pits. Only 15% of the ore from the North pit (C-series) was chlorite-rich, whereas ore blocks from the South pit (B-, D-, E- and F-series and Highway 11 outcrop: Figure 6.10) comprise at least 30% chlorite-rich volcaniclastic material. Blocks from the north pit have more abundant coarse magnetite and jasper. The differences in the facies distribution between the North and South pits (including the Highway 11 outcrop) support the suggestion that they are not part of a single BIF unit repeated by a regional fold but more likely represent two separate BIF horizons. We cannot exclude that the differences between the North and South pits could reflect facies changes within a single folded unit. However, evidence of consistent younging to the south does not support the existence of a synclinal structure.

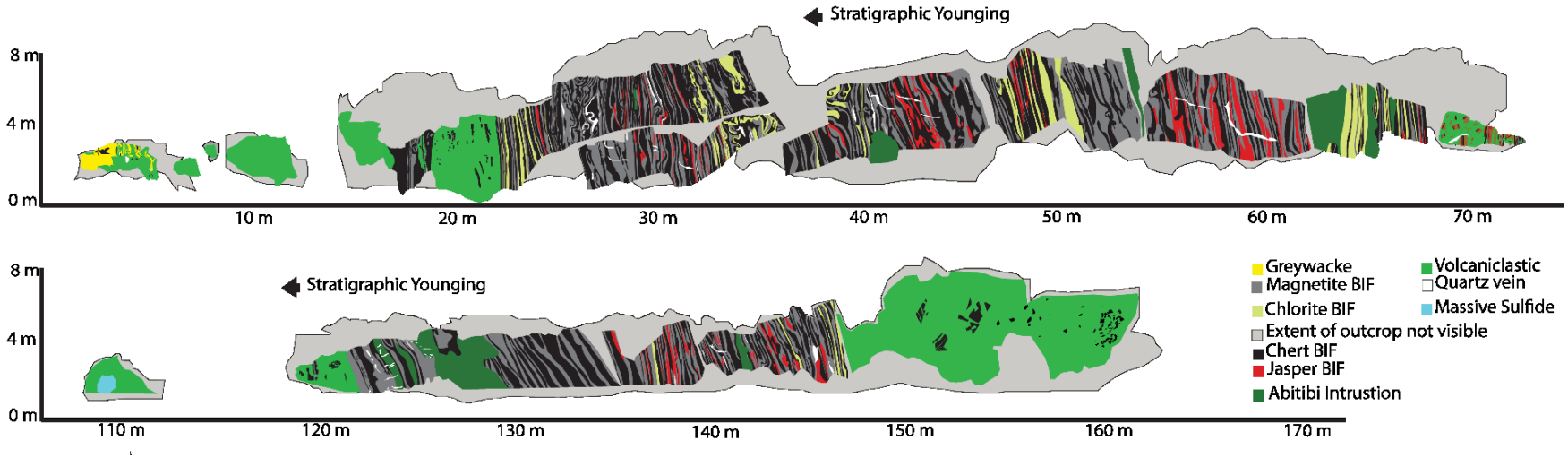

Figure 6.1 Measured section of the Highway 11 outcrop, a type section for the Temagami BIF. The outcrop is about 170 m in length and includes the detrital metasediment (volcanic sandstone) in the south, mafic metavolcanic rocks, and BIF members of the upper Temagami greenstone belt. The outcrop comprises two 30-50 m BIF sections flanked by mafic metavolcaniclastic rocks. An intervening section of basalt contains minor sulfide mineralization, partly covered by overburden. The BIF units are overturned and nearly vertically dipping. The mapped units include chert BIF, magnetite BIF, chlorite BIF, jasper BIF, greywacke (detrital metasedimentary unit), mixed mafic volcaniclastics and flows (mafic metavolcanic unit), and mafic intrusions. The chert BIF unit consists of 3-10 cm-thick layers which can be black or white or patchy in appearance, many with black and white microbands ~1 mm. The magnetite BIF unit consists of 1-4 cm-thick gray-to-black layers with a dull metallic luster. The chlorite BIF unit consists of 1-10 cm-thick green layers which may be weakly deformed. The jasper BIF unit consists of 1-5 cm-thick reddish to maroon layers. Quartz veinlets perpendicular to bedding are common. The figure is a summary of the first detailed measurements of what has become the only

remaining type section of Temagami BIF. Note: In the time since the production of this section, Google Inc. produced a Street View photomosaic that shows many of the mapped features.

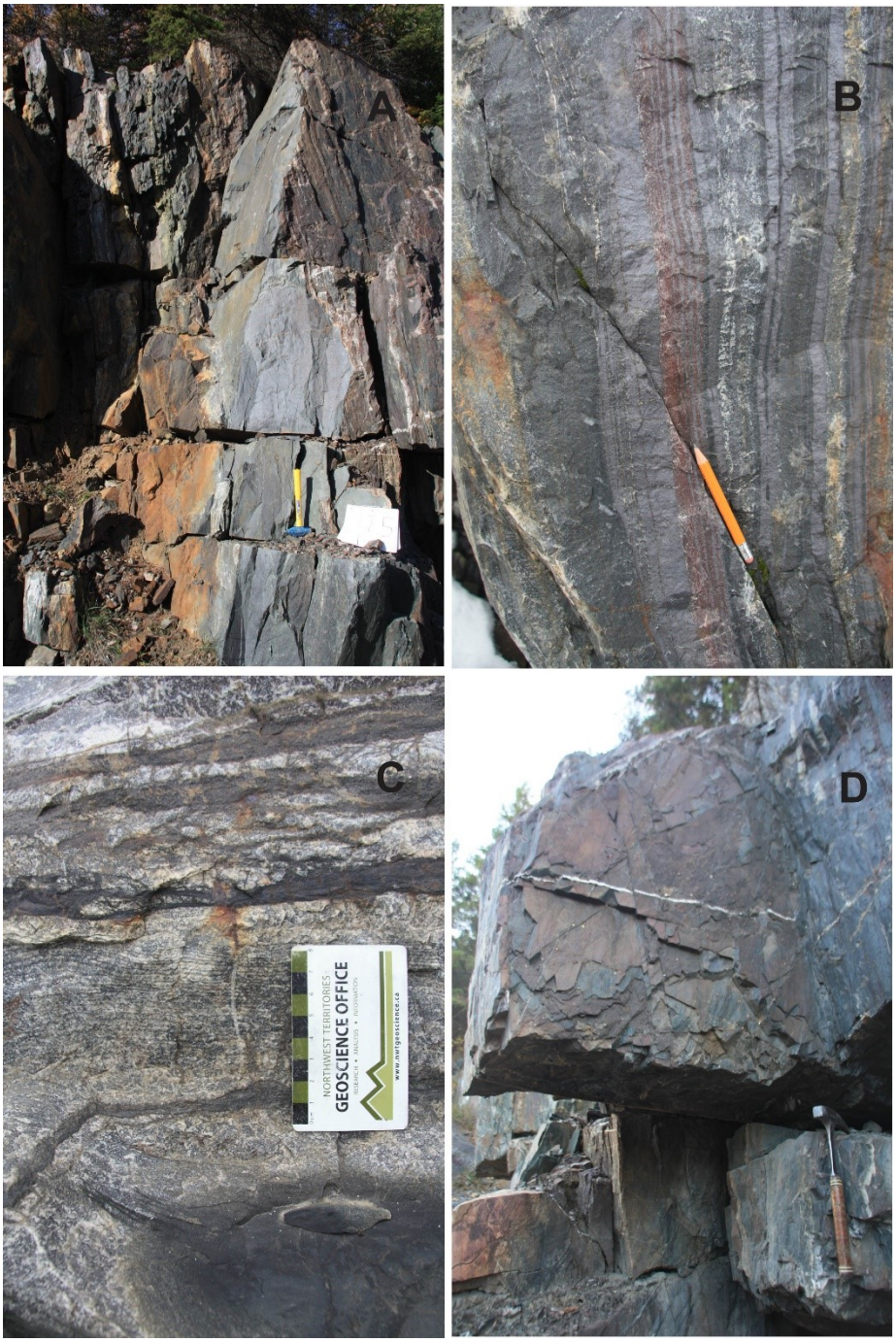

Figure 6.2 Field photographs of typical features in the Highway 11 outcrop. A) A mafic dike cross-cutting beds of the BIF. B) Typical magnetite, jasper and black chert beds in the same exposure. C) White chert bed with black chert laminae, referred to as “microbanded chert” in the thesis. D) A quartz vein cutting bedding in the BIF layers.

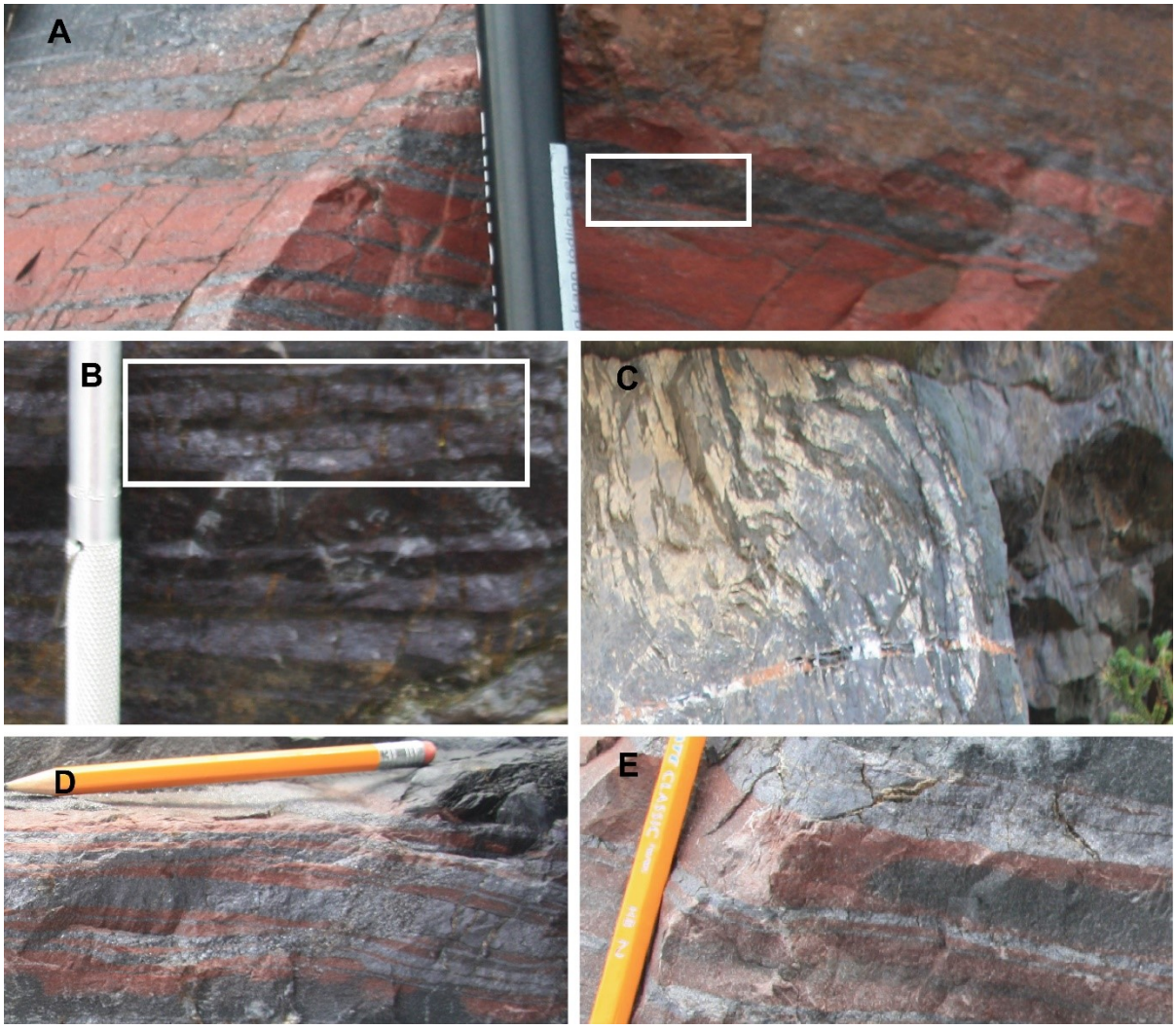

Figure 6.3 Field photographs of different layer Types of the Temagami BIF. A) Magnetite and jasper beds in an ore block from the southern pit of the Sherman Mine. The magnetite bands contain ~1mm jasper clasts (visible in the white box). B) Magnetite and black chert beds in a block from the northern pit of the Sherman Mine. Magnetite beds commonly include many white chert microbands (visible in the white box). C) Example of chlorite and chert beds with minor folding in the Highway 11 outcrop. D) Jasper, magnetite and black chert layers in a block from the southern pit of the Sherman Mine. E) Photograph showing black chert "encroaching" on an original jasper layer.

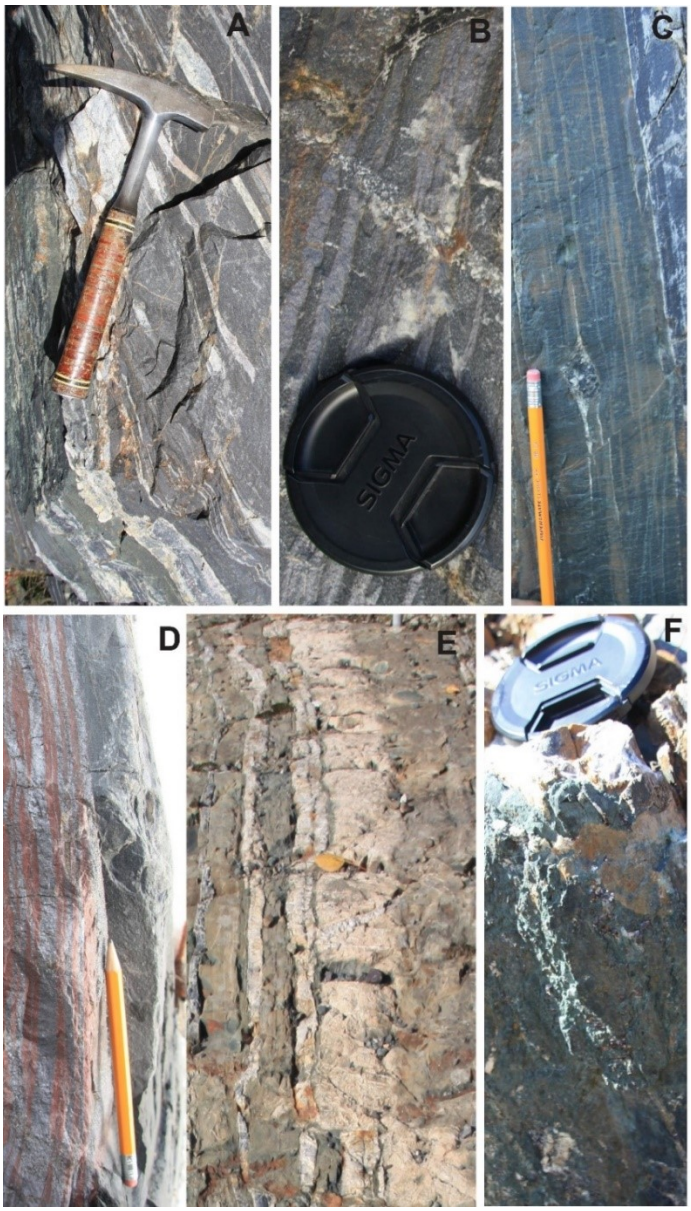

Figure 6.4 Additional field photographs of different layer Types of the Temagami BIF. A) Beds of chert BIF in the Highway 11 outcrop. B) Beds of magnetite BIF and black chert BIF in the Highway 11 outcrop. C) Chlorite BIF bed in the Highway 11 outcrop. D) Beds of jasper BIF and magnetite BIF in an ore block from northern pit of the Sherman Mine. E) Beds of greywacke and mafic volcaniclastic material at the south end of the Highway 11 outcrop. F) Mafic volcaniclastic material in the Highway 11 outcrop.

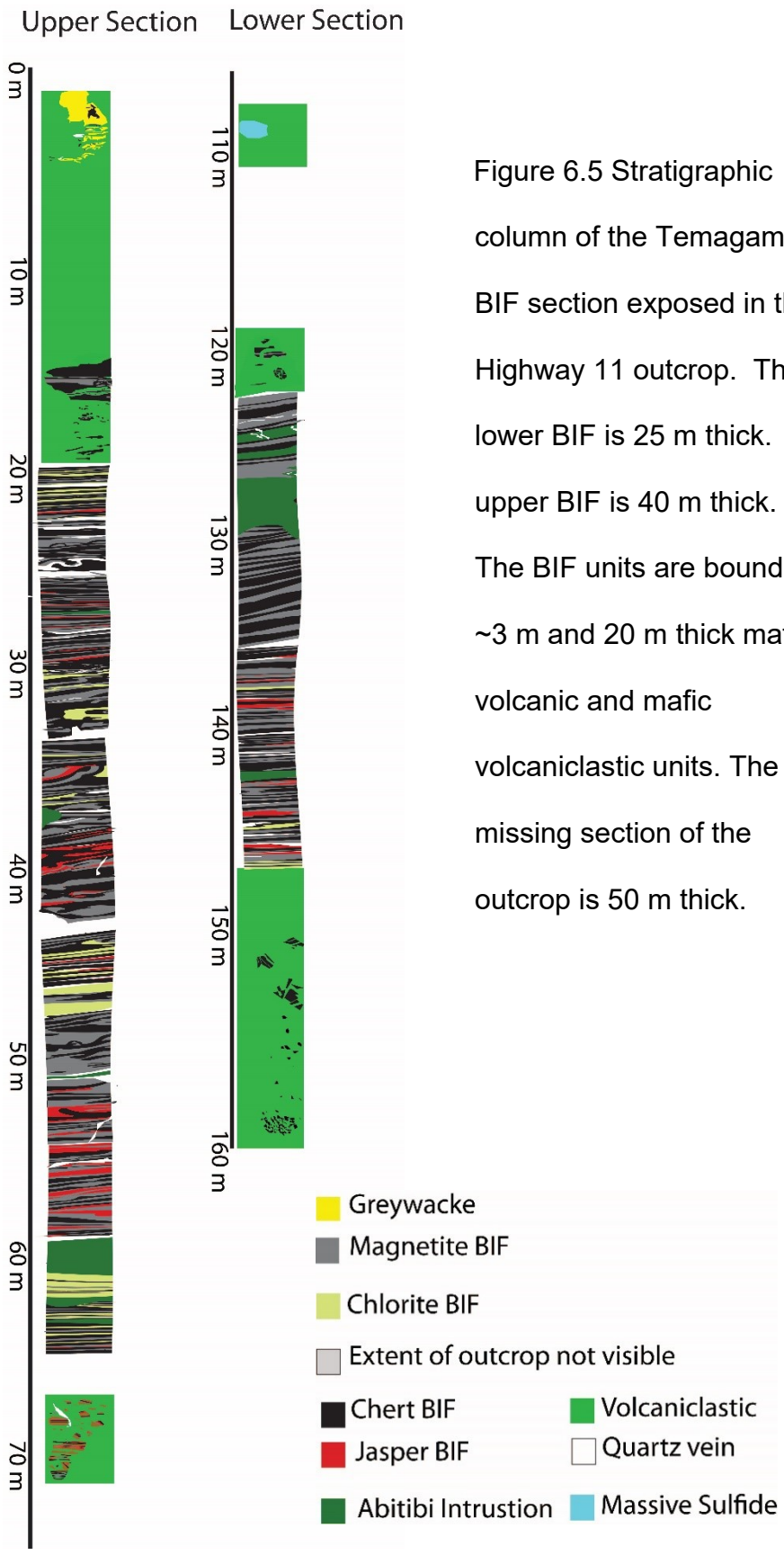

Figure 6.5 Stratigraphic column of the Temagami BIF section exposed in the Highway 11 outcrop. The lower BIF is 25 m thick. The upper BIF is 40 m thick. The BIF units are bound by ~3 m and 20 m thick mafic volcanic and mafic volcaniclastic units. The missing section of the outcrop is 50 m thick.

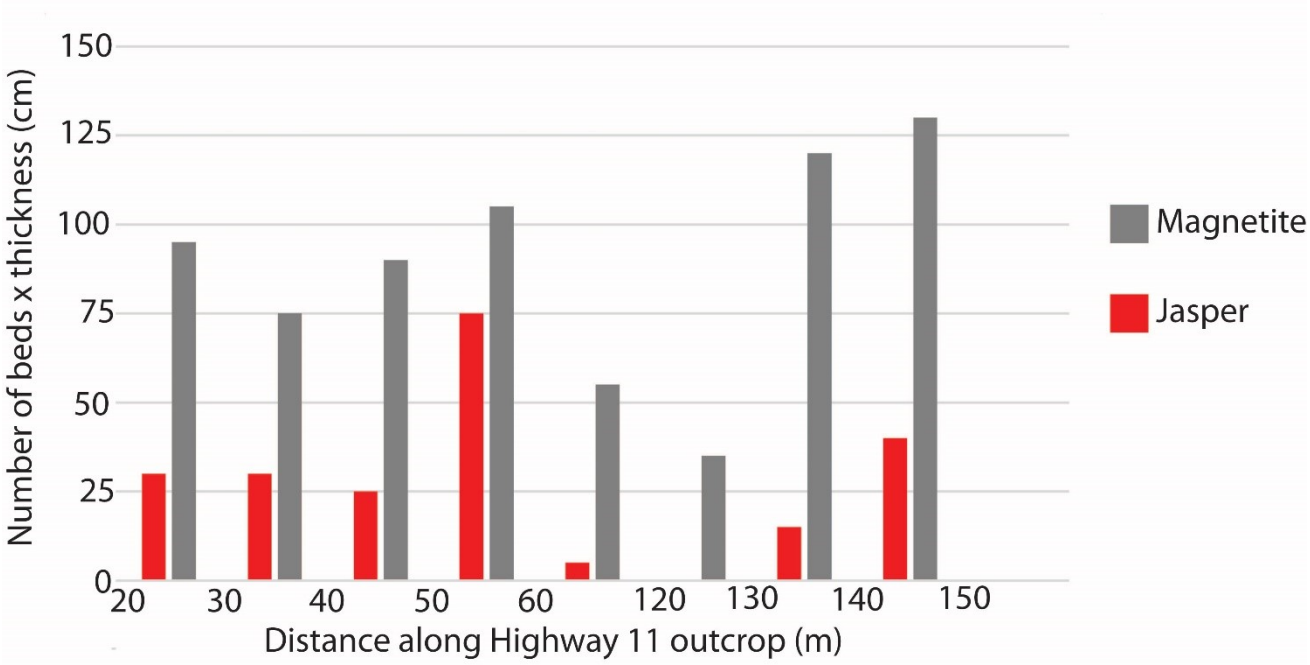

Figure 6.6 Relative proportions of jasper and magnetite along the Highway 11 outcrop. The histogram shows the average thickness of each layer Type in a 10-m section of the outcrop multiplied by the number of discrete beds, based on the stratigraphic column in Figure 6.5. The data show the prevalence of jasper beds at the bottom of the two major exposed sections compared to the top of the sections, possibly reflecting enhanced silica deposition in the early depositional history of each section and preservation of the jasper layers (see text for discussion).

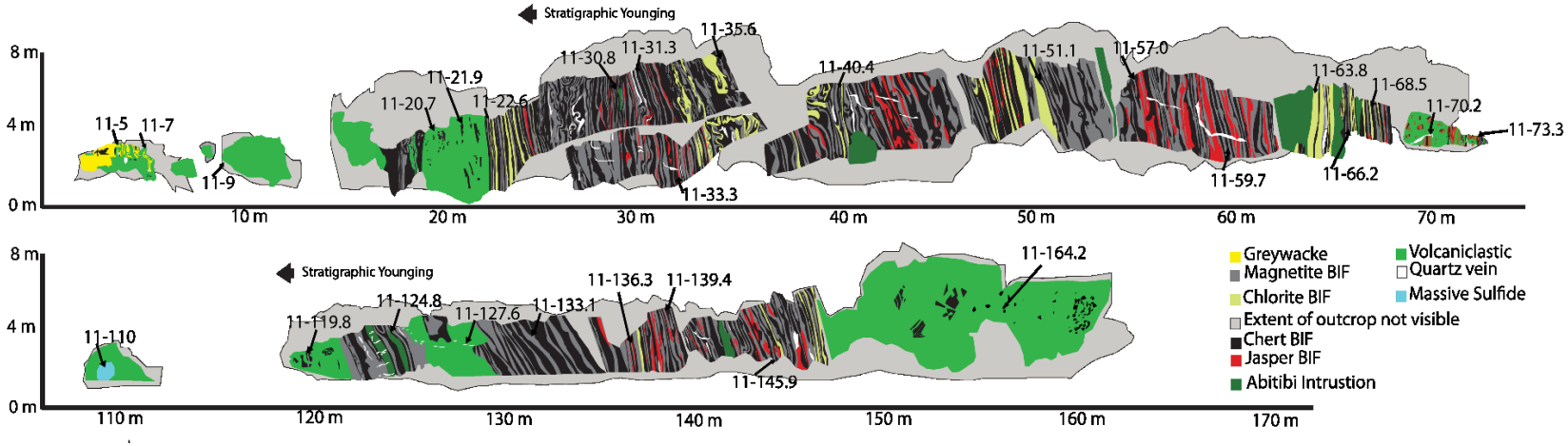

Figure 6.7 Sampling locations along the Highway 11 outcrop (H11 series). Samples were taken at regular, approximately 5 m, spacings to determine if any systematic variations in mineralogy and chemistry could be detected at the outcrop scale, irrespective of the very fine banding. Details of the different facies are given in Chapters 7 and 8.

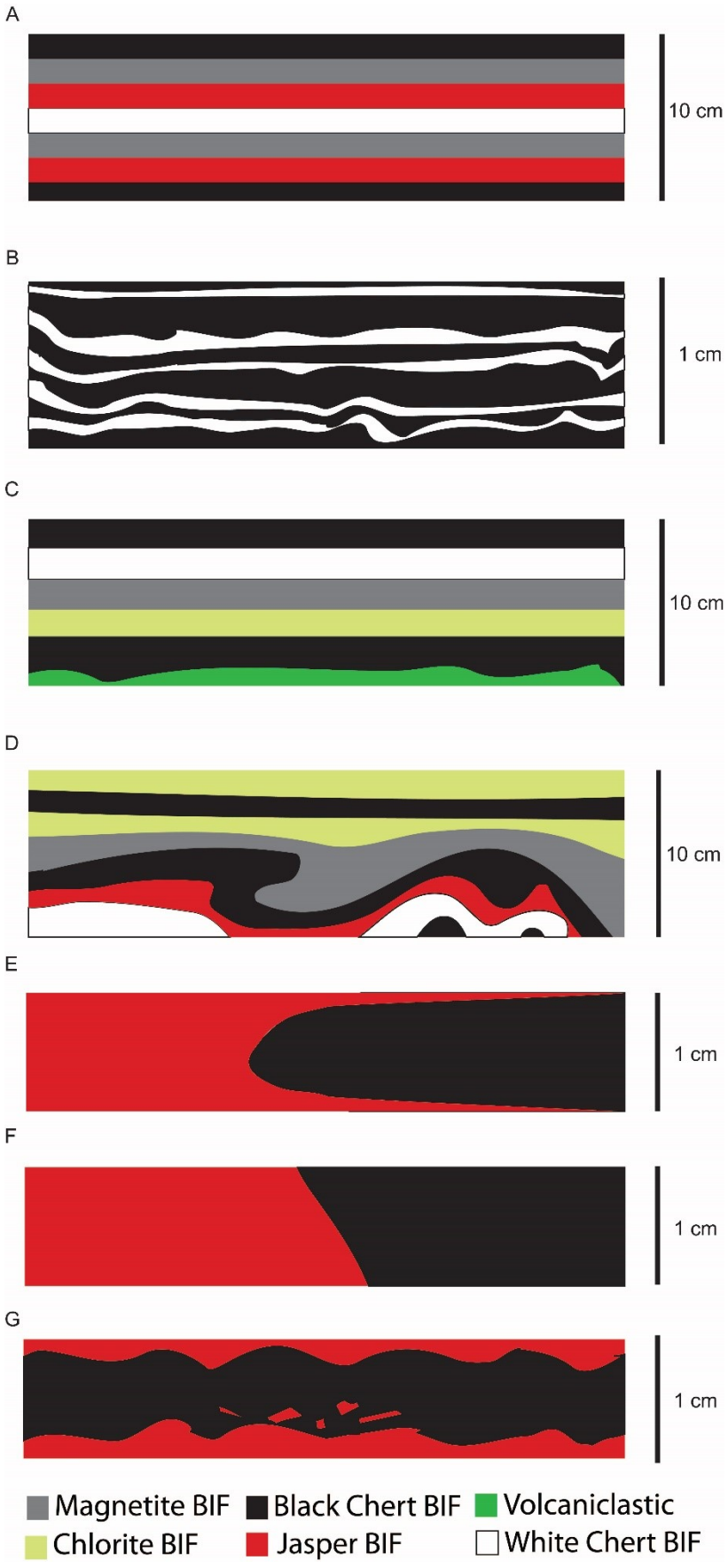
A
10 cm
B
1 cm
C
10 cm
D
10 cm
E
1 cm
F
1 cm
G
1 cm
Magnetite BIF
Black Chert BIF
Volcaniclastic
Chlorite BIF
Jasper BIF
White Chert BIF

Figure 6.8 Schematic representations of typical BIF textures observed in the field. A) Typical well-laminated BIF characterized by flat layer boundaries. Layer thickness in the laminated sections is typically 1-2 cm. B) Wavy microbanded chert BIF with alternating ~1 mm black chert and white chert microbands comprising a single ~1 cm layer. C) Layer of mafic volcaniclastic material in contact with black chert layers. Whereas chert layers show generally flat parallel bedding planes, contacts with volcaniclastic layers are commonly undulating. D) Typical synsedimentary folding confined to single beds of black and white chert or jasper. E) Incomplete replacement of hematite in jasper by magnetite at an "encroaching" replacement front. F) More abrupt transition from hematitic to magnetite-rich chert within a single layer. G) Jasper "pseudoclasts" in a magnetite-rich chert bed, possibly representing relics of jasper after magnetite replacement.

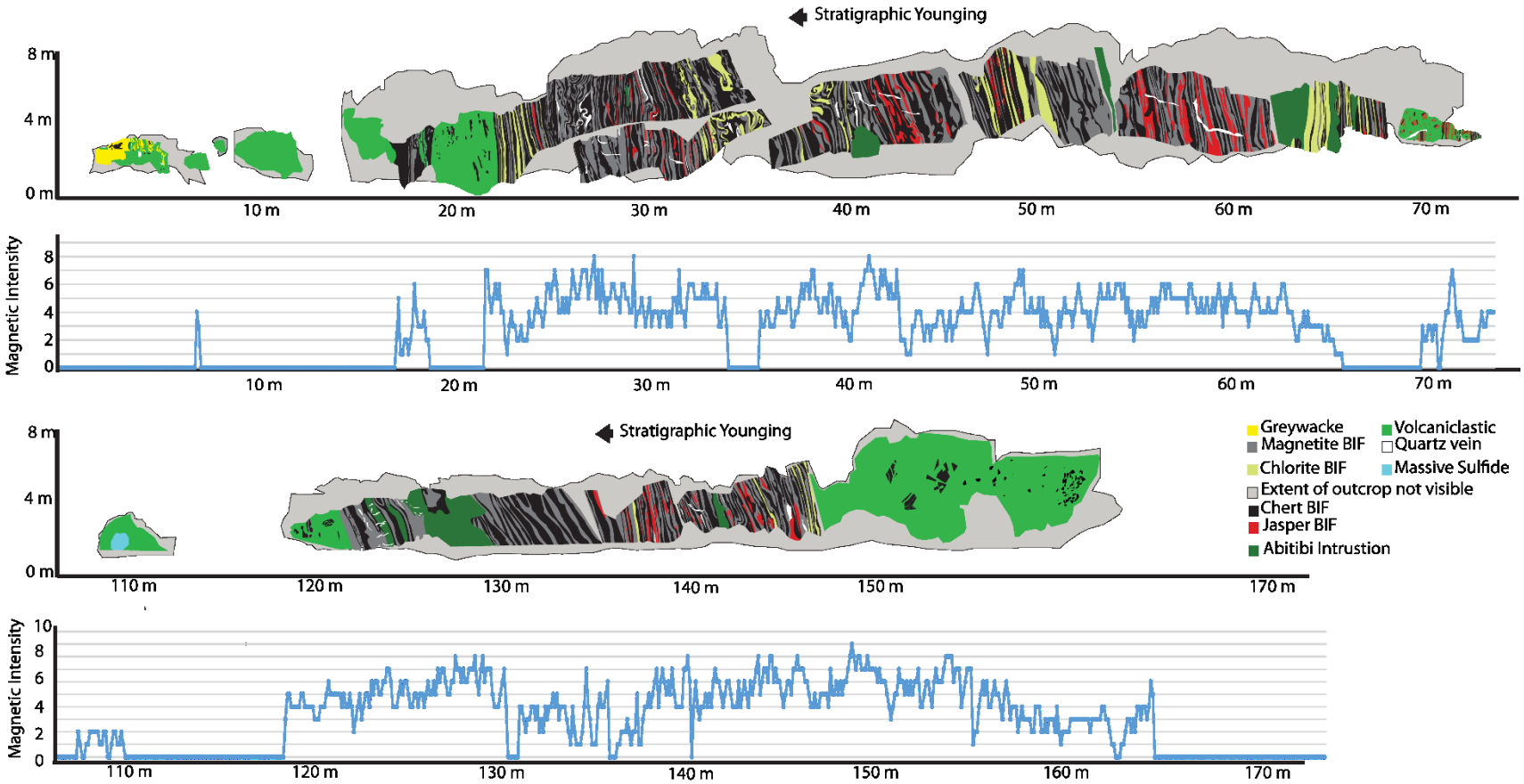

Figure 6.9 Semi-quantitative measurements of magnetic intensity along the Highway 11 outcrop (scale from 0 to 10, where 0 indicates no magnetic response with a hand-held magnet and 10 indicates a strong magnetic response). Magnetite is present in all facies of the BIF, including in some of the mafic volcaniclastic units. The chlorite-rich portions of the outcrop have somewhat lower magnetic intensity. Only the youngest volcaniclastic package and a mafic intrusion were found to be nonmagnetic.

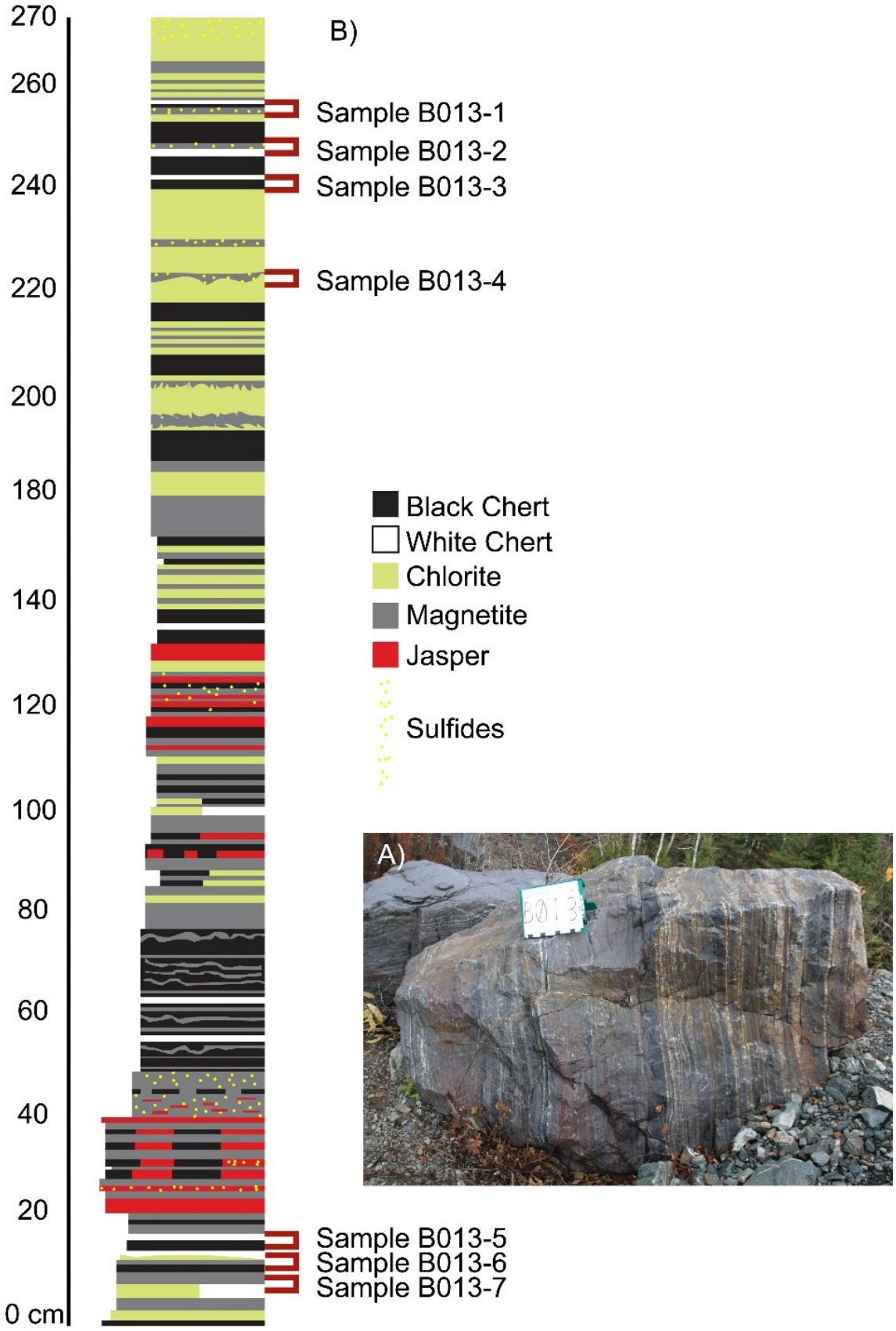
B)
270
260
240
220
200
180
140
120
100
80
60
40
20
0 cm
Sample B013-1
Sample B013-2
Sample B013-3
Sample B013-4
Sample B013-5
Sample B013-6
Sample B013-7
Black Chert
White Chert
Chlorite
Magnetite
Jasper
Sulfides
A)

Figure 6.10 Example of sampling profiles in several of the larger ore blocks from the Sherman Mine pits aimed at individual layer Types. The example shown is block B013 (A) together with a schematic profile of the BIF bedding and the sample locations (B). Nearly 150 discrete layers were logged in the 2.6 m long block, with no evidence of deformation. Chert layers are between 1 mm and 7 cm, magnetite layers are between 0.1 and 10 cm, chlorite layers are between 1 cm and 10 cm, jasper layers are between 1 and 3 cm. Jasper is partially replaced by black chert in many of the layers, and chert is interlayered with chlorite. Trace sulfides occur in black chert, magnetite, jasper and chlorite layers. There are undulatory boundaries between magnetite and chlorite beds. The thickness of the magnetite layers varies with crystal size (thick layers characterized by coarser >1 mm crystals).

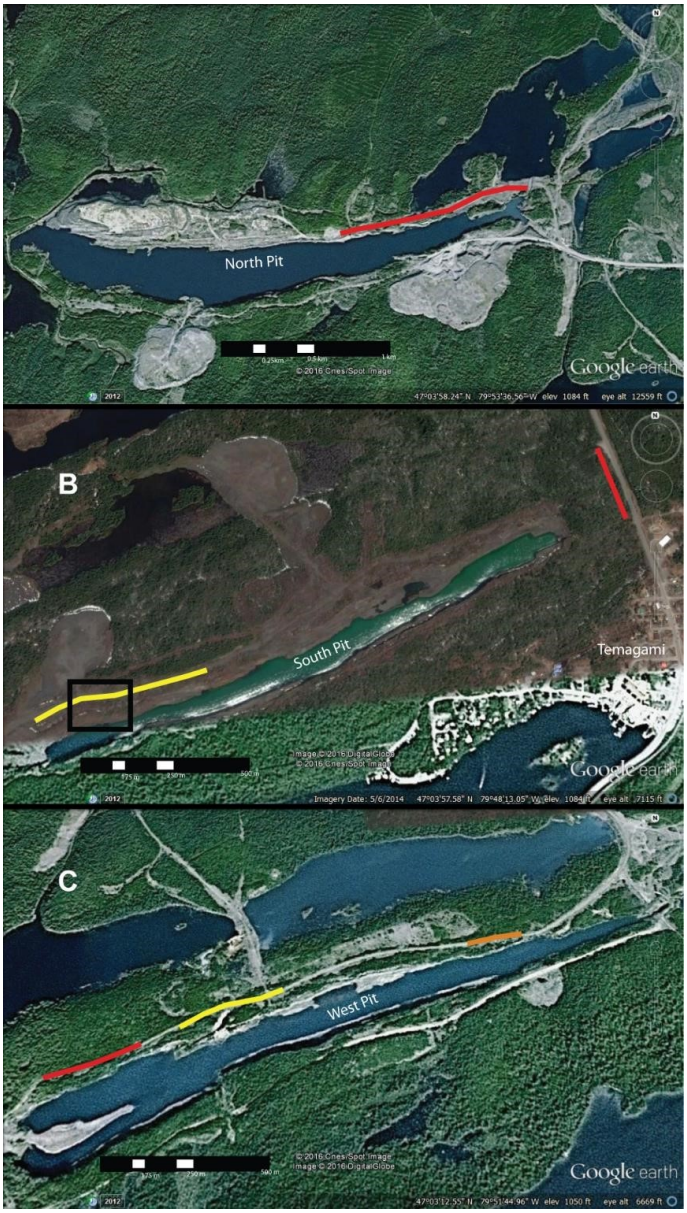

Figure 6.11 Satellite (Google Earth) images of the Sherman Mine area showing the locations of sampling sites (see also Figure 5.3). A) North pits of the Sherman Mine showing the location of the C-series blocks (see Appendix 3) along the red line. B) South pit of the Sherman Mine showing the location of the B-series ore blocks (see Appendix 3) along the yellow line. The box is shown in greater detail in C. The red line corresponds to the Highway

11 outcrop. C) West pit of the Sherman Mine showing the locations of the D-, E- and F-series ore blocks (see Appendix 3) along the yellow, orange and red lines, respectively.

7. Mineralogy and Paragenesis

7.1 Mineralogy

The different ore facies are dominated by quartz, hematite, magnetite, or chlorite. Representative photographs of different mineral assemblages in the main ore facies (jasper, black chert, white chert, magnetite and chlorite) are shown in Figures 7.1 to 7.5.

Quartz is the dominant mineral in all samples and exhibits four different habits. Type 1 quartz consists of fine (<50 um) anhedral grains (Figure 7.2a) and is a major component of the black chert facies. Type 2 quartz is much coarser (>100 μm), and forms euhedral crystals (Figure 7.3c). It dominates the white chert facies and is present, but less common, in the magnetite facies. Type 3 quartz occurs as ultrafine microveinlets (10-50 μm in thickness), which are common in fractures within the magnetite facies. Importantly, the microveinlets generally are confined to single bands and do not cross into adjacent layers (Figure 7.4f). Larger veins of quartz, >100 μm in thickness, are also found in all facies and, in general, are perpendicular to and cut layering (Figure 6.4b and Figure 7.2c).

Hematite is abundant in certain facies and exhibits two main habits. Type 1 hematite occurs as clusters of <1 μm, subhedral crystals (Figure 7.1b). The clusters are typically enclosed in spheroidal aggregates of quartz that range in size from 5 to 50 μm. Commonly, the hematite crystals are so fine that they cannot be clearly seen with an

optical microscope. Their presence as submicroscopic inclusions in the spheroidal quartz aggregates is indicated by a distinctive reddish tint under the microscope, and this is the main source of the red colour of the jasper bands. Where visible, the microcrystalline hematite has a dark red internal reflection under transmitted light. Type 2 hematite is coarser (>10 μm) but still forms clusters of fine subhedral crystals embedded in quartz (Figure 7.3b).

Magnetite has three distinct habits. Type 1 magnetite consists of small (<10 μm), subhedral grains that commonly occur together with Type 1 hematite as clusters in spheroidal quartz aggregates in the jasper facies (Figure 7.1b). Type 1 magnetite is the main Fe-oxide in the black chert and also in jasper facies. Type 2 magnetite consists of 10-70 μm, subhedral prismatic crystals that are concentrated locally at the margins of spheroidal aggregates of quartz and are generally disseminated in all facies of the BIF. Type 1 hematite is notably absent in parts of the spheroidal aggregates where Type 2 magnetite has formed, strongly suggesting that the coarser Type 2 magnetite is a replacement of the original Type 1 magnetite and hematite (Figure 7.1b). Type 3 magnetite consists of coarser (>70 μm), euhedral crystals, commonly with cubic habit (Figure 7.1d), that occur within and at the margins of quartz veinlets. Some grains of Type 3 magnetite are notably fractured (Figure 7.4b), suggesting some degree of deformation. Coarse-grained Type 3 magnetite is the dominant component of the magnetite facies but is also found in all other facies.

Chlorite has two habits. Type 1 chlorite consists of small (<10 μm), subhedral aggregates lacking any clear cleavage (Figure 7.5b). This type of chlorite dominates the banded chlorite subfacies but is also found in the magnetite facies, commonly in the intergranular spaces between magnetite crystals. Coarser-grained Type 2 chlorite (10-100 μm) occurs as subhedral prismatic grains in the massive chlorite subfacies (Figure 7.5c). These layers commonly contain lithic clasts, which strongly suggest that they are volcaniclastic in origin (i.e., ash). Ilmenite is a common accessory in the massive chlorite subfacies with lithic clasts (Figure 7.5c). Muscovite is found locally as an alteration product (most probably of feldspar) in the lithic clasts (Figure 7.5d).

Accessory minerals, such as pyrite and carbonate, make up less than 1% of the ore and typically exhibit the same mode of occurrence in all ore types. Dolomite and ankerite are present locally as 50-100 μm grains interstitial to coarse magnetite, together with chlorite, apatite and leucoxene, mainly in the magnetite facies (Figure 7.4c). Some carbonate also occurs in microveinlets that cut layering. Apatite is common as disseminated grains, typically >100 μm in size, in spaces between coarse magnetite crystals in the magnetite facies (Figure 7.4c and Figure 7.4d). Leucoxene commonly forms a fine-grained “reaction rim” around Type 2 and Type 3 magnetite in all facies (Figure 7.4b, Figure 7.4c).

Two types of pyrite are observed. Type 1 pyrite consists of small (10-50 μm) subhedral prismatic crystals (Figure 7.6a) in the magnetite facies and chlorite facies, in many cases as inclusions in Type 3 magnetite (Figure 7.6b). Rare Type 2 pyrite forms larger (>100 μm)

euhedral crystals in the magnetite facies and chlorite facies (Figure 7.6c). This appears to be mainly metamorphic in origin (i.e., porphyroblasts overgrowing magnetite).

7.2 Paragenesis

A key relationship examined in this study is the origin of mineralogically distinct bands of BIF and, in particular, the apparent replacement of hematitic bands by magnetite. To explore this in more detail, a careful mineral paragenesis was constructed based on the occurrence, grain size distribution and habit of the different Fe-oxide phases that are interpreted to reflect different stages of mineral growth.

The very fine-grained, dispersed nature of the Type 1 hematite, its tendency to form distinct clusters in well-preserved spheroidal aggregates of quartz (hereafter referred to as quartz “spherules”), and the small crystal sizes suggest that it is close to a primary feature of the ores. Similar quartz spherules and ultrafine disseminations of Fe-oxides have been observed in jasper bands in other BIF, where they are also interpreted to be primary features (Bekker et al., 2010; Slack et. al, 2007). Coarser-grained quartz is common in white chert facies and most probably a product of diagenetic or metamorphic recrystallization of primary spheroidal quartz aggregates. Type 1 magnetite, which occurs with Type 1 hematite but is generally coarser, is interpreted to have formed by replacement of the finer hematite (on its way to becoming Type 2 magnetite). This interpretation is also supported by observations from petrographic studies of other BIF (Mucke, 1996; Tompkins and Cowan, 2001). Type 2 magnetite occurs only at the

margins of quartz spherules in jasper bands (Figure 7.1b). The fact that a range of quartz and hematite textures is observed, including ultrafine “primary” hematite clusters, commonly in the same samples as coarser magnetite, strongly suggests that the different BIF layers have not been wholly recrystallized and that primary textures are well-preserved (see Discussion). Like Type 1 hematite, the finest-grained chlorite (Type 1) is interpreted to have originated as a direct chemical precipitate (most probably smectite or nontronite: Bekker et al., 2010). Coarser chlorite associated with lithic clasts is interpreted to be an alteration product of volcanic ash, although definitive evidence of glass shards could not be found.

Type 3 magnetite appears to have overgrown Type 2 magnetite (Figure 7.2c) and therefore also postdates all types of hematite. Abundant Type 1 and Type 2 magnetite are distributed throughout the matrix but are generally absent in the halo of the coarse Type 3 magnetite. Importantly, in bands where magnetite is not abundant, coarse-grained Type 3 magnetite occurs only where quartz microveinlets cut the bands, strongly suggesting recrystallization associated with late-stage metamorphic fluids. At the macroscopic scale, this magnetite is commonly associated with metamorphic quartz-epidote±biotite mineralization (Figure 7.2d).

Apatite and carbonate (dolomite-ankerite) are interpreted to be originally diagenetic phases (Bekker et al., 2010). Some carbonates overgrow Type 1 magnetite, consistent with dolomite and ankerite forming during diagenesis (Figure 7.2e). However, these minerals are now mainly in the interstices of coarse Type 3 magnetite and coarse

grained quartz, most probably remobilized during metamorphism (Figure 7.4c). Quartz microveinlets that do not cross individual laminae (Figure 7.4f) are interpreted to be early syndiagenetic, but later veins that contain coarse Type 3 magnetite and cut all bands (Figure 6.4b, Figure 7.2d) are probably metamorphic in origin. The latter contain greenschist facies metamorphic minerals (chlorite-epidote) that are not present in abundance in the BIF layers.

The interpreted paragenetic sequence is summarized graphically in Figure 7.7. To summarize, Type 1 hematite occurs in clusters with Type 1 magnetite. The clusters are overgrown by Type 2 hematite and Type 2 and Type 3 magnetite. All are cut by quartz veins. Type 1 and Type 2 hematite are dominant in the jasper facies. Type 2 and Type 3 magnetite are dominant in the black chert facies, with minor interstitial Type 2 hematite. The common coexistence and textural similarities of Type 1 hematite and Type 1 magnetite suggest that they were part of the earliest paragenesis and that not all magnetite was formed late in the diagenetic and/or metamorphic history. Type 1 magnetite is overgrown by Type 2 magnetite (Figure 7.2c) but both are cut by metamorphic quartz veins (Figure 7.2c and Figure 7.2d). Type 3 magnetite occurs with Type 2 magnetite in black chert and chlorite facies BIF (Figure 7.2e), but overgrows Type 2 magnetite in all facies (Figure 7.2c). The presence of Type 3 magnetite at the margins of late, crosscutting quartz veins suggests that it is mainly metamorphic (Figure 7.2d). Early chlorite in the banded chlorite subfacies is also overgrown by Type 2 and Type 3 magnetite (Figure 7.5b). Chloritized lithic clasts are common in the “ash” layers (Figure 7.5d). Type 1 pyrite occurs as inclusions within Type 2 or Type 3

magnetite in the banded chlorite and magnetite facies (Figure 7.6a and Figure 7.6b). Type 2 pyrite, which has inclusions of Type 2 magnetite, mostly occurs in the chloritized volcaniclastic layers but is also present locally in the magnetite facies (Figure 7.6c). Apatite and dolomite-ankerite are absent in bands that contain Type 1 hematite or magnetite and occur only in the interstices between Type 2 and Type 3 magnetite (Figure 7.4c). Late-stage alteration (weathering) of magnetite has produced some secondary Fe-oxide rims around magnetite, together with other secondary minerals such as leucoxene (amorphous TiO_2 that generally forms as an alteration product of titanite or ilmenite: Tyler, 1938) (Figure 7.4b and Figure 7.4c).

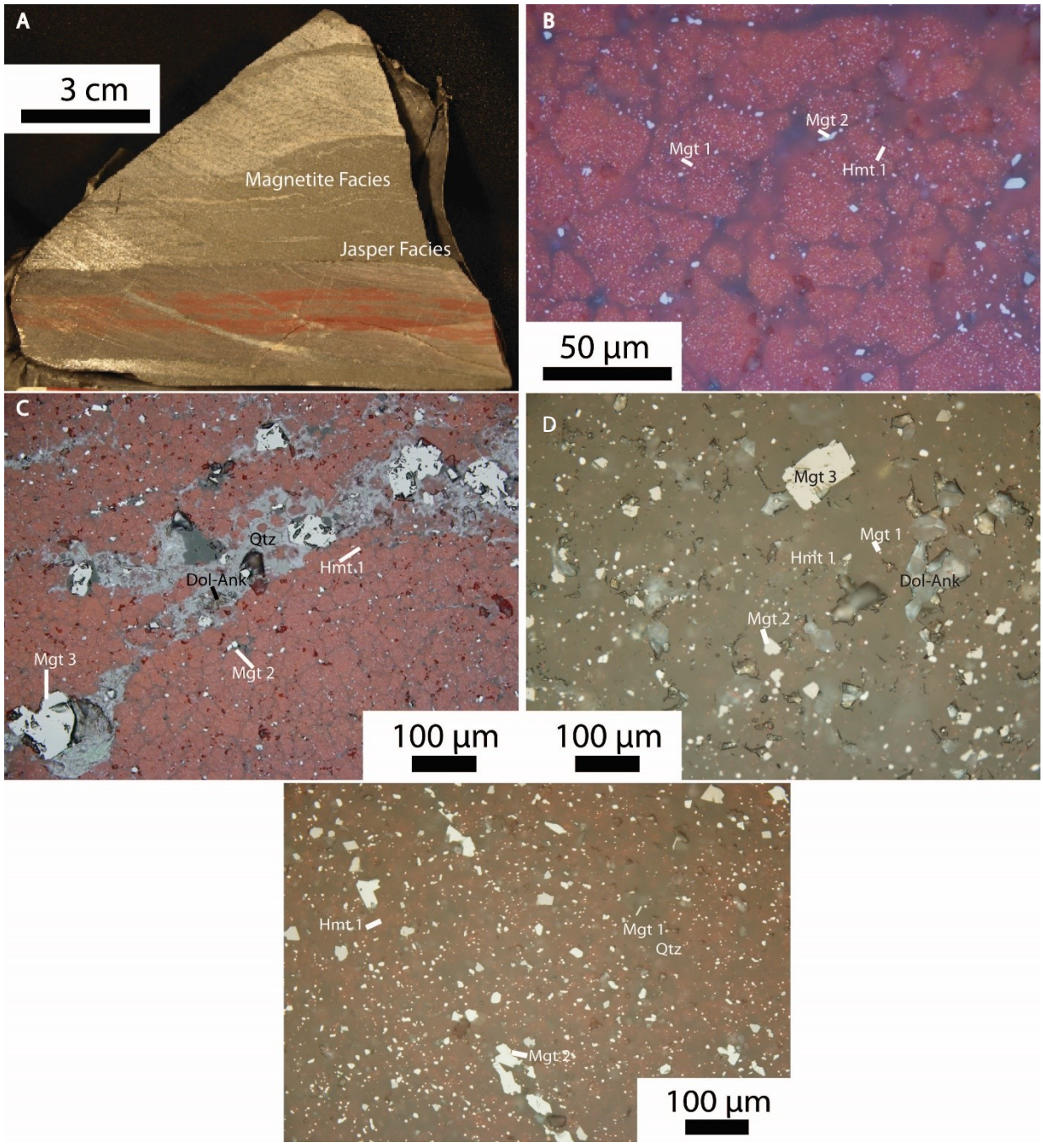
A
3 cm
Magnetite Facies
Jasper Facies
B
Mgt 2
Mgt 1
Hmt 1
50 µm
C
Qtz
Hmt 1
Dol-Ank
Mgt 3
Mgt 2
100 µm
D
Mgt 3
Mgt 1
Hmt 1
Dol-Ank
Mgt 2
100 µm
Hmt 1
Mgt 1
Qtz
Mgt 2
100 µm

Figure 7.1 Jasper facies BIF. A) Sample H11-136.3 with alternating jasper, chert and magnetite layers. B) Photomicrograph of a jasper layer. Spherules of Type 1 hematite, Type 1 magnetite and silica dominate the jasper facies. Type 2 magnetite is found between jasper spherules. Photomicrograph taken at 100x magnification. C) Photomicrograph of a jasper layer cut by a late quartz-carbonate veinlet. Photomicrograph taken at 100x magnification. D) Photomicrograph of the interior of a jasper pseudoclast within a magnetite layer. Coarse, Type 3 magnetite and dolomite-ankerite have partly replaced the jasper. Photomicrograph taken at 100x magnification. E) Photomicrograph of a diffuse boudnary between jasper and jasper-magnetite layers. Jasper spherules are absent where Type 2 magnetite has grown along internal laminae. Photomicrograph taken at 100x magnification.

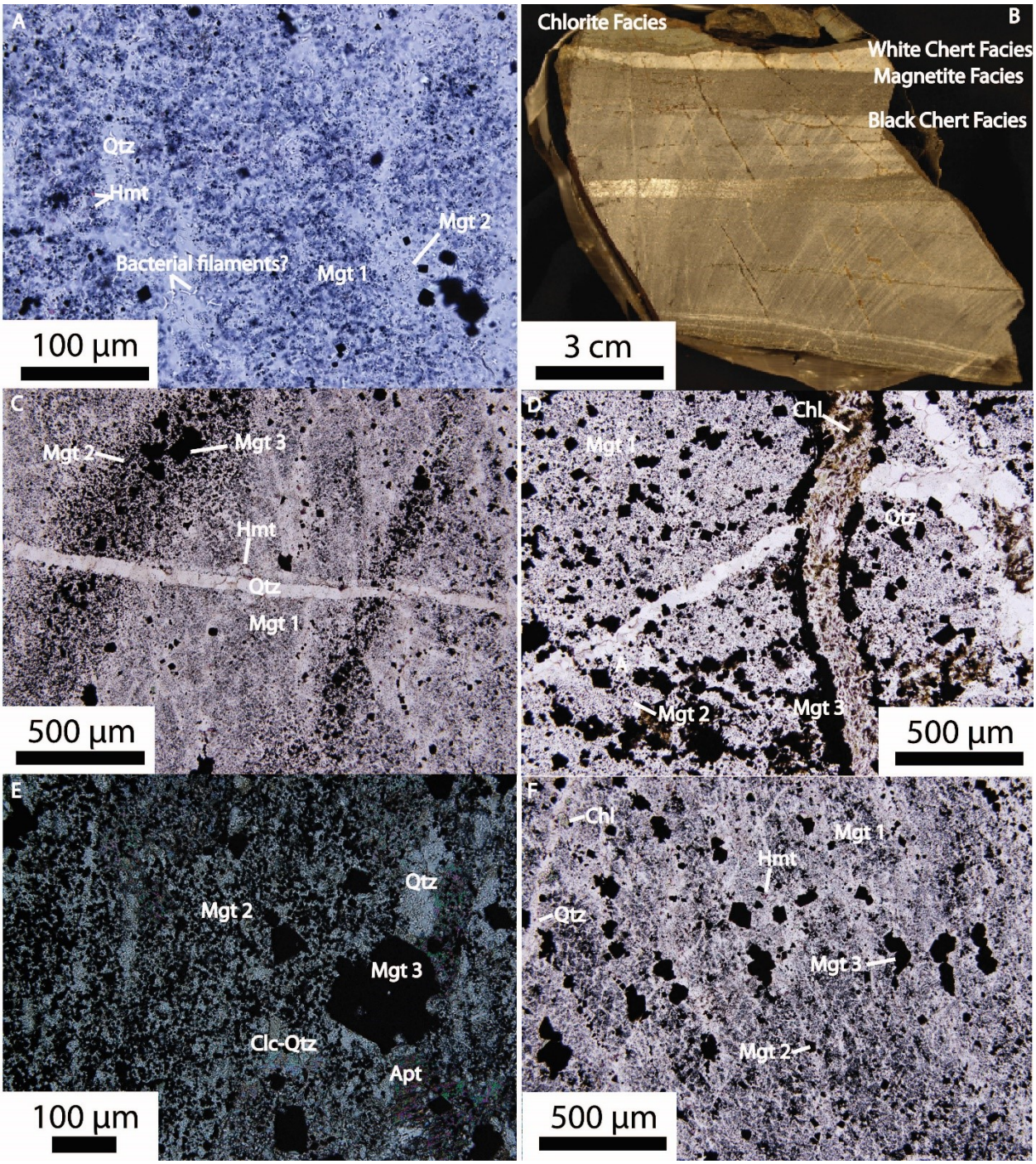
A
Qtz
Hmt
Mgt 2
Bacterial filaments?
Mgt 1
100 µm
Chlorite Facies
B
White Chert Facies
Magnetite Facies
Black Chert Facies
3 cm
C
Mgt 2
Mgt 3
Hmt
Qtz
Mgt 1
500 µm
D
Chl
Mgt 1
Qtz
Mgt 2
Mgt 3
500 µm
E
Qtz
Mgt 2
Mgt 3
Clc-Qtz
Apt
100 µm
F
Chl
Mgt 1
Hmt
Qtz
Mgt 3
Mgt 2
500 µm

Figure 7.2 Black chert facies BIF. A) Photomicrograph of the interior of black chert band in sample H11-119.8 with patchy submicroscopic Type 1 magnetite showing discontinuous veinlets of quartz with associated Type 2 magnetite. Type 1 magnetite grains are 1-2 μm to submicroscopic and have in a patchy distribution. Type 2 magnetite grains are 5- 50 μm in size. Abundant <10 μm long rod-shaped branching inclusions in quartz are possibly bacterial filaments (see Figure 8.3 for details). Disseminated fine grained Type 2 hematite is also present. Type 1 magnetite is mainly found in dark, fine-grained quartz, whereas Type 2 and Type 3 magnetite are always found in clear, coarse euhedral quartz. Photomicrograph taken at 100x magnification. B) Sample H11-21.9b in hand specimen showing black chert, magnetite, white chert and chlorite bands. The black chert bands pictured are 2 and 7 cm thick. C) Photomicrograph of the interior of a black chert band in sample H11-119.8. Types 1 and 2 magnetite are cut by a late quartz vein. Type 3 magnetite is confined to bands of earlier Type 2 magnetite. Photomicrograph taken at 20x magnification. D) Photomicrograph of the interior of a black chert band in sample H11-145.9. Type 1, Type 2 and Type 3 magnetite are widely disseminated in fine grained quartz cut by quartz veinlets. All are cut by a later, sinuous quartz-chlorite-magnetite-secondary hematite vein with a rim of coarse euhedral Type 3 magnetite grains >50 μm in size. Abundant Type 1 and Type 2 magnetite are distributed throughout the matrix but are generally absent in the halo of the coarse Type 3 magnetite. The vein relationship strongly suggests that the Type 3 magnetite is at least as old as the chlorite vein. Photomicrograph taken at 20x magnification. E) Photomicrograph of the interior of a black chert band in sample B013a showing abundant closely-packed aggregates of Type 2 magnetite and a large Type 3 magnetite crystal with a quartz inclusion. The Type 3 magnetite has overgrown quartz-dolomite-ankerite±apatite that form part of a vein in the band.

Photomicrograph taken at 20x magnification. F) Photomicrograph of a 150-300 μm thick black chert band in sample H11-119.8. Types 2 and 3 magnetite occur in clusters. A minor 10 μm quartz vein cuts Types 1 and 2 magnetite but is overgrown by Type 3 magnetite. Earlier Type 2 hematite (10 μm needles and rounded grains with a pink-red-purple halo) are distributed throughout.

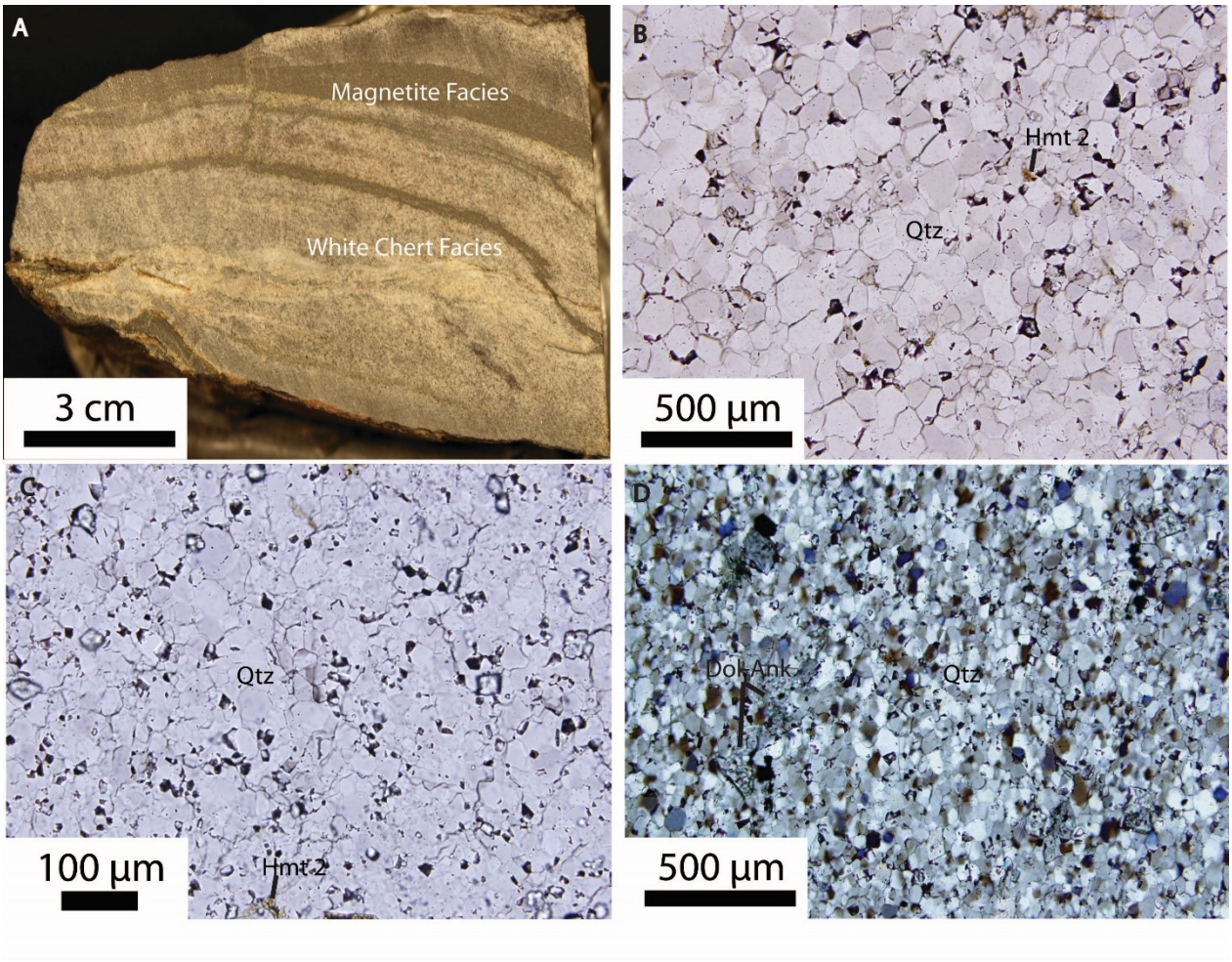
A
Magnetite Facies
White Chert Facies
3 cm
B
Hmt 2
Qtz
500 µm
C
Qtz
100 µm
Hmt 2
D
Dol-Ank
Qtz
500 µm

Figure 7.3 White chert facies BIF. A) Sample H11-57.0 in hand specimen with white chert and magnetite bands. The white chert bands are 3 cm, 2 cm, 0.7 cm, and over 1 cm thick. B) Photomicrograph of the interior of a white chert band in sample H11-68.5, which is composed mostly of recrystallized quartz. Quartz crystals are euhedral and 30-100 μm in size. Type 2 hematite is pervasive but magnetite is notably absent. Photomicrograph at 20x magnification. C) Photomicrograph of the interior of a white chert band in sample H11-125.6a. The band is composed mostly of coarse euhedral to subhedral quartz grains that are 30-100 μm in size. Type 2 hematite (1-10 μm) is pervasive. Photomicrograph at 100x magnification. D) Photomicrograph of the interior of a white chert band in sample C003 which is composed mostly of recrystallized quartz grains 30-100 μm in size. Minor dolomite-ankerite occurs interstitial to the recrystallized quartz. Photomicrograph at 20x magnification.

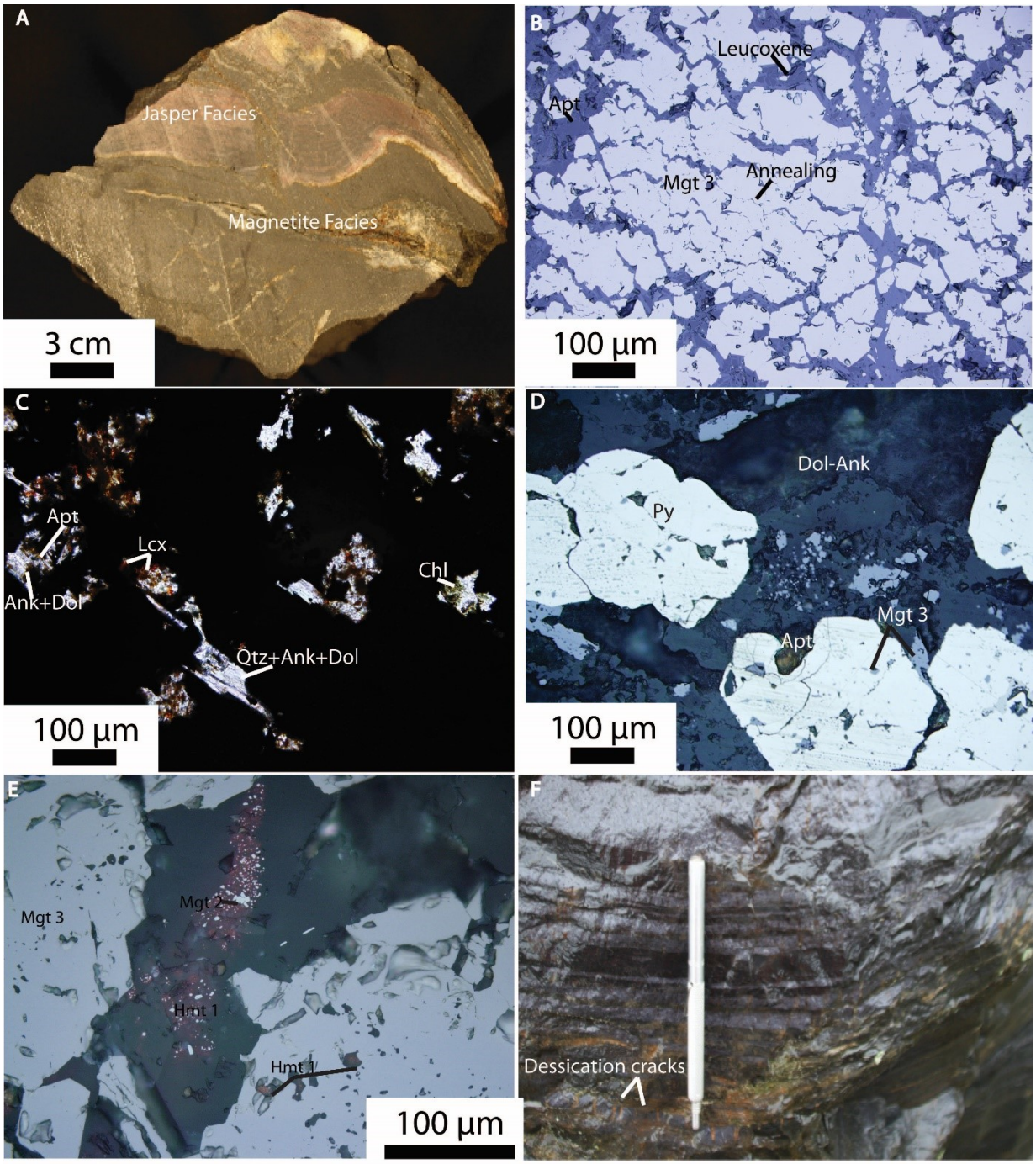
A
Jasper Facies
Magnetite Facies
3 cm
B
Leucoxene
Apt
Mgt 3
Annealing
100 µm
C
Apt
Lcx
Chl
Ank+Dol
Qtz+Ank+Dol
100 µm
D
Dol-Ank
Py
Mgt 3
Apt
100 µm
E
Mgt 3
Mgt 2
Hmt 1
Hmt 1
100 µm
F
Dessication cracks

Figure 7.4 Magnetite facies BIF. A) Sample H11-51.1 with alternating jasper and magnetite bands. The magnetite bands pictured are 4 cm, 1 cm and 0.7 cm. B) Reflected light photomicrograph of the interior of a magnetite band in sample H11-124.8. Magnetite bands are dominated by Type 3 magnetite. An irregular fracture pattern in the magnetite may be relict synerisis cracks but more likely are the result of deformation and metamorphic reaction, possibly by late metamorphic fluids. Interstitial apatite is a common secondary mineral in this sample, and leucoxene reaction rims occur on the coarse magnetite grains. Photomicrograph at 50x magnification. C) Transmitted light photomicrograph of the interior of a magnetite band in sample H11-164. The band is dominated by massive Type 3 magnetite with interstitial dolomite, ankerite, and coarse-grained chlorite. Brown translucent flecks are leucoxene, which occurs as an alteration rim around the Type 3 magnetite. Photomicrograph taken at 50x magnification. D) Reflected light photomicrograph of pyrite grains adjacent to a magnetite band in sample D060. The pyrite is interpreted to be related late metamorphic fluids, owing to the presence of abundant dolomite-ankerite and apparent inclusions of incompletely replaced Type 3 magnetite. Photomicrograph at 50x magnification. E) Combined relfected and transmitted light photomicrograph of the replacement front between magnetite facies and jasper facies in sample SM011. The jasper consists of very fine grained hematite in a siliceous matrix (possibly spherules) together with ultrafine Type 1 magnetite. Photomicrograph at 50x magnification. F) Syneresis or desiccation cracks in magnetite facies BIF photographed in ore block D041 in the Sherman Mine.

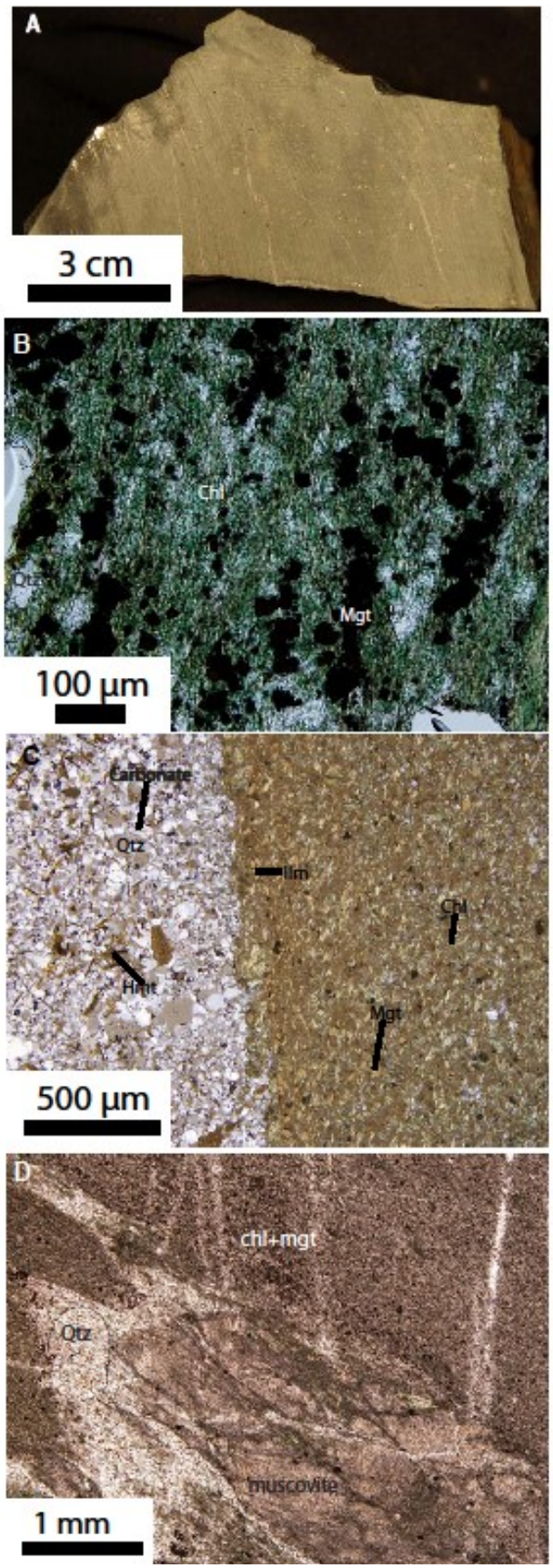
A
3 cm
B
Chl
Qtz
Mgt
100 µm
C
Carbonate
Qtz
Ilm
Chl
Hmt
Mgt
500 µm
D
chl+mgt
Qtz
muscovite
1 mm

Figure 7.5 Chlorite facies BIF. A) Cut section of sample H11-5 of massive, ultrafine-grained chlorite. B) Photomicrograph of sample H11-22.6 showing the diffuse internal layering of the chlorite band defined by Type 2 magnetite and quartz and by weak preferential alignment of the fine chlorite grains. Photomicrograph taken at 20x magnification. C) Photomicrograph of the sharp but finely “scalloped” contact between white chert and massive chlorite layers in sample H11-20.7. Photomicrograph taken at 10x magnification. D) Photomicrograph of a lithic clast (left) in massive chlorite (right) from sample H11-9. Massive chlorite with magnetite is unlayered and cut by quartz veins. The lithic clast is replaced by muscovite. Photomicrograph taken at 5x magnification.

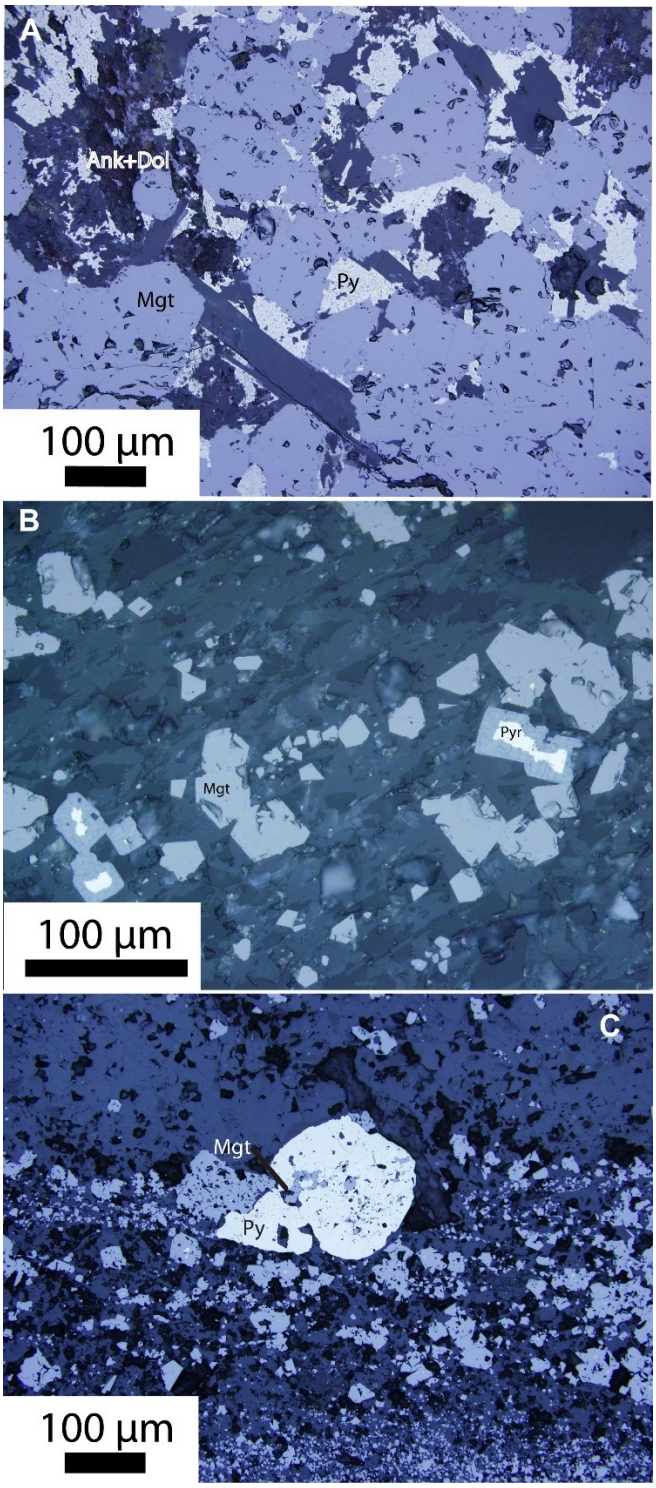
A
Ank+Dol
Mgt
Py
100 µm
B
Pyr
Mgt
100 µm
C
Mgt
Py
100 µm

Figure 7.6 Typical habit of trace pyrite in different facies of the Temagami BIF. A) Reflected light photomicrograph of subhedral Type 1 pyrite grains in a magnetite layer from sample H11-164.2. The pyrite grains are partly included in coarse Type 3 magnetite. B) Reflected light photomicrograph of subhedral Type 1 pyrite in coarse Type 3 magnetite from a chlorite layer in sample H11-22.6. C) Reflected light photomicrograph of subhedral Type 2 pyrite overgrowing Type 2 and Type 3 magnetite from sample C060.

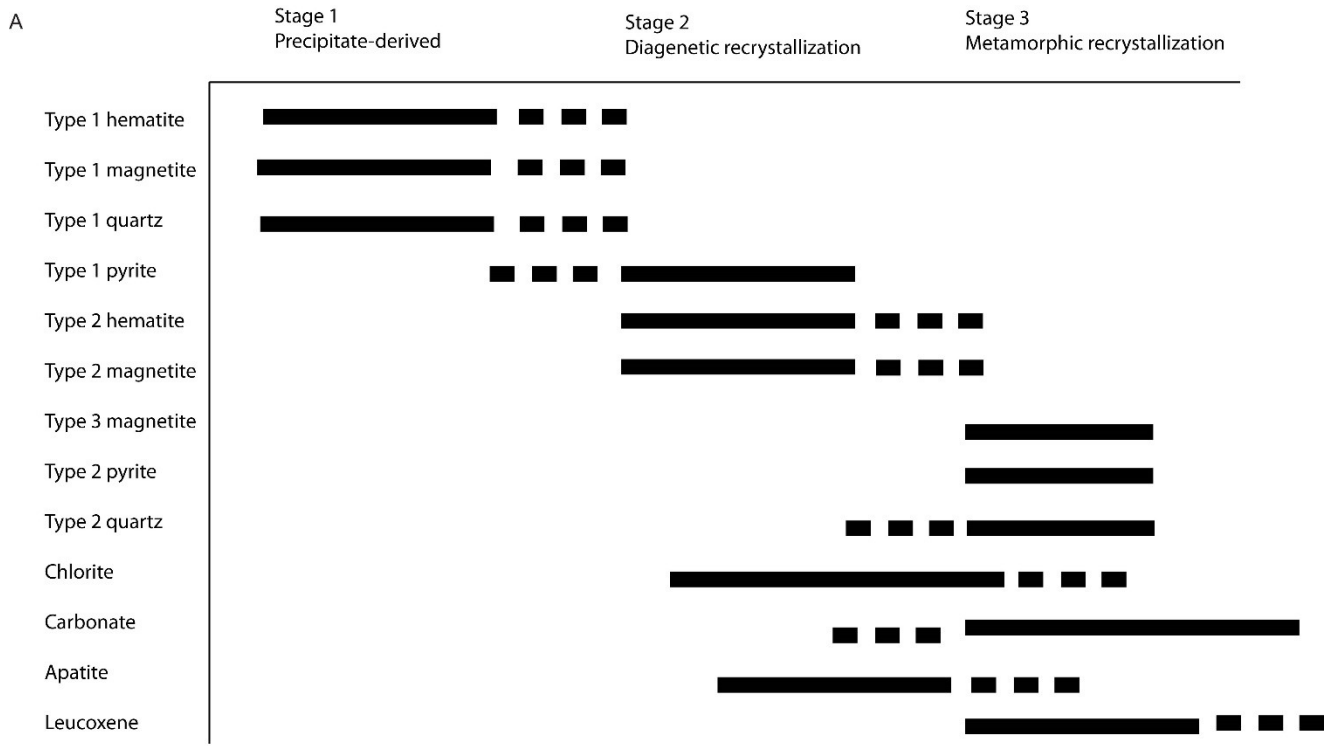
A
Stage 1
Precipitate-derived
Stage 2
Diagenetic recrystallization
Stage 3
Metamorphic recrystallization
Type 1 hematite
Type 1 magnetite
Type 1 quartz
Type 1 pyrite
Type 2 hematite
Type 2 magnetite
Type 3 magnetite
Type 2 pyrite
Type 2 quartz
Chlorite
Carbonate
Apatite
Leucoxene

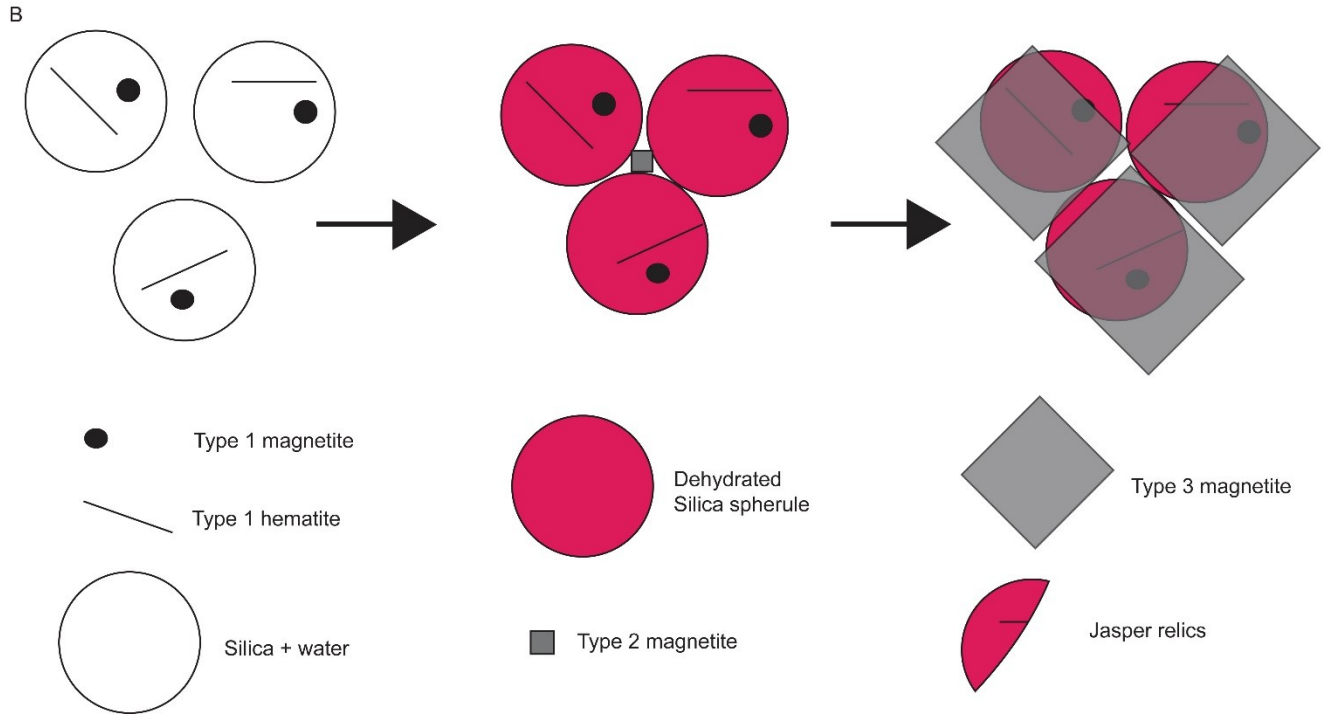
B
Type 1 magnetite
Type 1 hematite
Silica + water
Dehydrated
Silica spherule
Type 2 magnetite
Type 3 magnetite
Jasper relics

Figure 7.7 A) Proposed paragenetic history of the Temagami BIF. Type 1 hematite and Type 1 magnetite are considered to be the closest paragenetic “relative” of original ferric oxyhydroxide precipitated from an Archean water column. Type 2 hematite and Type 2 magnetite formed from these minerals during burial diagenesis and were recrystallized to form Type 3 magnetite, most probably during regional metamorphism. Relict Type 1 magnetite and Type 1 hematite are still found throughout the BIF layers, shielded by fine quartz. The fine quartz was most likely deposited originally as amorphous silica from the water column and formed quartz during diagenesis. Some quartz also may have been derived for original Fe-Si-oxyhydroxide phases that expelled Fe during diagenesis. Fine-grained Type 1 pyrite (e.g., pyrite inclusions in magnetite: Figure 7.6B) may have formed during diagenesis and was recrystallized to euhedral Type 2 pyrite during regional metamorphism. Chlorite in the Temagami BIF formed from precipitated Fe-silicate minerals that were transformed during diagenesis or is an alteration product of mafic volcaniclastic material (e.g., ash layers containing ilmenite: Figure 7.5C). Carbonate minerals and apatite may have been derived from microbial material (carbon and phosphorous) during diagenesis and were remobilized during regional metamorphism, now found in the interstices of Type 3 magnetite. Leucoxene is interpreted to be due to alteration during weathering and is only associated with Type 3 magnetite. B) Sketch illustrating the paragenesis of Type 1 magnetite, Type 1 hematite, Type 2 magnetite and Type 3 magnetite. Type 1 hematite and Type 1 magnetite were deposited within hydrated silica spherules on the paleoseafloor. Many are still preserved in the jasper facies. During burial, the spherules are compacted and dehydrated, accompanied by the formation of Type 2 magnetite in the void spaces between the

spherules. During metamorphism, Type 3 magnetite overgrew most of the jasper spherules forming magnetite facies BIF. Some remnants of jasper spherules remain as pseudoclasts.

8. Facies Relationships

Figure 8.1 summarizes the modal mineralogy of the different ore facies. The differences between visibly distinct facies can be small. For example, a very small amount of hematite (<1 vol. %) is required to make jasper bands red, and a very small amount of magnetite can make chert bands black. The following describes the specific mineralogical and textural relationships of the different ore facies.

8.1 Red Chert (Jasper) Facies

The jasper facies comprises about 7 vol. % of the Temagami BIF. It is most commonly associated with black chert and magnetite and occurs throughout the mine. The thicknesses of the jasper bands range from <1 up to 10 cm, with an average of 3 cm (Appendix 3 and Table 7.1; Figure 7.1a). Microbanding, with individual laminae of 1 mm is also observed locally. A typical band is composed of 35 vol. % Type 1 hematite, 35 vol.% coarse quartz, 20 vol.% fine quartz, and 10 vol.% Type 2 magnetite. The dominant microtexture of the jasper bands is the distinctive quartz “spherules” that contain clusters of Type 1 hematite and Type 1 magnetite (Figure 7.1b). Type 2 hematite, which probably represents an intermediate stage in the recrystallization of Type 1 hematite (and eventual replacement by Type 2 magnetite), is less common in the jasper bands than in the black chert bands (Figure 7.2c). Type 1 hematite is notably absent in the outer zones of quartz spherules where Type 2 magnetite has formed in the spaces between the spherules (Figure 7.1b and 7.1d). This may indicate that Fe from

Type 1 hematite was stripped from the spherules during diagenesis to make the Type 2 magnetite.

The jasper facies commonly grades into black chert along individual bands, from parts that contain subequal amounts of hematite and magnetite to entirely black chert (see below: Figure 6.3d, Figure 6.3e). Less commonly there is a transition from jasper to 100% magnetite. This transition has been interpreted to represent layer-by-layer replacement textures in other BIF studies (Gross, 1972; Mucke, 1996; Rasmussen, 2014). Remnants of the Type 1 hematite from the original jasper bands occur in the magnetite facies near the transition (Figure 7.4e). At the magnetite-jasper transition there is a notable increase in the concentration of Type 2 magnetite in the hematitic spherules compared to the adjacent jasper-rich part of the band. Locally, the replacement of jasper by black chert and magnetite has produced a pseudo-granular texture with some of the original jasper spherules preserved after most of the band has been replaced by magnetite (Figure 7.4e).

8.2 Black Chert Facies

Black chert, which comprises about 40 vol. % of the Temagami BIF, occurs in all units of BIF throughout the mine area. It is found with all other facies but is most commonly associated with white chert and magnetite bands (Figure 6.1). A typical black chert band is composed of ~10 vol. % of Type 1 magnetite, 40 vol. % fine quartz, 10 vol. % Type 2 magnetite, 20 vol. % coarse quartz, 12 vol. % Type 3 magnetite, and minor amounts of

chlorite, apatite, carbonate (dolomite-ankerite and calcite), leucoxene, biotite and Type 2 hematite (Appendix 2).

A peculiar subfacies of black chert consists of alternating, mm-scale layers of black and white chert bands (so-called “microbanded chert”, with tens of mm-scale bands within a single cm-thick layer: Figure 8.2b). The black microbands contain fine-grained Type 1 magnetite and fine quartz; white chert microbands are predominantly coarse quartz with minor Type 3 magnetite (Figure 8.2a). The boundaries between the microbands appear quite sharp at the hand-specimen scale, but they are marked by subtle changes in grain size and abundance of magnetite at the micro-scale (Figure 8.2d). Notably, the boundaries are not always parallel to the larger cm-scale layering of the samples (Figure 8.2c).

Typically, only one type of magnetite dominates in an individual black chert band, but the transition from Type 1 to Types 2 and 3 can be seen in some bands at the microscale (less than 1 cm). In this case, clusters of Type 2 and Type 3 magnetite can occur in isolated patches (20-200 μm: Figure 7.2a) or as larger millimeter-scale alignments of crystals within a band (Figure 7.2f). The distribution of the different textural types of magnetite is interpreted to reflect different degrees of preservation of fine primary(?) type 1 magnetite and replacement or overgrowth by coarser recrystallized Types 2 and 3 magnetite (Figure 7.2c).

Figure 6.3d and Figure 6.8 show black chert grading into jasper along individual bands (see also Appendix 7). Figure 8.2d (sample C012) shows the transition from microbanded white chert to black chert. At the transition, the growth of Type 2 magnetite appears to be mostly by scavenging of Fe from Type 1 magnetite (or Type 1 hematite), which is removed from the quartz in a halo of "depletion" around the coarser grained magnetite (Figure 8.2d). In other cases, as noted above, the Type 2 magnetite occurs as a halo around unreplaced clusters of Type 1 hematite (Figure 7.1b). Fine quartz (<50 μm) that is dark grey in color contains abundant Type 1 magnetite, but quartz that contains coarser Type 3 magnetite is generally clear and white (Figure 7.2a). Clusters of coarse Type 3 magnetite sometimes have haloes of unreplaced (?) Type 2 magnetite. These relationships argue strongly for progressive replacement of Type 2 magnetite by Type 3 magnetite, either during diagenesis or later metamorphism. Where magnetite is absent, structures that resemble bacterial filaments, similar to those in the white chert bands (see below) can be seen in the magnetite bands (Figure 7.2a).

8.3 White Chert Facies

The white chert facies comprises about 10 vol.% of the Temagami BIF. It occurs throughout the mine area, together with all other facies, but is most commonly associated with the black chert facies. The thicknesses of the white bands range from 0.1 cm up to 1 cm, with an average of 0.6 cm (Appendix 3 and Table 7.1; Figure 7.3a). A typical white chert band consist of 100% coarse (>100 μm) euhedral quartz (Figure 7.3b). Common

accessory minerals are Type 2 hematite (Figure 7.3b), Type 2 magnetite, and rare dolomite-ankerite.

Structures that resemble bacterial filaments are present widely in white chert samples. These features consist of 1-10 μm long, branching filaments (or ~1 μm "circles" and rods in cross-sections of the filaments: Figure 8.3), very similar to what have been interpreted as bacterial fossils in other Archean rocks (Walsh and Lowe, 1985; Walsh, 1992). In pure quartz, it is unclear what exactly defines the boundaries of the filaments (e.g., traces of carbon or simply grain boundaries of the quartz host: Westall et al., 2001), but they are nevertheless clearly visible. This observation has important implications for the origins of the chert layers and possibly the BIF as a whole.

8.4 Magnetite Facies

The magnetite facies represents about 20-25 vol. % of the Temagami BIF. It occurs throughout the mine area together with black chert and jasper. The thickness of the magnetite bands range from 0.3 cm up to 4 cm, with an average of 0.5 cm (Appendix 3 and Table 7.1; Figure 7.4a). A typical magnetite band is composed of 75 vol.% Type 3 magnetite, 10 vol.% coarse quartz, and subequal amounts of accessory minerals. Pyrite, secondary hematite, leucoxene and biotite occur in trace amounts (Appendix 2). Most of the pyrite is Type 2, containing inclusions of Type 2 and Type 3 magnetite (Figure 7.4d). Quartz, chlorite, carbonates (dolomite-ankerite) and apatite occur in the spaces between the coarser Type 3 magnetite grains (Figure 7.4c). As seen in outcrop, cracks that do not

penetrate adjacent bands are common in this facies (Figure 7.4f). This may reflect primary sedimentary structures or simply the brittle nature of the magnetite compared to other layers. The fact that the bands contain mostly coarse, Type 3 magnetite suggests that they represent the advanced stages of replacement of pre-existing Fe-rich bands. This is considered further in the Discussion.

8.5 Chlorite Facies

The chlorite facies comprises about 20 vol. % of the Temagami BIF and includes two subfacies: massive (volcaniclastic) and banded. The massive chlorite bands are most common, accounting for 70% of the chloritic material in the BIF (Appendix 3). Individual bands are up to several cm in thickness (between 0.1 cm and 5 cm, averaging 3 cm: Appendix 3 and Figure 7.5a) and in some cases are interbedded with chert (Figure 6.10). A typical band of massive chlorite is composed of 50 vol.% chlorite, 15 vol.% Type 3 magnetite, 20 vol.% ilmenite, 10 vol.% coarse quartz, and traces of dolomite-ankerite, muscovite, apatite, and leucoxene. The ilmenite and muscovite are mainly contained in lithic fragments that are common in the massive chlorite bands (Figure 7.5d).

Single, isolated bands of chlorite occur locally within a 1-5 m sections of BIF. Individual layers consist of 50 vol.% chlorite, 20 vol.% coarse quartz, 10-15 vol.% Type 3 magnetite, 10 vol. % Type 2 magnetite, and 5 vol. % of other phases (trace pyrite, dolomite-ankerite, apatite, leucoxene and calcite). However, they do not contain lithic clasts. Rather, they bear a close resemblance to chloritic bands in other BIF that have been interpreted as

primary Fe-Mg-silicate precipitates (James, 1954; Jakobsson, 1986; Lowe, 1991). The banding is due to discrete ribbons of Type 2 and Type 3 magnetite (Figure 7.5b). Lateral transitions between chlorite in these layers and other BIF facies have not been observed.

8.6 Sulfide-Bearing Volcaniclastics and Black Shale

Black shale is common in the Temagami Greenstone Belt, as seen in the regional geology map, and is also present in the BIF sections of the Sherman mine. However, pyritic black shales account for less than 5% of the lithologies of the belt and even less of the BIF sections. Several occurrences in the mine area were sampled and examined in this study. One occurrence was described from the footwall of the Sherman mine, exposed in the Temagami dump road. Another exposure of semi-massive pyrite was examined in the Highway 11 outcrop. The largest section of pyritic shale was located at the west end of the South pit (see Figure 5.1). The following from I.R. Jonasson describes the samples that were collected from this exposure shortly after the closure of the pit (I.R Jonasson and J.M. Franklin, 1983, unpublished data): “The BIF facies at this location consisted of banded magnetite and jasper with only trace pyrite. The south end ore section graded [stratigraphically] into broadly laminated pale green-to-white chert with fine magnetite beds and then into finely laminated siliceous greywacke (approx. 100 m thick). This was topped [see comment below] by a 100-m section of black phyllite with <10% up to 40% massive colloform pyrite in a carbonaceous matrix, interbedded with cm layers of siliceous wacke. The more massive pods of colloform, globular pyrite in carbonaceous cherty wacke were sampled in two sections between 30 and 60 m thick. The near massive nodular pyrite

shows distinctive, diagenetic, radial growth but low base metals. Bands of siliceous wacke and white chert are interspersed among the sulfides. Locally these appear to have slumped, producing a brecciated texture, including chert fragments, with a chloritic and carbonaceous matrix. Pyrite flooding of the breccia, plus minor quartz “sweats”, suggest syndeformation remobilization (possibly soft sediment). This unit grades into white chert with fine magnetite bands between darker shaley beds.” When sampled, this section was considered to be in the stratigraphic hangingwall of the BIF (see reference to the “top” of the section, which was thought to young from the south to the north). However, clear pillow facing directions in the adjacent volcanic units to the north indicate that bedding is facing to the south and that the 100-m thick section of greywacke and pyritic argillite was probably in the stratigraphic footwall of the BIF in the South Pit.

Figure 8.4 shows some of the features of the sulfides in hand sample and thin section (samples SH850, SH580, SH100). Anhedral pyrite grains, 10-100 μm in size, account for ~60 vol. % of the sulfide-rich sections (Figure 8.4b). The clastic component, making up ~20 vol. %, is well-sorted, fine-grained greywacke with 10-50 μm lithic clasts (Figure 8.4c). Euhedral, fractured, <100 μm pyrite grains comprises ~20 vol. % (Figure 8.4d). The absence of any banded iron oxide layers, and only pale green-to-white chert with fine magnetite, suggests that most of the sampled section is not a “facies” of the BIF but most probably a sulfidic shale unit belonging to the volcanic footwall of the mine. Although a small section of semi-massive sulfide in massive basalt is exposed in the Highway 11 outcrop, similar pyritic shale was not seen elsewhere in the BIF section or in the large collection of ore blocks.

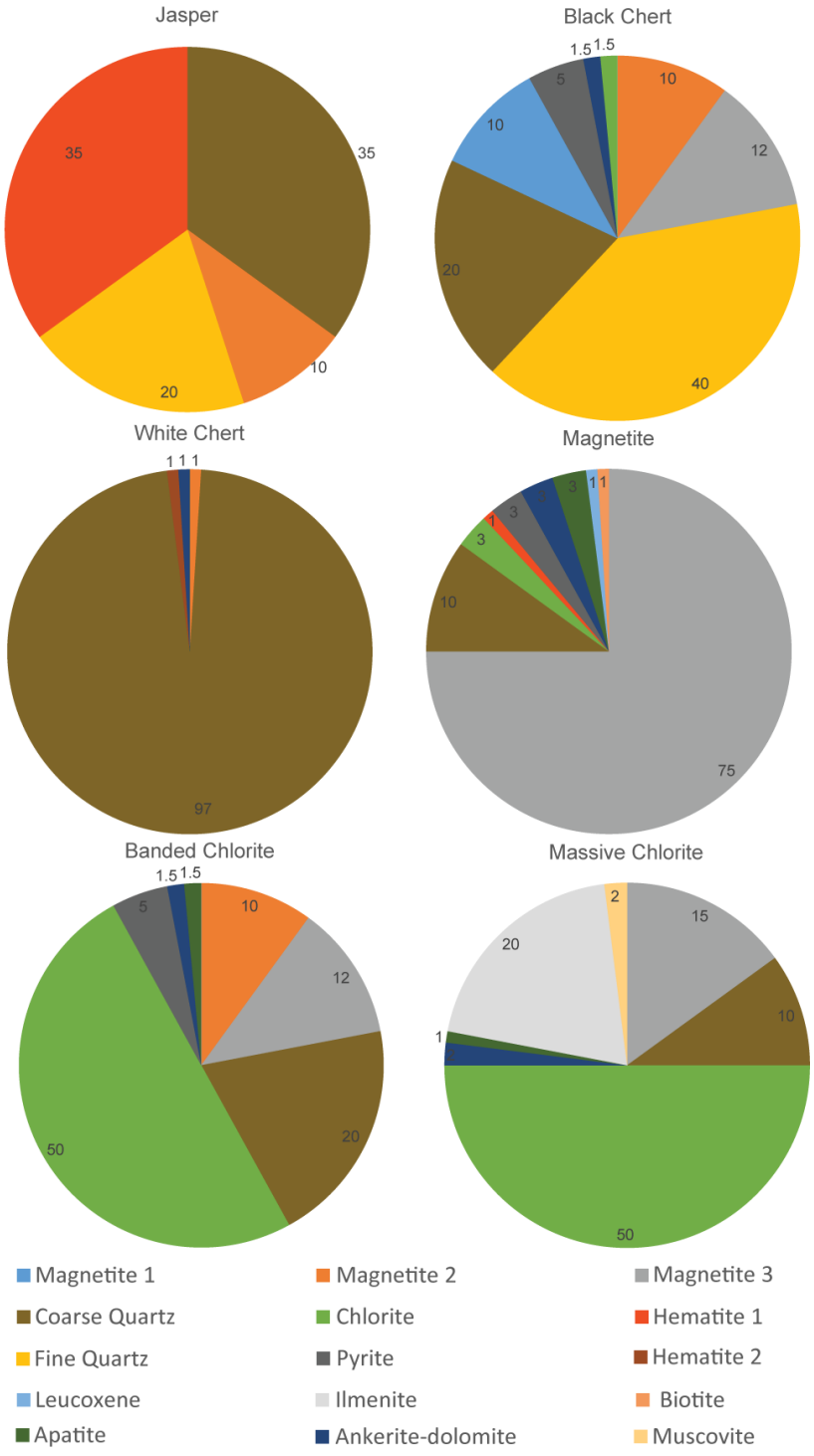

Figure 8.1 Modal mineralogy of different facies of the Temagami BIF determined by petrography.

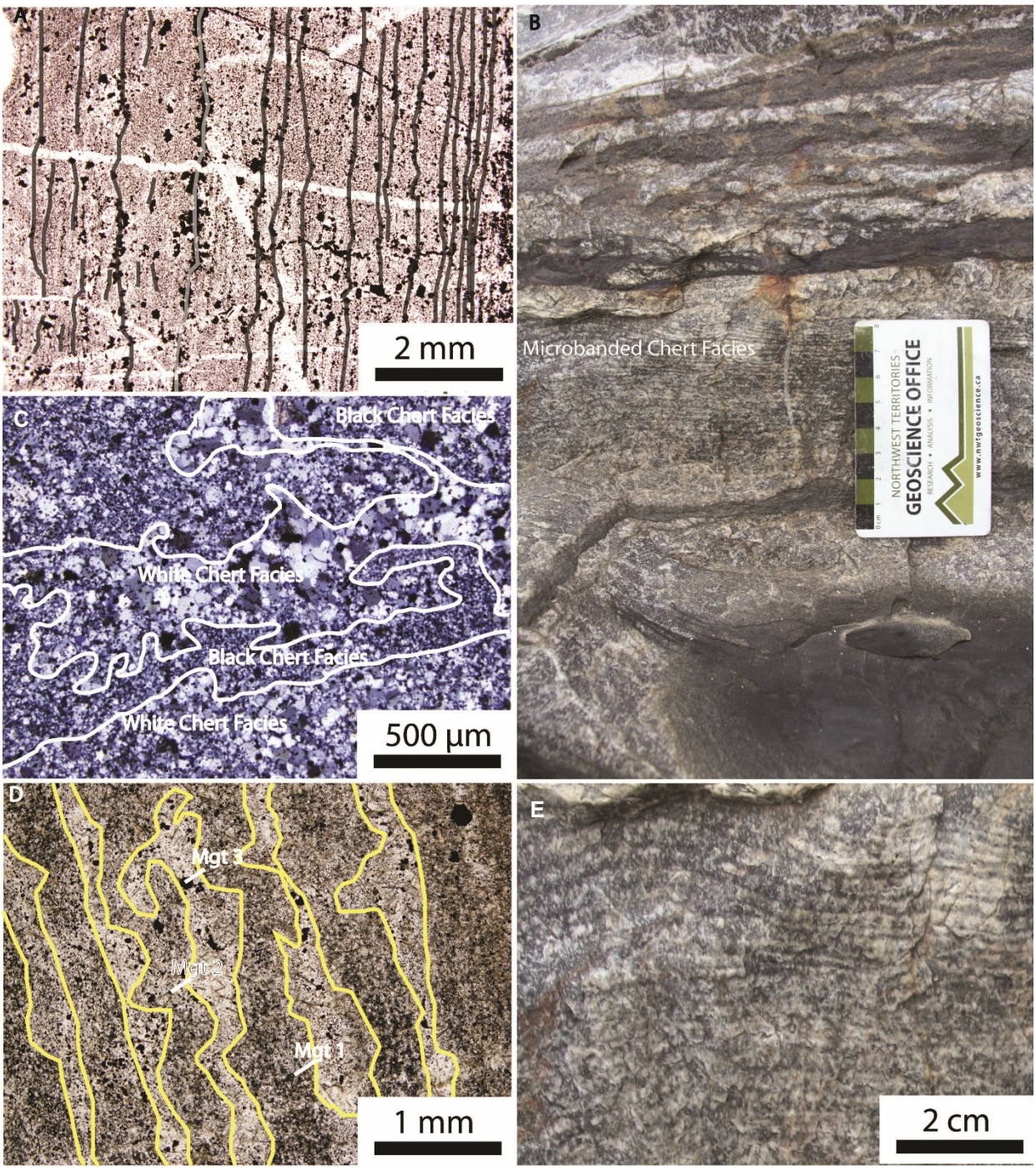

Figure 8.2 A) Photomicrograph of diffusely microbanded black and white chert in sample H11-21.9b showing alternating, 100-um bands of quartz plus Type 1 and Type 2 magnetite, and coarse Type 3 magnetite at the edges of the bands (solid lines). Quartz

microveinlets cut the microbanding, some associated with Type 3 magnetite. Later irregular, fracture-controlled magnetite also cuts the microbands. Photomicrograph at 2.5x magnification. B) Microbanded chert pictured in block B035. Other black and white chert layers in the same block have sharp boundaries with the microbanded layer. C) Photomicrograph of irregularly microbanded black and white chert in sample H11-145.9. Dark portions are characterized by abundant Type 1 patchy magnetite and fine grained, dark-colored quartz. White portions are characterized by widely dispersed Type 2 and 3 magnetite and coarse, transparent quartz. Photomicrograph taken at 20x magnification. D) Photomicrograph of regularly microbanded chert in sample C012. The internal banding is thought to be a diagenetic feature and not depositional. In some white microbands, Type 1 magnetite appears to have scavenged Fe from Fe-rich quartz, becoming Type 2 and Type 3 magnetite in clear quartz. Thus the uniform banding appears to have developed insipiently from recrystallization of Type 1 and Type 2 magnetite. Points of nucleation in Type 2 magnetite can be seen in darker layers as small isolated magnetite crystals surrounded by a rim of clean, coarse quartz. Photomicrograph at 5x magnification. E) Close-up of Figure 8.2B showing microbanding. A single bed of chert in this image comprises dozens of sub-millimeter microbands of black chert alternating with white chert.

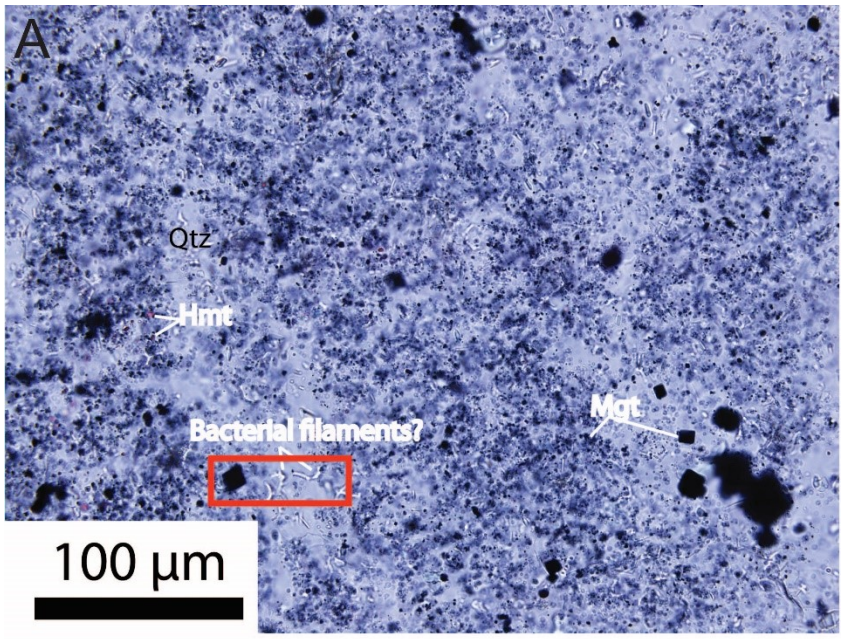
A
Qtz
Hmt
Bacterial filaments?
Mgt
100 µm

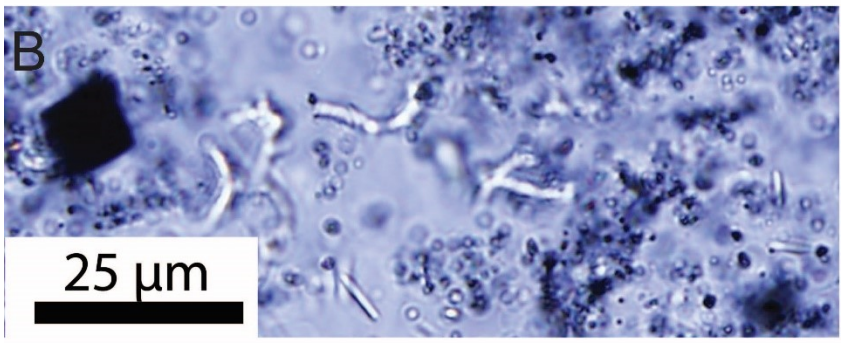
B
25 µm

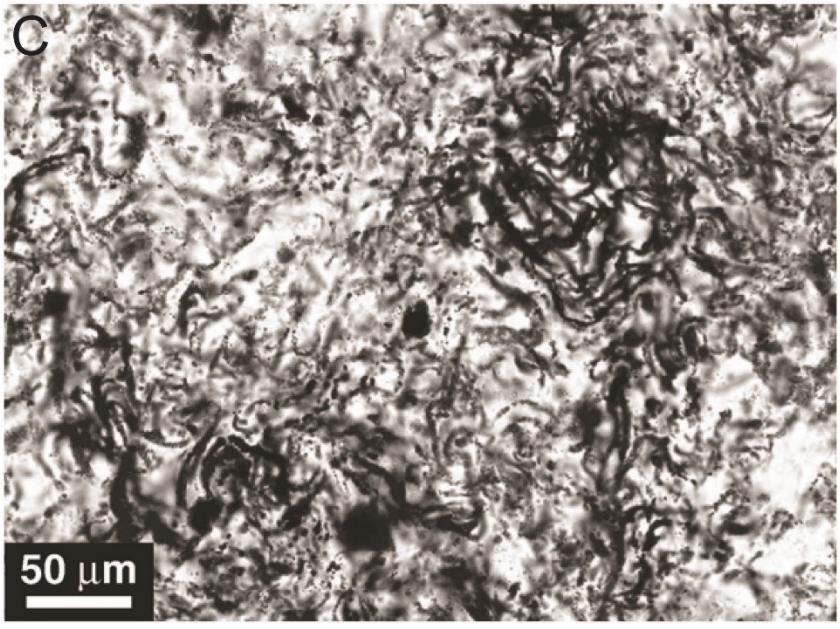
C
50 µm

Figure 8.3 A) Black chert from sample H11-119.8A (see Figure 7.2A) showing abundant 1 μm circular features and rod-shaped inclusions that resemble cross-sections of bacterial filaments. The filaments are highlighted in red and shown at higher magnification in B. B) Close-up of the indicated area in A showing diagnostic branching shapes typical of preserved bacterial filaments. C) Example of similar features in the Jerome District in central Arizona, USA (from Slack et al., 2007). In this case, some of the original carbon is still present outlining the bacterial filaments.

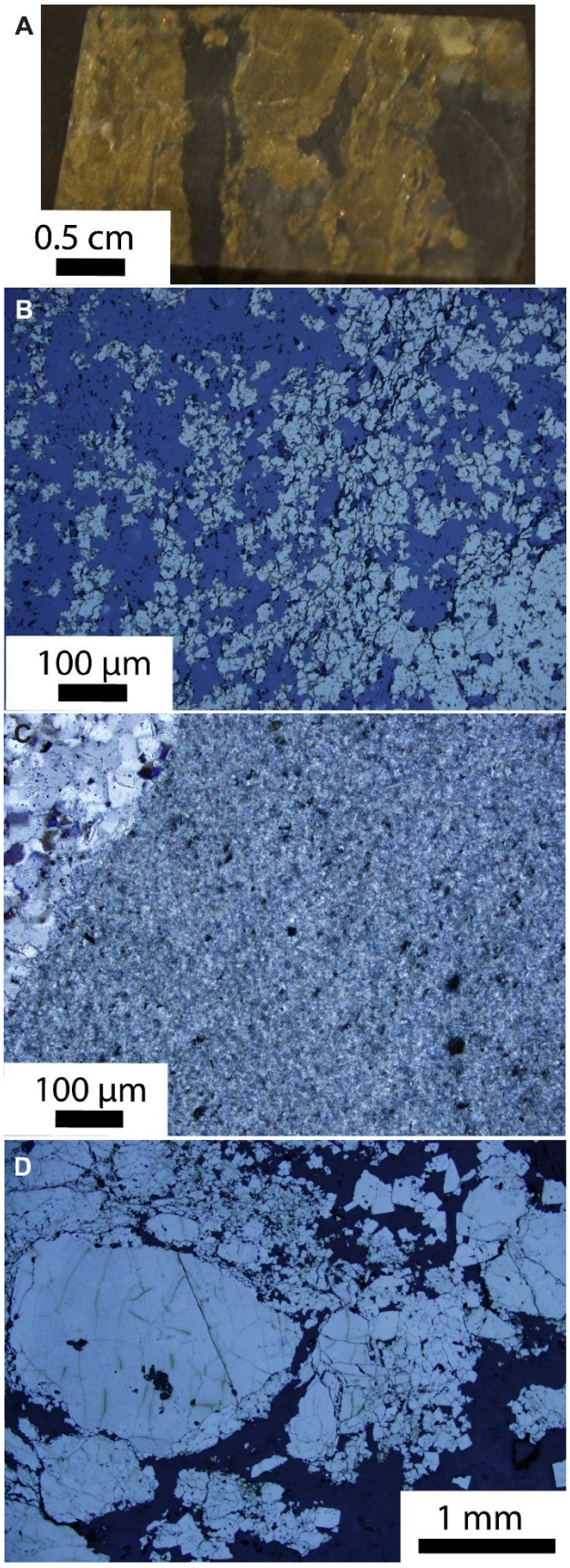
A
0.5 cm
B
100 µm
C
100 µm
D
1 mm

Figure 8.4 Sulfide-bearing volcaniclastic unit in the Temagami BIF. A) Cut section of sample SH850 composed of fine lithic clasts and pyrite. B) Reflected light photomicrograph of sample SH580 showing generally fine (<100 μm) anhedral pyrite. Photomicrograph taken at 20x magnification. C) Transmitted light photomicrograph of sample SH100 showing a matrix of fine lithic clasts with some magnetite cut by a metamorphic quartz vein. The matrix is composed of quartz and chlorite. Photomicrograph taken at 20x magnification. D) Reflected light photomicrograph of sample SH850 showing coarse subhedral and fractured pyrite (>100 μm). Photomicrograph taken at 5x magnification.

9. Mineral Compositions

A JEOL 8230 SuperProbe and a JEOL 6610LV SEM located at the University of Ottawa were used to perform in situ chemical analysis of individual minerals in the Temagami BIF. The SEM images in Figure 9.1 show the detailed textural relationships of Types 1-3 magnetite and Type 1 hematite. Figure 9.2 shows images of chlorite, ilmenite, apatite and rare monazite. Other trace minerals observed under the SEM were apatite, biotite, dolomite and ankerite, commonly in quartz-filled spaces between the magnetite grains.

The analyzed magnetite contains about 70 wt. % Fe, but can also contain up to 0.5 wt. % Si. Type 3 magnetite generally contains more Si and Mg than Type 2 magnetite (Table 9.1). Type 3 magnetite also contains minor P, which was not detected in Type 2 magnetite. None of the hematite grains were large enough to analyze. However, analyses of quartz typically have more than 0.5 wt. % Fe_2O_3, consistent with the presence of ultrafine Fe-oxide inclusions (Table 9.2).

Chlorite was analyzed from massive volcaniclastic layers (H11-7 and H11-20.7), white chert (H11-9) and from the greywacke at the south end of the Highway 11 outcrop (H11-5). The analyzed chlorite in all layers, including the white chert, is close to the Fe-rich endmember, chamosite, with a formula $Fe_{4.5}Mg_{0.5}Al(Al_{2.25}Si_{1.75}O_{10})$. The analyses do not include H_2O, which should account for ~10 wt.% of the mineral (Velde, 2014). The chlorite contains minor amounts of Cr, Zn, Mn and V. Zn concentrations are around 0.5 wt. %, and Mn concentrations vary between 0.77 and 0.97 wt. %. The compositions of

all of the analyzed chlorite are significantly more Fe-rich than typical greenschist facies chlorite from nearby greenstone belts (Figure 9.3), strongly suggesting that even the chlorite in altered volcaniclastic beds was part of the Fe-rich system of BIF formation.

Ilmenite from a massive chlorite layer (Figure 9.2b) is close to the stoichiometric composition, $Fe_{1.1}Ti_{0.9}O_3$ (Table 9.2). Mn concentrations are up to 0.05 wt %, but V is close to the detection limit of 0.01 wt %. The former indicates that ilmenite is the dominant host for Mn.

Quartz contains as much as 0.5 wt. % P and detectable LREE, indicating the presence of submicroscopic REE-phosphate minerals as well as Fe-oxides. Apatite is an important trace mineral in the magnetite and chlorite facies. Anhedral grains of apatite in magnetite-rich layers (Figure 9.2d) are Fe-rich, with a composition of $Ca_{3.5}(PO_4)_{3.2}(OH)_{2.8}$. Because F, Cl, and OH were not measured on the EPMA, the mineral formula for apatite was calculated assuming 5.6 wt.% the H_2O for an oxide total of 100% (Table 9.3). The apatite has low REE concentrations, but monazite was identified by SEM as ~1 μm inclusions in apatite (Figure 9.2c), and it contains several wt % of La- and Ce-oxide. The carbonate analysed contains 6 wt. % Fe and 1 wt. % Mg, with a mineral formula corresponding to dolomite-ankerite [$Ca_{0.7}(Fe_{0.1},Mg_{0.6})(CO_3)_{2.2}$] (Table 9.3).

Because of the trace amounts of Fe-oxides in the quartz, it is CL passive. Cathodoluminescence (CL) is only produced by certain elements (e.g. phosphorous,

manganese) in minerals with semiconducting properties. Other elements (e.g. iron) can shield cathodoluminescence, so that potentially CL active minerals such as apatite or quartz can appear inactive. Only in the late veins and in volcaniclastic layers does any of the quartz have active CL (Figure 9.3). The latter suggests that Fe was not mobile during the formation of late-stage metamorphic quartz.

Table 9.1: Element concentrations of magnetite

Sample	Mgt type	CaO 0.01%	SiO_2 0.01%	Cr_2O_3 0.01%	$Al2O_3$ 0.01%	ZnO 0.01%	Fe_2O_3 0.01%	TiO_2 0.01%	MnO 0.01%	V_2O_3 0.01%	NiO 0.01%	MgO 0.01%	Total
H11-5	2	0.12	0.24	0.01	<0.01	<0.01	100.6	0.01	<0.01	<0.01	<0.01	<0.01	101
11-30.8	2	<0.01	0.44	<0.01	0.020	<0.01	101	0.04	0.03	<0.01	<0.01	0.08	100.9
11-30.8	2	<0.01	0.47	<0.01	0.016	0.01	100	<0.01	<0.01	<0.01	<0.01	0.05	101.6
11-30.8	2	<0.01	0.53	<0.01	<0.01	0.03	101	<0.01	0.02	<0.01	0.01	0.10	101.8
11-30.8	2	<0.01	0.46	<0.01	<0.01	<0.01	101	<0.01	<0.01	<0.01	<0.01	0.09	101.5
11-30.8	2	<0.01	0.68	<0.01	0.013	<0.01	101	0.01	<0.01	<0.01	<0.01	0.11	101.4
11-30.8	2	<0.01	0.96	<0.01	<0.01	<0.01	99.9	<0.01	0.01	<0.01	<0.01	0.23	101.6
11-30.8	2	<0.01	0.35	<0.01	<0.01	<0.01	101	0.02	<0.01	<0.01	0.01	0.04	101.2
11-30.8	2	<0.01	0.49	<0.01	<0.01	<0.01	101	0.02	0.02	<0.01	<0.01	0.01	101.2
11-30.8	2	<0.01	0.19	<0.01	<0.01	<0.01	101	<0.01	0.02	<0.01	<0.01	0.01	101.9
11-30.8	3	<0.01	0.56	<0.01	<0.01	<0.01	101	0.03	<0.01	<0.01	<0.01	0.14	101.1
11-30.8	3	<0.01	0.72	<0.01	<0.01	<0.01	101	<0.01	<0.01	0.01	<0.01	0.01	101.5
11-30.8	3	<0.01	0.62	<0.01	0.020	0.06	101	<0.01	<0.01	<0.01	<0.01	0.07	101.4
11-30.8	3	<0.01	0.17	<0.01	<0.01	<0.01	101	0.05	0.02	<0.01	<0.01	<0.01	100.8
11-30.8	3	<0.01	0.78	<0.01	<0.01	<0.01	99.9	0.02	<0.01	<0.01	<0.01	0.11	101.7
11-30.8	3	0.02	0.59	<0.01	0.011	<0.01	101	0.04	0.01	<0.01	<0.01	0.13	101.3
11-30.8	3	<0.01	0.18	<0.01	<0.01	<0.01	101	<0.01	0.01	<0.01	<0.01	<0.01	101.2

Footnote: Sampling locations are shown in backscatter electron image (Figure 9.1). All data are reported as oxide weight percents with a detection limit of 0.01 weight %. The H11-5 sampling location is pictured in Figure 9.1b. The H11-30.8 sampling locations are pictured in Figure 9.1c and Figure 9.1d.

Table 9.2: Element concentrations of silicates and ilmenite

		CaO	SiO_2	Cr_2O_3	Al_2O_3	ZnO	Fe_2O_3	TiO_2	MnO	V_2O_3	NiO	MgO	Total
	Sample	0.01%	0.01%	0.01%	0.01%	0.01%	0.01%	0.01%	0.01%	0.01%	0.01%	0.01%	
ilm	H11-5	0.02	0.07	<0.01	0.02	<0.01	50.8	49.4	0.70	0.20	0.01	<0.01	101
	H11-5	0.02	0.27	0.02	0.10	0.03	51.0	48.8	0.64	0.20	0.01	0.02	101
chl	H11-5	<0.01	20.5	<0.01	20.1	0.02	43.8	0.06	0.08	<0.01	<0.01	5.42	90.0
	H11-5	0.05	20.8	0.01	20.0	0.06	44.1	0.07	0.08	0.01	<0.01	5.68	90.9
	H11-5	<0.01	20.7	0.02	20.3	0.06	44.2	0.07	0.06	0.01	<0.01	5.39	90.9
	H11-5	<0.01	20.9	0.01	20.5	0.03	44.3	0.10	<0.01	0.01	0.01	5.46	91.5
	H11-5	0.01	21.2	0.02	19.8	0.04	44.0	0.11	0.08	0.01	<0.01	5.75	91.1
	H11-7	<0.01	22.43	0.01	19.29	0.01	41.10	<0.01	0.04	<0.01	0.03	<0.01	7.97
	H11-7	0.02	23.56	<0.01	19.22	<0.01	41.57	0.06	0.03	<0.01	0.07	0.01	7.50
	H11-9b	<0.01	22.97	<0.01	19.60	0.02	33.04	0.04	0.04	0.02	0.06	0.03	12.3
	H11-9b	0.01	25.05	<0.01	19.34	0.02	33.45	0.07	0.07	<0.01	0.04	0.02	12.5
	H11-9b	<0.01	23.88	<0.01	19.84	0.04	33.58	0.10	0.05	0.02	0.05	0.03	12.6
	H11-20.7	<0.01	23.16	<0.01	18.92	0.05	39.69	0.05	0.10	<0.01	0.03	0.01	9.34
	H11-20.7	<0.01	23.11	<0.01	19.13	<0.01	39.60	0.07	0.09	0.01	0.03	0.01	9.28
	H11-20.7	<0.01	23.00	<0.01	19.25	0.04	39.66	0.04	0.10	0.01	0.05	0.01	9.23
	H11-20.7	<0.01	23.31	<0.01	19.10	<0.01	39.79	0.06	0.09	<0.01	0.06	<0.01	9.05
	H11-20.7	0.01	23.70	<0.01	18.66	0.04	39.67	0.07	0.09	<0.01	0.06	0.01	9.54
	H11-20.7	<0.01	23.82	<0.01	18.61	0.02	39.66	0.01	0.11	<0.01	0.04	<0.01	9.51
	H11-20.7	0.03	24.03	<0.01	18.67	0.01	39.33	0.13	0.09	<0.01	0.06	<0.01	9.32
qtz	11-22.9	<0.01	97.7	0.01	<0.01	0.02	0.84	<0.01	<0.01	<0.01	<0.01	<0.01	99.1
	11-22.9	<0.01	97.7	<0.01	<0.01	<0.01	0.59	<0.01	<0.01	<0.01	<0.01	<0.01	94.4

Footnote: Sampling locations are shown in backscatter electron image (Figure 9.2). All data are reported as oxide weight percents with a detection limit of 0.01 weight %. The H11-5 sampling location is pictured in Figure 9.2a and Figure 9.2b.

Table 9.3 Partial EPMA analysis of accessory minerals

	CaO 0.01%	SiO_2 0.01%	Cr_2O_3 0.01%	Al_2O_3 0.01%	ZnO 0.01%	Fe_2O_3 0.01%	TiO_2 0.01%	MnO 0.01%	V_2O_3 0.01%	NiO 0.01%	MgO 0.01%	Total
apt	43.8	0.02	<0.01	<0.01	<0.01	0.072	<0.01	0.03	<0.01	0.09	<0.01	87.1
mon	40.3	0.04	0.18	<0.01	0.46	0.09	<0.01	<0.01	<0.01	<0.01	<0.01	45.0
dol	23.5	0.08	<0.01	<0.01	0.02	6.05	0.021	1.04	<0.01	<0.01	14.1	101.5

Footnote: The EPMA was not calibrated to measure these minerals, but a reconnaissance analysis of apatite (apt), monazite (mon) and dolomite (dol) was performed to estimate their element compositions. All data are reported as oxide weight percents with a detection limit of 0.01 weight %. Insitu P concentrations could be semi-quantitatively estimated by WDS but is not reported here.

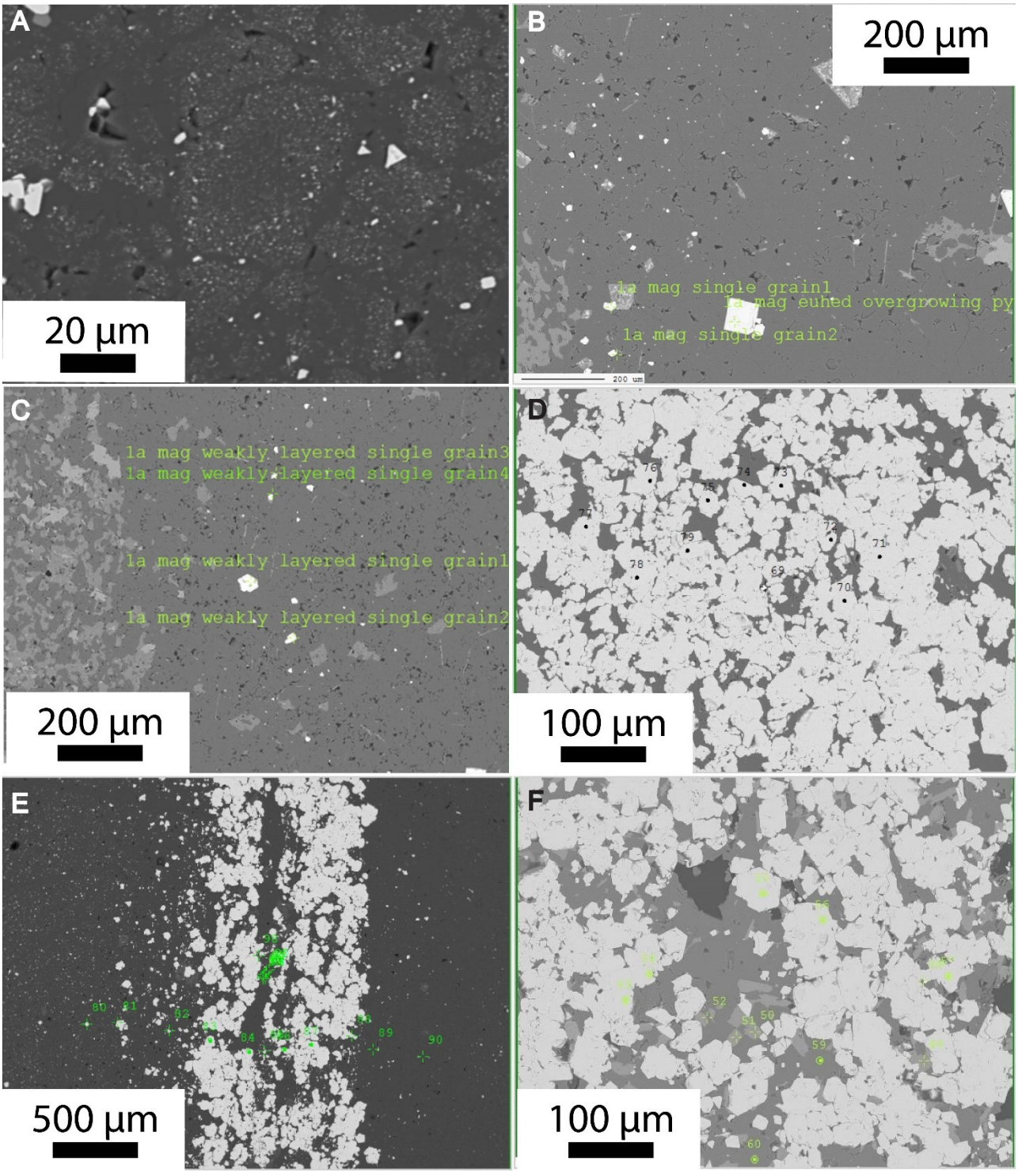
A
20 µm
B
200 µm
1a mag single grain1
1a mag euhed overgrowing py
1a mag single grain2
C
1a mag weakly layered single grain3
1a mag weakly layered single grain4
1a mag weakly layered single grain1
1a mag weakly layered single grain2
200 µm
D
100 µm
E
500 µm
F
100 µm

Figure 9.1 A) Electron backscatter image of jasper spherules (Type 1 hematite, Type 1 magnetite, and fine quartz) in a jasper layer in sample SM011. The interiors of the spherules show diffuse zoning, some with hematite-rich interiors and silica-rich rims. Type 2 magnetite occurs outside the spherules and most commonly in the interstices between multiple spherules. The image was taken on the JEOL 6610LV SEM. B) Electron backscatter image of Type 2 magnetite in a massive chlorite layer in sample H11-5. The image was taken on the JEOL 6610LV SEM. Points for microprobe analyses given in Table 9.1 are indicated. C) Electron backscatter image of Type 2 magnetite at a boundary between a massive chlorite bed and a white chert bed in sample H11-5. The image was taken on the JEOL 6610LV SEM. Points for microprobe analyses given in Table 9.1 are indicated. The images give sampling locations for the data displayed in Table 9.1. D) Electron backscatter image of Type 3 magnetite in a magnetite layer in sample H11-30.8. Euhedral to subhedral Type 3 magnetite grains are >50 μm in size and occur as aggregates. The image was taken on the JEOL 6610LV SEM. Points for microprobe analyses given in Table 9.1 are indicated. E) Electron backscatter image of a Type 3 magnetite in a magnetite bed and adjacent chert beds in sample H11-30.8. Type 3 magnetite microband consisting of >50 μm euhedral grains and aggregates of subhedral grains. The image was taken on the JEOL 6610LV SEM. Points for microprobe analyses given in Table 9.1 are indicated. F) Electron backscatter image of quartz and coarse Type 3 magnetite in a magnetite layer in sample H11-30.8. Quartz in this sample also contains apatite. The image was taken on the JEOL 6610LV SEM. Points for microprobe analyses given in Tables 9.1 and 9.5 are indicated.

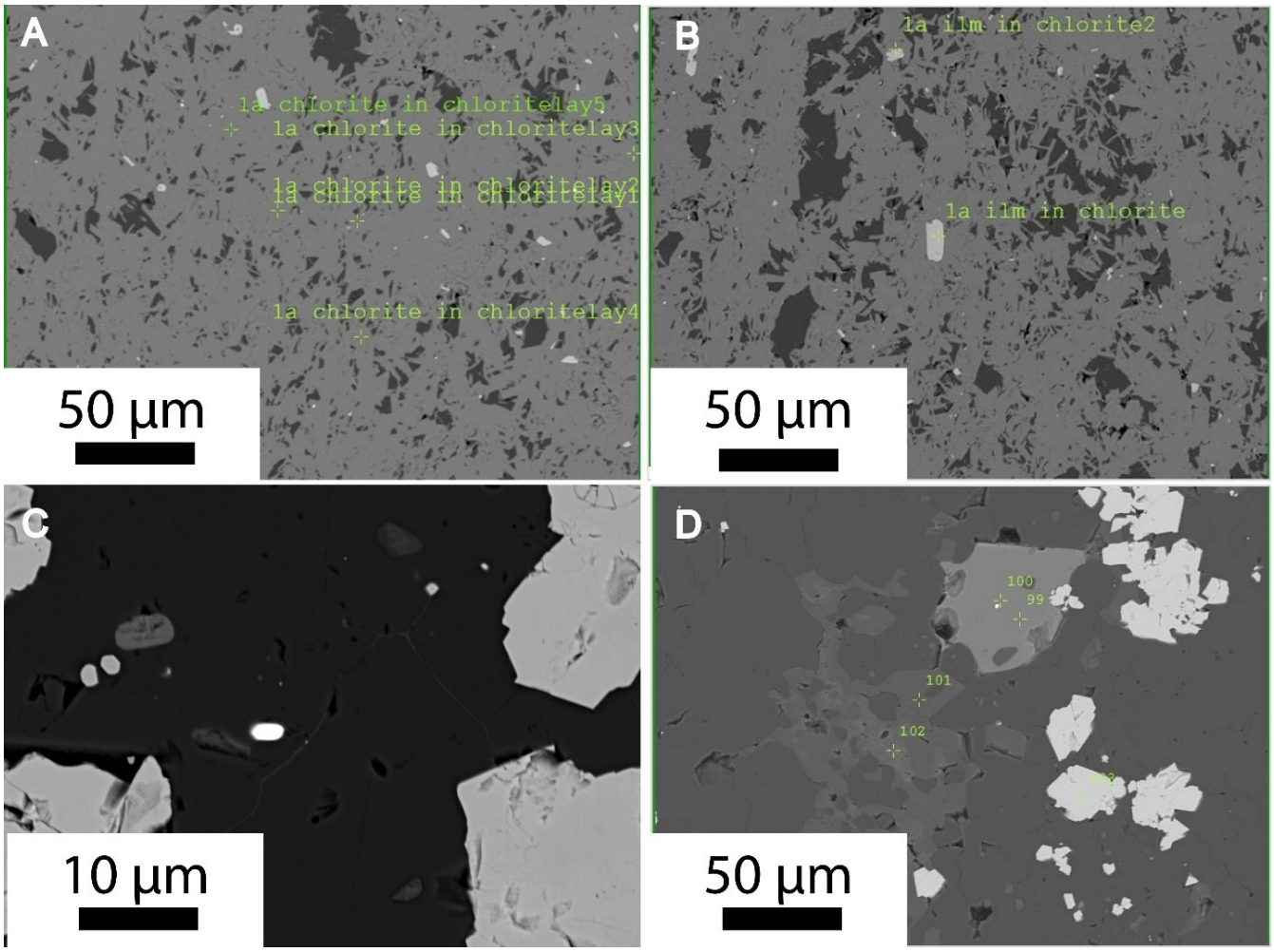

Figure 9.2 A) Electron backscatter images of chlorite in a massive chlorite layer in sample H11-5. Chlorite in this sample is derived from altered mafic volcaniclastic material. The image was taken on the 8230 Superprobe. Points for microprobe analyses given in Table 9.2 are indicated. B) Electron backscatter images of ilmenite in a massive chlorite layer in sample H11-5. The ilmenite in this sample supports the interpretation that the chlorite is an alteration product of volcaniclastic material and not from hydrothermal clays. The image was taken on the 8230 Superprobe. Points for microprobe analyses given in Table 9.2 are indicated. C) Electron backscatter image of a 2-3 µm subhedral monazite grain in sample H11-33.3. The

image was taken on the 6610LV SEM. D) Electron backscatter image of apatite (including monazite), dolomite and Type 2 magnetite at the boundary between a magnetite layer and a chert layer in sample H11-30.8. The subhedral apatite grain is ~50 μm in size with a monazite inclusion. The dolomite is anhedral and zoned. The image was taken on the 6610LV SEM. Points for microprobe analyses given in Table 9.2 are indicated.

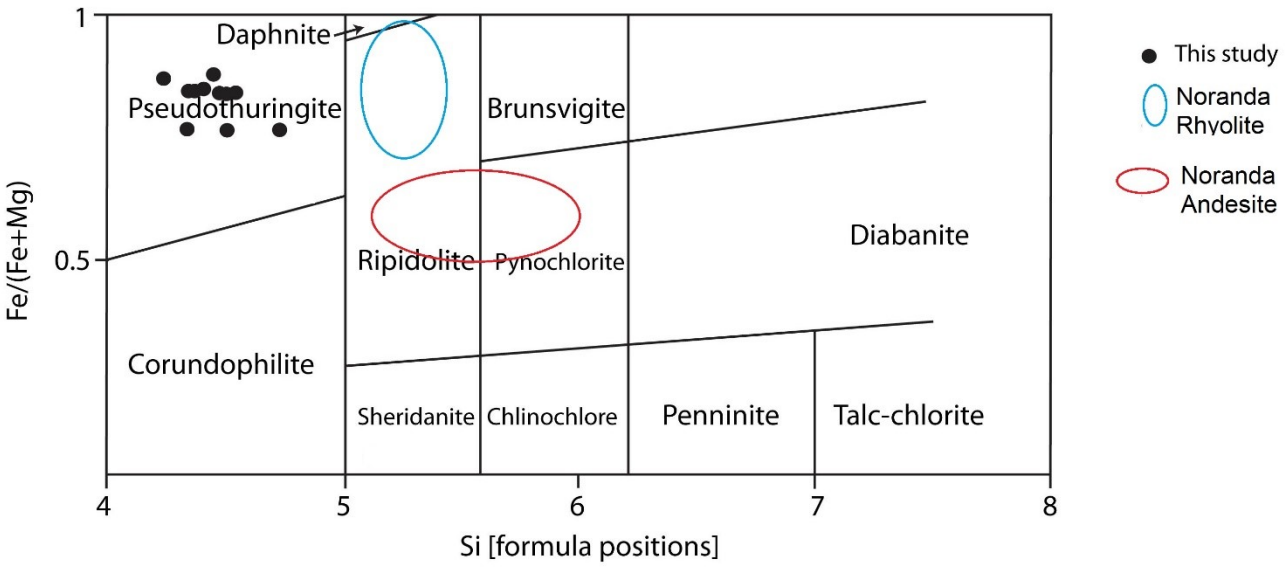

Figure 9.3 Compositions of chlorite in volcaniclastic and chert layers of the Temagami BIF in comparison to typical greenschist facies chlorite from comparable volcanic successions of the Abitibi Greenstone Belt (Noranda). Temagami samples have higher Fe and lower Si than most chlorite associate either with synvolcanic hydrothermal alteration or regional greenschist facies metamorphism. Data for chlorite in Noranda andesite and rhyolite is from (Hannington et al., 2003). Plot is after Hey (1954).

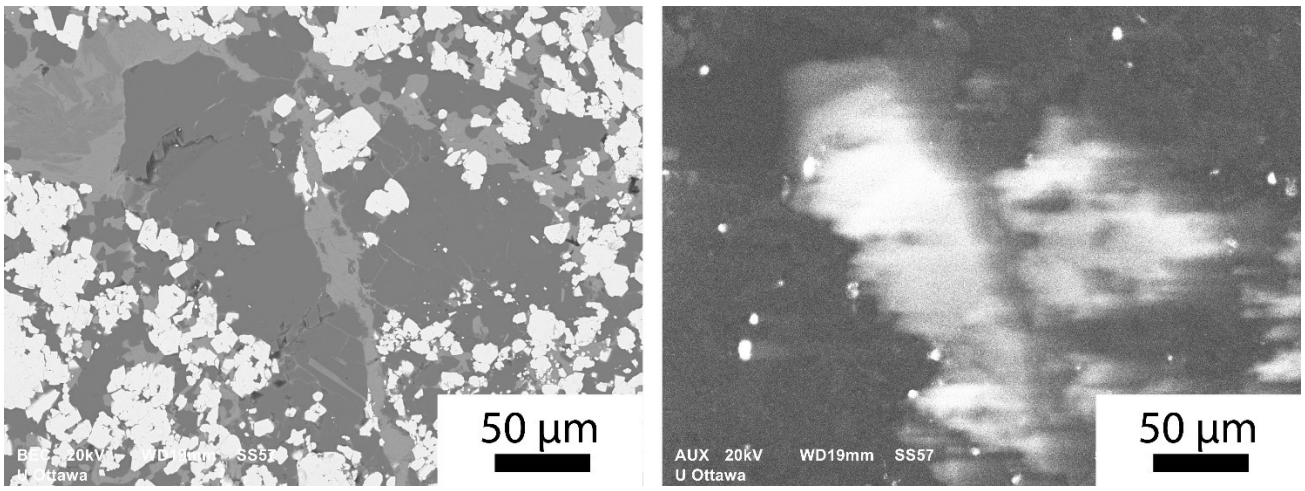

Figure 9.4 Electron backscatter image and corresponding cathodoluminescence (CL) image of a metamorphic quartz vein cutting a magnetite layer in sample H11-119.8. Most quartz in the Temagami BIF is not CL active because Fe-bearing inclusions in dissipate cathodoluminescence. CL activity is much greater in the metamorphic quartz veins.

10. Lithogeochemistry of the Temagami Iron Formation

A summary of whole-rock geochemical data for the different facies used in this study is given in Table 10.1 and Appendix 4. The full data, including quality control, are reported in Diekrup et al. (in preparation). Normative mineral abundances for quartz, Fe-oxides, and other phases calculated from these data are given in Table 10.2 and described in section 10.3 and can be directly compared with the petrographic estimates in Appendix 2.

The geochemical data constrain the abundance of different minerals based on normative calculations and also provide insight into the different minerals that control the distribution of elements in the different BIF facies, including the relative contributions of primary hydrothermal versus detrital versus secondary components. Figure 10.1 is a geochemical profile of the thickest exposed section of BIF along Highway 11, showing the variability in major element chemistry from the bottom to the top of the section in the south part of the Sherman Mine sequence. Figure 10.2 is an example of the geochemical variability (of Si, Al and Fe) at the scale of a single large ore block (B013). The profiles show that the geochemical variability is strictly dependent on the layer type sampled. Fe averages about 20% but varies from less than 5% to 40% over distances of only a few cm. Si varies between 5% and 40% over a few cm. Most chert beds have high Si and low Al and Fe. Jasper and some black chert beds have roughly equal proportions of Si and Fe. Magnetite beds have high Fe and chlorite beds have high Al. Few trends can be observed at the scale of the Highway 11 outcrop because of the

spacing of the samples, although Al concentrations are higher close to the top and bottom of BIF sequences.

10.1 Comparison with Typical Algoma-Type BIF

Major elements

The major chemical components of the BIF are Si (28.0 wt. %) and Fe (22.0 wt. %) (average of all samples: Table 10.1). Si concentrations range from 1.29 wt. % to 46.0 wt. %. Fe concentrations range from 0.881 wt. % to 63.2 wt. %. Al concentrations range from 0.021 wt. % to 7.95 wt. %. Except in the chlorite-rich samples, Al concentrations are uniformly low, which indicates that the volcaniclastic component and any hydrothermal aluminosilicate components in the chert beds, although likely present, are small. Fe-Al-Si and Fe-Al-Mn relationships among the different facies are shown in Figure 10.3.

Ca concentrations range from 0.014 wt. % to 4.37 wt.%. Ca (and carbon) is mostly present as carbonate, except in shale where carbonaceous material is present. Based on the C content of the samples, the Temagami BIF contains between 0.1 and 5 wt.% carbonates. Rare Ca-rich samples contain an estimated 35 wt.% dolomite. Mg concentrations range from 0.024 wt. % to 4.99 wt. %, which is mostly present in late dolomite. In the chlorite-rich samples Mg concentrations are generally higher than about 2.5 wt.%. Based on the microprobe analyses of the chlorite, which contain about 5 wt.% MgO, the bulk MgO (excluding Mg in dolomite) indicates a chlorite content of about 70%

in the chlorite-rich samples. Na concentrations range from less than 0.002 wt.% to over 5 wt.%. The highest concentrations are in massive chlorite and likely reflect the presence of lithic clasts. K concentrations range from less than 20 ppm to 2.41 wt.%. The latter is mostly present in metamorphic biotite.

Minor elements

Mn concentrations range from 16 to 5680 ppm. Samples with over 1 wt. % carbonate have between 0.3 and 0.5 wt.% Mn, and ankerite can account for most of the Mn in those samples. If the dominant carbonate is dolomite, however, some of the Mn must be hosted in chlorite or magnetite (e.g., magnetite in BIF from the Thompson Ni Belt contains ~500 ppm Mn: Dare et al., 2014). Bulk-rock Mn in the Temagami BIF is generally higher than average compared to other Algoma-type BIF (Table 10.1). Ti concentrations range from 6 ppm to 0.6 wt.%, with chlorite samples containing 0.2 to 0.3 wt. %. In chlorite-rich samples, Ti is hosted in ilmenite (~50 wt. %), and in high-Fe samples, Ti is hosted in magnetite (~100 ppm). P concentrations range from less than 0.004 wt.% to 0.190 wt.%. It is present mainly in apatite. Compared to the average Algoma-Type BIF, Temagami is slightly depleted in P with an average of 0.04 wt.%.

Base metals

Zn concentrations range from 1.3 ppm to 185 ppm, Cu concentrations range from less than 0.04 ppm to 668 ppm, and Pb concentrations range from less than 0.1 ppm to 9

ppm. Most of the base metals (esp. Cu) appear to be related to trace amounts of pyrite. Some of this enrichment is likely related to minor sulfides associated with late carbonate. However, several 10s of ppm Zn still occur in samples with litle or no S or C. This may indicate that some metal (esp. Zn) is contained in chlorite or magnetite (e.g., magnetite from the BIF in the Thompson Nickel belt contains 15-50 ppm Zn: Dare et al., 2014). There is a poor correlation between Cu and Zn, which suggests that the precipitation mechanisms for these metals were decoupled. This might occur, for example, if one metal is mainly present in diagenetic sulfide and another in chlorite, a common feature in carbonaceous argillite horizons elsewhere in the Abitibi (Hannington et al., 2012). In particular, this may also account for the much higher Cu/Zn ratio and Pb/Cu ratio than in other AlgomaType BIF (e.g., Figure 10.4).

Trace metals

Analyses of Au in FER-3 and FER-4 by INAA indicated generally low concentrations (less than 2 ppb) in the Sherman mine ore. Therefore additional analyses were not performed. In general, the precious metal concentrations of the BIF are considered to be very low. Ag concentrations range from less than 0.01 ppm to 1.46 ppm, less than the Algoma BIF average of 4.36 ppm. In contrast, As concentrations range from less than 0.02 ppm to as high as 918 ppm (in the sulfide outcrop on Highway 11). The average As concentrations are notably higher than other Algoma-Type BIF and likely reflect locally high As concentrations in hydrothermal fluids that altered the footwall (one of the small lakes in the altered felsic volcanic rocks of the Sherman Mine is named

“Arsenic Lake”: Figure 4.1). Concentrations of Sb (0.02 to 24.5 ppm), Hg (2 to 333 ppb), Tl (0.01 to 0.52 ppm), and Cd (0.02 to 0.20 ppm) are mainly associated with trace sulfide. The highest concentrations are found in the sulfide sample taken from Highway 11. Concentrations of these elements are generally low in the BIF itself.

Co concentrations range from 0.05 to 49 ppm, and Ni concentrations range from 0.1 to 79 ppm. A pyrite-rich chlorite sample has 520 ppm Ni. The Algoma-Type BIF averages 14.7 ppm and 0.15 ppm, respectively. Samples that contain high Ni, Mo, Cr, and Se appear to be mainly related to the presence of trace (diagenetic?) pyrite. The highest concentration of pyrite in the BIF layers was about 1.6 wt.% (sample B013-1: see Table 12.5). At the highest bulk Ni concentration in the BIF (79 ppm: Diekrup et al., in preparation), this would correspond to a Ni content in pyrite of about 1.27 wt.% Ni, if all the Ni was hosted in pyrite. Co and Ni, like As, Sb, Hg, and Tl, are particularly enriched in the footwall shale unit, together with Se and Mo. All are redox sensitive elements and appear to be mainly associated with the presence of diagenetic sulfide. Cr concentrations range from 2.9 to 90.3 ppm. A jasper sample with very coarse magnetite has a bulk Cr concentration of 1130 ppm, and Cr concentrations correlate positively with Ni and Mo (Table 10.3). Cr concentrations are generally higher than the Algoma-Type BIF average. V concentrations range from less than 0.2 to 159 ppm.

Traces of Te, Bi, In and Sn are also mostly related to the presence of chlorite or shale, most probably in pyrite; they are absent in the oxide facies of the BIF. W concentrations range from less than 0.02 to 72.1 ppm; W is variably but slightly enriched with Mn and C

(in late carbonate), which might indicate the presence trace amounts of wolframite in the late stage veins. Several chert and jasper samples have anomalously high W, ranging from 11.0 ppm in a jasper sample to 72.1 in a white chert sample. Unlike the other trace metals, Ge concentrations, which range from less than 0.5 ppm to 14.3 ppm, do not correlate well with pyrite content. LA-ICP-MS analyses of hydrothermal magnetite in BIF from the Thompson Ni Belt (Dare et al., 2014) have found concentrations of 5 to15 ppm Ge. Considering about 50% magnetite in FeR-3 and FeR-4 (Abbey et. al, 1983), a similar range of Ge concentrations (5-15 ppm) in magnetite could easily account for the 5 ppm bulk Ge in FeR-4. However, Ge also could be present in silica where it has been previously detected in other types of BIF (e.g., in the Dales Gorge member of the Hammersley BIF: Hamade et al., 2003).

Other trace elements

Boron concentrations range from less than 0.2 ppm to 68.8 ppm. B has the highest correlation with Si and has a strong negative correlation with base metals, Zn and Co. Although B is known to be enriched in Archean cherts from other locations (Baldwin, 2009; Baldwin et al., 2011), samples of Temagami BIF have never been analyzed for boron. Ga concentrations range from 0.08 to 35.7 ppm and most strongly correlate with Ti and Al. Zr concentrations range from less than 0.2 ppm to 149 ppm. Samples with high Zr likely contain detritus from felsic volcanic sources in the area. By comparison, the average

Zr concentration in Algoma-Type BIF is 66.3 ppm. Hf concentrations range from less than 0.1 ppm to 3.90 ppm, Nb concentrations range from less than 0.2 ppm to 12.8 ppm, and Ta concentrations range from less than 0.01 ppm to 1.15 ppm. These elements most strongly correlate with Zr and Ti and have not previously been measured in Algoma-Type BIF. Sc concentrations range from less than 1 ppm to 21.0 ppm. Th concentrations range from less than 0.05 ppm to 11.4 ppm, and U concentrations range from less than 0.01 ppm to 3.11 ppm. These elements also correlate strongly with Al and Ti. The average concentrations in Algoma-Type BIF are 1.1 ppm and 10.1 ppm, respectively, about the same as those measured in the Temagami samples.

Ba concentrations range from 0.5 ppm to 553 ppm. Ba, Sr, Rb and Cs correlate strongly with K, indicating that these elements are hosted in secondary phyllosilicates (e.g., muscovite and biotite). Several chert samples at the top or bottom of BIF sequences contain anomalously high Ba. These samples also contain metamorphic biotite.

10.2 Compositions of the Different BIF Facies

The chert facies of the Sherman mine samples contains 25-45 wt.% Si and typically <10 wt.% Fe. The most Fe-rich samples contain minor amounts of Mg and P, as well as several hundred ppm Ti, in part indicating a minor detrital component containing ilmenite. This is supported by the few ppm of Th, Sc, Y, Hf, and Zr (up to 1 ppm) as well as ΣREE (up to 100 ppm). However, some Ti may also be present in ilmenite derived

from an unknown primary precipitate (e.g., amorphous Fe-Ti-oxide or clay). The Mn concentrations are slightly higher on average than in other facies, and this is likely related to late carbonate veinlets that are developed in the more brittle chert bands. Cu and Zn concentrations are generally less than 10 ppm, and Pb concentrations are less than 1 ppm. All other trace metal concentrations are extremely low, except for minor Co (to 10 ppm) and Ni (to 40 ppm), which correlates with minor enrichment in Zn (to 40 ppm). These samples all contain higher than average Ca and Mg, and some contain slightly higher S, consistent with metal enrichment associated with late-stage carbonate and rare sulfide. Trace elements like Ge are uniformly low; W concentrations are anomalous (to 70 ppm) in the carbonate-bearing samples. Cr concentrations are uniformly high (30 ppm). Several of the Cr-rich samples (up to 90 ppm) also contain high V (to 50 ppm) as well as Ba (to 500 ppm), Cs (1 ppm), Rb (to 70 ppm) and Li (28 ppm), the latter most probably indicating the presence of biotite (up to 2 wt.% K) in the late-stage alteration. Boron concentrations (to 60 ppm) are uniformly high in the chert facies; an interference, for example with Si, during ICP-MS analysis seems unlikely as there is no clear correlation with Si between samples.

The jasper facies contains 30-40 wt.% Si and 10-20 wt.% Fe. The most Fe-rich samples contain minor amounts of Ca and Mg and Ti, most likely related to late-stage carbonate and leucoxene. However, the Fe-rich samples contain little or no Th, Sc, Y, Hf, or Zr and they have low ΣREE, indicating that there is a much smaller or no detrital component in the jasper samples compared to the background chert. The Mn concentrations are high (average 240 ppm) and likely correlated with carbonate as in

other sample types. The Mn concentrations correlate weakly with the other metals, which are uniformly low and similar to the chert samples. Traces of Ni, Mo, Cr and Se may be related to the presence of trace amounts of pyrite. Trace elements like U and REE are uniformly low, despite the abundance of iron oxides, which may contain these elements (e.g., Bowins, 1989). Boron concentrations (~35 ppm) are similar to those of the chert facies.

The magnetite facies contains 5-25 wt.% Si and 10-60 wt.% Fe, but otherwise is very similar in terms of major element concentrations to the chert and jasper facies. Minor amounts of Mg and P are present, as well as several hundred ppm Ti, indicating a minor detrital component or the presence of late-stage alteration (e.g., leucoxene rims on magnetite). However, the Th, Sc, Y, Hf, and Zr concentrations are generally low, as is ΣREE (average less than 20 ppm). The Mn concentrations are slightly higher than in the chert and jasper facies, but the Cu and Zn concentrations are low. The highest Mn concentrations are clearly related to late-stage carbonate (up to 4 wt.% Ca and 2 wt.% C), which also likely accounts for the slightly higher Rb and Sr. The trace metals are notably enriched in the magnetite facies compared to the chert and jasper facies (except black chert which also has high magnetite content). Two groups of trace metals are observed. As (to 25 ppm), Sb (to 2.5 ppm), Tl (to 0.5 ppm), Ni (to 30 ppm), Mo (to 6 ppm) and Se (to 2.3 ppm) are positively correlated with sulfur (maximum 1 wt.%), which reflects the presence of trace (diagenetic?) sulfide in the magnetite. Germanium is notably enriched in the magnetite facies (to 14 ppm) but does not appear to be related to S content. V and Cr are also uniformly high (8 ppm and 20 ppm, respectively) and

positively correlated but unrelated to S, suggesting that they too are contained in the magnetite. Titanium also appears to be enriched in magnetite, but in these samples it is mainly related to leucoxene alteration rims on the magnetite from near-surface weathering. Minor amounts of Ti are likely also present in chlorite in this facies. U (to 0.66 ppm), Th (to 2.9 ppm), and Be (to 1 ppm) are possibly elevated in the magnetite-rich samples compared to other BIF facies. Zr (to 59 ppm), Ba (to 200 ppm), and Cs (to 46 ppm) are correlated with K (to 0.5 wt.%), consistent with enrichment in late-stage muscovite or biotite. There is slightly more P in the magnetite-rich samples, as well. This might be due to late-stage alteration rims on magnetite, but EPMA analyses of magnetite also show up to 0.1 wt. % P_2O_5. The ΣREE concentrations are variable but high (to 100 ppm). B concentrations (~20 ppm) are more variable and slightly lower than in black chert.

The chlorite facies contains 15-25 wt.% Si, 5-30 wt.% Fe, 2-5 wt.% Mg, and 3-6.5 wt.% Al. Titanium concentrations are significantly higher than in other BIF facies (av. 2500 ppm Ti). Cr (to 1100 ppm) and V (to 150 ppm) are also notably higher than in the other BIF facies, as is Ga (to 30 ppm). The sampled material also contains variable amounts of Ca (to 8 wt.%) but generally low K and P. LOI is ~5 wt.%, which consists of a combination of structural water, S, and CO_2. However, the samples do not appear to be significantly more enriched in sulfides or late carbonates than the other BIF facies. Mn concentrations, which are normally associated with carbonates, average about 675 ppm. The chlorite facies is also notably enriched in base metals (Zn to 97 ppm, Cu to 29 ppm, Pb to 2.6 ppm, Cd to 0.2 ppm, Ag to 0.3 ppm) compared to the other BIF

facies. Zr (to 500 ppm), Sc (to 20 ppm) and U and Th (5-6 ppm) are likely related to a detrital component in the chlorite facies. ΣREE (>100 ppm) are generally higher than in the other BIF facies. The very high Zr and ΣREE is a strong indication that the volcaniclastic component was felsic and probably related to the abundant felsic volcanic rocks in the footwall of the mine.

Most of the trace metals in the chlorite facies are associated with diagenetic sulfide. This interpretation is supported by one sample of pyrite from the sulfide found outcropping on Highway 11 (Sample H11-110, see Figure 6.7: Diekrup et al., in preparation). The sample contains 670 ppm Cu, 9 ppm Pb, 1.5 ppm Ag, 918 ppm As, 1.5 ppm Sb, 45 ppm Co, 26 ppm Ni, and 23 ppm Se, but little Zn (<5 ppm) (Diekrup et al., in preparation) show that sulfidic black shale that is spatially associated with the BIF at the west end of the south pit has similar metal concentrations. Although there is a correlation between carbon and sulfur in the black shale samples, neither are always clearly linked to metal enrichment. This may indicate that metal deposition in the local basins was sulfur-limited, as not all metals appear to be contained in the sulfide fraction. Pyrite concentrates from black shale at the west end of the south pit contain less than 100 ppm Zn, and mostly less than 50 ppm, but have high average Co (180 ppm) and Ni (225 ppm), typical of diagenetic sulfides, as well as high Ag (10 ppm), Pb (150 ppm), and Cu (480 ppm). The very high As concentrations probably are reflective of the As enrichment of sulfides within the footwall felsic volcaniclastic units north of the mine area.

10.3 Normative Mineralogy

The geochemical data for the different BIF facies allow a quantitative assessment of the mineralogy. Normative mineral abundances in Table 10.2 were calculated by assuming the proportions of elements which could reasonably be expected in each mineral. Except for the jasper facies and chlorite facies, all Fe in the chert samples and magnetite-rich samples is assumed to be present in magnetite. In the jasper samples, hematite and magnetite are present in subequal amounts, and Fe was apportioned accordingly (69.9 wt. % Fe in hematite, 72.4 wt. % Fe in magnetite). The most obvious difference between the calculated mineralogy and that presented in Appendix 3 is the abundance of quartz, as SiO_2 was not included in the calculated abundance of chlorite, biotite, and muscovite. Normative chlorite is calculated from the bulk Al in all samples, assuming all Al is in chlorite and using the mineral compositions in Table 9.2. Normative carbonate is calculated from bulk C and dolomite compositions in Table 9.3. Normative pyrite is calculated from bulk S; normative apatite is calculated from bulk P in all samples. Normative leucoxene was calculated assuming all Ti in magnetite facies samples was present in late leucoxene rims; Ti in all other facies was assigned to ilmenite. Normative biotite is calculated from bulk K in all samples.

The calculations highlight that some field and hand specimen characterizations can misrepresent the mineralogy of the different facies. They confirm that the abundance of Fe-oxides in the black chert samples can be as low as 1 wt.% but chlorite contents can be as high as 9 wt.%. White chert samples can contain up to 18 wt.% Fe oxides and

less than 1 wt.% chlorite. Jasper contains no chlorite and can contain up to 21 wt.% Fe oxide. The magnetite facies can contain up to 5 wt.% chlorite. Some chlorite-rich layers contain only 10 wt.% chlorite but 17-30 wt.% Fe oxides as determined by calculating mineral concentrations from bulk chemical composition.

The normative abundances also permit an assessment of the mineralogical siting of a number of the different trace elements. For example, in the magnetite facies, if all of the Ge in the most Ge-rich samples was contained in normative magnetite, the Ge content of the magnetite would be ~10 ppm, similar to that indicated by LA-ICP-MS analyses in other studies (Dare et al., 2014). The likely concentrations of other elements can be similarly calculated. (e.g., chloritic samples contain an average of 23 ppm Ga and ~10 wt.% chlorite, which would contain 230 ppm Ga if all Ga is hosted in chlorite).

10.4 Contributions from Clastic Deposition

The presence of ilmenite, altered feldspar, and lithic clasts in some layers of the Temagami BIF, especially in chloritic layers, indicate an important volcaniclastic component of the rocks. Previous work on Archean interflow sedimentary rocks (e.g., Cameron and Garrels, 1980; Feng and Kerrich, 1990) has shown that whole-rock geochemical data may be used to identify the local volcanic source rocks from which the sediments were eroded. In contrast to graphitic argillite units, chemical sedimentary rocks, such as iron formation or chert units, contain only a few percent or less of Al_2O_3 that could reflect volcaniclastic input (e.g., tuffaceous components), diluted by a large

chemical component. However, even at low concentrations the volcaniclastic component can sometimes be identified on the basis of major element and immobile element ratios. In particular, ratios of Al, Ti, and P, as well as high-field-strength elements (HFSE) such as Zr, Y, Th, Nb, Ta and the rare-earth elements (REE) are commonly preserved through the sedimentation process (Hannington et al., 2012). As most sediments are sourced locally, at least at the scale of the major volcanic centres of the southern Abitibi belt (e.g., Thurston et al. 2008), it can be assumed that the volcaniclastic component in the Temagami BIF was derived mainly from the locally exposed footwall succession (see Figure 4.2).

An estimation of the volcaniclastic component of the Temagami BIF can be made by comparing trace element ratios of the BIF and mafic and felsic volcanic rocks typical of the local bimodal volcanism. This is illustrated for Zr/Ti in Figure 10.5. These data show that the volcaniclastic material in the Temagami BIF is mainly derived from volcanic rocks (or their sedimentary equivalent) with a large component of felsic material, similar to that observed in the lower part of the Temagami Greenstone Belt. The array of data approaching the origin represents the significant dilution by silica in the BIF. Similar results are obtained from a ternary Zr-Sc-Th plot which shows a much larger component of felsic rich (Zr-rich) rather than mafic-rich (Sc-rich material) (Figure 10.6, after Feng and Kerrich, 1990). The proportions of mafic and felsic end-members can be estimated from the departure of the Zr/Ti ratios from the basalt and rhyolite lines (Figure 10.7). The volcaniclastic component in the chlorite facies contains between 10% and 40% percent mafic material. The volcaniclastic components of the black chert, white chert and jasper

facies contain between 0% and 10% mafic material. The clastic component of the magnetite facies contains between 15% and 20% mafic components.

10.5 Multielement Correlations

Figure 10.8 shows a trace element multiple element variation diagram (sorted by element abundance in FeR-4) for the different BIF facies and FeR-3 and FeR-4. Similar plots for the different facies of BIF in Temagami are shown in Figure 10.9. Several groups of trace elements account for the largest proportion of the variance in the data set and, like the volcanic-derived clastic material, can be assigned to different components of the BIF. Simple multielement correlations in the data set can help to identify the geochemical contributions from different sources. These correlations can be readily identified through simple techniques for analysis of covariance. A common metric is Pearson's correlation coefficient (r), which is obtained by dividing the covariance of two variables by the product of their standard deviations. Pearson's coefficient of correlation assumes that all data are normally distributed, which is generally not the case in geochemical data. An alternative approach for data that are not normally distributed is the Spearman rank correlation. More sophisticated statistical applications are also possible, for example using principal components analysis (PCA). Table 10.3 lists the Pearson's correlation coefficient (r) for the complete set of analytical data. Although subject to the limitations of Pearson’s analysis, inspection of the r values reveals a limited number of consistent positive and negative correlations among the major and trace elements that can be readily interpreted in terms of mineralogical components or contributions from different

chemical and clastic sources. From this simple analysis it is possible to identify those elements that relate to different processes of BIF deposition and alteration.

Some negative correlations, such as that between Si and Al (r=-0.6) or between Si and Fe (r=-0.9), logically reflect dilution (by SiO_2). Some multielement correlations have low scores but are consistently negative or positive; for example, the correlation coefficients for different metals and Eu are generally low, but the Eu anomaly is consistently positively correlated with all metals. This most likely reflects the general enrichment related to hydrothermal input into the BIF (see below). A summary of the interpreted correlations and the likely components responsible is provided in Table 10.4.

10.6 Rare Earth Elements

Phosphorous correlates generally with ΣREE, suggesting that most of the REE and Y are present as trace phosphates, mainly apatite and monazite. Y concentrations range from less than 0.5 ppm, the lower limit of detection, to 48.2 ppm. Total REE (Table 10.3) concentrations are 0.755 to 146 ppm. Among the REE, La and Ce are present at the highest concentrations, from 0.12 ppm to 72.6 ppm La and from 0.27 ppm to 162 ppm Ce. If all of the LREE are hosted in phosphate minerals (apatite or apatite with monazite inclusions: see above), the ΣCe+La content of the phosphate component would be as high as 800 ppm.

Four different REE signatures, based on overall REE concentration, presence of a Eu anomaly, and degree of LREE enrichment are evident in the data. The first is characterized by high concentrations of REE, a slight LREE enrichment and, no Eu anomaly (Figure 10.10). The second REE profile is characterized by high concentrations of REE and a strong LREE enrichment, but no Eu anomaly. This group includes a number of samples of the chlorite facies BIF that may be products of proximal low-temperature hydrothermal venting responsible for the LREE enrichment. The third REE profile shows low total concentrations, little LREE enrichment and a positive Eu anomaly (Figure 10.11). This group includes mostly magnetite facies BIF. The fourth REE is characterized by low concentrations of REE, LREE enrichment, and a positive Eu anomaly (Figure 10.12). The majority of the Temagami BIF samples fit the profile for this latter group. The positive Eu anomaly, calculated as Eu/Eu* =

$2Eu_{CN}/(Sm_{CN}+Gd_{CN})$, is interpreted to indicate a hydrothermal source for the REE (Bau & Alexander, 2009). This may also be indicated by the LREE enrichment (e.g., La/Yb ratio) reflecting the greater solubility of the LREE in hydrothermal fluids. The average value of the Eu anomaly is 2.58 for jasper, 2.32 for magnetite, 2.17 for white chert, 1.85 for black chert, and 1.02 for chlorite. The average La/Yb ratio is 3.26 for jasper, 5.77 for magnetite, 5.31 for white chert, 5.91 for black chert, and 7.03 for chlorite.

Previous work on REE in the Temagami BIF interpreted the data to reflect paleoweathering of adjacent volcanic rocks, direct addition of volcaniclastic material, ambient seawater and hydrothermal venting (Bowins, 1989). The results of this study can be similarly interpreted in terms of mixed mafic and felsic detrital components in some samples, but the dominant pattern is one of hydrothermal input indicated by the positive Eu anomalies. The evidence for seawater components in the chert remains unclear. Bau and Alexander (2009) showed that a false negative Ce anomaly was likely calculated using PAAS (Post Archean Australian Shale) normalization in previous studies.

Table 10.1: Summary data from whole-rock lithogeochemistry of the Temagami BIF (samples listed in Appendix 1).

				Temagami Facies avg					
		Temagami BIF avg n=54	Jasper n=5	Black Chert n=13	White Chert n=9	Magnetite n=19	Massive Chlorite n=4	Banded Chlorite n=4	**Algoma -Type Avg***
Si	%	**28.0**	35.6	37.7	39.3	16.6	22.8	19.7	**41.4**
Al	%	**1.28**	0.095	1.05	0.345	0.433	6.46	5.56	**0.571**
Fe	%	**22.0**	15.4	8.94	6.49	41.5	15.3	25.3	**20.5**
Ca	%	**0.559**	0.250	0.264	0.384	0.833	1.40	0.456	**2.33**
Mg	%	**1.14**	0.208	0.825	0.514	1.09	3.99	2.87	**1.32**
Na	%	**0.108**	0.007	0.043	0.007	0.027	1.26	0.012	**0.402**
K	%	**0.090**	0.011	0.171	0.032	0.130	0.010	0.013	**0.225**
P	%	**0.040**	0.045	0.025	0.017	0.053	0.086	0.049	**4.54**
LOI	%	**2.65**	-0.142	1.91	3.72	0.556	6.51	4.61	**4.93**
C_{tot}	%	**0.426**	0.050	0.226	0.787	0.477	0.390	0.110	**2.80**
S_{tot}	%	**0.114**	0.010	0.077	0.128	0.169	0.010	0.000	**2.09**
Ti	ppm	**540**	12.5	23.0	40.2	150	3314	2083	**0.878**
Mn	ppm	**894**	129	295	884	1252	639	416	**93.4**
Zn	ppm	**30.1**	10.9	24.3	11.7	27.2	79.2	99.9	**106.1**
Cu	ppm	**22.0**	0.832	16	5.18	8.772	38.2	4.24	**7.35**
Pb	ppm	**1.62**	1.38	1.12	0.859	1.70	1.78	3.25	**0.005**
Au**	ppm	**bdl**	na	na	na	na	na	na	**bdl**
Ag	ppm	**0.091**	0.027	0.067	0.023	0.045	0.235	0.180	**4.36**
As	ppm	**20.1**	1.12	1.35	4.39	3.705	9.1	1.09	**0.400**
Sb	ppm	**0.53**	0.568	0.301	0.205	0.980	0.080	0.133	**10.2**
Hg	ppm	**0.022**	0.013	0.043	0.044	0.005	0.002	0.003	**na**
Tl	ppm	**0.036**	0.006	0.027	0.007	0.081	0.005	0.006	**na**
Cd	ppm	**0.048**	0.023	0.044	0.020	0.040	0.160	0.103	**22.0**
Co	ppm	**5.7**	0.683	5.113	2.665	3.128	25.8	6.12	**14.7**
Ni	ppm	**28.3**	15.7	29.82	11.51	17.042	33	16.8	**0.145**
Se	ppm	**0.90**	0.10	0.4	0.2	0.6	1.90	0.728	**1.62**
Mo	ppm	**2.41**	3.235	4.426	1.860	2.020	0.780	0.276	**na**
Te	ppm	**0.069**	0.020	0.04	0.03	0.05	0.108	0.055	**na**
Sn	ppm	**0.236**	0.100	0.354	0.100	0.174	0.575	0.425	**na**
Ge	ppm	**4.97**	4.817	3.477	2.627	7.621	3.60	6.43	**na**
Bi	ppm	**0.059**	0.010	0.03	0.03	0.05	0.066	0.015	**na**
In	ppm	**0.016**	0.010	0.013	0.011	0.013	0.045	0.030	**na**
Re	ppm	**0.0012**	0.001	0.001	0.001	0.001	0.002	0.0021	**5.792**
W	ppm	**4.38**	1.47	8.338 5	0.866 7	1.1879	0.323	0.313	**19.6**
Cr	ppm	**48.5**	32.72	45.01	20.60	23.09	36	31.2	**16.8**
V	ppm	**15.3**	1.50	10.7	3.6	8.5	85.5	48.9	**na**

Ga	ppm	**4.44**	0.400	3.1	0.92	2.03	22.7	18.9	**34.5**
Zr	ppm	**22.0**	0.667	1.50	4.073	9.07	115	87.7	**66.3**
Ba	ppm	**34.1**	30.5	7.9	4.00	30.77	8.85	12.8	**na**
Cs	ppm	**2.01**	0.200	0.3	0.257	5.633	0.203	0.161	**na**
Li	ppm	**5.76**	0.508	5.927	0.650	1.48	29.1	25.5	**1.62**
Be	ppm	**0.626**	0.380	0.44	0.165	1.07	0.865	0.698	**na**
B	ppm	**30.2**	36.500	46.8	42.464	19.13	7.98	10.3	**na**
Hf	ppm	**0.615**	0.200	0.47	0.127	0.2	3.08	2.60	**na**
Nb	ppm	**1.28**	0.500	1.29	0.100	0.453	6.28	4.88	**na**
Ta	ppm	**0.137**	0.040	0.11	0.048	0.069	0.565	0.528	**na**
Rb	ppm	**5.46**	0.537	6.70	1.042	11.025	0.273	0.855	**37.1**
Sr	ppm	**22.5**	25.017	10.18	21.65	28.5	50.7	9.56	**na**
U	ppm	**0.339**	0.100	0.350	0.098	0.178	1.36	1.24	**1.14**
Th	ppm	**1.11**	0.034	0.842	0.196	0.481	4.75	5.76	**27.0**
Y	ppm	**6.69**	4.000	4.596	2.673	6.247	25.9	12.9	**6.70**
La	ppm	**5.52**	1.22	4.95	1.93	4.87	17.2	16.4	**10.7**
Ce	ppm	**10.7**	2.01	9.89	3.42	7.98	38.1	34.6	**1.57**
Pr	ppm	**1.23**	0.240	1.12	0.382	0.89	4.71	3.89	**4.77**
Nd	ppm	**4.75**	0.998	4.20	1.510	3.415	19.0	14.3	**0.716**
Sm	ppm	**0.94**	0.225	0.79	0.300	0.64	4.21	2.64	**0.623**
Eu	ppm	**0.401**	0.219	0.295	0.184	0.443	1.16	0.755	**1.04**
Gd	ppm	**0.87**	0.320	0.697	0.326	0.678	3.75	1.92	**0.258**
Tb	ppm	**0.1407**	0.058	0.104	0.051	0.109	0.648	0.305	**0.961**
Dy	ppm	**0.85**	0.363	0.626	0.301	0.674	3.88	1.79	**0.332**
Ho	ppm	**0.177**	0.083	0.130	0.064	0.144	0.775	0.383	**0.991**
Er	ppm	**0.536**	0.255	0.393	0.190	0.454	2.26	1.16	**0.144**
Tm	ppm	**0.083**	0.039	0.061	0.029	0.072	0.336	0.183	**8.940**
Yb	ppm	**0.5459**	0.245	0.411	0.195	0.477	2.16	1.24	**0.125**
Lu	ppm	**0.089**	0.039	0.066	0.032	0.080	0.337	0.204	**0.639**
Sc	ppm	**2.12**	0.500	1.654	0.682	0.868	12.5	6.00	**na**
ΣREE	ppm	**26.84**	6.32	23.73	8.91	20.93	98.44	79.84	**31.78**

Footnote: The Temagami BIF average is the average composition of all samples included in this study. The full data set is reported in Diekrup et al. (submitted). Outliers were removed from the statistical data set to avoid skewing the averages of certain elements: black cherts H11-9a (Ba, Ti, Zr), H11-40.4 (Ti, Zr), H11-73.3 (Mn), A028-2 (Ti, Mn), B013-5 (Mn); white cherts H11-30.8 (Ba), H11-59.7a (Ti),

B013-2 (W), B013-3 (W); magnetite samples H11-133.1 (Ti); B013-1 (Ba); jasper sample SM011 (Mn, W, Ba); massive chlorite samples H11-65.8 (As, Ni, Cr).

* Algoma-Type BIF average database is compilation of BIF element concentrations from Adams Mine, Kirkland Lake, Griffith Mine (Red Lake, ON) and Jerome, AZ. The database is reported in (Diekrup et al., in preparation)

** Au concentrations were measured by INAA for BIF standards FeR-3 and FeR-4 and found to be below the detection limit of 2 ppm, so Au concentrations were not measured for this samples collected by this study.

Table 10.2: Normative Mineralogy of the Temagami BIF based on whole-rock lithogeochemical data reported in Diekrup et al., (in preparation)

Facies	Sample	% Fe oxide	% Qtz	% Chl*	% Carb	% Pyr	% Apt	% Lcx	% Ilm	% Mica
Black Chert										
	H11-73.3	5.3	94.2	0.4	0	0	0	0.1		0.1
	H11-9a	3.6	76.5	7.3	0	0	0		3.4	9
	H11-31.3	2.4	97.1	0.3	0.1	0	0	0		0.1
	H11-66.2	1.5	97.4	0.2	0.7	0	0	0.1		0.1
	H11-40.4	16.2	68.3	8.6	0.1	0.3	0	6.5		0.1
	S2A030	2.8	96.8	0.2	0	0	0	0		0.1
	S2A028b	24.6	73.8	0.3	0.1	0.3	0	0.4		0.6
	S2B013b	2.4	96.6	0.1	0.8	0	0	0		0.1
	S2C012	4.7	95	0.1	0.2	0	0	0		0
	S2D020	0.7	99.1	0	0.1	0	0	0		0.1
White Chert										
	H11-30.8	10.6	87.8	0.2	1	0.1	0	0.1		0.1
	H11-68.5	3.6	95.8	0.4	0	0	0	0.1		0.1
	H11-9b	0.6	98.9	0.5	0	0	0	0		0
	H11-70.4	18.1	79.2	0.9	0	0	0.1	0.6		1.1
	H11-125.6a	0.8	98.3	0.5	0.1	0	0	0		0.3
	S2A027	0.5	99.3	0.1	0	0	0	0		0.1
	S2B013c	0.9	98	0.3	0.7	0	0	0		0
	S3C303	0.6	99.2	0.2	0	0	0	0		0
Magnetite										
	H11-145.9	7.1	92.5	0.2	0	0	0	0.1		0
	H11-21.9b	16.7	82.9	0.2	0	0	0	0.1		0
	H11-119.8	30.5	67.4	0.6	0.4	0	0	0.3		0.9
	H11-124.8	44.5	51.7	1	0.2	0.1	0.1	0.6		1.8
	H11-133.1	36	51.4	5.5	0	0	0	3.3		3.7
	H11-139.4	21.1	73.2	1.7	0	0	0	1.2		2.8
	H11-164.2	26.1	64.8	1.2	2.9	0.7	0	0.9		3.4
	H11-35.6	36.2	62.4	0.5	0	0	0.1	0.2		0.7
	S2D020	26.3	72.5	0.1	0.3	0	0	0.4		0.3
	S2B013a	49.4	36	1.8	7.3	1.6	0.2	2.5		1.2
	S2D015	74	25.6	0.1	0	0	0	0.1		0.2
Banded Chlorite	H11-21.9a	17.5	75.6	5	0	0	0	1.8		0
	H11-5	19.4	57.5	12.7	0	0	0.1	10		0.1
	H11-125.6b	17.2	64.9	10.6	0.3	0	0	6.9		0.1
	H11-22.6	31.6	57.4	8.4	0	0	0	2.5		0.1

Massive Chlorite	H11-7	17.1	67.4	9.8	0	0	0		5.7	0
	H11-20.7	16.7	69.6	10.6	0	0	0		3	0
	H11-65.8	12.1	69.8	8.6	0.9	0	0.1		8.4	0
	S2D001	3.7	71	10.9	0	0	0.1		14.1	0.1
Jasper										
	S211b-50	18.9	80.6	0.2	0	0	0	0.1		0.2
	S211b-51	17.4	82.4	0.1	0	0	0	0		0
	S2SM052	6.2	93.7	0.1	0	0	0	0		0
	S2C060-2	17.8	82	0.1	0	0	0	0		0.1
	S2SM011-2	21	78.8	0.1	0	0	0	0		0

* A typical chamosite $(Fe,Mg)_5Al(AlSi_3O_{10})(OH)_8$ was used to determine the mineral concentration of chlorite from a sample's bulk composition.

Table 10.3: Pearson's correlation coefficient matrix of major and trace element concentrations in the Temagami BIF (n=64).

	Si	*Al*	*Fe*	*Ca*	*Mg*	*Na*	*K*	*P*	*LOI*	*C*	*S*	*Ti*	*Mn*	*Zn*	*Cu*	*Pb*	*Ag*	*As*	*Sb*	*Hg*	*Tl*	*Cd*	*Co*	*Ni*	*Se*	*Mo*	*Te*	*Sn*	*Ge*
Si	1.00																												
Al	-0.60	1.00																											
Fe	-0.91	0.26	1.00																										
Ca	-0.07	-0.15	-0.04	1.00																									
Mg	-0.91	0.44	0.87	-0.01	1.00																								
Na	-0.25	0.70	-0.09	-0.13	0.25	1.00																							
K	-0.25	0.69	-0.08	-0.13	0.27	1.00	1.00																						
P	-0.56	0.69	0.33	0.05	0.20	0.35	0.34	1.00																					
LOI	-0.22	0.33	-0.07	0.71	-0.05	0.13	0.13	0.56	1.00																				
C	0.20	-0.33	-0.12	0.30	-0.34	-0.24	-0.25	0.10	0.39	1.00																			
S	-0.86	0.29	0.94	-0.05	0.81	-0.17	-0.17	0.37	-0.05	-0.33	1.00																		
Ti	-0.66	0.97	0.38	-0.16	0.49	0.49	0.48	0.69	0.32	-0.32	0.44	1.00																	
Mn	-0.58	-0.20	0.69	0.41	0.72	-0.15	-0.12	-0.12	0.03	-0.04	0.64	-0.16	1.00																
Zn	-0.73	0.64	0.55	-0.16	0.83	0.70	0.72	0.27	-0.03	-0.38	0.47	0.56	0.43	1.00															
Cu	0.07	-0.16	-0.02	-0.13	-0.05	-0.10	-0.08	-0.11	0.06	-0.36	0.21	-0.17	0.04	0.09	1.00														
Pb	0.08	0.03	-0.15	-0.03	-0.15	-0.01	0.00	0.13	0.32	-0.35	0.20	0.02	-0.11	0.04	0.90	1.00													
Ag	-0.51	0.84	0.19	-0.06	0.41	0.64	0.65	0.52	0.42	-0.44	0.26	0.79	-0.09	0.67	0.34	0.45	1.00												
As	-0.25	0.19	0.21	-0.03	0.13	-0.10	-0.08	0.36	0.33	-0.31	0.79	0.25	0.05	0.19	0.79	0.85	0.54	1.00											
Sb	-0.45	-0.19	0.63	-0.09	0.65	-0.12	-0.10	-0.26	-0.29	-0.17	0.60	-0.15	0.74	0.52	0.53	0.25	0.11	0.40	1.00										
Hg	-0.12	-0.24	0.26	-0.19	0.01	-0.16	-0.15	0.13	0.01	0.69	-0.01	-0.22	0.15	-0.03	0.34	0.14	-0.08	0.14	0.34	1.00									
Tl	-0.20	0.67	-0.14	-0.15	0.20	0.98	0.98	0.35	0.18	-0.24	-0.19	0.46	-0.18	0.69	0.08	0.17	0.71	0.07	-0.07	-0.10	1.00								
Cd	-0.47	0.73	0.22	-0.23	0.42	0.58	0.59	0.49	0.30	-0.29	0.34	0.68	-0.04	0.71	0.47	0.59	0.90	0.67	0.27	0.01	0.68	1.00							
Co	-0.67	0.36	0.62	-0.19	0.66	0.32	0.34	0.34	0.12	-0.06	0.64	0.35	0.46	0.74	0.58	0.48	0.62	0.61	0.73	0.49	0.40	0.74	1.00						
Ni	-0.13	-0.19	0.25	-0.18	0.15	-0.12	-0.09	0.01	-0.05	0.32	0.29	-0.18	0.25	0.22	0.75	0.55	0.16	0.68	0.71	0.58	0.03	0.39	0.68	1.00					
Se	-0.65	0.74	0.40	-0.06	0.51	0.54	0.55	0.69	0.42	-0.32	0.55	0.71	0.11	0.71	0.41	0.54	0.88	0.71	0.28	0.03	0.62	0.93	0.78	0.38	1.00				
Mo	0.26	-0.37	-0.09	-0.23	-0.30	-0.27	-0.25	-0.06	-0.14	0.56	-0.26	-0.37	-0.14	-0.23	0.44	0.24	-0.20	0.34	0.28	0.58	-0.17	-0.01	0.18	0.80	-0.04	1.00			
Te	-0.34	0.55	0.18	-0.16	0.38	0.34	0.35	0.22	0.10	-0.48	0.27	0.57	0.00	0.45	-0.02	0.07	0.63	0.20	0.01	-0.24	0.35	0.47	0.28	-0.22	0.45	-0.53	1.00		
Sn	-0.54	0.84	0.22	-0.19	0.52	0.93	0.93	0.48	0.11	-0.34	0.15	0.70	0.01	0.85	-0.13	-0.05	0.74	0.00	0.02	-0.14	0.90	0.68	0.48	-0.09	0.68	-0.35	0.47	1.00	
Ge	-0.55	0.23	0.65	-0.30	0.39	0.01	-0.01	0.43	-0.28	0.03	0.69	0.29	0.14	0.22	-0.22	-0.30	-0.05	-0.06	0.15	0.29	-0.07	-0.02	0.24	0.05	0.14	0.05	-0.19	0.19	1.00
Bi	-0.48	0.08	0.58	-0.04	0.57	-0.22	-0.20	0.02	-0.05	-0.32	0.66	0.21	0.50	0.30	0.11	0.05	0.22	0.29	0.46	0.02	-0.21	0.16	0.39	0.04	0.25	-0.35	0.73	0.01	0.00
In	-0.59	1.00	0.26	-0.16	0.45	0.68	0.67	0.67	0.31	-0.34	0.29	0.97	-0.21	0.63	-0.16	0.02	0.84	0.19	-0.18	-0.24	0.65	0.73	0.35	-0.19	0.73	-0.37	0.57	0.83	0.22
Re	-0.34	-0.16	0.53	-0.20	0.22	-0.22	-0.22	0.26	-0.12	0.49	0.41	-0.10	0.28	0.09	0.21	0.05	-0.15	0.29	0.47	0.71	-0.20	0.04	0.47	0.67	0.15	0.64	-0.34	-0.15	0.62
W	-0.18	-0.19	0.31	-0.14	0.06	-0.12	-0.12	0.14	-0.05	0.70	-0.02	-0.17	0.16	-0.04	-0.04	-0.24	-0.22	-0.20	0.18	0.92	-0.14	-0.20	0.29	0.31	-0.15	0.44	-0.27	-0.08	0.42
Cr	0.17	-0.25	-0.01	-0.27	-0.25	-0.29	-0.27	0.04	-0.12	0.49	-0.15	-0.22	-0.19	-0.20	0.40	0.22	-0.13	0.39	0.25	0.52	-0.19	0.06	0.19	0.77	0.03	0.98	-0.48	-0.31	0.12
V	-0.62	0.96	0.29	-0.14	0.47	0.68	0.68	0.70	0.39	-0.33	0.34	0.93	-0.13	0.69	0.08	0.26	0.93	0.41	-0.03	-0.14	0.70	0.87	0.54	0.01	0.88	-0.28	0.57	0.82	0.17
Ga	-0.58	0.99	0.23	-0.14	0.45	0.78	0.78	0.68	0.33	-0.32	0.24	0.92	-0.17	0.69	-0.14	0.04	0.85	0.17	-0.16	-0.20	0.76	0.75	0.40	-0.16	0.76	-0.36	0.55	0.90	0.20
Zr	-0.60	1.00	0.27	-0.17	0.45	0.69	0.69	0.68	0.32	-0.33	0.29	0.97	-0.20	0.65	-0.15	0.03	0.84	0.20	-0.17	-0.22	0.67	0.74	0.37	-0.17	0.74	-0.36	0.57	0.84	0.23
Ba	-0.22	0.68	-0.12	-0.13	0.22	0.99	1.00	0.34	0.15	-0.25	-0.21	0.48	-0.17	0.69	-0.04	0.03	0.66	-0.06	-0.11	-0.13	0.99	0.60	0.33	-0.06	0.55	-0.21	0.33	0.92	-0.03
Cs	-0.37	0.55	0.12	-0.18	0.44	0.83	0.84	0.27	0.11	-0.33	0.11	0.39	0.14	0.84	0.36	0.39	0.73	0.32	0.33	-0.01	0.89	0.79	0.70	0.28	0.75	-0.15	0.42	0.82	-0.07
Li	-0.64	0.97	0.36	-0.15	0.46	0.49	0.48	0.69	0.33	-0.32	0.42	1.00	-0.19	0.54	-0.17	0.02	0.79	0.25	-0.17	-0.23	0.47	0.68	0.32	-0.19	0.70	-0.36	0.56	0.69	0.28
Be	-0.70	0.74	0.45	-0.12	0.71	0.84	0.84	0.46	0.09	-0.28	0.34	0.63	0.28	0.93	-0.13	-0.11	0.67	0.01	0.24	0.00	0.79	0.63	0.61	0.01	0.68	-0.33	0.47	0.95	0.28
B	0.64	-0.36	-0.57	0.15	-0.78	-0.46	-0.48	-0.15	0.05	0.30	-0.58	-0.30	-0.59	-0.90	-0.40	-0.33	-0.55	-0.43	-0.76	-0.13	-0.51	-0.70	-0.88	-0.49	-0.71	0.06	-0.34	-0.60	-0.14
Hf	-0.63	0.99	0.32	-0.18	0.48	0.61	0.60	0.68	0.30	-0.36	0.37	0.99	-0.18	0.62	-0.12	0.06	0.84	0.25	-0.14	-0.23	0.59	0.74	0.38	-0.17	0.75	-0.37	0.57	0.79	0.25
Nb	-0.69	0.97	0.40	-0.11	0.52	0.55	0.54	0.71	0.33	-0.33	0.44	0.99	-0.11	0.60	-0.19	0.00	0.78	0.20	-0.15	-0.22	0.51	0.67	0.36	-0.23	0.71	-0.44	0.55	0.76	0.32
Ta	-0.66	0.99	0.35	-0.11	0.49	0.62	0.61	0.71	0.33	-0.33	0.39	0.98	-0.14	0.62	-0.20	0.00	0.80	0.18	-0.17	-0.23	0.58	0.69	0.35	-0.24	0.72	-0.44	0.54	0.80	0.31
Rb	-0.24	0.69	-0.09	-0.13	0.25	1.00	1.00	0.35	0.14	-0.24	-0.17	0.49	-0.14	0.71	-0.08	0.00	0.65	-0.08	-0.11	-0.15	0.98	0.59	0.33	-0.09	0.55	-0.25	0.35	0.93	-0.01
Sr	0.02	0.07	-0.15	0.40	-0.06	0.24	0.20	0.00	0.21	-0.14	-0.08	0.00	0.01	0.01	-0.13	0.01	0.01	-0.20	-0.22	-0.27	0.18	-0.05	-0.18	-0.38	-0.05	-0.44	-0.12	0.11	0.15
U	-0.79	0.95	0.51	-0.12	0.68	0.62	0.62	0.65	0.25	-0.38	0.53	0.95	0.07	0.76	-0.16	-0.02	0.80	0.20	0.04	-0.19	0.58	0.71	0.49	-0.14	0.76	-0.44	0.57	0.84	0.35
Th	-0.66	0.98	0.35	-0.10	0.48	0.55	0.54	0.71	0.37	-0.32	0.40	1.00	-0.16	0.57	-0.18	0.02	0.80	0.23	-0.18	-0.24	0.52	0.69	0.34	-0.21	0.72	-0.40	0.56	0.74	0.27
Y	-0.73	0.86	0.44	0.04	0.51	0.45	0.45	0.79	0.55	-0.28	0.55	0.88	0.04	0.60	0.18	0.36	0.88	0.59	0.08	-0.05	0.49	0.83	0.61	0.14	0.93	-0.20	0.51	0.64	0.21
La	-0.70	0.98	0.39	-0.16	0.56	0.66	0.66	0.70	0.32	-0.35	0.42	0.96	-0.07	0.73	-0.05	0.12	0.88	0.31	-0.02	-0.17	0.65	0.81	0.51	-0.06	0.83	-0.34	0.58	0.84	0.26
Ce	-0.69	0.99	0.37	-0.16	0.54	0.66	0.66	0.70	0.32	-0.35	0.41	0.97	-0.09	0.71	-0.07	0.10	0.87	0.30	-0.05	-0.18	0.65	0.80	0.48	-0.08	0.82	-0.35	0.58	0.84	0.26
Pr	-0.68	0.99	0.36	-0.16	0.54	0.67	0.66	0.70	0.33	-0.35	0.40	0.96	-0.10	0.71	-0.06	0.11	0.88	0.30	-0.05	-0.18	0.66	0.80	0.49	-0.08	0.82	-0.34	0.58	0.84	0.25
Nd	-0.69	0.98	0.37	-0.15	0.53	0.64	0.64	0.71	0.34	-0.34	0.41	0.97	-0.09	0.70	-0.05	0.13	0.88	0.32	-0.05	-0.18	0.64	0.80	0.49	-0.07	0.83	-0.33	0.58	0.82	0.25
Sm	-0.69	0.97	0.38	-0.13	0.53	0.61	0.61	0.72	0.37	-0.34	0.44	0.96	-0.08	0.68	0.01	0.18	0.89	0.38	-0.03	-0.16	0.62	0.82	0.52	-0.03	0.86	-0.32	0.57	0.79	0.24
Eu	-0.75	0.92	0.46	-0.06	0.57	0.58	0.58	0.77	0.41	-0.33	0.52	0.92	0.03	0.71	0.08	0.23	0.89	0.48	0.08	-0.10	0.59	0.83	0.60	0.10	0.92	-0.22	0.53	0.77	0.27
Gd	-0.72	0.94	0.41	-0.08	0.54	0.60	0.60	0.75	0.42	-0.33	0.47	0.93	-0.02	0.70	0.08	0.26	0.91	0.46	0.04	-0.11	0.62	0.85	0.59	0.05	0.91	-0.28	0.56	0.79	0.23
Tb	-0.72	0.93	0.42	-0.07	0.54	0.56	0.56	0.75	0.44	-0.33	0.49	0.93	-0.02	0.68	0.12	0.29	0.91	0.50	0.05	-0.10	0.59	0.86	0.60	0.07	0.91	-0.25	0.55	0.75	0.22
Dy	-0.74	0.90	0.46	-0.05	0.55	0.49	0.50	0.76	0.46	-0.32	0.54	0.92	0.02	0.65	0.14	0.31	0.90	0.53	0.08	-0.08	0.52	0.85	0.61	0.09	0.91	-0.25	0.55	0.70	0.23
Ho	-0.75	0.90	0.46	-0.01	0.56	0.50	0.50	0.76	0.49	-0.31	0.54	0.92	0.04	0.65	0.12	0.29	0.89	0.53	0.07	-0.09	0.52	0.83	0.60	0.09	0.91	-0.26	0.54	0.70	0.23
Er	-0.73	0.92	0.43	-0.01	0.55	0.55	0.55	0.75	0.48	-0.32	0.50	0.92	0.02	0.68	0.12	0.30	0.91	0.51	0.06	-0.10	0.58	0.85	0.60	0.08	0.92	-0.26	0.55	0.74	0.21
Tm	-0.75	0.92	0.46	-0.01	0.58	0.55	0.55	0.74	0.46	-0.33	0.52	0.92	0.05	0.70	0.10	0.26	0.90	0.49	0.08	-0.11	0.57	0.84	0.60	0.07	0.91	-0.28	0.56	0.75	0.22
Yb	-0.78	0.92	0.50	-0.04	0.62	0.53	0.53	0.73	0.42	-0.33	0.56	0.94	0.07	0.71	0.06	0.21	0.88	0.46	0.10	-0.12	0.54	0.82	0.60	0.05	0.89	-0.29	0.56	0.74	0.26
Lu	-0.80	0.91	0.52	-0.05	0.64	0.50	0.50	0.72	0.41	-0.34	0.59	0.93	0.09	0.71	0.08	0.23	0.88	0.48	0.13	-0.11	0.51	0.82	0.61	0.07	0.89	-0.29	0.56	0.72	0.26
Sc	-0.64	0.97	0.35	-0.19	0.47	0.54	0.53	0.68	0.34	-0.35	0.42	0.98	-0.17	0.61	0.00	0.18	0.87	0.39	-0.07	-0.19	0.54	0.80	0.45	-0.06	0.80	-0.31	0.59	0.73	0.23

	Bi	*In*	*Re*	*W*	*Cr*	*V*	*Ga*	*Zr*	*Ba*	*Cs*	*Li*	*Be*	*B*	*Hf*	*Nb*	*Ta*	*Rb*	*Sr*	*U*	*Th*	*Y*	*La*	*Ce*	*Pr*	*Nd*	*Sm*	*Eu*	*Gd*	*Tb*	*Dy*	*Ho*	*Er*	*Tm*	*Yb*	*Lu*	*Sc*
Bi	1.00																																			
In	0.10	1.00																																		
Re	0.05	-0.17	1.00																																	
W	-0.04	-0.19	0.65	1.00																																
Cr	-0.32	-0.25	0.63	0.39	1.00																															
V	0.15	0.96	-0.09	-0.19	-0.17	1.00																														
Ga	0.05	0.99	-0.16	-0.16	-0.26	0.96	1.00																													
Zr	0.10	1.00	-0.15	-0.18	-0.24	0.97	0.99	1.00																												
Ba	-0.23	0.67	-0.22	-0.11	-0.23	0.67	0.77	0.68	1.00																											
Cs	0.10	0.54	-0.04	-0.15	-0.18	0.67	0.64	0.56	0.83	1.00																										
Li	0.19	0.97	-0.11	-0.18	-0.21	0.93	0.92	0.97	0.48	0.38	1.00																									
Be	0.20	0.73	0.04	0.06	-0.31	0.74	0.81	0.75	0.81	0.81	0.61	1.00																								
B	-0.41	-0.35	-0.23	0.02	0.07	-0.50	-0.41	-0.37	-0.45	-0.81	-0.28	-0.73	1.00																							
Hf	0.15	0.99	-0.15	-0.20	-0.24	0.96	0.97	0.99	0.60	0.50	0.99	0.70	-0.36	1.00																						
Nb	0.19	0.97	-0.14	-0.16	-0.30	0.93	0.94	0.97	0.53	0.43	0.99	0.69	-0.34	0.99	1.00																					
Ta	0.14	0.99	-0.14	-0.17	-0.31	0.95	0.97	0.99	0.60	0.48	0.98	0.72	-0.34	0.99	0.99	1.00																				
Rb	-0.21	0.67	-0.22	-0.12	-0.26	0.68	0.78	0.69	1.00	0.84	0.49	0.84	-0.47	0.61	0.54	0.61	1.00																			
Sr	-0.26	0.06	-0.14	-0.23	-0.50	0.04	0.09	0.06	0.20	0.09	0.01	0.09	0.05	0.04	0.08	0.13	0.20	1.00																		
U	0.27	0.95	-0.06	-0.13	-0.32	0.93	0.94	0.96	0.59	0.57	0.94	0.82	-0.52	0.96	0.97	0.97	0.61	0.07	1.00																	
Th	0.18	0.98	-0.14	-0.18	-0.25	0.94	0.95	0.98	0.53	0.42	1.00	0.66	-0.30	0.99	0.99	0.99	0.54	0.05	0.96	1.00																
Y	0.28	0.86	0.05	-0.14	-0.09	0.94	0.84	0.86	0.45	0.54	0.88	0.62	-0.50	0.88	0.88	0.87	0.45	-0.01	0.87	0.89	1.00															
La	0.20	0.98	-0.07	-0.17	-0.22	0.98	0.97	0.98	0.65	0.62	0.96	0.79	-0.50	0.98	0.97	0.98	0.66	0.03	0.98	0.97	0.92	1.00														
Ce	0.18	0.99	-0.08	-0.17	-0.22	0.98	0.98	0.99	0.65	0.60	0.96	0.78	-0.47	0.99	0.97	0.98	0.66	0.04	0.98	0.98	0.91	1.00	1.00													
Pr	0.18	0.99	-0.09	-0.17	-0.22	0.98	0.98	0.99	0.66	0.61	0.96	0.78	-0.48	0.99	0.97	0.98	0.67	0.04	0.97	0.97	0.91	1.00	1.00	1.00												
Nd	0.19	0.98	-0.07	-0.17	-0.21	0.99	0.97	0.99	0.63	0.60	0.97	0.76	-0.47	0.99	0.97	0.98	0.64	0.03	0.97	0.98	0.92	1.00	1.00	1.00	1.00											
Sm	0.21	0.97	-0.06	-0.18	-0.19	0.99	0.96	0.97	0.60	0.59	0.96	0.74	-0.48	0.98	0.97	0.97	0.61	0.02	0.96	0.97	0.95	0.99	0.99	0.99	1.00	1.00										
Eu	0.24	0.92	0.05	-0.15	-0.11	0.97	0.92	0.93	0.57	0.61	0.91	0.74	-0.55	0.93	0.92	0.92	0.58	-0.02	0.94	0.93	0.97	0.97	0.97	0.97	0.97	0.98	1.00									
Gd	0.23	0.94	-0.02	-0.16	-0.16	0.99	0.94	0.94	0.60	0.63	0.93	0.74	-0.54	0.95	0.94	0.94	0.61	0.01	0.95	0.94	0.97	0.98	0.98	0.98	0.98	0.99	0.99	1.00								
Tb	0.24	0.93	-0.01	-0.16	-0.14	0.98	0.92	0.93	0.56	0.61	0.92	0.71	-0.53	0.94	0.93	0.93	0.56	-0.01	0.93	0.94	0.98	0.97	0.97	0.97	0.97	0.99	0.99	1.00	1.00							
Dy	0.29	0.90	0.02	-0.15	-0.13	0.96	0.89	0.91	0.49	0.57	0.92	0.67	-0.52	0.93	0.92	0.91	0.50	-0.02	0.92	0.93	0.99	0.96	0.95	0.95	0.96	0.98	0.99	0.99	1.00	1.00						
Ho	0.28	0.90	0.02	-0.15	-0.13	0.96	0.89	0.90	0.49	0.56	0.91	0.68	-0.52	0.92	0.92	0.91	0.50	0.00	0.92	0.92	0.99	0.95	0.95	0.95	0.96	0.97	0.99	0.99	0.99	1.00	1.00					
Er	0.26	0.91	0.00	-0.17	-0.15	0.97	0.91	0.92	0.55	0.61	0.91	0.71	-0.53	0.93	0.92	0.92	0.56	0.02	0.93	0.93	0.99	0.96	0.96	0.96	0.97	0.98	0.99	0.99	1.00	1.00	1.00	1.00				
Tm	0.27	0.92	0.01	-0.16	-0.16	0.97	0.91	0.92	0.55	0.61	0.92	0.72	-0.55	0.93	0.93	0.92	0.55	0.02	0.94	0.93	0.98	0.97	0.96	0.96	0.97	0.98	0.99	0.99	1.00	1.00	1.00	1.00	1.00			
Yb	0.30	0.92	0.02	-0.15	-0.17	0.96	0.91	0.93	0.52	0.58	0.93	0.73	-0.55	0.94	0.94	0.93	0.53	0.01	0.95	0.94	0.98	0.97	0.97	0.97	0.97	0.98	0.99	0.99	0.99	0.99	0.99	0.99	1.00	1.00		
Lu	0.33	0.91	0.03	-0.15	-0.16	0.95	0.89	0.91	0.49	0.57	0.92	0.72	-0.56	0.93	0.93	0.92	0.50	-0.01	0.95	0.93	0.98	0.96	0.96	0.96	0.96	0.98	0.99	0.99	0.99	0.99	0.99	0.99	0.99	1.00	1.00	
Sc	0.21	0.97	-0.09	-0.21	-0.17	0.97	0.94	0.97	0.53	0.50	0.98	0.65	-0.40	0.99	0.97	0.97	0.53	0.00	0.94	0.98	0.92	0.98	0.98	0.98	0.99	0.99	0.95	0.97	0.97	0.96	0.95	0.95	0.96	0.96	0.96	1.00

Footnote: Elements are ordered and grouped by geochemical behavior: major elements (Si, Al, Fe, Mg, Ca, Na, K, P, Ti), volatile elements (C, S and LOI as a proxy), trace metals (As, Sb, Hg, Tl, W, Ag, Zn, Cd, Cu, Pb, Ni, Co, Bi, Ga, In, Mo,

Sn, Re, Te, and Se), minor elements (Ge, Nb, Ta, Th, Y, Mn, Ba, Sr, Rb, Cs, Li, B, Be, V, Cr, Zr, Hf, Sc, and U) and rare earth elements (La, Ce, Pr, Nd, Sm, Eu, Gd, Tb, Dy, Ho, Er, Tm, Yb, Lu). The r values are coloured to show their P-values. Red cells indicate $P<0.0005$, yellow cells indicate $P<0.005$, green cells indicate $P<0.0025$ and blue cells indicate $P<0.05$. R values given in white cells are not statistically significant correlations.

Table 10.4: Inferred mineralogical components responsible for observed multielement correlations in the BIF.

Component	Hosted Elements
Chert	Si, Fe, B, ± P, ± LREE
Magnetite	Fe, ± Si, ±Ge, ± Mg, ± Be, ± P
Chlorite	Al, Si, Mg, Fe, ± Ti, ± V, ± Mn, ± Ga
Carbonate	Ca, Mg, Mn, ± W, ±Re, ± Hg, C, LOI
Phyllosilicate	K, Ba, Sr, Rb, Cs, Li, ±V, ±Cr, ±Ti (in leucoxene)
Phosphate	Ca, LREE, ±Ni (apatite), ±Cr (monazite), ±Y, ± Na (xenotime)
Detrital	Ti, Hf, Zr, Sc, Y, ± REE, ± Cr, ± U, ± Th, ± Nb, ± Ta
Hydrothermal REE	LREE (no Eu anomaly) with chlorite LREE (+Eu anomaly) with magnetite
Diagenetic Sulfide/Black Shale	Co, Ni, Mo, Se, As, Sb, Tl, Ag, Sn, In, S
Low-temperature hydrothermal polymetallic sulfide	Zn, Cd, Pb, Cu, Te, Bi, ± Hg

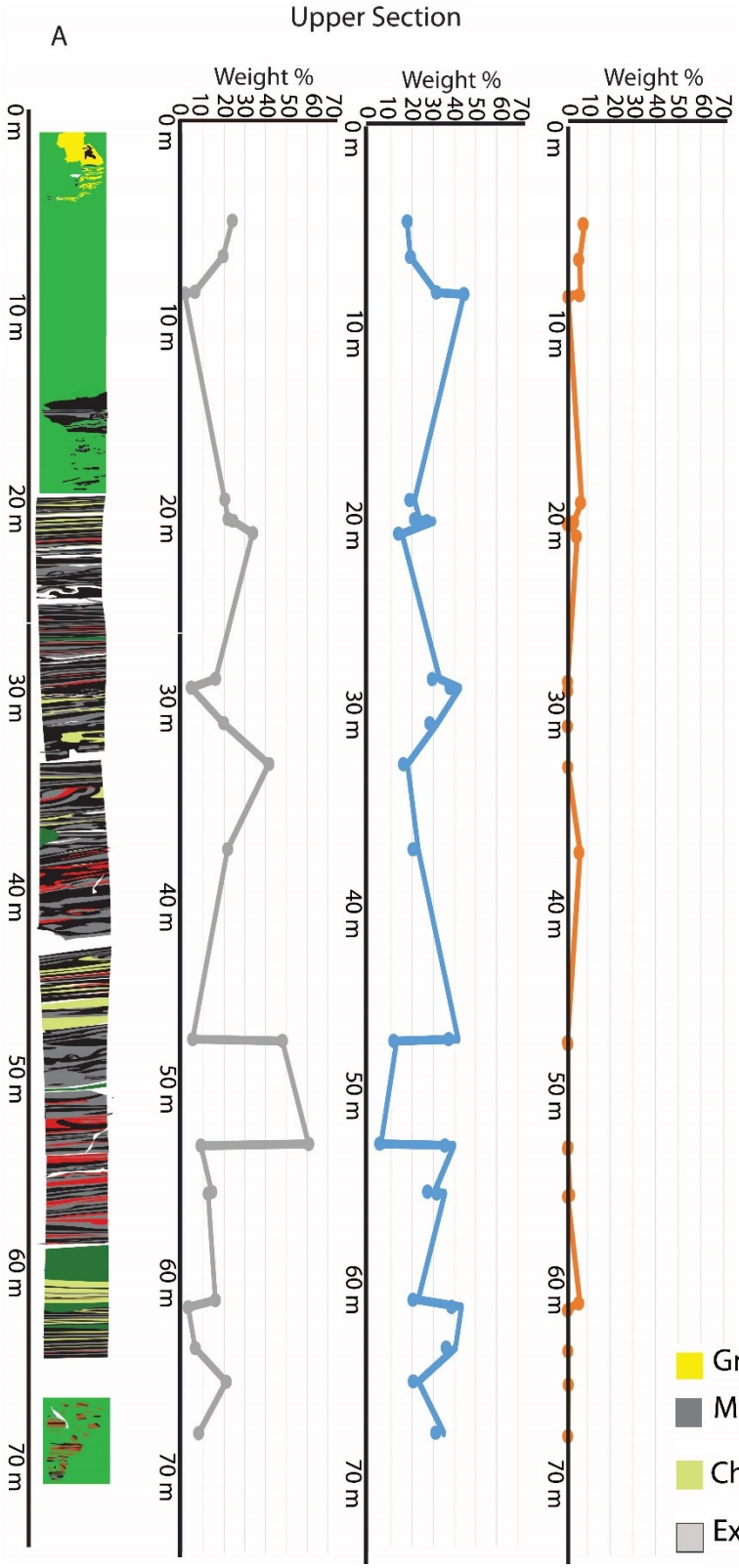

Figure 10.1 A) Geochemical profile of the upper Highway 11 outcrop. Weight % Si, Al and Fe are shown to give a general impression of the bulk composition of the BIF. The observed variations generally reflect the dominant facies, despite the very fine layering within and between samples (see Figure 10.2 for comparison). Al is always less than 10 wt. %, and samples with over 1 wt. % Al are from chlorite beds. Si concentrations are highest approaching the top and bottom of the section. Si and Fe concentrations display an anti-correlation, consistent with dilution effects in Si-rich samples.

Figure 10.1 B) Geochemical profile of the lower Highway 11 outcrop.

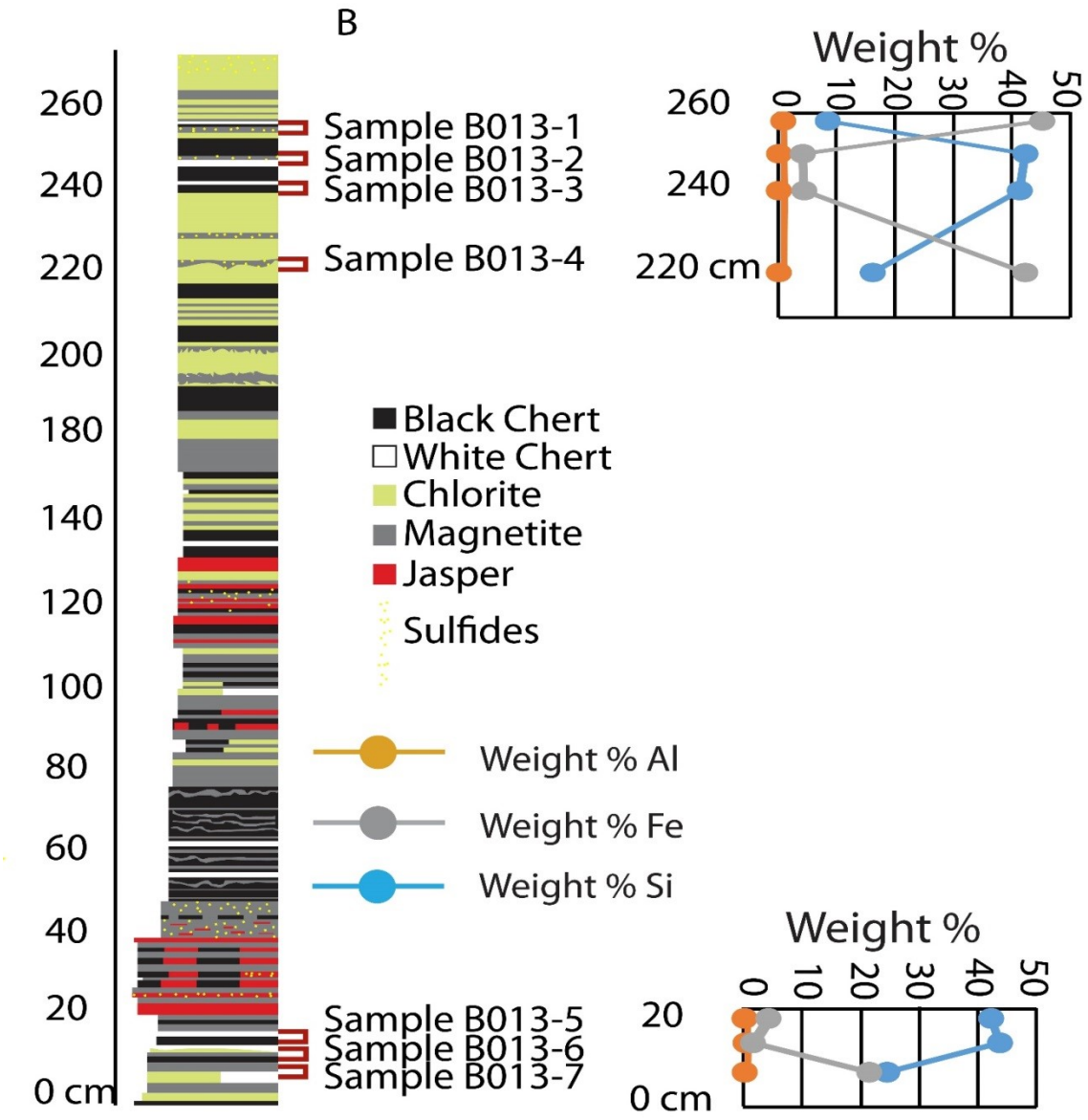

Figure 10.2 Detailed geochemical profiles of two sections of block B013 from the southern pit of the Sherman Mine. The plotted data show that layer-by-layer variations in major elements Fe, Si, Al, over distances of a just few centimeters, are as large as those across the entire Highway 11 outcrop (Figure 10.1). Samples B013-1, B013-4 and B013-7 are from magnetite beds; B013-2, B013-3, B013-5 and B013-6 are chert samples.

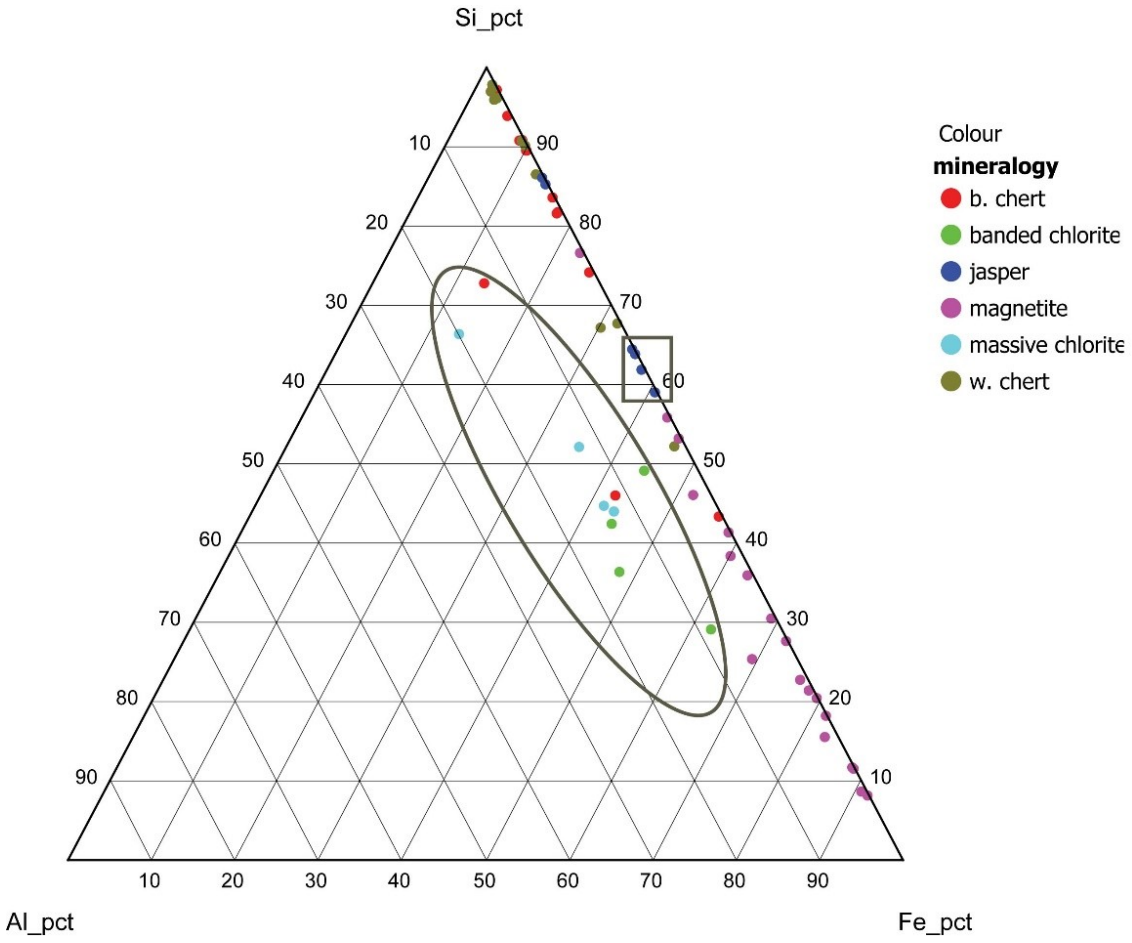

Figure 10.3 A) Bulk geochemical compositions of all Temagami BIF samples plotted on Fe-Al-Si ternary diagram. The samples plot along a continuum from Si-rich (chert facies) to Fe-rich (magnetite facies). Chlorite samples and two black chert samples are Al-rich and highlighted by the gray oval; jasper samples have intermediate Si contents and are highlighted by the gray box.

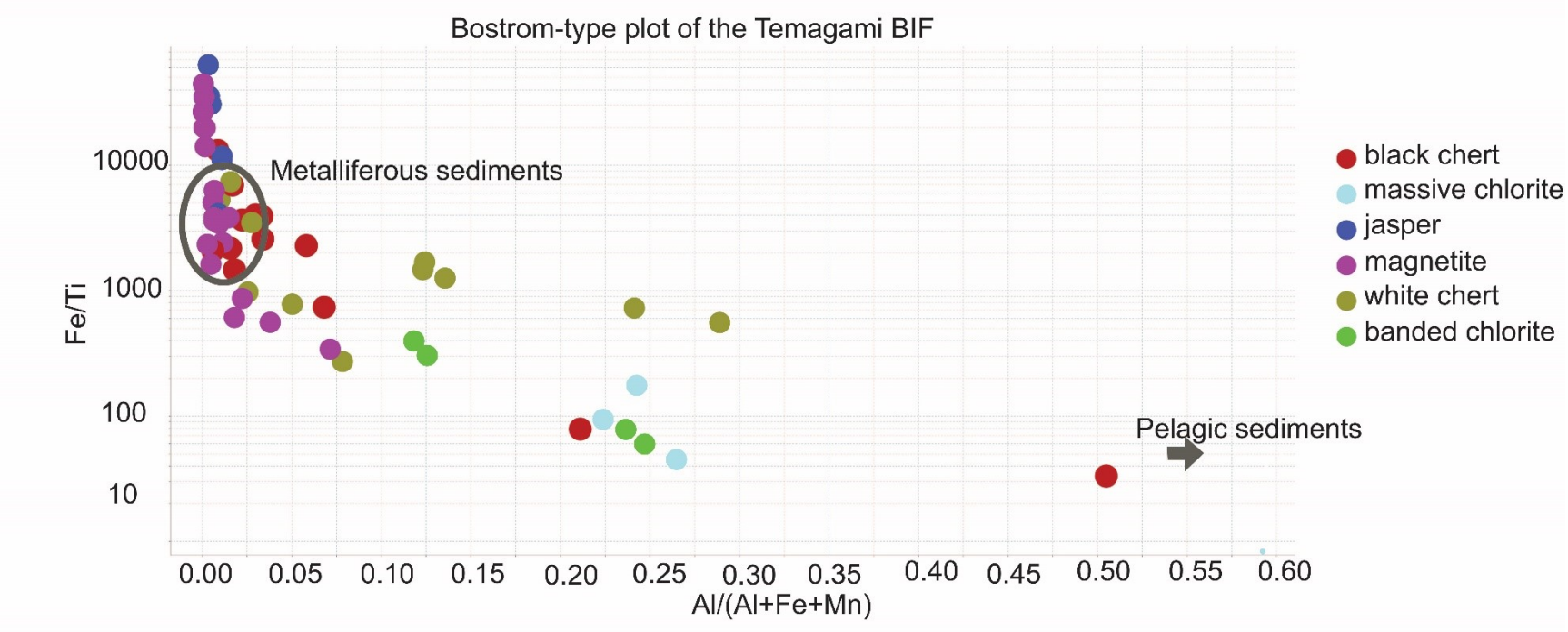

Figure 10.3 B) Bulk geochemical compositions of all Temagami BIF samples plotted on a Bostrom-type Fe-Al plot. The majority of black chert and magnetite samples plot within the metalliferous sediment field which represents the chemistry of metalliferous sediments from the Red Sea and East Pacific Rise (Cronan, 1976; Backer, 1976). All samples are less Al-enriched than Pacific Ocean pelagic sediments (Cronan, 1976). Plot is after Bostrom, 1973.

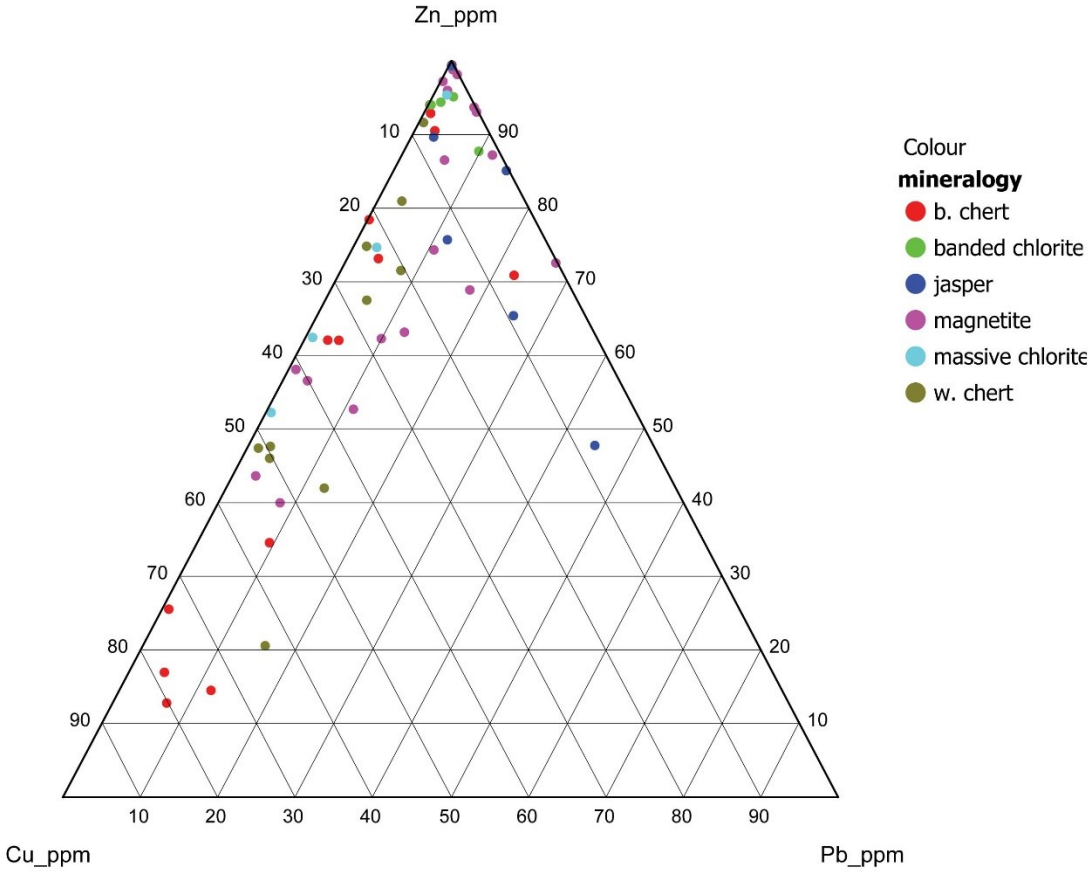

Figure 10.4 Cu-Pb-Zn ternary diagram of bulk samples from Temagami BIF. Cu and Zn appear to be decoupled in the different facies (e.g., a higher proportion of Zn in the chlorite facies). This could reflect variable hydrothermal input into the basin or preferential siting of Zn in chlorite.

A

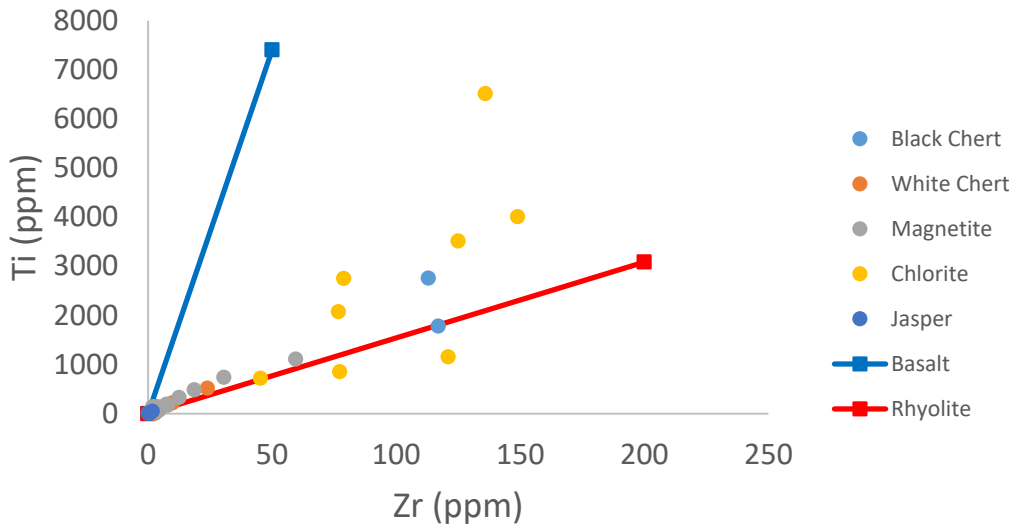
8000
7000
6000
5000
4000
3000
2000
1000
0
Ti (ppm)
0
50
100
150
200
250
Zr (ppm)
Black Chert
White Chert
Magnetite
Chlorite
Jasper
Basalt
Rhyolite

B

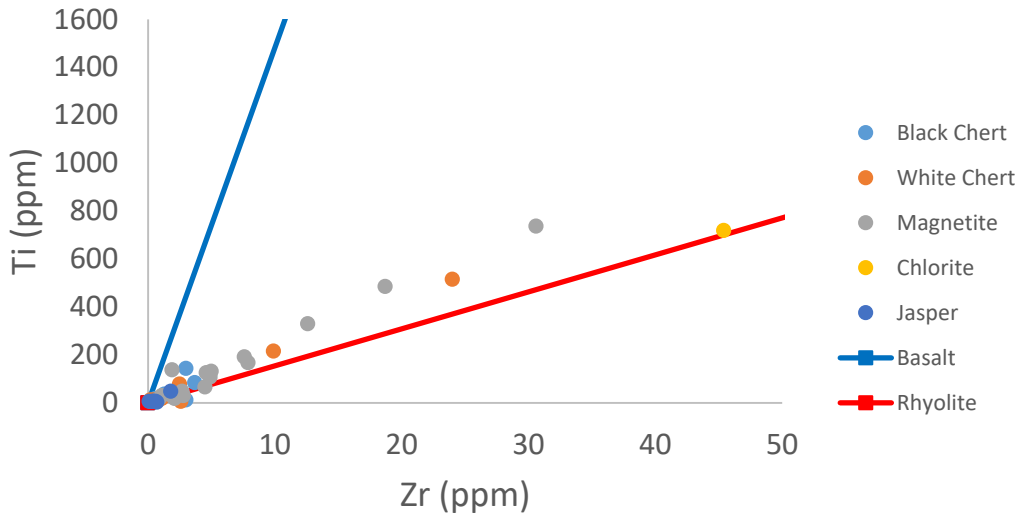
1600
1400
1200
1000
800
600
400
200
0
Ti (ppm)
0
10
20
30
40
50
Zr (ppm)
Black Chert
White Chert
Magnetite
Chlorite
Jasper
Basalt
Rhyolite

C

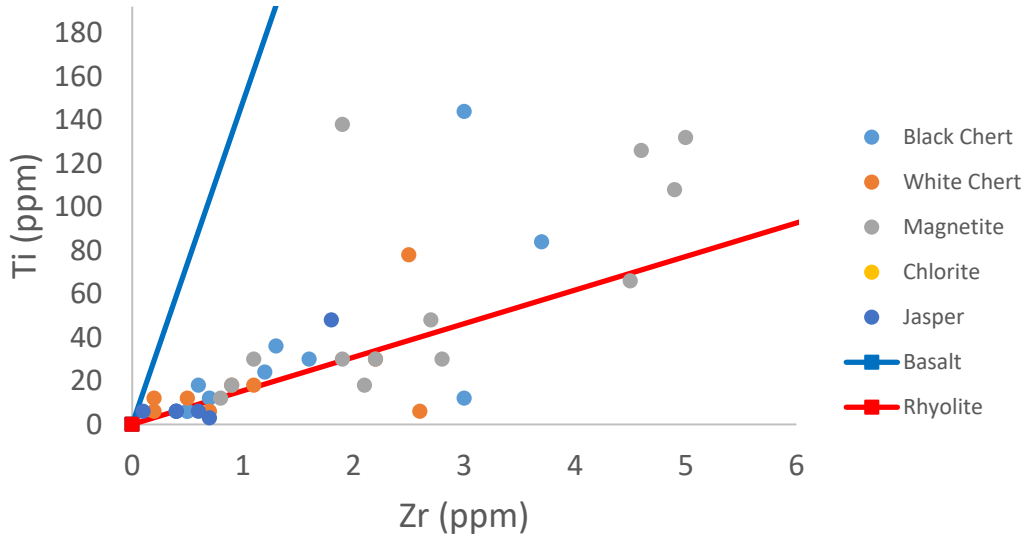
180
160
140
120
100
80
60
40
20
0
Ti (ppm)
0
1
2
3
4
5
6
Zr (ppm)
Black Chert
White Chert
Magnetite
Chlorite
Jasper
Basalt
Rhyolite

Figure 10.5 Plot of Zr versus Ti in bulk samples from the Temagami BIF. Reference lines passing through the origin for basalt and rhyolite are from Taylor and McLennan (1985) are shown for comparison. The plotted data show that a high proportion of the BIF samples, including the volcaniclastic layers, plot close to the felsic end member in terms of these “immobile” elements, suggesting that any detrital material entering the basin and incorporated in the BIF was derived from local felsic volcanic sources with a smaller contribution from mafic volcanics. A) Plot showing all samples. Some chlorite samples and one black chert sample containing more than 50 ppm Zr have a significant basalt component. Magnetite, white chert and jasper samples are clustered distributed close to the origin. B) Close-up of samples in A containing less than 50 ppm Zr, showing the same general trend as the more Zr-rich samples. C) Close-up of samples containing 5 ppm or less Zr. At this scale, the scatter in the data is likely due to analytical precision at low Zr and Ti concentrations.

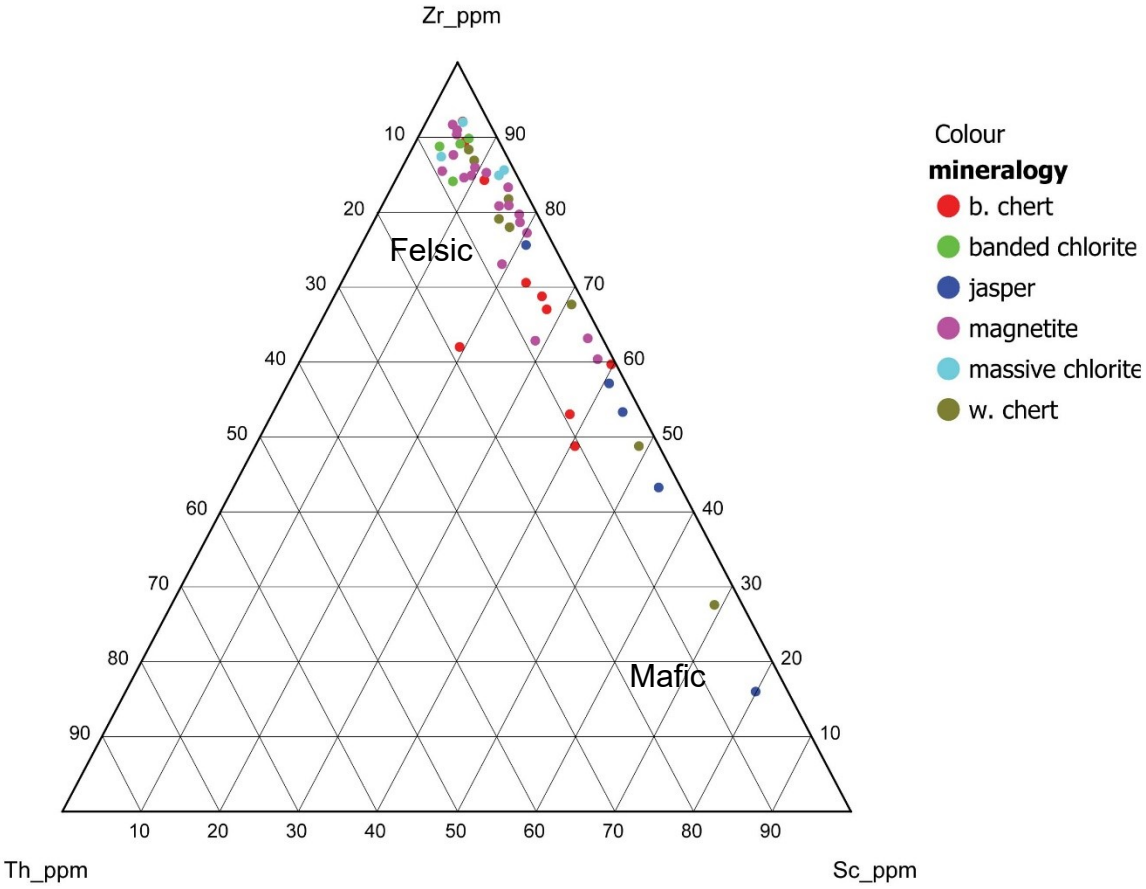

Figure 10.6 Zr-Th-Sc ternary diagram of bulk samples from the Temagami BIF (modified from Feng and Kerrich, 1990). The distribution of the samples is consistent with mixtures of mafic and felsic components in the detrital fraction of the BIF. Samples show a higher proportion of Zr/Sc, suggesting clastic input was derived from a felsic source.

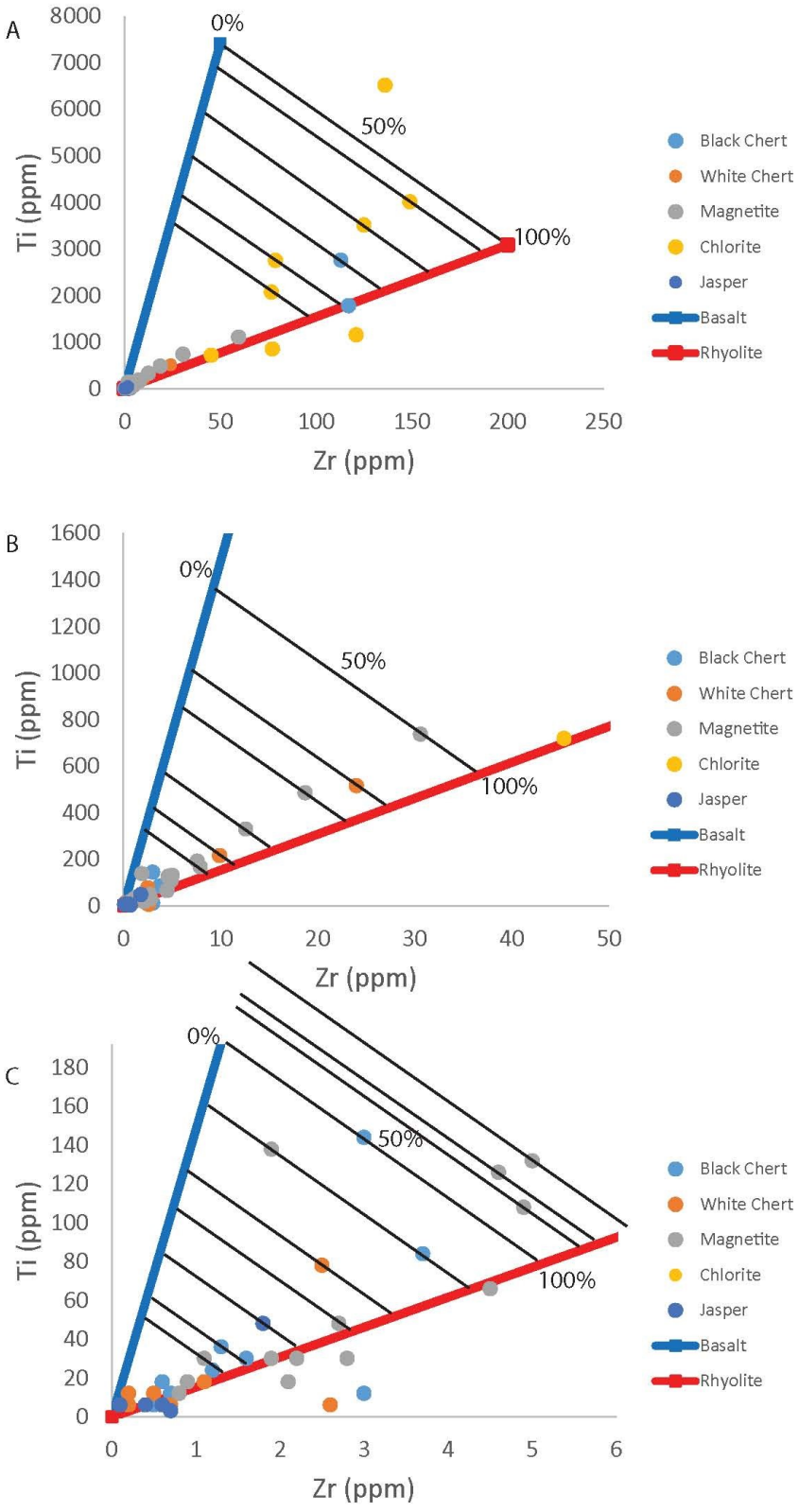
A
8000
7000
6000
5000
4000
3000
2000
1000
0
Ti (ppm)
0%
50%
100%
0
50
100
150
200
250
Zr (ppm)
Black Chert
White Chert
Magnetite
Chlorite
Jasper
Basalt
Rhyolite
B
1600
1400
1200
1000
800
600
400
200
0
Ti (ppm)
0%
50%
100%
0
10
20
30
40
50
Zr (ppm)
Black Chert
White Chert
Magnetite
Chlorite
Jasper
Basalt
Rhyolite
C
180
160
140
120
100
80
60
40
20
0
Ti (ppm)
0%
50%
100%
0
1
2
3
4
5
6
Zr (ppm)
Black Chert
White Chert
Magnetite
Chlorite
Jasper
Basalt
Rhyolite

Figure 10.7 Schematic illustration showing the calculation of the mafic/felsic component of clastic input in the Temagami BIF. (A-C plotted at different scales to show sample distribution.) Using the lever rule and the compositions of end-member basalt and rhyolite, the volcaniclastic component in the chlorite facies contains between 10% and 40% percent mafic material. The clastic component in the black chert, white chert and jasper facies contains between 0% and 10% mafic material. One black chert sample contains just over 50% of mafic material in its clastic components. The magnetite facies contains between 15% and 20%.

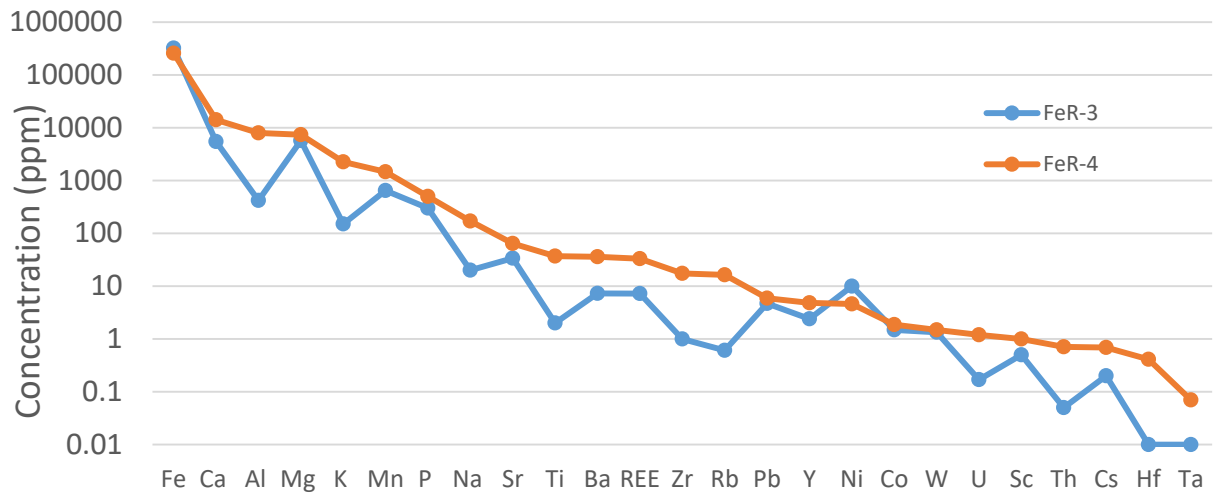

Figure 10.8 Trace element multiple element variation diagram of BIF standards FeR-3 and FeR-4 from the Sherman Mine. The elements are ordered according to decreasing abundance in FeR-4, which has a significant silicate component. The plot shows a clear chemical difference that can be explained by their mineralogy. FeR-3 is from banded chert and magnetite ore that has lower concentrations of all elements except Fe and Ni, which are likely hosted in magnetite. FeR-4 is otherwise similar to FeR-3 but contains chlorite and other volcaniclastic material which accounts for the higher Ca, Al, K, Ti, U and Th.

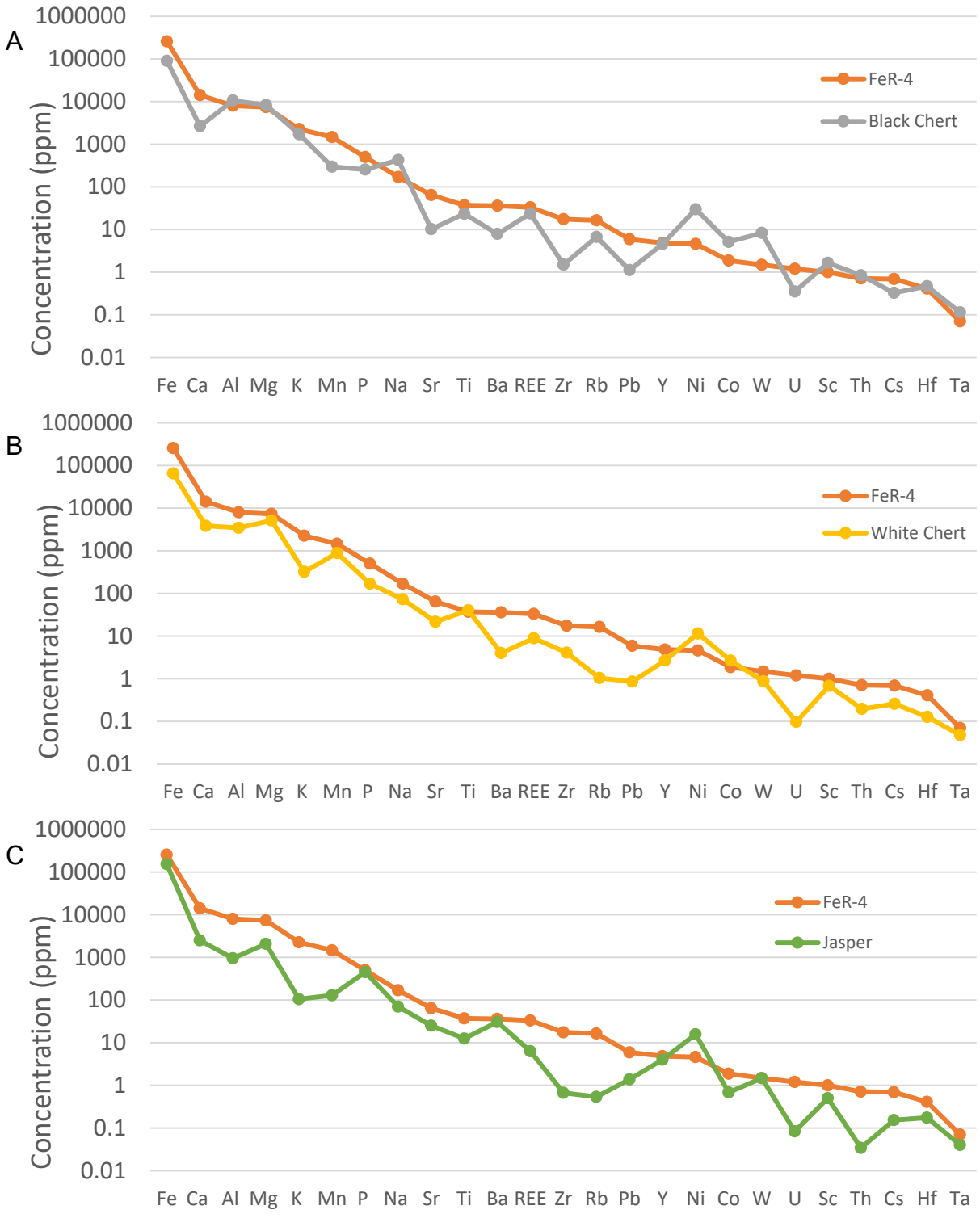
A
Concentration (ppm)
1000000
100000
10000
1000
100
10
1
0.1
0.01
Fe Ca Al Mg K Mn P Na Sr Ti Ba REE Zr Rb Pb Y Ni Co W U Sc Th Cs Hf Ta
FeR-4
Black Chert
B
Concentration (ppm)
1000000
100000
10000
1000
100
10
1
0.1
0.01
Fe Ca Al Mg K Mn P Na Sr Ti Ba REE Zr Rb Pb Y Ni Co W U Sc Th Cs Hf Ta
FeR-4
White Chert
C
Concentration (ppm)
1000000
100000
10000
1000
100
10
1
0.1
0.01
Fe Ca Al Mg K Mn P Na Sr Ti Ba REE Zr Rb Pb Y Ni Co W U Sc Th Cs Hf Ta
FeR-4
Jasper

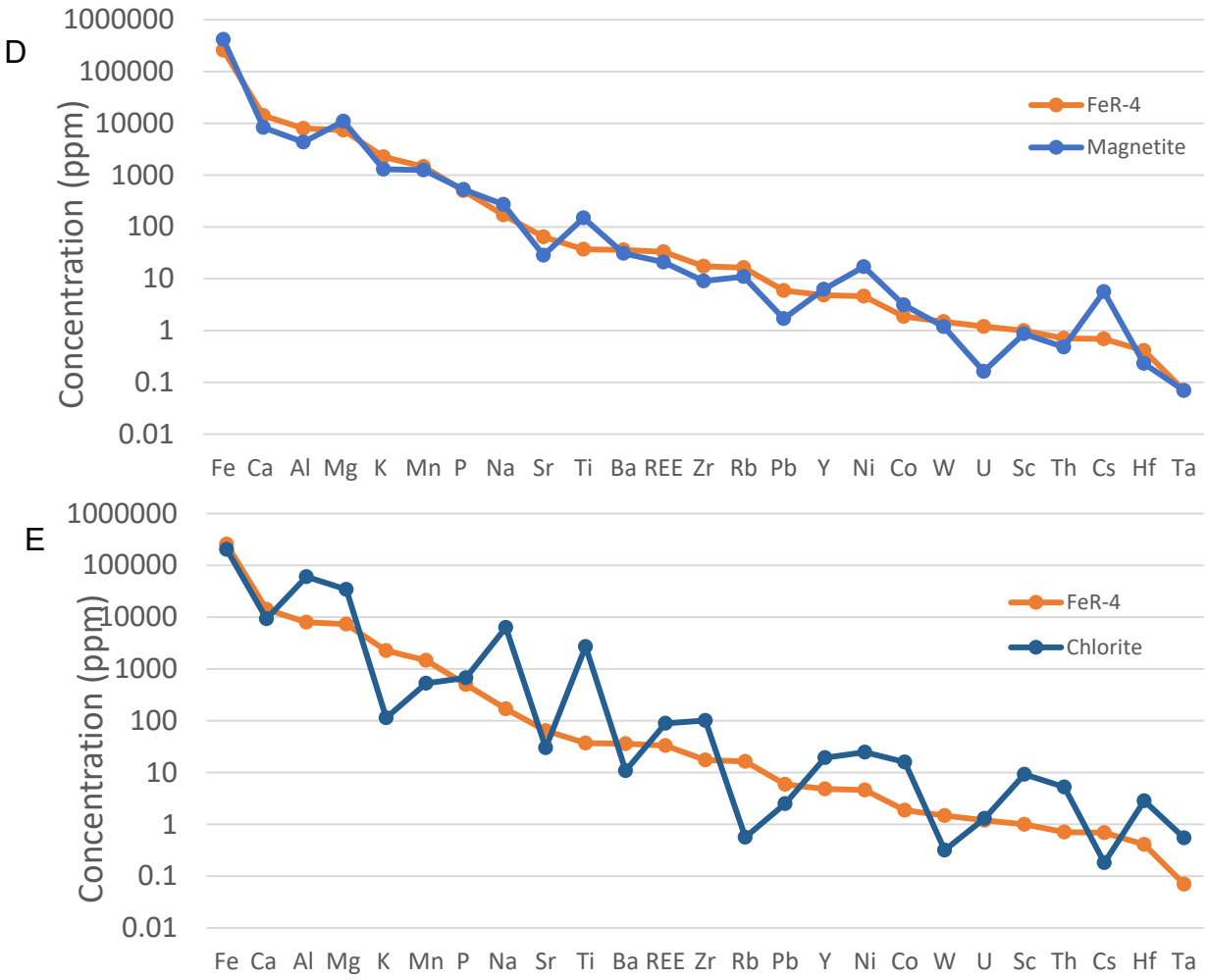

Figure 10.9 Trace element multiple element variation diagram of different BIF facies from the Temagami mine area. The elements are ordered according to decreasing abundance in FeR-4 for comparison. The black chert (plot A) and magnetite facies (D) show the greatest similarity to FeR-4, but with notable enrichments in Ni, Co and Ti (in the magnetite facies). These samples more closely resemble FeR-3. The white chert (B) and jasper (C) are depleted in most elements, except Ni. The chlorite facies is least similar to FeR-4, with significant enrichments in Al, Mg, Ti, Na, Th, and Sc, most ikely reflecting the large volcaniclastic component in this facies.

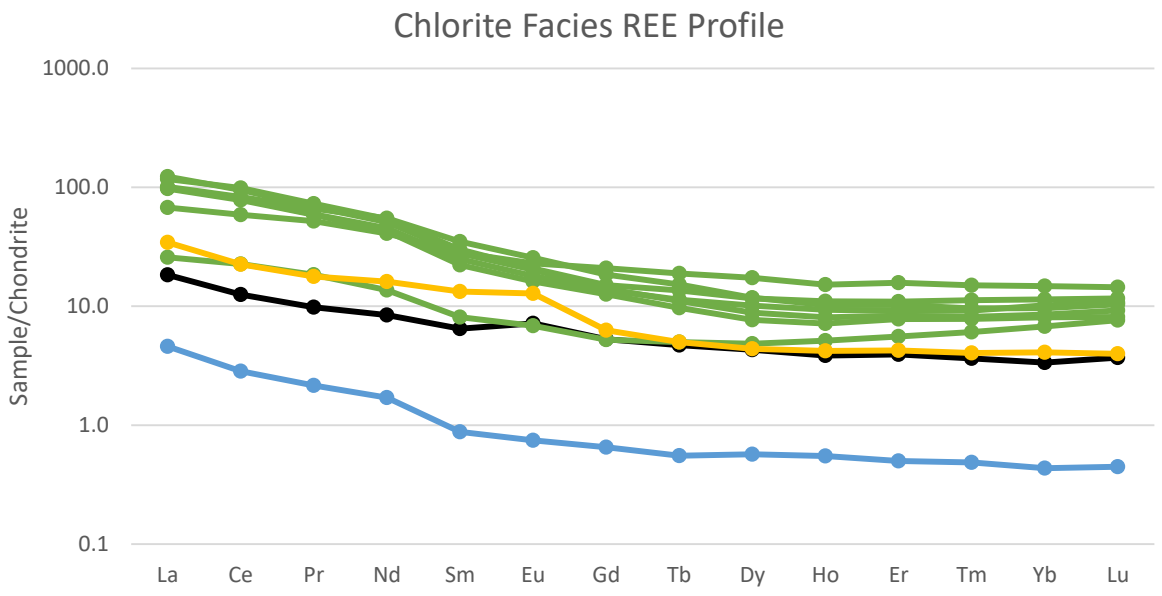

Figure 10.10 Chondrite-normalized REE profile of the chlorite facies BIF. The typical profile has a LREE enrichment with no Eu anomaly. The BIF standard FeR-4 (yellow line), which has a significant silicate component, has a similar profile with a slight positive Eu anomaly. A black chert sample with a similar profile and a slight positive Eu anomaly is indicated by the black line. A white chert sample with a similar profile but lower total REE is indicated in blue.

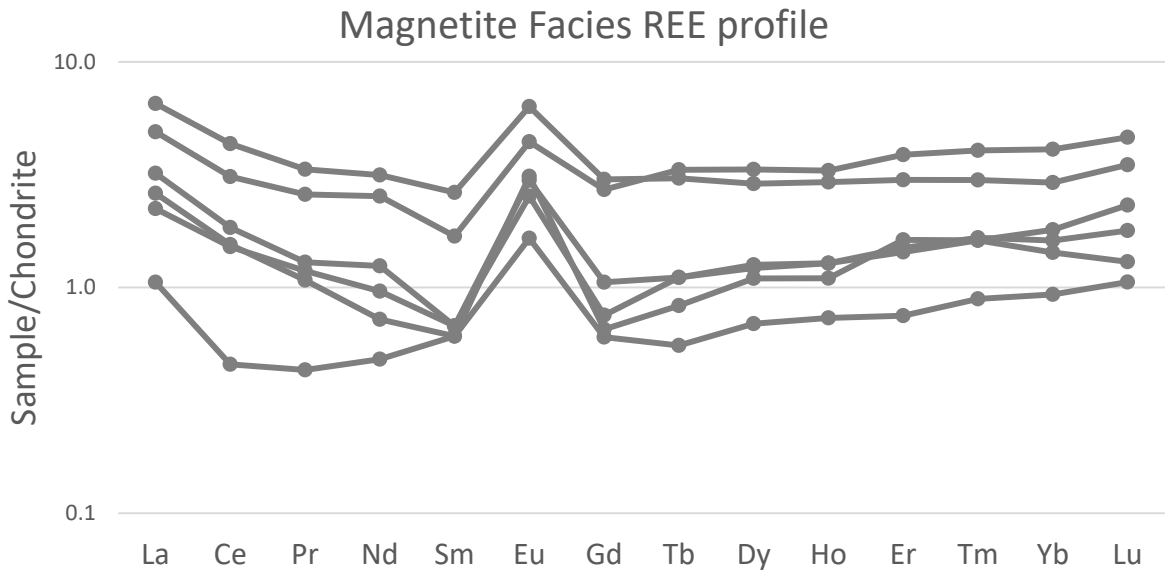

Figure 10.11 Chondrite-normalized REE profile of the magnetite facies BIF. The typical profile has low total REE concentrations and a large positive Eu anomaly suggesting input of hydrothermal fluids.

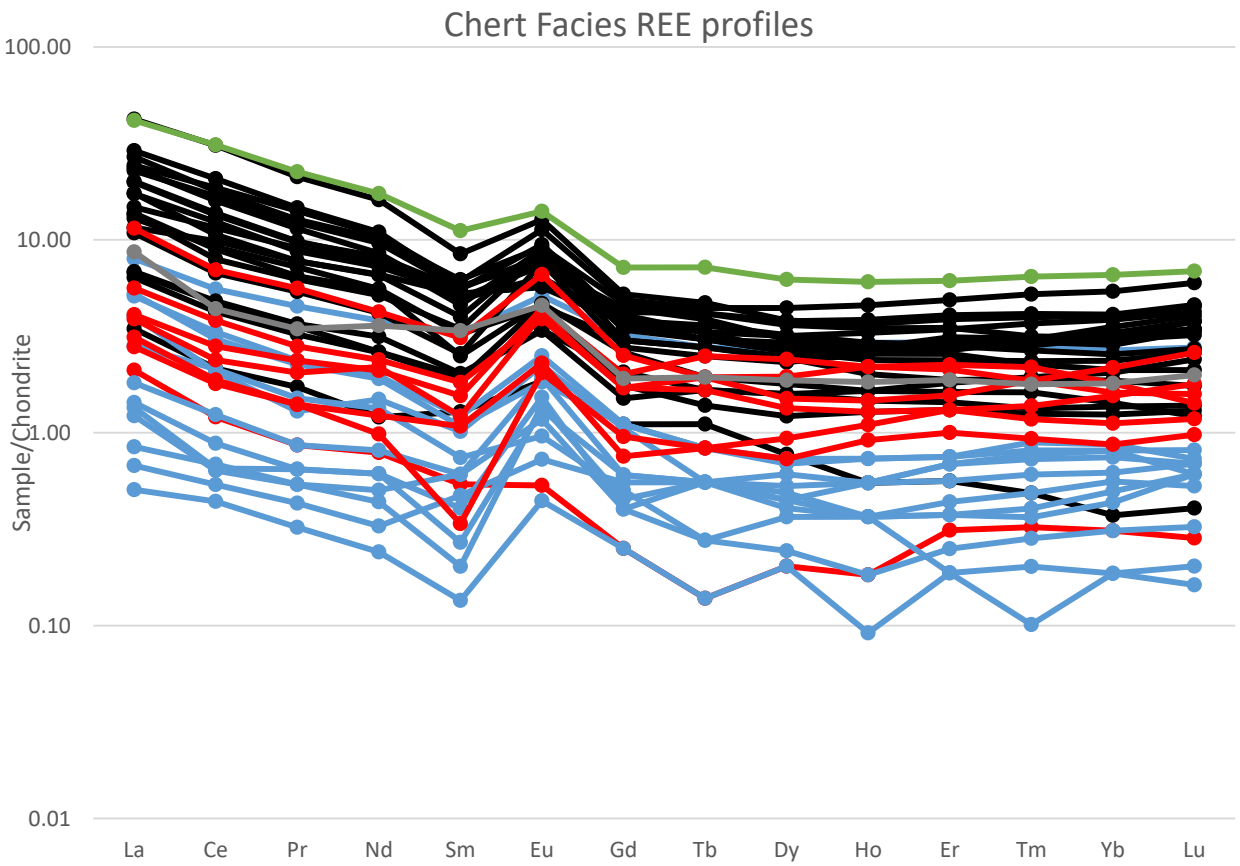

Figure 10.12 Chondrite-normalized REE profile of black chert, white chert and jasper facies BIF. The typical black chert profile (black lines) has high total REE concentrations and a positive Eu anomaly. The typical jasper profile (red) has lower total REE concentrations and a positive Eu anomaly. The white chert profile (blue) has lower total REE concentrations than both black chert and jasper but still shows a positive Eu anomaly. The chert-dominated BIF standard FeR-3 is plotted in gray and resembles the black chert profile. A chlorite sample with a profile similar to that of black chert samples is plotted in green. The prevalence of the positive Eu anomaly in all samples of the chert facies suggests that this signal is at least partly contained in the chert and not just in magnetite.

11. Discussion

The paragenetic relationships of mineralogically distinct layers in the Temagami BIF are summarized in Figure 7.7. Petrographic observations show a much more complex paragenesis than originally suggested by field observations, including 2 paragenetically distinct types of hematite and 3 types of magnetite, distinguished by different habits and grain size, cross-cutting relationships and growth features. Other minor and trace mineral phases are also more common than expected, and a variety of quartz vein stages are recognized at the microscopic scale. Petrographic observations show that some facies of BIF were less affected by regional metamorphism than others, some preserving apparently primary depositional features within the chert layers. A number of post-depositional but premetamorphic effects seen at the outcrop-scale, in the individual bands, and at the micro-scale are interpreted to be mainly diagenetic (Table 11.1). These features are considered in the following sections, and their relationship to the possible original depositional conditions and environment are discussed.

Table 11.1: Post-depositional features that inform the structural, sedimentological and paragenetic history of the Temagami BIF.

Process	Feature	Example
Dewatering	Syneresis cracks	Figure 6.3b
Diagenetic recrystallization	Type 2 magnetite in jasper	Figure 7.1b
	Microbanded chert	Figure 8.2e
Deformation	Quartz veins	Figure 6.2d
	Overturned beds	Figure 6.1
	Penetrative faulting	Figure 4.1
Metamorphic recrystallization	Type 3 magnetite	Figure 7.4b, Figure 7.7b
Hydrothermal input	REE profiles	Figure 10.10, Figure 10.11, Figure 10.12

11.1 Primary Features

Among the primary sedimentary structures that have been noted at the outcrop scale and in hand specimen are the rythmic layering of 0.5 to 1-cm laminae, scouring and undulating layer boundaries, thickening and thinning of beds beneath flat bedding planes, local slumping and loading features. Cracks that do not cross the banding but terminate within or at the edges of the chert and magnetite bands are interpreted to have formed by dewatering (syneresis cracks), and have since become filled with quartz or magnetite. Cracks that formed during later deformation cross multiple bands and entire beds. Synsedimentary faults have been recognized by decreasing offset between layers and confinement of faults to individual units. These features are seen in the Highway 11 outcrop and also in the individual ore blocks. In the Highway 11 outcrop, poorly exposed boundaries between metavolcanic rocks and BIF appear to be brecciated but broadly conformable, suggesting that they are primary depositional surfaces.

The finest grains of Type 1 hematite, visible only at 50X to 100X magnification, bear the closest resemblance to fine <1 μm Fe-oxide crystals that have been interpreted to be primary precipitates in other BIF (e.g., Bekker et al., 2010). These crystals occur in clusters that are embedded in spheroidal quartz, very similar to some forms of silica aggregates found in subaerial hot springs (so-called “opal pellets”: Jones and Segnit, 1971; Ayres, 1972; Gaillou et al., 2008; Stefurak et al., 2014). The original amorphous silica was likely transformed during diagenesis, first to cristobalite or tridymite and

eventually to euhedral crystalline quartz (Segnit, 1971; Jones and Renaut, 2007). The close spatial and paragenetic relationship of the fine grained Fe-oxides and silica suggests that at least some of the textures preserved in the Fe-rich chert layers were products of deposition of original Si-Fe-oxyhydroxide particles that released Fe to form the small crystals of Type 1 hematite (see below). However, silica colloids documented in younger jasper occurrences (Grenne and Slack, 2003) also have been interpreted as being partly diagenetic, resulting from coprecipitation of Si around iron oxyhydroxides in response to their positive surface charge (Williams and Crerar, 1985).

Some clay minerals were also likely to have been incorporated in the different BIF layers as primary precipitates. Chlorite-rich bands, especially lacking any lithic clasts, may be a product of the direct chemical precipitation of an FeSi-Al precursor, such as nontronite, a common Fe-rich and Al-poor smectite in modern low-temperature seafloor hydrothermal systems (Jakobsson, 1986; Hannington and Jonasson, 1992). Smectite might also have been derived from the weathering of basalt that is spatially associated with the BIF, but the discrete chloritic layers argue against a process involving only weathering. Some layers may represent clastic material (e.g., ash) that was altered to chlorite, in particular where the presence of ilmenite, altered feldspar, and lithic clasts indicate a clastic origin. Thus, both types of chlorite layers appear to be present in the Temagami BIF: primary chemical precipitates and altered ash.

Other compelling evidence of primary deposition is the preservation of apparent biogenic relics in the chert layers of the BIF. The 1-10 μm branching filaments and rods

(many with ~1 μm circular cross sections) are very similar to other well-documented fossils of bacterial filaments. In black chert, they are clearly visible at high magnification in layers with a high proportion of pure quartz (Figure 8.3a). Similar filamentous microstructures of the same size have been documented in chemical sediments of the Archean Barberton Greenstone Belt in South Africa (Walsh and Lowe, 1985; Walsh, 1992), although some rod-like structures in other Archean iron formations (Awramik et. al, 1966) have been shown to be modern contamination (Walsh and Lowe, 1985). The microbanded chert, with mm-scale black and white alternating laminae, is also similar to chert bands that are interlayered with some Archean stromatolites (e.g., in the Mapepe Formation of the Swaziland Supergroup: Lowe et al. 1999). However, other forms of microbanding are also suggested (see below).

A number of apparently primary geochemical features are also recognized. A majority of the Temagami BIF samples are characterized by low concentrations of REE, but have LREE enrichment and a positive Eu anomaly. High concentrations of LREE but no Eu anomaly (e.g., in some chlorite-rich samples) may reflect mainly low-temperature hydrothermal venting. These are both features normally associated with primary seafloor hydrothermal deposition (Bowins, 1989; Laurila, 2015). The distinctly clastic signature of some bands is indicated by elevated concentrations of Ti, Nb, Sr, Y or LREE (cf. Feng and Kerrich, 1990; Hannington et al, 2012). However, a lack of trace element enrichment in many bands is unexpected, considering the important role of scavenging by ferric oxyhydroxides in the water column of modern Fe-rich basins (Berrang and Grill, 1974). Trace elements like U and REE, which are normally enriched

in ferric oxyhydroxides by adsorption from seawater in modern hydrothermal plumes, are uniformly low. In contrast, certain trace element enrichments, such as B (up to 60 ppm in chert facies), may be reflective of primary deposition. Similarly high concentrations of Ge, ±V, ±Cr in the magnetite may be recording a direct hydrothermal input from the metal-enriched basin. The chlorite facies, in particular, has high base metal concentrations (Zn to 97 ppm, Cu to 29 ppm, Pb to 2.6 ppm, Cd to 0.2 ppm, Ag to 0.3 ppm) compared to the other BIF facies. The shale samples in the immediate footwall of the BIF contain very high As (Diekrup et al., in preparation), which is also enriched in the sulfide and altered felsic volcaniclastic rocks in the footwall of the mine.

11.2 Secondary (Diagenetic) Features

One of the most challenging issues in BIF genesis is the origin of the fine rhythmic layers of alternating silica, Fe-oxide, and Fe-silicate. Some of the layers may reflect chemical changes in the local bottom waters from which the minerals were precipitated, as described in modern metalliferous sediments (Bostrom and Peterson, 1969; Dymond, 1972). Centimeter-scale layering could conceivably be produced by short-term changes in the bottom water chemistry, but it is difficult to imagine basin-scale processes that would contribute to finer-scale banding. Other layers may reflect a process of diagenetic segregation after deposition of a compositionally uniform chemical precipitate dominated by amorphous Si-Fe-oxhydroxides, as observed in modern chemical sediments (Murray et. al, 1992; Milliken, 2004; Bekker et. al, 2007; see further below). Diffusion and scavenging of Fe within the sediment column may result in sharp

boundaries between laminae that result in microbanding, as seen in modern sediments (Laurila et. al, 2015).

Considerable debate also has surrounded the observed replacement of hematitic layers by magnetite, which produces the highest-grade ores. We have observed replacement of hematite by magnetite through several different paragenetic stages. In jasper bands, the formation of Type 1 magnetite appears to have scavenged Fe from Fe-rich silica spherules as it grew into coarser-grained Type 2 magnetite, leaving “clean” chert behind (Figure 8.2d). Some spherulitic jasper clearly shows Fe-depletion at the edges of the spherules, where Type 1 hematite is no longer present and Type 2 magnetite has grown in the interstices between the spherules (Figure 7.1b). Type 2 magnetite that is found in the spaces between the spherules and at their boundaries (Figure 7.1b) often completely occupies the space which would have been vacant or filled with water early in the diagenesis. Jasper relicts (i.e., clusters of Type 1 hematite in quartz) are also found overgrown by magnetite, and pseudoclasts of jasper in magnetite layers (e.g., Figure 6.3a, Figure 7.4e, Figure 7.1e) may be relict features remaining after incomplete replacement by magnetite. These transformations are unlikely to have occurred in the water column and therefore must represent diagenetic replacement. The replacement textures are also well-preserved in discrete bands that show no evidence of having been affected by later metamorphism (e.g., a lack of coarser Type 3 magnetite, which may be partly metamorphic in origin; a lack of quartz veining, and no late-stage structural disturbance).

In black chert, the growth of Type 2 magnetite appears to be mostly at the expense of Type 1 magnetite. It appears to be an intermediate step in the eventual formation of Type 3 magnetite. Type 1 magnetite is never seen in close proximity to Type 3 magnetite. It is mainly found in dark, Fe-rich quartz, whereas Type 2 and Type 3 magnetite are always found in clear, coarse euhedral quartz (Figure 7.2a and Figure 8.2d). The fine cracks in magnetite bands possibly record volume changes that accompanied the growth of Type 3 magnetite (Figure 8.4f), but also possibly reflect the brittleness of those bands as noted above. Some growth of magnetite also appears to have occurred in the banded chlorite layers that contain no lithic clasts.

11.3 Metamorphic and Deformation Features

Regional greenschist facies metamorphism has affected the Temagami BIF and its host rocks. The extent of metamorphic recrystallization is evident mainly in the volcanic rocks that contain abundant hydrous alteration minerals (esp. chlorite, epidote and muscovite). By contrast, the different BIF facies contain few hydrous minerals that would have been affected by metamorphism and, therefore, many of the primary (or at least) diagenetic mineral phases are preserved. There is little development of microfabric in these rocks and also limited brittle deformation, except as manifested by the quartz microveinlets that cut some of the Fe-rich bands. This quartz veining is pervasive throughout the Temagami BIF, but there appear to have been multiple generations of veins, some containing Type 3 magnetite or pyrite, some confined to only a few bands and others cross-cutting all parts of the BIF.

Many facies of BIF appear to have been completely unaffected by metamorphism, in particular those that still contain submicron iron-oxides shielded by quartz. Other phases (esp. coarse Type 3 magnetite) have textures that are more typical of metamorphic recrystallization (e.g., Figure 7.4b). Along some clearly late folds, faults and veins, magnetite is notably coarsened (Figure 7.2d). Some coarse Type 3 magnetite is closely spatially associated with late quartz veins, suggesting fluid-assisted growth. This magnetite also contains inclusions of quartz, ilmenite, and pyrite, which may be metamorphic, and leucoxene, apatite, dolomite-ankerite, and biotite occur as rims. Apatite and carbonate minerals are mainly intergranular phases between grains of Type 3 magnetite. It is unclear from petrographic observations whether they were remobilized from primary phases or if they are entirely metamorphic. Some chlorite is also found as a reaction rim on Type 3 magnetite (Figure 7.4c), which may be part of the regional greenschist metamorphism.

11.4 Processes of Mineral Deposition and Transformation

The primary deposition is interpreted to be directly from seawater that was saturated with silica and reduced iron from volcanic and hydrothermal sources (Bekker et al., 2014). Details of the possible primary minerals and their transformations during diagenesis and metamorphism have been described by Krapez et al. (2003); Bekker et al. (2010), Busigny et al. (2013), Rasmussen et al. (2013, 2014) and Sun et al. (2015). In the Temagami section, individual bands rarely have an internal structure at the

outcrop or even hand specimen scale, which is consistent with deposition as a homogenous chemical precipitate. Silica flocculation textures, which have been documented in other deposits of black chert and jasper (e.g. Grenne and Slack, 2003) also may be present in the Temagami BIF (e.g., preserved as jasper spherules). The microbanded chert subfacies also has been previously documented in the Mapepe Formation of the Swaziland Supergroup, where the occurrence of ancient Archean stromatolites may indicate that the formation of chert laminae was partly biogenic (Lowe, 1999).

Fe-oxide paragenesis:

Most models of BIF invoke primary deposition of hydrated amorphous Fe-oxides that are progressively transformed to hematite and eventually magnetite. A number of different mechanisms for that transformation have been proposed. Ferric iron can precipitate from aqueous solutions directly under a variety of redox conditions (Garrels and Christ, 1965; Gross, 1980; Holland, 1983). Many authors have proposed that the original hematite in BIF was a product of dehydration of a ferrihydrite precursor precipitated from the water column by Fe(II) oxidation (Ahn and Buseck, 1990; Morris, 1993; Widdel et al., 1993; Konhauser et al., 2002, 2007; Kappler et al., 2005; Pecoits et al., 2009; Bekker et al., 2010). Some models appeal to direct photooxidation of Fe (II) to Fe(III) prior to deposition; others suggest that the oxidation of Fe(II) was facilitated by cyanobacteria (Konhauser et al. 2002, 2007), remnants of which might be preserved in the samples studied here. In the metalliferous sediments of the Atlantis II Deep,

noncrystalline Si-Fe-OOH phases that form the muds are thought to have flocculated as Fe-rich silica “gels” that were stabilized by Si-Fe-O bonds (Cornell et al., 1987; Schwertmann et al., 1998; Taitel-Goldman and Singer, 2001). The original ferric oxyhydroxide is precipitated from the water column due to oversaturation at a chemocline or as a result of biologically mediated iron oxidation (Holland, 1973; Gross, 1983; Bekker, 2004). Taitel-Goldman and Singer (2002a, b) reproduced these particles in the laboratory and found that the high Si in the brine of the Atlantis II Deep (26 ppm: Anschutz and Blanc, 1995) likely contributed to the stability of the Si-Fe-OOH particles, which are still forming in the brine pool today. The only record of that original deposition in the Temagami samples is the hematitic quartz spherules in the jasper-rich BIF and possibly the biogenic filaments preserved in the quartz.

Post-depositional transformation of original ferric oxyhydroxide to ultrafine-grained hematite (Type 1 in this study) has been suggested as the first stage of formation of Algoma-Type BIF (Gross, 1983; Rouxel et al., 2005; Rasmussen et al., 2014; Sun et al., 2015). The transformation to more stable hematite in the presence of Fe(II) could take place in a solid state (Liu et al., 2005; Koehler et al., 2013; Posth et al., 2013a, 2013b). The finest hematite still preserved in the Temagami jasper and in other Algoma-Type BIF is similar to the hematite nanocrystals in the Atlantis II muds (Laurila et al., 2015) and hematite microspheres in the Marra Mamba BIF of Hamersley, Australia (Ahn and Buseck, 1990). The latter are thought to have been deposited from colloids that were recrystallized during the transformation of the surrounding amorphous silica to quartz, similar to the spheroidal quartz found in the Temagami jasper. Similar Fe-oxide

paragenesis also has been documented in oxide-facies BIF in the Kuruman formation of the Transvaal Supergroup and in an occurrence of oxide-facies BIF from the Hunter Mine Group of the Abitibi Greenstone Belt (Sun et al., 2015). In those occurrences, coarsening of the ultrafine hematite crystals is thought to have been due to Ostwald ripening, in which growth takes place via repeated dissolution and recrystallization (Morse and Casey, 1988), possibly facilitated by water trapped within the original Si-Fe-OOH gels.

The facies variations in the Temagami BIF also can be compared to facies variations in the Atlantis II Deep (James, 1969; Bischoff, 1969a). Fe-(oxy)hydroxides and authigenic clays are the dominant hydrothermal precipitates in the Fe-rich muds in the Red Sea. In thin section, they are commonly observed as diffuse patches of Fe enrichment in a poorly crystalline silica-rich matrix, similar to the Fe-rich spherules preserved in the Temagamai jasper facies (e.g., Laurila et al., 2015). Although some of this very fine-grained, poorly crystalline material is preserved in the uppermost water-saturated layers of sediment cores, most has been transformed into more crystalline Fe-oxides and clay minerals during burial. In particular, ferrihydrite, goethite (±limonite), lepidocrocite, and variably crystalline hematite, as well as magnetite, become increasing abundant in the deeper sediments. Similar transformations could account for some of the facies variations in the Temagami BIF.

Origin of the fine banding:

The origin of mm-scale laminae in BIF layers also has been the subject of considerable debate. It may reflect original deposition of amorphous Si-Fe-OOH phases in which differential settling of Fe- and Si-rich particles from the water column was caused by changes in basin chemistry (cf. Wang et al., 2009; Stefurak et al., 2014). As noted above, some authors have argued that ferrihydrite-rich sediment layers formed when the supply or the oxidization rate of Fe(II) overwhelmed the precipitation rate of silica due to seasonal cycling or temperature fluctuations (e.g., Holland, 1973; Morris, 1993; Posth et al., 2008; Sun et al., 2015). Short-term fluctuations in the chemistry of enclosed, especially anoxic, basins have been widely documented (e.g., Black Sea and Cariaco Basin: Lewis and Landing, 1991; Yarincik et al., 2000), as well as in some freshwater lakes (Davison, 1993; Holmstrom and Ohlander, 2001). However, Laurila et al. (2015) suggested that mineralogical and chemical segregation occurred during diagenesis, and this contributed to the fine layering of the Atlantis II sediments. Comparison of samples from different depths in the sediment profile of the Atlantis II Deep showed that the fine layering changes from diffuse to well-defined at depth; the laminations are mostly absent in the uppermost sediment but are present within a few meters of burial, suggesting that they must have formed as a result of diagenetic recrystallization (e.g., within a few thousand years of deposition: Laurila et al., 2015). A similar process was suggested by Lowe (1999) and Slack et al. (2007) for the delicate banding in chert. The exact mechanism is not known, but it may be considered a type of Liesegang banding, which is common in sedimentary rocks (Mozley, 2003).

Evidence for the involvement of bacteria:

A number of authors have suggested that Fe(II) oxidation was mediated by Fe(II)-oxidizing bacteria (Widdel et al., 1993; Konhauser et al., 2002; Hegler et al., 2008; Wu et al., 2014), or at least by oxygen produced by cyanobacteria (Konhauser et al., 2002, 2007). SEM analysis of modern hydrothermal sediments contining ferric oxyhydroxides and nontronite show an abundance of bacterial filaments, strongly suggesting that hydrothermal precipitation of both Fe-oxides and clay minerals is assisted by bacteria (Dekov, 2007). In the Temagami BIF, possible remanants of filamentous bacteria have been observed in the black chert and white chert facies. Similar bacterial structures have been documented in BIF from the Barberton Greenstone Belt (Walsh et al., 1985; Westall et al., 2001). Given the age of the Temagami BIF, the presence of bacteria in the depositional basin is not unexpected (cf. Sun et al., 2015) and may be reflective of the gradual emergence of oxic basins leading up to the GOE (Farquhar et al., 2000). In either case, Fe(II) oxidation, either by direct or indirect biological mechanisms, clearly existed in local marine basins from which BIF material was deposited (Rasmussen et al., 2014; Sun et al., 2015).

Origin of chlorite:

Fe-rich, Al-poor silicates, including chamosite [$(Fe^{2+},Mg,Fe^{3+})_5Al(Si_3Al)O_{10}(OH,O)_8$] and nontronite [$(Na,K,_{0.5}Ca)_{0.3}Fe_2(Si,Al)_4O_{10}(OH)_2n(H_2O)$] are also thought to have formed directly from the enriched water column of Archean BIF basins (Klein, 2005; Bekker et al., 2014). Primary precipitates of iron silicates as very fine (<4 μm) microgranules have been reported from other BIFs (Krapez et al., 2003; Rasmussen et al., 2013, 2014).

What is now chlorite in the most Fe-rich chlorite facies of the Temagami BIF (lacking evidence of volcaniclastic material) was most likely originally deposited as a smectite-like clay. During diageneis, and certainly under greenschist facies metamorphism, these clays would have recrystallized to Fe-oxides and chlorite (Odin, 1988; Velde, 2014). In other bands, the smectite may have replaced glass (i.e., volcanic ash) that also settled out of the water column. The endmember Fe-rich chlorite identified in this study is common in BIF, locally together with the Fe-rich serpentine mineral berthierine (Orcel et. al, 1949). Berthierine was not identified in the Temagami samples, but it may be represented by Al-rich zones in the banded chlorite beds.

Origin of apatite:

Apatite is a common accessory in Superior-Type BIF or ironstones, as a biological product (James, 1954; Gross, 1983). Recycling from marine organisms has been shown to be the most common mechanism for introduction of phosphorous (Kohn et al., 2002), mainly derived from settling of organic matter and hard parts from the water column. The origin of apatite in Archean BIF is less clear. It is found mainly in the interstices between magnetite grains, suggesting that it was either introduced during diagenesis or during metamorphism. The jasper facies, which appears to have undergone the least amount of recrystallization, contains no phosphates, consistent with a late-stage introduction. Although possible bacterial structures have been identified, it is unclear that the apatite in the Temagami BIF could have had a biogenic source, as suggested for other iron formations (Walsh et al., 1985; Westall et al., 2001).

Hematite replacement by magnetite:

Most authors agree that the magnetite bands in Algoma-Type BIF formed mainly by replacement of pre-existing Fe-rich bands, either hematite or finer-grained magnetite, as seen at the transitions between black chert and jasper (Bekker et al., 2010). Textural evidence of lateral replacement along individual bands is common, with locally incomplete transformation of hematite to magnetite. This may have been a diagenetic process or partly metamorphic, but textural evidence presented above strongly suggests that Type 2 and Type 3 magnetite grew from earlier hematite while the quartz spherules were still intact. In black chert, the growth of Type 2 magnetite appears to be mostly by scavenging of Fe from the Fe-rich chert, as suggested by magnetite growth at the margins of the jasper spherules. The coexistence of magnetite and hematite in many bands is interpreted to reflect mainly incomplete replacement reactions. Some hematite-bearing silica spherules are still preserved as relics in magnetite-bearing chert, and incomplete replacement of jasper bands by magnetite possibly indicates fluid transport along the bands when the sediments were still unconsolidated.

The replacement of hematite by magnetite along individual bands contrasts with earlier thinking that precipitation of the different oxides was a result of changing redox potential of the ocean water (James, 1954; Gross, 1983). At the scale of the Highway 11 outcrop, the variable abundance of magnetite versus well-preserved jasper bands in different parts of the section might be interpreted to reflect variable permeability of the

layers to reactive fluids as the BIF section was buried on the seafloor, similar to the replacement reactions observed as a result of burial of the modern Red Sea muds (Laurila et al., 2014, 2015). Alternatively, the better preservation of some jasper bands may reflect pulses of SiO_2-rich fluids and more effective shielding of the primary hematite by quartz.

In the presence of any reductant (phosphate, organic carbon, reducing metamorphic fluid etc.) a reaction converting hematite to magnetite could proceed with the form:

$$3Fe_2O_3\ (hm) + H_2 = 2Fe_3O_4\ (mt) + H_2O$$

In one model, oxidation of buried organic matter and reduction of Fe(III) is interpreted to have been the source of Fe(II) for magnetite formation (Walker, 1984; Koehler et al., 2013; Posth et al., 2013a,b; Konhauser et al., 2005; Li et al., 2013a). However, petrographic evidence does not support the redox transformation of primary iron (oxy)hydroxide to magnetite by carbonaceous material, as no organic carbon is present in the rocks and little evidence that the buried organic matter was oxidized to CO_2 in large quantities (i.e., no significant carbonate as a by-product). Ohmoto (2003) and Ohmoto et al. (2006) pointed out that the transition between hematite and magnetite along individual bands could not be due to large-scale changes in the redox chemistry of the basin but was more likely the result of local variability (in his model related to local hydrothermal activity). He suggested that the conversion of hematite to magnetite only required reduced Fe sourced from hydrothermal fluids.

Fe_2O_3 (hm) + Fe^{2+} + H_2O = Fe_3O_4 (mt) + $2H^+$

This “nonredox” transformation of hematite to magnetite may have occurred with the introduction of reduced hydrothermal fluids into the unlithified sediments. Calculations by Mucke and Cabral (2005) confirm that the large volume increase accompanying this reaction can only have been accommodated in unconsolidated material. During burial, hydrothermal fluids could easily have infiltrated the unlithified BIF, similar to what has been observed in sediment of the Atlantis II Deep (Laurila et al., 2015), promoting the nonredox conversion of hematite to magnetite. This model is relevant where biogenic reduction may have played a lesser role. Thus a variety of reactions under both diagenetic and metamorphic conditions could have been responsible for the transformation of hematite to magnetite. However, the balance of the textural evidence presented here strongly suggests that the hematite-to-magnetite transition occurred after deposition of the ferric-oxyhydroxides and before regional metamorphism.

11.5 Sources of Elements for Primary Deposition

The main sources of iron in banded iron formation are thought to include Fe^{3+} from weathering of volcanic rocks and Fe^{2+} from volcanic and hydrothermal sources, as illustrated in Figure 11.2. The lack of trace element enrichment overall is unexpected, considering the important role of scavenging by ferric oxyhydroxides in the water column of modern Fe-rich basins (Benjamin and Leckie, 1981). However, the trace element

geochemistry of the different facies sheds some light on the possible precipitation pathways. These include: (i) input from proximal low-temperature hydrothermal sources (esp. diagenetic As, Co, Ni, Cu, Ag, and Pb enriched in minor sulfide components), (ii) distal high-temperature hydrothermal sources that enrich basinal waters far from local sources (esp. Eu and possibly Zn), (iii) primary Fe-rich silicate deposition, and (iv) minor detrital (volcaniclastic) deposition. These pathways are, to some degree, decoupled from the dominant silica and ferric oxyhydroxide deposition of the BIF.

It is difficult to produce a lot of Fe^{2+} (or other reduced species such as Eu^{2+}) from hydrothermal or volcanic sources without also producing a lot of other metals and H_2S. This H_2S must be consumed by deposition close to the vent source (e.g., in the well-mineralized felsic volcaniclastic rocks in the footwall of the Temagami BIF), especially if the fluids have a high metal/H_2S ratio. Under S-limited conditions most trace metals also would have been deposited close to the hydrothermal vents. The trace amounts of Zn, especially in non-sulfidic chlorite facies BIF, well away from known sites of sulfide or black shale, likely reflect something fundamental about the depositional conditions in the basin. Sulfur-limited deposition might account for the separation of Cu and Zn, if Cu is preferentially deposited with available sulfur and Zn remains in solution. In the Red Sea muds, some of the more crystalline Fe-oxides have distinct rims that are enriched in Zn (>5 wt.%) and Si (~15 wt.%), suggesting the Fe-oxides initially incorporated Zn into their structure as they formed (Laurila et al., 2015). Mineralogical controls are clearly important in the different BIF facies (Table 10.4).

Whereas base metal deposition is clearly dominated by the small amount of sulfur in the sediments, other elements appear to have been more closely linked to deposition of primary Fe-oxyhydroxides and silica, probably reflecting adsorption onto surface-active Si-FeOOH particles descending through the water column. Aqueous complexing and/or adsoption onto Fe-oxyhydroxides is strongly dependent on local seawater chemistry, including pH, which might account for some of the variability in the trace element geochemistry of the BIF layers (e.g., Pierce and Moore, 1982; Konhauser et al., 2007; Bekker et al., 2014). Short-term decreases in pH, caused by enhanced submarine volcanic activity might also have destabilized some aqueous complexes that were otherwise soluble in the bottom waters. For example, complexes of boron, $B(OH)_3$ and $B(OH)_4^-$, are only stable at high pH. Notable enrichments (up to 20 ppm B) in Archean cherts have been interpreted to reflect an alkaline pH of the Archean oceans and a high boron concentration that could be destabilized by addition of H^+ from hydrothermal fluids (Lemarchand et al., 2009). The consistent REE profiles of the different BIF facies, including LREE enrichments and the small positive Eu anomaly, confirm that the local BIF basin had a direct hydrothermal input.

Curiously, there are no significant enrichments in the oxyanions (Mo, V, As, U, P) in the Fe-oxide layers of the BIF, as observed in modern ferric oxhydroxide precipitates (Berrang and Grill, 1974). This is most likely related to the anoxic conditions, with very low free oxygen for the formation of stable aqueous oxyanions that could be scavenged by the Fe-oxyhydroxides. The distribution of so-called redox sensitive elements, such as Mo, Ni, or U, also do not appear to be reflecting S or C systematics of the type normally

associated with anoxic basins (e.g., Large et al., 2013). Rather, a lack of enrichment in these elements overall reflects uniformly low S and C concentrations. The distribution of other elements may reflect redistribution within the sediment during diagenesis and crystal growth, especially of magnetite (e.g., Ge, ±V, ±Cr).

11.6 Mass Accumulation Rates

Detailed mapping of the Highway 11 outcrop documents a typical section of the Temagami BIF. The present-day thickness of the BIF section is 170 m. Modern marginal basin sedimentation rates are typically ~1 cm/1000 yr (Sadler, 1981), but hydrothermal deposition in basins like the Atlantis II Deep of the Red Sea was at least ~100-120 cm/1000 yr averaged over the entire section (Shanks and Bischoff, 1980) or ~1 mm annually. The latter corresponds closely to the thickness of many of the fine laminations in the Temagami BIF, although it is probable that there were other controls on the layering, and the thickness of the layers cannot be linked directly to depositional events. Nevertheless, at these very high rates of sedimentation, the entire section of Temagami BIF could have formed in 200,000 years, ignoring compaction and dewatering. Comparisons with modern metalliferous sediment, indicate that the original water content of the saturated Fe-oxide and chert layers, at least in the upper part of the section, could have been as high as 90 vol. %, meaning that the original uncompacted BIF section on the seafloor was probably thicker and a period of ~200,000 years for the accumulation is a minimum estimate. Because compaction is ongoing during deposition of the sediments, it is likely that only the top 10% of the section would have been

saturated with water (as in the Atlantis II Deep). In this case, the original thickness of sediment on the seafloor would have been closer to 300 m, requiring ~300,000 years to accumulate. Both estimates are well within the error of any age determinations for the ore-hosting volcanic rocks.

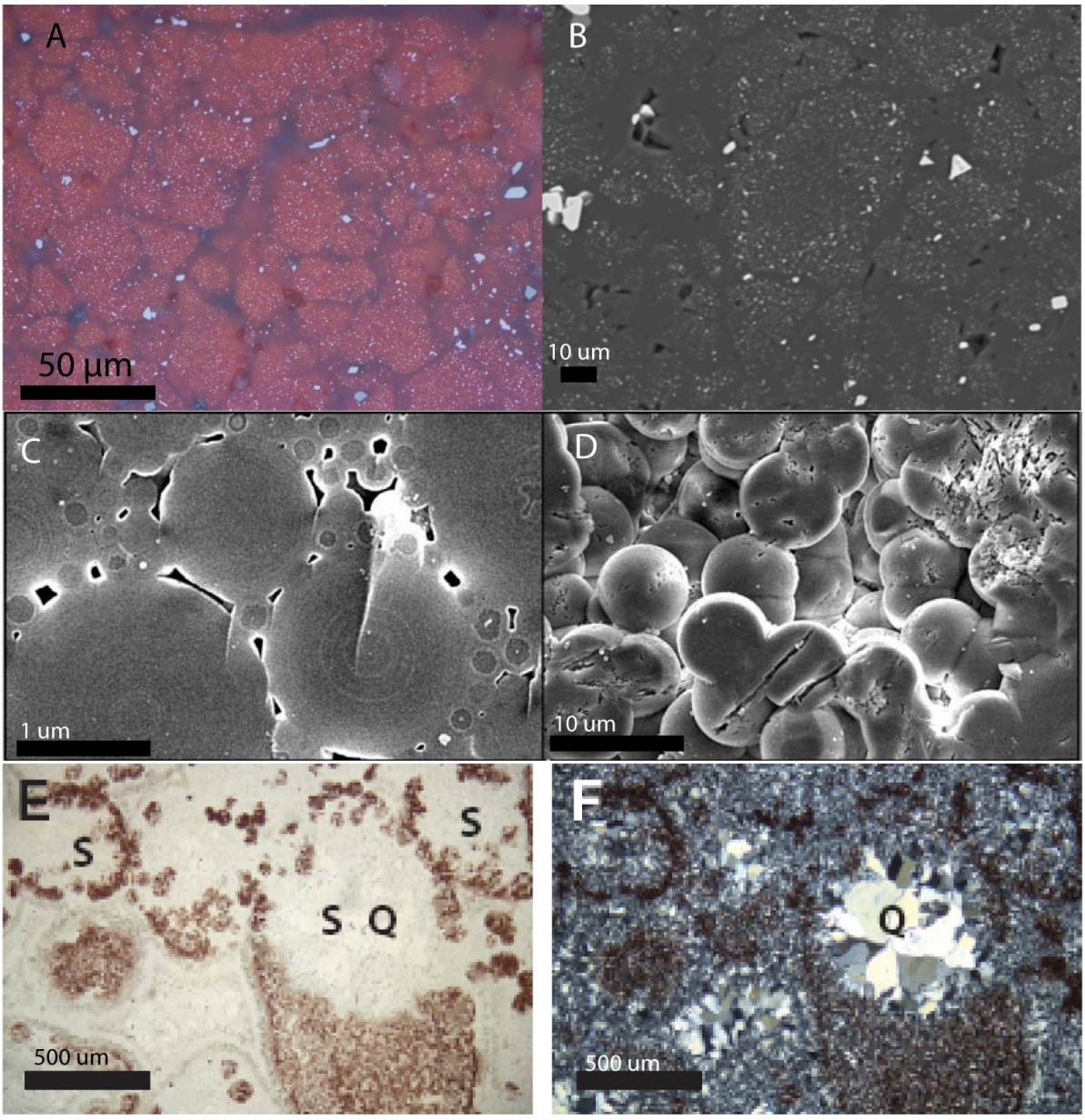

Figure 11.1 Typical appearance of jasper, opal and silica “granules” in different Types of chert, showing the similar habit of jasper BIF from Temagami and in other chemcial sediments described in the literature. A) Photomicrograph of jasper BIF in sample SM011 from the southern pit of the Sherman Mine. Jasper spherules are spheroidal aggregates of silica (now fine quartz), ranging in size from 10-50 µm, with disseminations of Type 1 magnetite and Type 1 hematite. Some larger spherules appear

to be aggregates of smaller spherules. Type 2 magnetite can be seen in the interstices between the spherules. B) SEM backscatter image of jasper BIF in sample SM11 from the southern pit of the Sherman Mine. Fine-grained inclusions of Type 1 hematite and Type 1 magnetite are distributed concentrically. C) SEM backscatter image of HF-etched opal from Minas Iris, Mexico, showing typical amorphous silica spheres (1-5 μm) that may be the building blocks of larger japser spherules in the Temagami BIF (from Gaillou et al., 2008). D) SEM backscatter image of HF-etched opal from Saint Nectaire, France, showing larger amorphous silica spheres that are comparable in size to the jasper spherules (from Gaillou et al., 2008). E) Plane-polarized light photomicrograph of much larger “silica granules” from the the Mount Ada Basalt (from Stefurak et al., 2014). F) Silica granules from the Antarctic Creek member of the Mount Ada Basalt in cross-polarized light. Very fine-grained crystalline quartz comprises the bulk of the larger granules (from Stefurak et al., 2014).

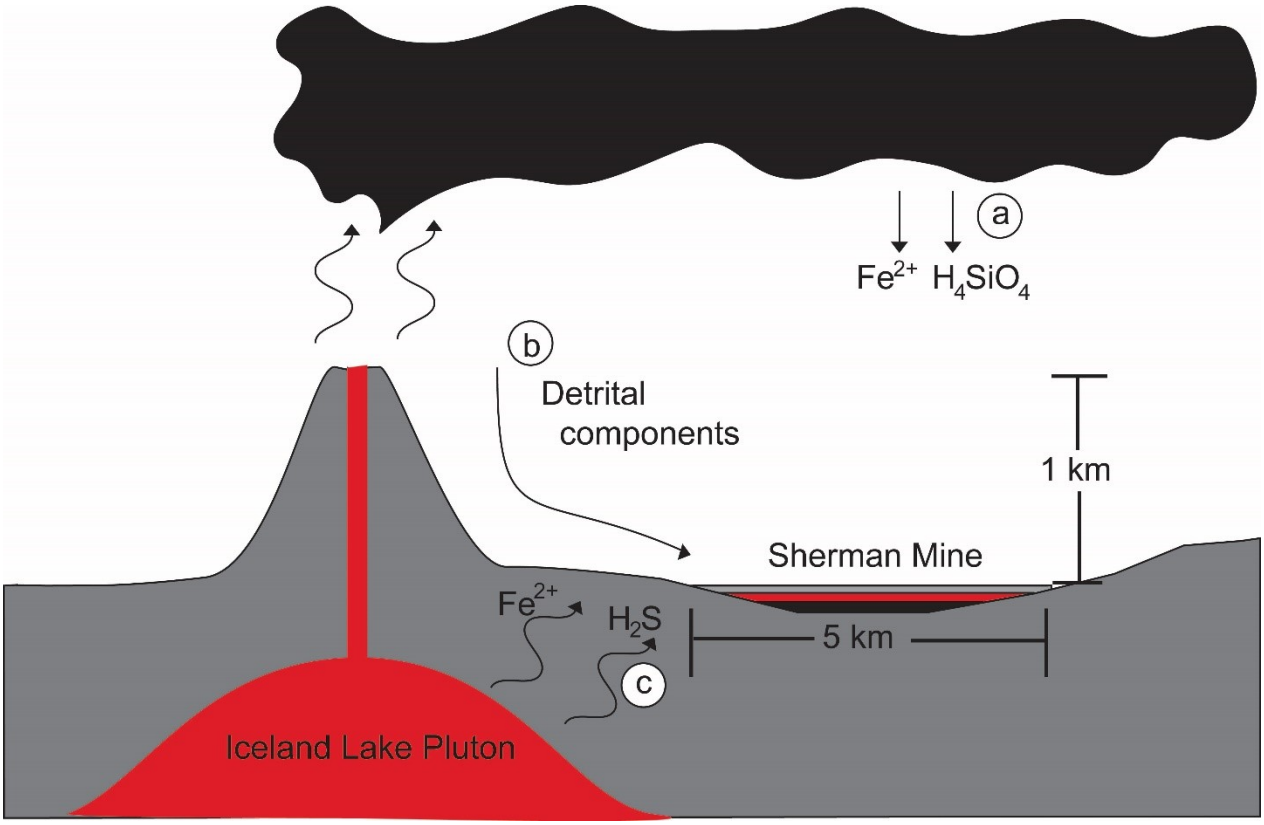

Figure 11.2 Schematic Illustration of possible Fe sources and pathways in typical Archean Algoma-Type BIF. Path a) includes mainly Fe^{2+} that is oxidized and precipitated from the water column as Fe-oxyhydroxides. In Algoma-Type BIF this is likely reduced iron introduced to the water column from hydrothermal vent sites. Additionally, iron-oxidizing bacteria can facilitate the precipitation of free iron in an otherwise reduced water column. Path (b) may include Fe leached from exposed volcanic substrate or transported in fine volcaniclastic material. Path (c) is Fe introduced by direct hydrothermal precipitation from fluids passing through unconsolidated sediments. The strong positive Eu anomaly in all chert facies of the Temagami BIF suggest that proximal hydrothermal sources were important and likely related to hydrothermal alteration observed in felsic rocks in the stratigraphic footwall of the mine.

In contrast the chlorite facies BIF, which lacks the Eu anomaly, was mainly sourced via path (b).

12. Conclusions

Previous studies of Archean Algoma-Type BIF in the Superior Province have been based on remarkably few and generally poorly documented samples – in some cases only one or two grab samples (e.g., Ohmoto et al., 2006; Shimada et al., 2007; Bau and Alexander, 2009; Konhauser et. al, 2009; Sun et al., 2015). The few samples that have been studied are rarely considered in their larger depositional context and often in occurrences that do not reflect large-scale BIF formation. The present study is one of the most detailed and comprehensive sampling efforts in Temagami, including one of the key outcrops that has been sampled by many visitors but not fully described. Earlier work by G.A. Gross, summarized in Gross (2009), compared bulk analyses of ore from the main open pits with other Superior Province BIF, and Bowins (1989) performed some of the earliest work on the REE geochemistry. However, there have been no detailed studies that have closely linked the mineralogy and paragenesis of intact sections of BIF to layer-by-layer chemistry. This study examined the local geology and field relationships to better constrain the architecture of the deposits and the origin of the different BIF facies. 50 samples from the Highway 11 outcrop and 70 samples from blocks taken from the main open pits provide a quantitative analysis of the BIF facies. The study established the distribution and relationships of the ore facies, considered the possibility that folding is responsible for the repetition in BIF unit, and documented the nature of transitions and breaks in BIF deposition.

Typical Algoma-Type BIF comprise both chemical and clastic components; the first derived from regional or local volcanic and hydrothermal activity and the second from erosion of associated volcanic rocks or direct volcanic input (e.g., ash). The dominant BIF facies in Temagami are chert (black, white and diffusely microbanded), accounting for ~60% of the section, chlorite-rich facies making up ~25%, and jasper accounting for 15%. Two types of chlorite bands were recognized; one consisting of very fine-grained chlorite that may represent primary Fe-Mg clays, and another associated with lithic clasts that are likely volcaniclastic in origin. As most sediments are sourced locally, at least at the scale of the major volcanic centres of the greenstone belt (cf. Thurston et al. 2008), the volcaniclastic component generally reflects the dominant lithologies in the footwall. In the case of the Temagami BIF, this is a bimodal succession of mafic and felsic volcanic rocks, including altered and mineralized felsic volcaniclastics. Although pyritic shale is present in the immediate stratigraphic footwall of the BIF section, true sulfide facies iron formation is not present in the Sherman mine. Various attempts at U-Pb dating, which have yielded ages in the south that are ~49 m.yr. older than volcanic units immediately to the north (e.g., Bowins and Heaman, 1991), are clearly inconsistent with pillow facing directions in the same rocks (Bennett, 1978; and confirmed in this study). The balance of observations suggest that the Temagami mine sequence is a homoclinal succession of mafic flows and altered felsic volcanic rocks in the footwall, with intervening black shale and BIF horizons and an overall younging direction to the south.

Although the BIF ores of the Sherman mine were dominated by chert and magnetite, the different facies are unevenly distributed. Chlorite facies accounted for only ~15% of the ore from the North pit, whereas ore blocks from the South pit comprise at least 30% chlorite facies. Blocks from the north pit also have more abundant coarse magnetite. In the Highway 11 outcrop, jasper layers are more abundant in some sections than in others. This may reflect better preservation where there has been less extensive diagenetic replacement of hematite by magnetite or it may reflect larger scale changes in basin conditions. Detailed petrographic examination of the different facies of the Temagami BIF has revealed a number of features that shed light on its formation, including the fine, sometimes rhythmic banding of Fe-oxide, chert and clastic layers, the different paragenetic relationships between minerals, and local deformation features that reflect synsedimentary and diagenetic processes. Several different types of quartz, hematite, and magnetite are recognized, corresponding to progressive recrystallization and replacement of primary silica and ferric-oxyhydroxides, first during early diagenesis and then during metamorphism. The presence of ilmenite, altered feldspar, and lithic clasts in other layers, especially in some chloritic bands, confirm an important volcaniclastic component.

Features interpreted as mainly primary deposition include submicron inclusions of Type 1 hematite in “jasper spherules”, submillimeter laminations in microbanded chert, the occurrence of banded chlorite, the possible preservation of bacterial relics, and abundant soft-sediment deformation. The quartz spherules that enclose Type 1 hematite and Type 1 magnetite in the jasper bands are very similar to those preserved

in younger BIF and chert sediments. They are interpreted to be directly analogous to "opal pellets" in present-day chert deposits. The analyzed chlorite is close to the Fe-rich endmember, chamosite, which is also typical of direct precipitation of Fe-silicates from hydrothermal fluids in modern metalliferous sediments. Mn is present mainly in late carbonates, and P is present in apatite and monazite. Samples that contain high Ni, Mo, Cr, and Se appear to be mainly related to the presence of trace (diagenetic?) pyrite. However, several 10s of ppm Zn still occur in samples with litle or no S or C. This likely reflects the presence of some metal in the chlorite bands. Certain other trace elements are unexpectedly enriched compared to other Algoma-Type BIF. In particular, the high As concentrations appear to reflect strong geochemical enrichment in altered and mineralized felsic volcanic rocks in the footwall. Other elements, such as Ge ($\pm$V,$\pm$Cr) appear to be mainly associated with coarse Type 3 magnetite, although the finer magnetite could not be analyzed. Boron concentrations (to 60 ppm) are uniformly high in the chert facies and likely represent a primary feature of the sediments.

The REE data are consistent with a range of chemical and clastic components contributing to the sediments, but consistently show LREE enrichment and positive Eu anomalies, implicating high-temperature hydrothermal activity at the source of the Fe. Monazite and apatite are likely the dominant hosts of REE, and therefore probably contain the +Eu anomaly. Very high Zr/Ti ratios and ΣREE in the chlorite facies is a strong indication that the volcaniclastic component was felsic and probably related to the abundant felsic volcanic rocks in the footwall of the mine. The proportions of mafic and felsic sources are indicated by Zr/Ti ratios intermediate between basalt and rhyolite.

The replacement of hematite by magnetite along individual bands after burial contrasts with earlier thinking that the different oxides (hematite or magnetite) were precipitated independently as a result of changing redox conditions of the ocean water (James, 1954; Gross, 1983). It is generally accepted that hematite in Algoma-Type BIF originated as a dehydration product of primary ferric hydroxide formed by oxidation of Fe(II) by Fe-oxidizing bacteria in the photic zone or by reaction with O_2 produced by cyanobacteria (Ahn and Buseck, 1990; Morris, 1993; Widdel et al., 1993; Konhauser et al., 2002, 2007; Kappler et al., 2005; Pecoits et al., 2009; Bekker et al., 2010; Sun et al., 2015). There is clear evidence of post-depositional transformation of this ultrafine-grained hematite to Type 1 and Type 2 magnetite, most likely in the later stages of diagenesis. The earliest growth of magnetite appears to have been by scavenging of Fe from these early precipitates. Iron appears to have been removed from the quartz in a halo of "depletion" around the coarser-grained magnetite. In other cases, the Type 2 magnetite occurs as a halo around unreplaced clusters of Type 2 hematite. The replacemant of hematite bands may reflect processes that were ongoing before lithification, as in modern metalliferous sediments. Two prevailing theories about the reduction of Fe^{3+} required to make magnetite have emerged: one related to the presence of reductants such as organic carbon; the other interpreted to be a "nonredox" reaction with ferrous Fe derived from local hydrothermal activity. Although evidence of bacterial remnants is preserved in the chert facies of the samples studied here, the lack of organic carbon in the rocks and little evidence that buried organic matter was

oxidized to CO_2 in large quantities suggests that reduction involving organic carbon was not responsible for the wholesale conversion of hematite to magnetite.

Algoma-Type BIF, including from the Sherman Mine, have been studied extensively as an archive of chemical conditions in the Late Archean oceans, although the context of the sampled material is rarely provided. Fe(II) oxidation clearly existed in local marine basins from which BIF was deposited, although the dominant processes (bacterially mediated versus inorganic) may have varied between locations. Comparisons with modern volcanosedimentary basins reveal a number of similarities, including the rate of BIF accumulation on the paleoseafloor. Assuming sedimentation rates similar to those for modern metalliferous sediments, the preserved section of BIF exposed in the Highway 11 outcrop likely accumulated in less than 300,000 years. This has important implications for interpreting the time breaks that have been inferred from other BIF sections elsewhere in the region (Thurston et al., 2008).

Following is a summary of the major conclusions derived from this work:

- Local geology and field relationships in the Sherman Mine area constrain the architecture of the deposits and the origin of the different BIF facies and suggest that folding is not responsible for repetition of the BIF horizons.
- More than 300 ore blocks at the edges of the open pits illustrate the facies variation throughout the mine.
- The transitions and breaks in BIF deposition are reflected in the mineral paragenesis, including both chemical and clastic sedimentation.

- Five principal ore facies are recognized: jasper, white chert, black chert, magnetite and chlorite.
- Magnetite-bearing facies are interpreted to be products of diagenetic and metamorphic replacement of earlier, especially jasper, facies
- Jasper facies is more abundant in some sections than in others, which may reflect better preservation where there has been less extensive diagenetic replacement of hematite by magnetite.
- Several different types of quartz, hematite, and magnetite are recognized, corresponding to progressive recrystallization and replacement of primary silica and ferric-oxyhydroxides, first during early diagenesis and then during metamorphism.
- Features interpreted as mainly primary include submicron inclusions of Type 1 hematite in “jasper spherules”, submillimeter laminations in microbanded chert, the possible preservation of bacterial relics, and abundant soft-sediment deformation.
- Quartz spherules that enclose Type 1 hematite and Type 1 magnetite in the jasper bands are very similar to those preserved in younger BIF and chert sediments (analogous to “opal pellets” in present-day chert deposits).
- Ore blocks from the North pit contain ~15% chlorite facies, whereas ore blocks from the South pit contain at least 30% chlorite facies.
- Two types of chlorite bands were recognized: very fine-grained chlorite, which are interpreted to represent primary Fe-rich clays, and chloritized lithic clasts in volcaniclastic layers.
- The mineralogy of the different ore facies is closely reflected in the major and trace element geochemistry.

- REE data are consistent with both chemical and clastic components in the sediments, but consistently show LREE enrichment and positive Eu anomalies, implicating hydrothermal activity at the source of the Fe.
- The proportions of mafic and felsic clastic sources are indicated by Zr/Ti ratios intermediate between basalt and rhyolite.
- Several 10s of ppm Zn occur in samples with little or no S, possibly reflecting metal enrichment in chlorite.
- Mn is present mainly in late carbonates, and P is present in apatite and monazite. Samples that contain high Ni, Mo, Cr, and Se appear to be mainly related to the presence of trace (diagenetic?) pyrite.
- There is clear evidence of post-depositional transformation of Type 1 ultrafine-grained hematite to Type 1 and Type 2 magnetite, most likely in the later stages of diagenesis (e.g., hematite appears to have been removed from quartz in a halo of “depletion” around the coarser-grained magnetite).
- The replacement of hematite by magnetite along individual bands after burial contrasts with earlier thinking that the different oxide facies (hematite vs. magnetite) were precipitated independently as a result of changing redox conditions.
- Although evidence of bacterial remnants is preserved, the lack of carbon suggests that reduction involving organic carbon was not responsible for the wholesale conversion of hematite to magnetite.

References

Abbey, S., McLeod, C.R., and Liang-Guo, W., 1983, FeR-1, FeR-2, FeR-3 and FeR-4: Four Canadian iron-formation samples prepared for use as reference materials: Geological Survey of Canada Paper 83-19.

Ahn, J.H., and Buseck, P.R., 1990, Hematite nanospheres of possible colloidal origin from a Precambrian banded iron formation. Science, v. 250, p. 111–113.

Anschutz, P. and Blanc, G., 1995, Geochemical dynamics of the Atlantis II Deep (Red Sea): silica behavior: Marine geology, v. 128, p.25-36.

Ayer, J.A, Amelin, Y., Corfu, F., Kamo, S., Ketchum, J.F., Kwok, K., and Trowell, N.F., 2002, Evolution of the Abitibi greenstone belt based on U–Pb geochronology: autochthonous volcanic construction followed by plutonism, regional deformation and sedimentation: Precambrian Research v. 115, p. 63–95.

Ayer, J.A., Chartrand, J.E., Grabowski, G.P.B., Josey, S., Rainsford, D. and Trowell, N.F., 2007, GIS compilation of the Cobalt–Temagami area, Abitibi greenstone belt: Ontario Geological Survey, Miscellaneous Release—Data 214.

Ayres, D.E., 1972, Genesis of iron-bearing minerals in banded iron formation mesobands in the Dales Gorge Member, Hamersley Group, Western Australia: Economic Geology, v. 67, p. 1214-1233.

Awramik, S.M., Schopf, J.W., and Walter, M.R., 1966, Filamentous fossil bacteria from the Archean of Western Australia: Precambrian Research, v. 20, p. 357-274.

Backer, H., 1976, Fazies und chemische Zusammensetzung rezenter Ausfallungen aus Mineralquellen in Roten Meer: Geologisches Jahrbuch, v. 17, p. D151-D172.

Bau, M., and Alexander, B.W., 2009, Distribution of high field strength elements (Y, Zr, REE, Hf, Ta, Th, U) in adjacent magnetite and chert bands and in reference standards FeR-3 and FeR-4 from the Temagami iron-formation, Canada, and the redox level of the Neoarchean ocean: Precambrian Research, v. 174, p. 337-346.

Baldwin, G.J., 2009, The sedimentology and geochemistry of banded iron formations of the Deloro assemblage, Bartlett Dome area, Abitibi greenstone belt, Ontario, Canada: Implications for BIF deposition and greenstone belt formation. In Masters Abstracts International (Vol. 48, No. 05).

Baldwin, G.J., Thurston, P.C. and Kamber, B.S., 2011. High-precision rare earth element, nickel, and chromium chemistry of chert microbands pre-screened with in-situ analysis: Chemical Geology, v. 285, p.133-143.

Bekker, A., Kaufman, A.J., Karhu, J.A., Beukes, N.J., Swart, Q.D., Coetzee, L.L., and Eriksson, K.A., 2001, Chemostratigraphy of the Paleoproterozoic Duitschland Formation, South Africa: Implications for coupled climate change and carbon cycling: American Journal of Science, v. 301, p. 261–285.

Bekker, A., Holland, H.D., Wang, P. L., Rumble, D., Stein, H.J., Hannah, J.L., Coetzee, L.L., and Beukes, N.J., 2004, Dating the rise of atmospheric oxygen: Nature, v. 427, p. 117−120.

Bekker, A., Barley, M.E., Fiorentini, M.L., Rouxel, O.J., Rumble, D., and Beresford, S.W., 2009, Atmospheric sulfur in Archean komatiite-hosted nickel deposits: Science, v. 326, p. 1086−1089.

Bekker, A., Slack, J.F., Planavsky, N., Krapez, B., Hofmann, A., Konhauser, K.O., Rouxel, O.J., 2010, Iron formation: The sedimentary product of a complex interplay among mantle, tectonic, oceanic, and biospheric processes: Economic Geology, v. 105, p. 467-508.

Bennet, G., 1978, Geology of the northeast Temagami area, district of Nipissing: Ontario Geological Society, report 163.

Benjamin, M.M., Leckie, J.O., 1981, Multiple-site adsorption of Cd, Cu, Zn and Pb on amorphous iron oxyhydroxide: Journal of Colloid Interface Science, v. 79, p. 209-221.

Berrang, P.G., Grill, E.V., 1974, The effect of manganese oxide scavenging on molybdenum in Saanich Inlet, British Columbia: Marine Chemistry, v. 2, p. 125–148.

Bischoff, J.L., 1969, Red Sea geothermal brine deposits: Their mineralogy, chemistry and genesis in Degens, E. T., and Ross, D. A., eds., Hot brines and recent heavy metal deposits in the Red Sea: New York Inc., Springer-Verlag, p. 525-532

Boutroy, E., Dare, S. A., Beaudoin, G., Barnes, S. J., & Lightfoot, P. C., 2014, Magnetite composition in Ni-Cu-PGE deposits worldwide: application to mineral exploration, Journal of Geochemical Exploration, v. 145, p. 64-81.

Bostrom, K., 1973, The origin and fate of ferromanganoan active ridge sediments: Stockholm Contributions to Geology, v. 27, p. 147-243.

Bostrom, K., Peterson, M.N.A., 1969, Precipitates from hydrothermal exhalations on the East Pacific Rise: Economic Geology, v. 61, p. 1258-1265.

Bowins, R. J., and Heaman, L. M., 1991, Age and timing of igneous activity in the Temagami greenstone belt, Ontario: a preliminary report: Canadian Journal of Earth Sciences, v. 28, p. 1873-1876.

Bowins, R.J., 1989, Rare earth and other geochemical studies of Archean banded iron formations: Sherman and Adams Mines, Ontario: Open Access Dissertations and Theses, McMaster University, Paper 1915.

Busigny, V., Lebeau, O., Ader, M., Krapež, B., and Bekker, A., 2013, Nitrogen cycle in the Late Archean ferruginous ocean: Chemical Geology, v. 362, p. 115-130.

Card, K.D., 1990, A review of the Superior Province of the Canadian Shield, a product of Archean accretion: Precambrian Geology, v. 48, p. 99-156.

Cameron, E.M., and Garrels, R.M., 1980, Geochemical composition of some Precambrian shales from the Canadian Shield: Chemical Geology, v. 28, p. 181-197.

Cornell, R.M., Giovanoli, R., and Schindler, P.W., 1987, Effect of silicate species on the transformation of ferrihydrite into goethite and hematite in alkaline media: Clays and Clay Minerals, v. 35, p. 21-28.

Cronan, D., 1976, Basal metalligerous sediments from the eastern Pacific: Geological Society of America, Bulletin, v. 87, p. 928-934.

Dare, S.A.S, Barnes, S.-J., Beaudoin, G., Meric, J., Boutroy, E., and Potvin-Doucet, C., 2014, Trace elements in magnetite as petrogenetic indicators: Mineralium Deposita, v. 49, p. 785-796.

Davison, W., 1993, Iron and manganese in lakes: Earth-Science Reviews, v. 34, p.119163.

de Ronde, C.E.J., de Wit, M.J., Spooner, E.T.C., 1994, Early Archean (>3.2 Ga) Feoxide-rich, hydrothermal discharge vents in the Barberton greenstone belt, South Africa: Geological Society of America Bulletin, v. 106, p. 86-104.

Dekov, V.M., Kamenov, G.D., Stummeyer, J., Thiry, M., Savelli, C., Shanks, W.C., Fortin, D., Kuzmann, E., Vertes, A., 2007, Hydrothermal nontronite formation at Eolo Seamount (Aeolian volcanic arc, Tyrrhenian Sea): Chemical Geology, v. 245, p. 103119.

Donaldson, J. A., and Garrett, R. G., 1991, Iron-Formation in Temagami and Sherman Mine Area, in Gross, G. A., and Donaldson, J. A., eds., Geological Survey of Canada Open File 2163 - Iron-Formation and Metalliferous Sediments in Central Canada [Field Trip 8], 66 p.

Dupuis, C., and Beaudoin, G., 2011, Discriminant diagrams for iron oxide trace element fingerprinting of mineral deposit Types: Mineralium Deposita, v. 46, p. 319-335.

Dymond, J., Corliss, J.B., Heath, G.R., Field, C.W., Dasch E.J., and Veeh, H.H., 1973, Origin of metalliferous sediments from the Pacific Ocean: Geological Society of America Bulletin, v. 84, p. 3355-3372.

Farquhar, J., Bao, H., and Thiemens, M., 2000, Atmospheric evidence of Earth's earliest sulfur cycle: Science, v. 289, p. 756-758.

Feng, R., and Kerrich, R., 1990, Geochemistry of fine-grained clastic sediments in the Archean Abitibi greenstone belt, Canada: Implications for provenance and tectonic setting: Geochimica et Cosmochimica Acta, v. 54, p. 1061-1081.

Garrels, R. M., and Christ, C. L., 1965, Solutions, minerals and equilibria: New York, Harper and Row, 450 p.

Gaillou, E., Fritsch, E., Rondeau, B., Aguilar-Reyes, B., Barreau, A., Ostroumov, M., Post, J., 2008, Common gem opal: An investigation of micro- to nano-structure: American Mineralogist, v. 93, p. 1865–1873.

Grenne, T., and Slack, J.F., 2003, Paleozoic and Mesozoic silica-rich seawater: Evidence from hematitic chert (jasper) deposits: Geology, v. 31, p. 319−322.

Grenne, T., and Slack, J.F., 2005, Geochemistry of jasper beds from the Ordovician Løkken ophiolite, Norway: Origin of proximal and distal siliceous exhalites: Economic Geology, v. 100, p. 1511−1527.

Gross, G.A., 1972, Primary features in cherty iron-formations: Sedimentary Geology, v. 7, p. 241-261.

Gross, G.A., 1980, A classification of iron formations based on depositional environment: Canadian Mineralogist, v. 18, p. 215-222.

Gross, G. A., 1983, Tectonic systems and the deposition of iron-formation: Developments in Precambrian Geology, v. 7, p. 63-79.

Gross, G.A., 2009, Iron formation in Canada, genesis and geochemistry: Geological Survey of Canada, Open File 5987.

Gruner, J.W., 1926, Magnetite-martite-hematite: Economic Geology, v. 21, p. 375-393.

Govindaraju, K., 1994. 1994 compilation of working values and sample descriptions for 383 geostandards: Geostandards Newsletter v. 18, p. 1–158.

Hoashi, M., Bevacqua, D.C., Otake, T., Watanabe, Y., Hickman, A.H., Utsunomiya, S. and Ohmoto, H., 2009, Primary haematite formation in an oxygenated sea 3.46 billion years ago: Nature Geoscience, v. *2*, p.301-306.

Hamade, T., Konhauser, K.O., Raiswell, R., Goldsmith, S. and Morris, R.C., 2003, Using Ge/Si ratios to decouple iron and silica fluxes in Precambrian banded iron formations: Geology, v. 31, p.35-38.

Hannington, M.D., and Jonasson, I.R., 1992, Fe and Mn oxides at seafloor hydrothermal vents, In Skinner, H.C.W. and Fitzpatrick, R.W., eds., Biomineralization Processes of Iron and Manganese: Catena v. 21, p. 351-370.

Hannington, M.D., Jonasson, I.R., Herzig, P.M., and Petersen, S., 1995, Physical and chemical processes of seafloor mineralization: Geophysical Monograph, v. 91, p. 115−157.

Hannington, M., Santaguida, F., Kjarsgaard, I., Cathles, L., 2003, Regional greenschist facies hydrothermal alteration in the central Blake River Group, western Abitibi subprovince, Canada: Mineralium Deposita, v. 38, p. 393-422

Hannington, M.D., de Ronde, C.E.J., and Petersen, S., 2005, Sea-floor tectonics and submarine hydrothermal systems: Economic Geology 100th Anniversary Volume, p. 111−141.

Hannington, M.D., Coombs, A., van Hees, G., Duff, S. and Campos-Alvarez, N., 2012, Regional lithogeochemical study of the Kidd–Munro MEGATEM® survey areas, Timmins–Kirkland Lake, northern Ontario: Discover Abitibi Initiative; Ontario Geological Survey, Miscellaneous Release—Data 291.

Hegler, F., Posth, N.R., Jiang, J. and Kappler, A., 2008, Physiology of phototrophic iron (II)-oxidizing bacteria: implications for modern and ancient environments: FEMS microbiology ecology, v. 66, p.250-260.

Hey, M.H., 1954, A new review of the chlorites, Mineral. Mag., v. 30, p. 217-292.

Holland, H.D., 1973, The Oceans; A possible source of iron in iron-formations: Economic Geology, v. 68, p. 1169-1172.

Holmström, H. and Öhlander, B., 2001, Layers rich in Fe-and Mn-oxyhydroxides formed at the tailings-pond water interface, a possible trap for trace metals in flooded mine tailings: Journal of Geochemical Exploration, v. 74, p.189-203.

Hornibrook, E.R. and Longstaffe, F.J., 1996, Berthierine from the lower cretaceous clearwater formation, Alberta, Canada: Clays and Clay Minerals, v. 44, p.1-21.

Hurd, D.C., Theyer, F., 1977, Changes in the physical and chemical properties of biogenic silica from the central equatorial Pacific: Part II. Refractive index, density, and water content of acid-cleaned samples: American Journal of Science, v. 277, p. 1168–1202.

Hurd DC, Pankratz HS, Asper V, Fugate J, and Morrow H (1981) Changes in the physical and chemical properties of biogenic silica from the central equatorial Pacific: Part III. Specific pore volume, mean pore size, and skeletal ultrastructure of acid-cleaned samples: American Journal of Science, v. 281, p. 833–895.

Isley, A.E., Abbot, D.H., 1991, Plume related mafic volcanism and the deposition of banded iron formation: Journal of Geophysical Research, v. 104, p.15461-15477.

James, H. L., 1954, Sedimentary facies of iron-formation: Economic Geology, v. 49, p. 235-293.

James, H.L., 1969, Comparison between Red Sea deposits and older ironstone and iron-formation, in Degens, E. T., and Ross, D. A., eds., Hot brines and recent heavy metal deposits in the Red Sea: New York Inc., Springer-Verlag, p. 525-532.

Jakobsson, S.P., Moore, J.G., 1986, Hydrothermal minerals and alteration rates at Surtsey Volcano, Iceland: Geological Society of America Bulletin, v. 97, p. 648-659.

Jones, B., Renaut, R. W., 2007, Microstructural changes accompanying the opal-A to opal-CT transition: new evidence from the siliceous sinters of Geysir, Haukadalur, Iceland: Sedimentology, v. 54, p. 921-948.

Jones, J.B., Segnit, E.R., 1971, The nature of opal I. nomenclature and constituent phases: Journal of the Geological Society of Australia, v. 18, p. 57-68.

Kappler, A. and Straub, K.L., 2005, Geomicrobiological cycling of iron: Reviews in Mineralogy and Geochemistry, v. 59, p.85-108.

Köhler, I., Konhauser, K.O., Papineau, D., Bekker, A. and Kappler, A., 2013, Biological carbon precursor to diagenetic siderite with spherical structures in iron formations: Nature communications, v. 4, p. 1741.

Konhauser, K.O., Hamade, T., Raiswell, R., Morris, R.C., Ferris, F.G., Southam, G. and Canfield, D.E., 2002, Could bacteria have formed the Precambrian banded iron formations?: Geology, v. 30, p.1079-1082.

Konhauser, K.O., Amskold, L., Lalonde, S.V., Posth, N.R., Kappler, A. and Anbar, A., 2007, Decoupling photochemical Fe (II) oxidation from shallow-water BIF deposition: Earth and Planetary Science Letters, v. 258, p.87-100.

Kohn, M.J. and Cerling, T.E., 2002, Stable isotope compositions of biological apatite: Reviews in mineralogy and geochemistry, v. 48, p.455-488.

Laurila, T. E., Hannington, M. D., Leybourne, M., Petersen, S., Devey, C. W., and GarbeSchönberg, D, 2015, New insights into the mineralogy of the Atlantis II Deep metalliferous sediments, Red Sea: Geochemistry, Geophysics, Geosystems, v. 16, p. 4449-4478.

Laurila, T., Hannington, M., Petersen, S., Garbe-Schoenberg, D., 2014, Metal distribution in the Atlantis II Deep (Red Sea) sediments: Chemical Geology, v. 386, p. 80-100.

Large, R.R., Meffre, S., Burnett, R., Guy, B., Bull, S., Gilbert, S., Goemann, K., Danyushevsky, L., 2013, Evidence for an intrabasinal source and multiple concentration processes in the formation of the Carbon Leader Reef, Witwatersrand Supergroup, South Africa: Economic Geology, v. 108, p. 1215–1241.

Lemarchand, D., Jeambrun, M., van Bergen, M.J. and van Cappellen, P., 2009, Boron isotopes in Archean cherts: investigating early Earth marine conditions: In AGU Fall Meeting Abstracts, v. 1, p. 1335.

Li, Y.L., Sun, S. and Chan, L.S., 2013, Phosphogenesis in the 2460 and 2728 millionyear-old banded iron formations as evidence for biological cycling of phosphate in the early biosphere: Ecology and evolution, v. 3, p.115-125.

Liu, H., Wei, Y. and Sun, Y., 2005, The formation of hematite from ferrihydrite using Fe (II) as a catalyst: Journal of molecular catalysis A: Chemical, v. 226, p.135-140.

Lewis, B.L. and Landing, W., 1991. The biogeochemistry of manganese and iron in the Black Sea. Deep Sea Research Part A. Oceanographic Research Papers, 38, pp.S773S803.

Lowe, D.R., 1991, Petrology and sedimentology of cherts and related silicified sedimentary rocks in the Swaziland Supergroup, in Lowe, D.R., ed., Geologic evolution of the Barberton Greenstone Belt: Geological Society of America Special Papers, v. 329 p. 83-114.

Mason, B., 1982, Principles of Geochemistry; John Wiley and Sons Limited, New York, 329p.

McDonough, W.F. and Sun, S.S., 1995, The composition of the Earth: Chemical Geology, v. 120, p.223-253.

Middleton, G.V., Church, M.J., Coniglio, M., Hardie, L.A., Longstaffe, F.J., 2003, Encyclopedia of Sediments and Sedimentary Rocks. Kluwer Academic Publishers, Dordrecht., p. 221, 224.

Milliken, K. L., 2014, "Late diagenesis and mass transfer in sandstone-shale sequences" in Mackenzie, F.T., Holland, H.D., and Turekian, K.K., ed., Treatise on Geochemistry: Sediments, Diagenesis and Sedimentary rocks: v. 3, Elsevier, p. 159190.

Moorehouse, W.W., 1942, The northeastern portion of the Temagami Lake area: Ontario Department of Mines, v.51.

Morris, R.C., 1993, Genetic modelling for banded iron-formation of the Hamersley Group, Pilbara Craton, Western Australia: Precambrian Research, v. 60, p.243-286.

Morse, J.W. and Casey, W.H., 1988, Ostwald processes and mineral paragenesis in sediments: American Journal of Science, v. 288, p.537-560.

Mozley, P.S., 2003, Diagenetic structures, in Middleton, G., ed., Encyclopedia of sediments and sedimentary rocks: Kluwer Academic Press, p. 219–225.

Mucke, A., Annor, A., 1993, Examples and genetic significance of the formation of iron oxides in the Nigerian banded iron-formations: Mineralium Deposita v. 28, p. 136–145.

Mucke, A., Annor, A., Neumann, U., 1996, The Algoma-Type iron-formations of Nigerian metavolcanosedimentary schist belts: Mineralium Deposita, v. 31, p. 113–122.

Mucke, A., Cabral, R.A., 2005, Redox and nonredox reactions of magnetite and hematite in rocks: Chemie der Erde, v. 65, p. 271-278.

Noffke, N., Eriksson, K.A., Hazen, R.M., and Simpson, E.L., 2005, A new window into Early Archean life: Microbial mats in Earth's oldest siliciclastic tidal deposits (3.2 Ga Moodies Group, South Africa): Geology, v. 34, p. 253-256.

Odin G., and Lamboy M, 1988, "Glaucony from the margin off northwestern Spain" in Odin G., ed., Green Marine Clays: Developments in Sedimentology: v. 45, Elsevier, p. 249–276.

Ohmoto, H., 2003, Nonredox transformations of magnetite-hematite in hydrothermal systems: Economic Geology, v. 98, p. 157-161.

Ohmoto, H., Watanabe, Y., Yamaguchi, K. E., Naraoka, H., Haruna, M., Kakegawa, T., Hayashi, K.-i., and Kato, Y., 2006, “Chemical and biological evolution of early Earth: Constraints from banded iron formations” in Kesler, S.E. and Ohmoto, H., ed., Evolution of Early Earth’s Atmosphere, Hydrosphere and Biosphere- Constraints from Ore Deposits: v. 198, Geological Society of America Memoirs, p. 291-331.

Orcel J., Henin S., and Caillere S., 1949, Sur les silicates phylliteux des minerais de fer Oolithiques: Comptes Rendus de l’Academie des Sciences, v. 229, p. 134–135.

Pecoits, E., Gingras, M.K., Barley, M.E., Kappler, A., Posth, N.R. and Konhauser, K.O., 2009, Petrography and geochemistry of the Dales Gorge banded iron formation: Paragenetic sequence, source and implications for palaeo-ocean chemistry: Precambrian Research, v. 172, p. 163-187.

Orcel, J., 1927, Analyse thermique des chlorites, Bull. Soc. Franc. Min., v. 50, p. 75-454.

Peter, J.M. and Goodfellow, W.D., 1996, Mineralogy, bulk and rare earth element geochemistry of massive sulphide-associated hydrothermal sediments of the Brunswick Horizon, Bathurst Mining Camp, New Brunswick: Canadian Journal of Earth Sciences, v. 33, p. 252-283.

Pierce, M.L., Moore, C.B., 1982, Adsorption of arsenite and arsenate on amorphous iron hydroxide. Water Res. 16, 1247–1253.

Posth, N.R., Hegler, F., Konhauser, K.O. and Kappler, A., 2008, Alternating Si and Fe deposition caused by temperature fluctuations in Precambrian oceans: Nature Geoscience, v. 1, p.703-708.

Posth, N.R., Köhler, I., Swanner, E.D., Schröder, C., Wellmann, E., Binder, B., Konhauser, K.O., Neumann, U., Berthold, C., Nowak, M. and Kappler, A., 2013, Simulating Precambrian banded iron formation diagenesis: Chemical Geology, v. 362, p. 66-73.

Posth, N.R., Konhauser, K.O. and Kappler, A., 2013, Microbiological processes in banded iron formation deposition: Sedimentology, v. 60, p.1733-1754.

Planavsky N., Rouxel O., Bekker A., Shapiro R., Fralick P. and Knudsen A. (2009) Iron-oxidizing microbial ecosystems thrived in late Paleoproterozoic redox-stratified oceans. Earth Planet. Sci. Lett. 286, 230–242.

Rasmussen, B., Krapez, B., Meier, D.B., 2014, Replacement origin for hematite in 2.5 Ga banded iron formation: Evidence for postdepositional oxidation of iron-bearing minerals: GSA Bulletin, v.126, p. 438-446.

Riedel, R. W., 1969, General Geology of the Iron-Formation at Sherman Mine, Temagami, Ontario. Exploration Project Report, 6 p.

Rouxel, O.J., Bekker, A., and Edwards, K.J., 2005, Iron isotope constraints on the Archean and Paleoproterozoic ocean redox state: Science v. 307 p. 1088–1091.

Sadler, P.M., 1981, Sediment accumulation rates and the completeness of stratigraphic sections: The Journal of Geology, v. 89, p. 569-584.

Schwertmann, U., Friedl, J., Stanjek, H., Murad, E. and Bender Koch, C., 1998, Iron oxides and smectites in sediments from the Atlantis II Deep, Red Sea: European Journal of Mineralogy, v. 10, p.953-968.

Shimada, Y., Yasumatsu, A., Motomura, Y., Okazaki, R., Nakamura, T., Ohmoto, H., Okaue, Y., Yokoyama, T., 2007, A study on the formation mechanism of Temagami iron-formations, Canada: Goldschmidt Conference Abstracts, p. A930.

Slack, J.F., Grenne, T., Bekker, A., Rouxel, O.J., and Lindberg, P.A., 2007, Suboxic deep seawater in the late Paleoproterozoic: Evidence from hematitic chert and iron formation related to seafloor-hydrothermal sulfide deposits, central Arizona, USA: Earth and Planetary Science Letters, v. 255, p. 243−256.

Slack, J.F., Grenne, T., and Bekker, A., 2009, Seafloor-hydrothermal Si-Fe-Mn exhalites in the Pecos greenstone belt, New Mexico, and the redox state of ca. 1720 Ma deep seawater: Geosphere, v. 5, p. 302−314.

Smith, A.J.B., Beukes, N.J., Gutzmer, J., 2013, The composition and depositional environments of Mesoarchean iron formations of the West Rand Group of the Witwatersrand Supergroup, South Africa: Economic Geology, v. 108, p. 111-134.

Stefurak, E.J.T., Lowe, D.R., Zentner, D., Fischer, W.W., 2014, Primary silica granules-a new mode of Paleoarchean sedimentation: Geology, v. 42, p. 283-286.

Sun, S., Konhauser, K.O., Kappler, A., and Li, Y-L., 2015, Primary hematite in Neoarchean to Paleoproterozoic oceans: GSA Bulletin; May/June 2015; v. 127; no. 5/6; p. 850–861; doi: 10.1130/B31122.1

Taitel-Goldman, N., and Singer, A., 2001, High-resolution transmission electron microscopy study of the newly formed sediments in the Atlantis II Deep, Red Sea: Clays and Clay Minerals, v. 49, p. 174-182.

Taitel-Goldman, N. and Singer, A., 2002a, Metastable Si-Fe phases in hydrothermal sediments of Atlantis II Deep, Red Sea: Clay Minerals, v. 37, p.235-248.

Taitel-Goldman, N. and Singer, A., 2002b, Synthesis of clay-sized iron oxides under marine hydrothermal conditions: Clay Minerals, v. 37, p.719-731.

Taner, M.F., Chemam, M., 2015, Algoma-Type banded iron formation (BIF), Abitibi Greenstone belt, Quebec, Canada: Ore Geology Reviews, v. 70, p. 31-46.

Thurston, P.C., Ayer, J.A., Goutier, J., and Hamilton, M.A., 2008, Depositional gaps in Abitibi Greenstone Belt stratigraphy: A key to exploration for syngenetic mineralization: Economic Geology, v. 103, p. 1097-1134.

Thurston, P. C., Kamber, B. S., and Whitehouse, M., 2012, Archean cherts in banded iron formation: Insight into Neoarchean ocean chemistry and depositional processes: Precambrian Research, v. 214–215, p. 227-257.

Tilley, C.E., 1938, The status of hornblende in low grade metamorphic zones of green schists: Geol. Mag., v. 75, p. 497-51.

Tompkins, L.A., Cowan, D.R., 2001, Opaque mineralogy and magnetic properties of selected banded iron-formations, Hamersley Basin, Western Australia: Australian Journal of Earth Sciences, v. 48, p. 427-437.

Tyler, S.A., Marsden, R.W., 1938, The nature of leucoxene: Journal of Sedimentary Research, v. 8, p. 55-58.

Velde, B., 2014, Green clay minerals in Mackenzie, F.T., Holland, H.D., and Turekian, K.K., ed., Treatise on Geochemistry: Sediments, Diagenesis and Sedimentary rocks: v. 3, Elsevier, p. 351-364.

Walker, J.C., 1984. Suboxic diagenesis in banded iron formations: Nature, v. 309, p. 340-342.

Walsh, M.M., Lowe, D.R., 1985, “Filamentous microfossils from the 3,500-Myr-old Onverwacht Group, Barberton Mountain Land, South Africa”: Nature, v. 314, p. 530532.

Walsh, M.M, 1992, “Microfossils and possible microfossils from the early Archean Onverwacht group, Barberton mountain land, South Africa”: Precambrian Research, v. 54, p. 271-293.

Wang, Y., Xu, H., Merino, E. and Konishi, H., 2009, Generation of banded iron formations by internal dynamics and leaching of oceanic crust: Nature Geoscience, v. 2, p. 781-784.

Westall, F., de Wit, M.J., Dann, J., van der Gaast, S., de Ronde, C.E.J., and Gerneke, D., 2001, Early Archean fossil bacteria and biofilms in hydrothermally-influenced sediments from the Barberton greenstone belt, South Africa: Precambrian Research, v. 106, p. 93-116.

Widdel, F., Schnell, S., Heising, S., Ehrenreich, A., Assmus, B. and Schink, B., 1993, Ferrous iron oxidation by anoxygenic phototrophic bacteria: Nature, v. 362, p.834-836.

Williams, L.A., and Crerar, D.A., 1985, Silica diagenesis, II. General mechanisms: Journal of Sedimentary Research, v. 55 p. 3.

Wilson, A., 2012, Ontario Ministry of Northern Development and Mines (http://www.geologyontario.mndmf.gov.on.ca/gosportal/gos?command=mndmsearchdetails:mdi&uuid=MDI31M04SW00025.)

Wu, W., Swanner, E.D., Hao, L., Zeitvogel, F., Obst, M., Pan, Y. and Kappler, A., 2014, Characterization of the physiology and cell–mineral interactions of the marine anoxygenic phototrophic Fe (II) oxidizer Rhodovulum iodosum–implications for Precambrian Fe (II) oxidation: FEMS microbiology ecology, v. 88, p.503-515.

Yarincik, K.M., Murray, R.W., Lyons, T.W., Peterson, L.C. and Haug, G.H., 2000, Oxygenation history of bottom waters in the Cariaco Basin, Venezuela, over the past 578,000 years: Results from redox-sensitive metals (Mo, V, Mn, and Fe): Paleoceanography, v. 15, p.593-604.

Zierenberg, R. A., and Shanks, W. C., 1983, Mineralogy and geochemistry of epigenetic features in metalliferous sediment, Atlantis II Deep, Red Sea: Economic Geology, v. 78, p. 57-72.

Appendix 1: Sample Description

The following is a description of each sample included in this thesis for geochemistry or thin section. Whole-rock (WR) samples were cut from beds of different facies, isolated to provide a geochemical composition of the particular layers. Thin sections were made to document mineralogical features and the paragenesis of the BIF. Typically, one thin section and one WR sample were prepared from each sample.

<table>
<tr><td>Sample: H11-5</td><td>Lat: 47.06840 N</td><td>Long: 79.7907 W</td></tr>
<tr><td colspan="3"> 
Sample H11-5 in situ

 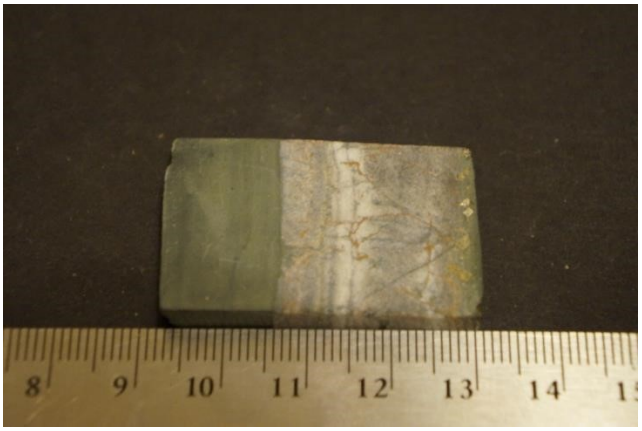
Cut section of H11-5</td></tr>
<tr><td colspan="3">Facies represented: mafic volcaniclastic, greywacke</td></tr>
<tr><td colspan="3">Description: Sample H11-5 was taken from the upper section of the Highway 11 outcrop. Interlayered beds of greywacke and mafic volcaniclastics in H11-5 are 7-10 cm thick. 1-5 mm euhedral pyrite occurs in the mafic volcaniclastic beds.</td></tr>
</table>

Sample: H11-7	Lat: 47.06842 N	Long: 79.7907 W
 Sample H11-7 in situ	 Cut section of H11-7	
Facies represented: mafic volcaniclastic		

Description: Sample H11-7 was taken from the upper section of the Highway 11 outcrop. Massive, unlayered chlorite is cut by quartz veinlets in this sample.

Sample: H11-9a	Lat: 47.06844 N	Long: 79.7907 W
 Sample H11-9 in situ	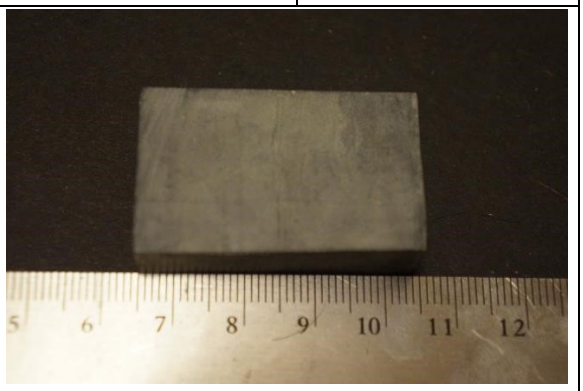 Cut section of H11-9a	
Facies represented: black chert		
Description: Sample H11-9 was taken from the upper section of the Highway 11 outcrop. The sample contains a 5 cm of a <10 thick white chert bed and 4 cm of a <15 cm thick black chert bed. H11-9 was cut along the white chert-black chert layer boundary to make samples H11-9a and H11-9b. H11-9a is the cut section of the black chert layer.		

Sample: H11-9b	Lat: 47.06844 N	Long: 79.7907 W
 Sample H11-9 in situ	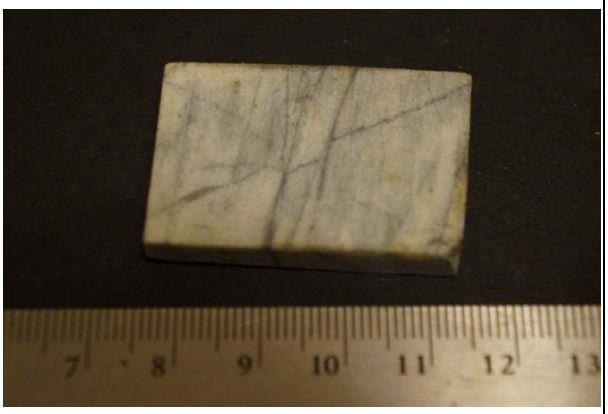 Cut section of H11-9b	
Facies represented: white chert		
Description: Sample H11-9 was taken from the upper section of the Highway 11 outcrop. The sample contains a 5 cm of a <10 thick white chert bed and 4 cm of a <15 cm thick black chert bed. H11-9 was cut along the white chert-black chert layer boundary to make samples H11-9a and H11-9b. H11-9a is the cut section of the white chert layer.		

Sample: H11-20.7	Lat: 47.06847 N	Long: 79.7907 W
 Sample H11-20.7 in situ	 Cut section of H11-20.7	
Facies represented: chlorite BIF		
Description: Sample H11-20.7 was taken from the upper section of the Highway 11 outcrop. Unlayered, massive chlorite with ~1mm euhedral pyrite make up this sample.		

Sample: H11-21.9a	Lat: 47.06847 N	Long: 79.7907 W
 Sample H11-21.9 in situ	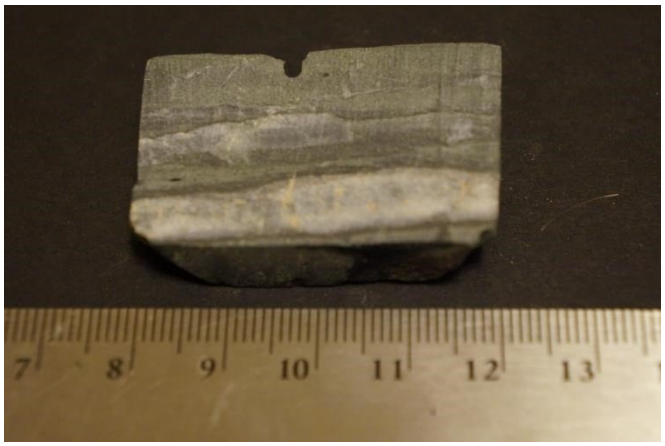 Cut section of H11-21.9a	
Facies represented: chlorite BIF, white chert, black chert		
Description: Sample H11-21.9 was taken from the upper section of the Highway 11 outcrop. Laminated chlorite, magnetite, black and white chert beds 1-3 cm thick comprise this sample. This sample was cut to make H11-21.9a with 3 chlorite beds, 2 black chert beds and 1 white chert bed.		

Sample: H11-21.9b	Lat: 47.06847 N	Long: 79.7907 W
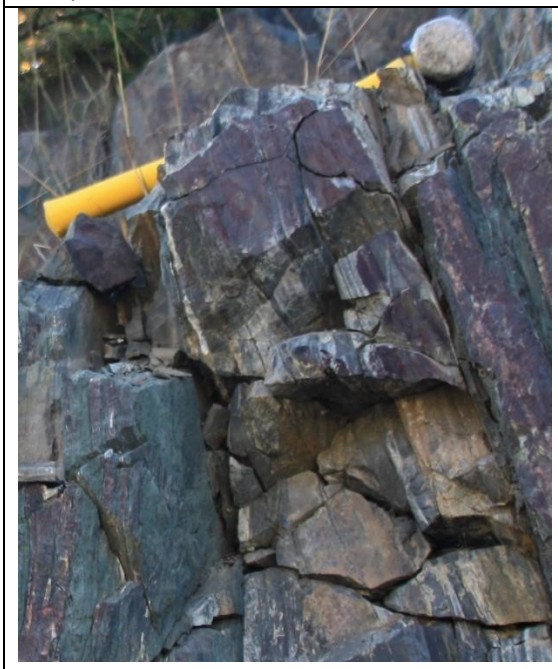 Sample H11-21.9 in situ	 Cut section of H11-21.9b	
Facies represented: white chert, magnetite, black chert		
Description: Sample H11-21.9 was taken from the upper section of the Highway 11 outcrop. Laminated chlorite, magnetite, black and white chert beds 1-3 cm thick comprise this sample. This sample was cut to make H11-21.9b with 3 black chert beds, 3 magnetite beds and 1 white chert bed.		

Sample: H11-22.6	Lat: 47.06845 N	Long: 79.7907 W
 Sample H11-22.6 in situ, green bed on the right	 Cut section of H11-22.6	
Facies represented: chlorite BIF		
Description: Sample H11-22.6 was taken from the upper section of the Highway 11 outcrop. The sample is a single bed of layered chlorite.		
Sample: H11-30.8	Lat: 47.06854 N	Long: 79.7907 W
 Sample H11-30.8 in situ	 Cut section of H11-30.8	
Facies represented: black chert, white chert, chlorite BIF		
Description: Sample H11-30.8 was taken from the upper section of the Highway 11 outcrop. ~1 cm thick beds of black chert, white chert and minor chlorite BIF comprise this sample. Syndepositional folds occur in this sample.		

Sample: H11-31.3	Lat: 47.06856 N	Long: 79.7907 W
	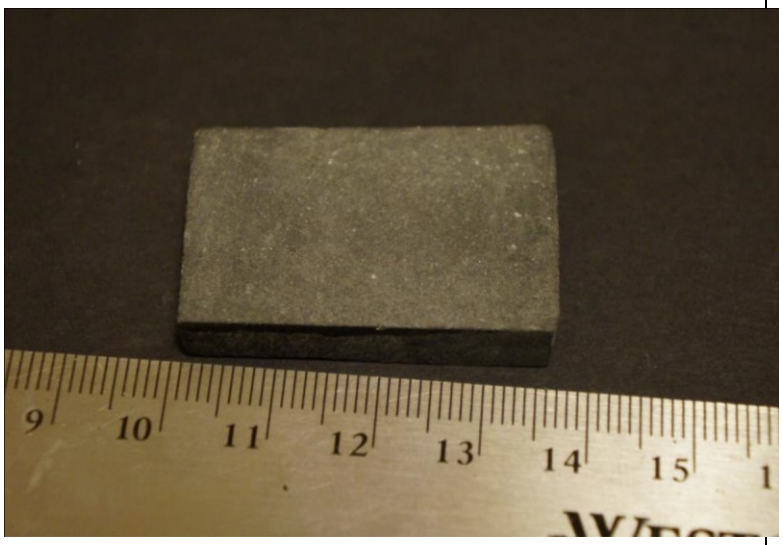	
Sample H11-31.3 in situ	Cut section of H11-31.3	
Facies represented: black chert		
Description: Sample H11-31.3 was taken from the upper section of the Highway 11 outcrop. H11-31.3 is a 13 cm thick black chert bed adjacent to a mafic intrusion.		

Sample: H11-33.3	Lat: 47.06861 N	Long: 79.7907 W
	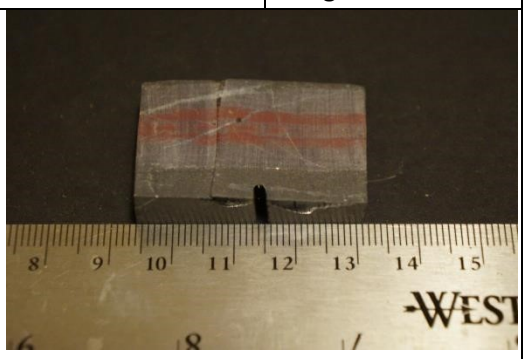	
Sample H11-33.3 in situ	Cut section of H11-33.3	
Facies represented: Jasper, black chert, magnetite		
Description: Sample H11-33.3 was taken from the upper section of the Highway 11 outcrop. ~0.5 cm laminated beds of jasper, black chert and magnetite comprise this sample. Jasper clasts are found in black chert beds adjacent to jasper beds. Jasper beds transition to black chert along strike in this sample.		

Sample: H11-35.6	Lat: 47.06862 N	Long: 79.7907 W
		
Sample H11-35.6 in situ	Cut section of H11-35.6	
Facies represented: magnetite, jasper, white chert		
Description: Sample H11-35.6 was taken from the upper section of the Highway 11 outcrop. White chert beds are 0.1-2 cm thick and magnetite beds are 0.3 to 5 cm thick. Jasper lenses occur at magnetite-white chert boundaries. Quartz veinlets cut bedding in this sample.		

Sample: H11-40.4	Lat: 47.06863 N	Long: 79.7907 W
		
Sample H11-40.4 in situ	Cut section of H11-40.4	
Facies represented: black chert, white chert, chlorite		
Description: Sample H11-40.4 was taken from the upper section of the Highway 11 outcrop. Laminated black chert, white chert and chlorite beds make up this sample.		

Sample: H11-51.1a	Lat: 47.06867 N	Long: 79.7907 W
 Sample H11-51.1 in situ	 Cut section of H11-51.1a	
Facies represented: black chert, magnetite, jasper		
Description: Sample H11-51.1 was taken from the upper section of the Highway 11 outcrop. The sample contains laminated 0.5-2 cm thick beds of black chert, jasper and magnetite. A 2 cm thick black chert bed was cut from H11-51.1 to make analytical sample H11-51.1a. A 3 cm thick magnetite bed was cut from H11-51.1 to make analytical sample H11-51.1b. Thin sections were not made of this sample.		

Sample: H11-57.0a	Lat: 47.06869 N	Long: 79.7907 W
 Sample H11-57.0 in situ	 Cut section of H11-57.0	
Facies represented: magnetite, white chert, black chert		
Description: Sample H11-57.0 was taken from the upper section of the Highway 11 outcrop. The sample contains laminated 0.1-3 cm thick beds of black chert, white chert and magnetite. A 1 cm thick magnetite bed was cut from H11-57.0 to make analytical sample H11-57.0a. A 2.5 cm thick black chert bed was cut from H11-57.0 to make analytical sample H11-57.0b. A No thin sections were made of this sample.		

Sample: H11-59.7a	Lat: 47.06871 N	Long: 79.7907 W
 Sample H11-59.7 in situ	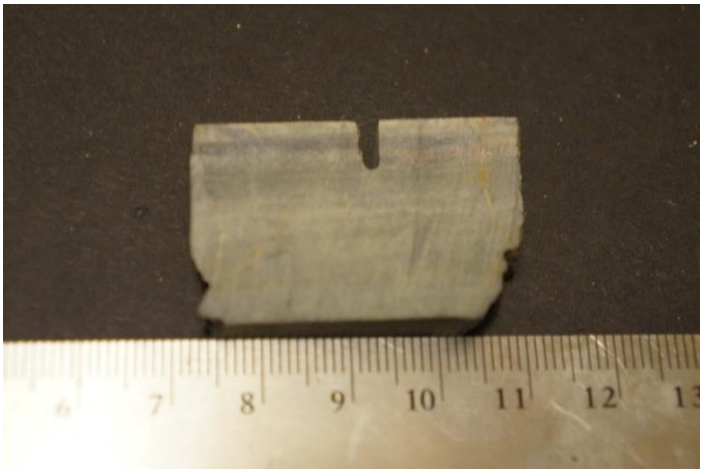 Cut section of H11-59.7a	
Facies represented: white chert		
Description: Sample H11-59.7 was taken from the upper section of the Highway 11 outcrop. The sample contains 4-10 cm thick beds of black chert, white chert and magnetite. Synsedimentary folding and quartz veinlets are prevalent in the sample. A 6 cm thick white chert bed was cut from H11-57.0 to make analytical sample H11-57.0b. No thin sections were made of this sample. When cut, the white chert bed appears to have an internal structure and layering. Dark colored parts of H11-57.0b indicate presence of magnetite and green colored parts of the sample indicate chlorite.		

Sample: H11-59.7b	Lat: 47.06871 N	Long: 79.7907 W
 Sample H11-59.7 in situ	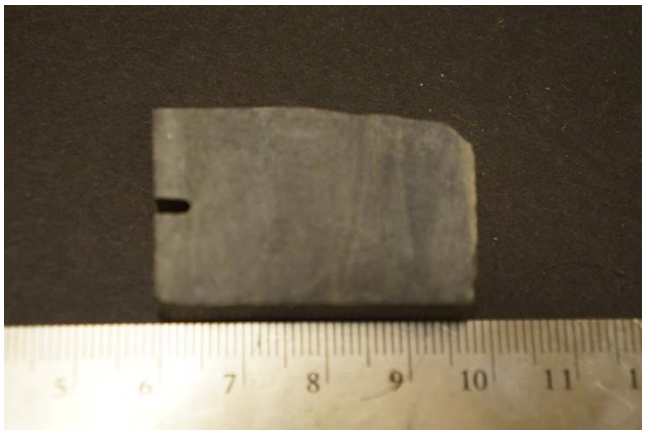 Cut section of H11-59.7b	
Facies represented: black chert		
Description: Description: Sample H11-59.7 was taken from the upper section of the Highway 11 outcrop. The sample contains 4-10 cm thick beds of black chert, white chert and magnetite. Synsedimentary folding and quartz veinlets are prevalent in the sample. A 7 cm thick, folded black chert bed was cut from H11-57.0 to make analytical sample H11-57.0b. No thin sections were made from this sample.		

Sample: H11-65.8	Lat: 47.06874 N	Long: 79.7907 W
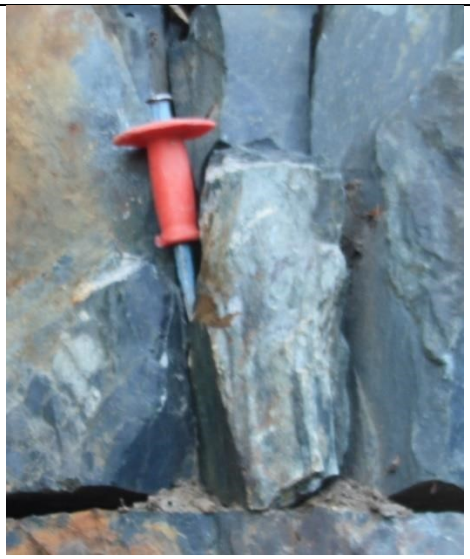 Sample H11-65.8 in situ	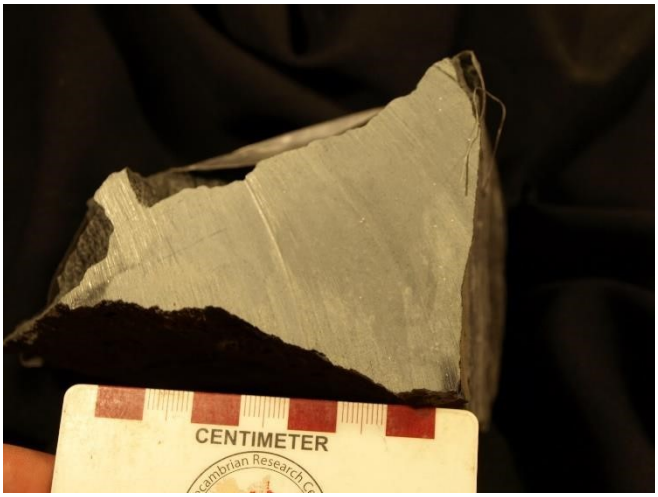 Cut section of H11-65.8	
Facies represented: chlorite		
Description: Sample H11-65.8 was taken from the upper section of the Highway 11 outcrop. The sample is a single 9 cm thick chlorite bed with synsedimentary folds.		

Sample: H11-66.2	Lat: 47.06878 N	Long: 79.7907 W
 Sample H11-66.2 in situ	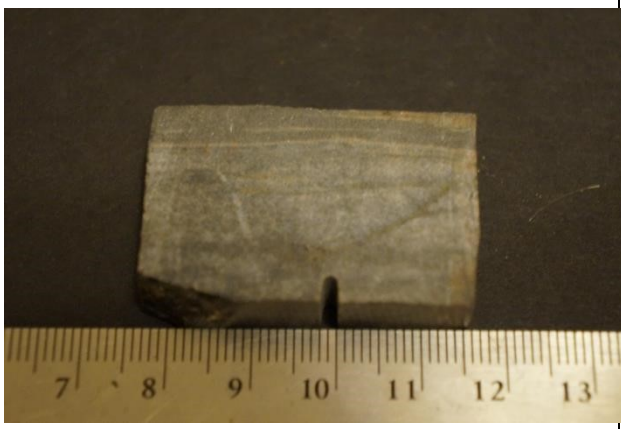 Cut section of H11-66.2	
Facies represented: black chert, magnetite, chlorite		
Description: Sample H11-66.2 was taken from the upper section of the Highway 11 outcrop. The sample contains 2-4 cm thick, laminated beds of black chert, chlorite and magnetite. Quartz veinlets cut bedding in this sample.		

Sample: H11-68.5	Lat: 47.06880 N	Long: 79.7907 W
 Sample H11-68.5 in situ	 Cut section of H11-68.5	
Facies represented: black chert, magnetite, white chert		
Description: Sample H11-68.5 was taken from the upper section of the Highway 11 outcrop. The sample contains 1-3 cm thick, laminated beds of black chert and magnetite. Some chert displays mm-scale layering which is referred to as microbanding in this thesis.		

Sample: H11-70.4	Lat: 47.06881 N	Long: 79.7907 W
 Sample H11-70.4 in situ	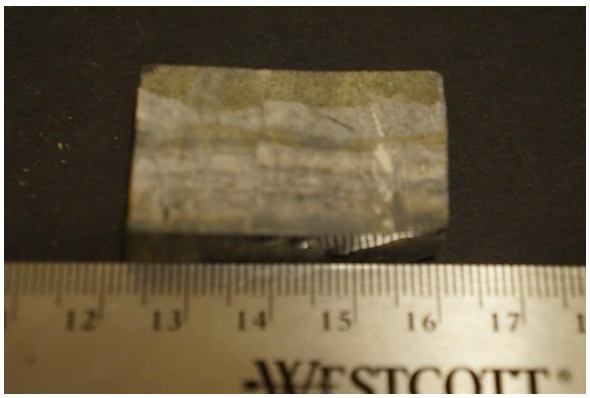 Cut section of H11-70.4	
Facies represented: white chert, chlorite		
Description: Sample H11-70.4 was taken from the upper section of the Highway 11 outcrop. The sample contains 0.5-2 cm thick beds of white chert and chlorite. Brittle faults cut bedding in this sample. White chert is microbanded and contains an internal layering defined by presence of magnetite. Thin sections H11-70.4a and H11-70.4b were cut from this sample.		

Sample: H11-73.3	Lat: 47.06887 N	Long: 79.7907 W
 Sample H11-73.3 in situ	 Cut section of H11-73.3	
Facies represented: black chert		
Description: Sample H11-73.3 was taken from the upper section of the Highway 11 outcrop. This sample comes from the brecciated section of the outcrop just above the sulfide mineralization. Clasts of black chert in a chloritic matrix are found in this sample. Biotite occurs in this sample.		

Sample: H11-110.0	Lat: 47.06890 N	Long: 79.7907 W
		
Sample H11-110.0 in situ	Sample H11-110 in situ	
Facies represented: sulphide		
Description: Sample H11-110.0 is taken from the sulphide mound which divides the Highway 11 outcrop into upper and lower sections. Euhedral grains of pyrite were collected from the mineralized mound. No thin section was made from this sample.		

Sample: H11-119.8	Lat: 47.06896 N	Long: 79.7907 W
	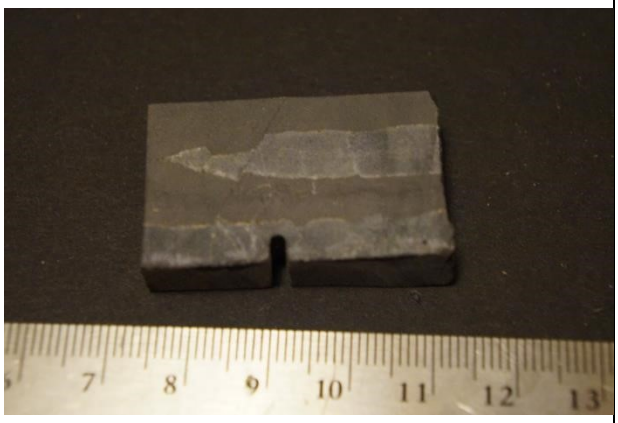	
Sample H11-119.8 in situ	Cut section of H11-119.8	
Facies represented: magnetite, black chert		
Description: Sample H11-73.3 was taken from the lower section of the Highway 11 outcrop. The sample contains 0.5-2 cm thick beds of magnetite and black chert. Syndepositional folds and faults terminate a black chert bed in this sample.		

Sample: H11-124.8	Lat: 47.06898 N	Long: 79.7907 W
 Sample H11-124.8 in situ, to the left of the hammer	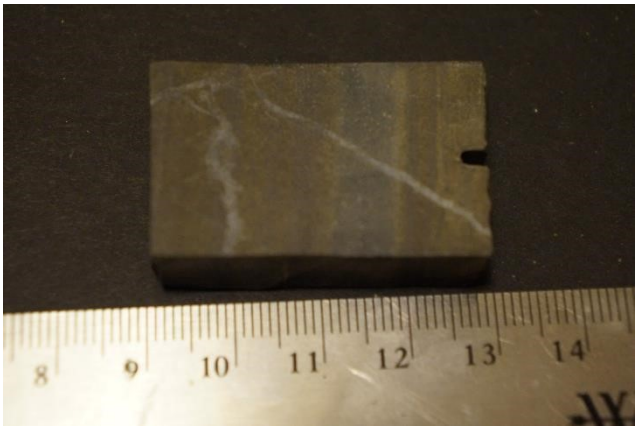 Cut section of H11-124.8	
Facies represented: magnetite, chlorite		
Description: Sample H11-124.8 was taken from the lower section of the Highway 11 outcrop. The sample contains 1-5 cm thick beds of magnetite and chlorite. Syndepositional folds thicken beds and quartz veinlets are pervasive in the sample.		

Sample: H11-125.6	Lat: 47.06899 N	Long: 79.7907 W
 Sample H11-125.6 in situ, to the right of the hammer	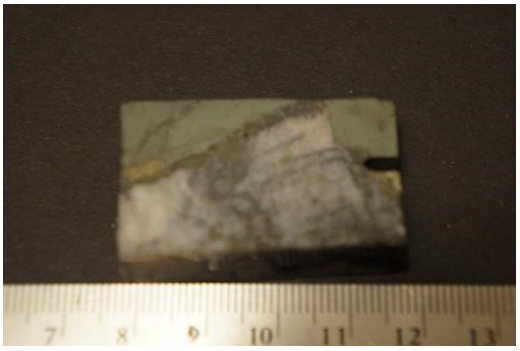 Cut section of H11-127.6	
Facies represented: white chert, chlorite		
Description: Sample H11-125.6 was taken from the lower section of the Highway 11 outcrop. The sample contains 4 cm of a >10 cm thick chlorite bed and a 3 cm white chert bed. H11-125.6a is an analytical sample cut to isolate the white chert bed. H11-125.6b is an analytical sample cut to isolate the chlorite bed. The white chert bed contains ~20 volume % chlorite.		

Sample: H11-133.1	Lat: 47.06908 N	Long: 79.7908 W
 Sample H11-133.1 in situ	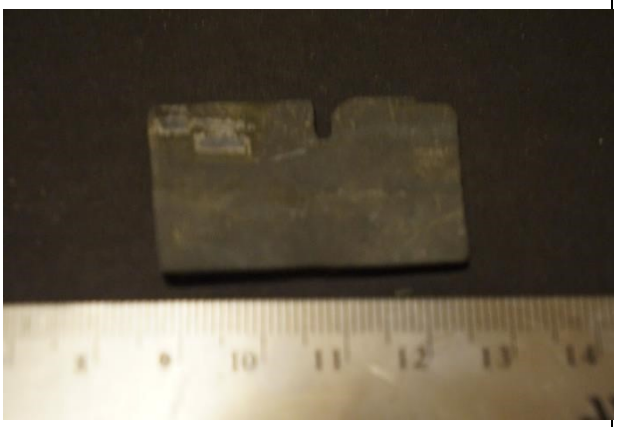 Cut section of H11-133.1	
Facies represented: magnetite, black chert		
Description: Sample H11-133.1 was taken from the lower section of the Highway 11 outcrop. The sample is a 3 cm thick magnetite bed and a 5 cm thick black chert bed. Syndepositional faults cut bedding in this sample.		

Sample: H11-136.3	Lat: 47.06910 N	Long: 79.7908 W
 Sample H11-136.3 in situ	 Cut section of H11-136.3	
Facies represented: magnetite, white chert, jasper		
Description: Sample H11-136.3 was taken from the lower section of the Highway 11 outcrop. The sample contains 1-3 cm thick magnetite, white chert and jasper beds. Minor syndepositional folding deforms the otherwise laminated bedding.		

Sample: H11-139.4	Lat: 47.06915 N	Long: 79.7908 W
 Sample H11-139.4 in situ	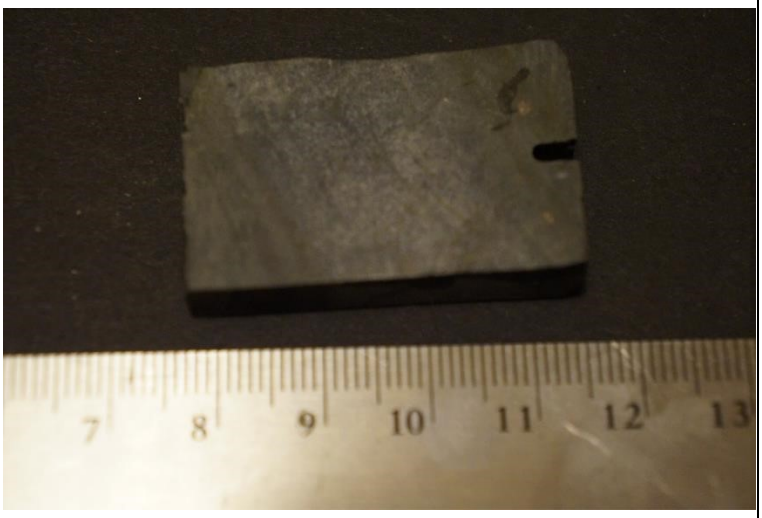 Cut section of H11-139.4	
Facies represented: magnetite, black chert		
Description: Sample H11-139.4 was taken from the lower section of the Highway 11 outcrop. The sample contains 0.5-1.5 cm thick laminated black chert and magnetite beds.		

Sample: H11-145.9	Lat: 47.06917 N	Long: 79.7908 W
 Sample H11-145.9 in situ	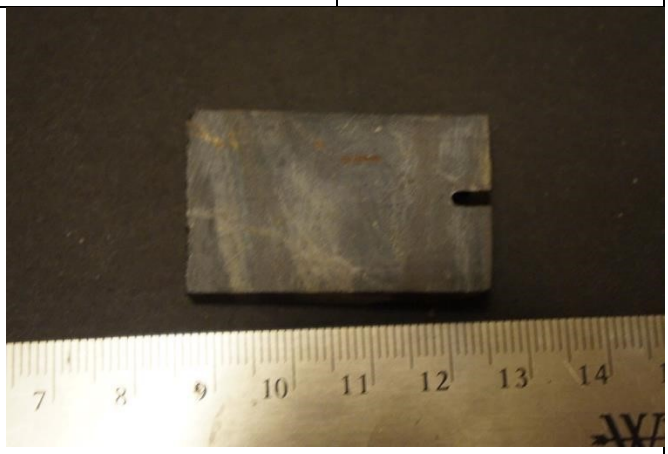 Cut section of H11-145.9	
Facies represented: magnetite, chlorite		
Description: Sample H11-145.9 was taken from the lower section of the Highway 11 outcrop. The sample contains 0.5-1.5 cm thick laminated black chert and magnetite beds.		

Sample: H11-164.2	Lat: 47.06923 N	Long: 79.7908 W
 Sample H11-164.2 in situ	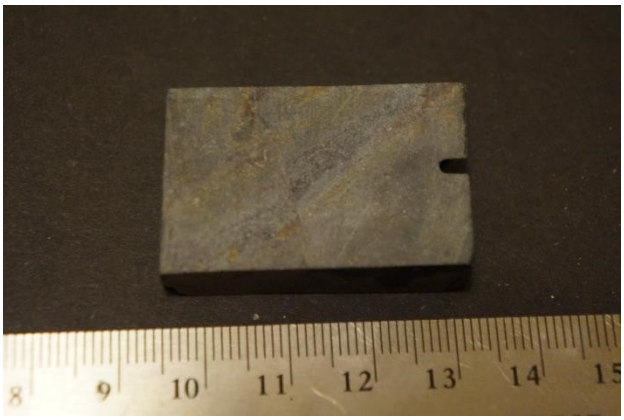 Cut section of H11-164.2	
Facies represented: magnetite, black chert chlorite		
Description: Sample H11-145.9 was taken from the lower section of the Highway 11 outcrop. This sample comes from the brecciated section at the bottom of the Highway 11 outcrop. Clasts of magnetite and black chert in a chloritic matrix are found in this sample. Biotite occurs in this sample.		

Sample: A027	Lat: 47.06346 N	Long: 79.8756 W
 Block A027	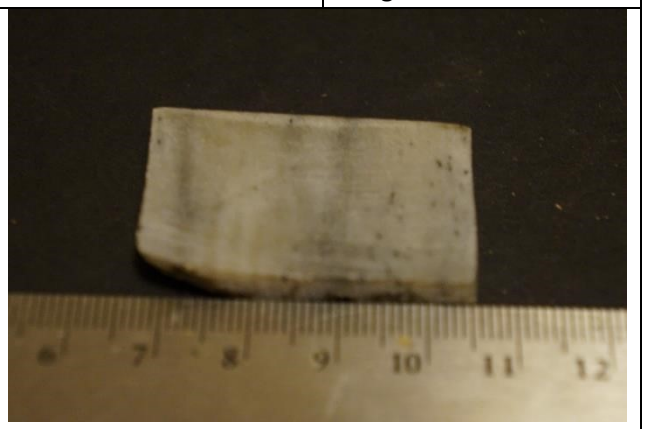 Cut section of A027	
Facies represented: white chert		
Description: Sample A027 was taken from the A-series of blocks, in the southern Sherman Mine. The sample is taken from a >20 cm white chert bed. White chert has minor chlorite.		

Sample: A028	Lat: 47.06345 N	Long: 79.8756 W
 Block A028	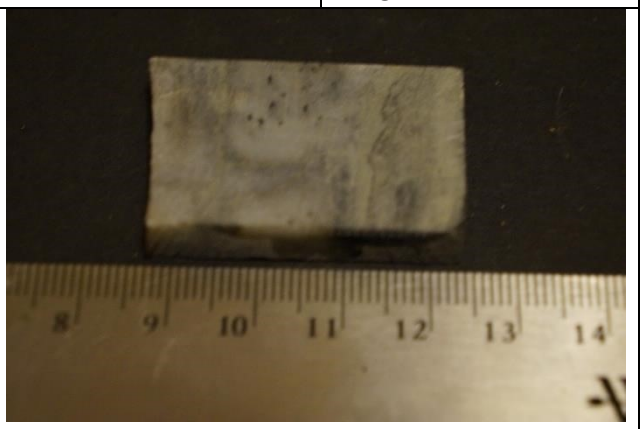 Cut section of A028-2	
Facies represented: black chert		
Description: Sample A028 was taken from the A-series of blocks in the southern Sherman Mine. The sample is taken from a 5 cm black chert bed. Black chert has minor chlorite. Two thin sections were made from sample A028, named A028a and A028b.		

Sample: A030	Lat: 47.06347 N	Long: 79.8758 W
 Block A030	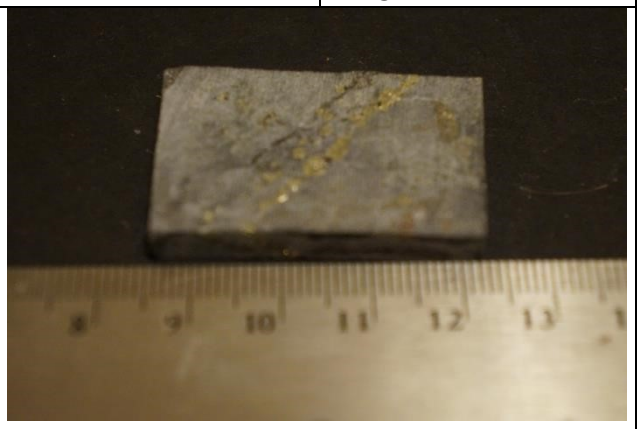 Cut section of A030	
Facies represented: black chert		
Description: Sample A030 was taken from the A-series of blocks in the southern Sherman Mine. The block is a breccia with black chert clasts in a magnetite and chlorite-rich matrix. The sample was taken from a black chert clast with euhedral pyrite.		

Sample: B013a	Lat: 47.06663 N	Long: 79.8758 W
 Block B013	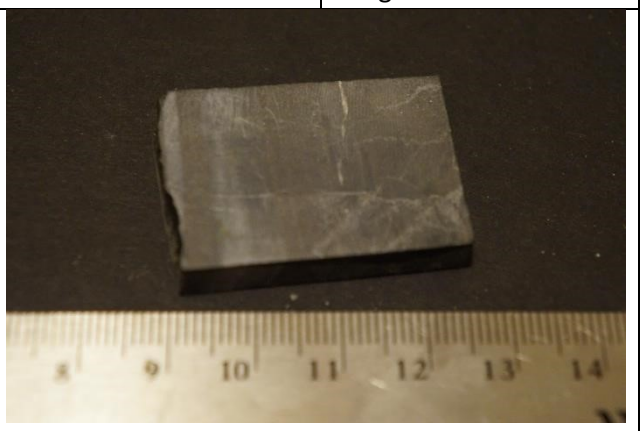 Cut section of B013a	
Facies represented: black chert, magnetite, white chert		
Description: Sample B013a was taken from the B-series of blocks in the southern Sherman Mine. The block is sketched in detail in Figure 6.10. A thin section B013a was cut from the right hand side of the block. From B013a, analytical samples B013-1 (a magnetite bed) and B013-2 (a white chert bed) were made by cutting out individual beds.		
Sample: B013b	Lat: 47.06663 N	Long: 79.8758 W
 Section of block B013 from which B013a and B013b were sampled	 Cut section of B013b	
Facies represented: black chert, magnetite, white chert		
Description: Sample B013b was taken from the B-series of blocks in the southern Sherman Mine. The block is sketched in detail in Figure 6.10. A thin section B013b was cut from the right hand side of the block. From B013b, analytical samples B013-3 (a white chert bed) and B013-4 (a magnetite bed) were made by cutting out individual beds.		

Sample: B013c	Lat: 47.06663 N	Long: 79.8758 W
 Section of block B013 from which B013c was sampled	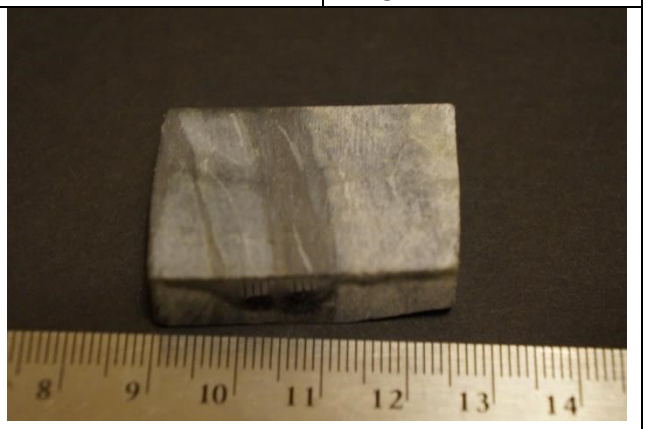 Cut section of B013c	
Facies represented: black chert, magnetite, white chert		
Description: Sample B013b was taken from the B-series of blocks in the southern Sherman Mine. The block is sketched in detail in Figure 6.10. A thin section B013b was cut from the right hand side of the block. From B013c, analytical samples B013-5 (a white chert bed) and B013-6 (a magnetite bed) and B013-7 (a black chert bed) were made by cutting out individual beds.		

Sample: C003	Lat: 47.06999 N	Long: 79.8727 W
 Block C003	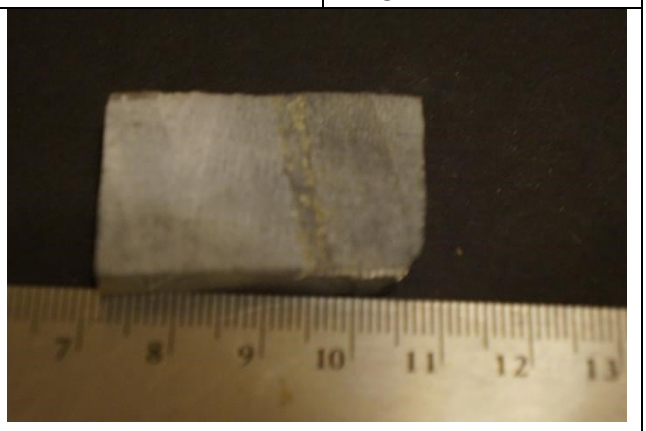 Cut section of C003	
Facies represented: white chert, chlorite		
Description: Sample C003 was taken from the C-series of blocks in the northern Sherman Mine. The sample is a 7 cm thick white chert bed flanked by 1-2 cm of adjacent chlorite beds. Pyrite mineralization occurs within the white chert bed.		

Sample: C012	Lat: 47.06886 N	Long: 79.8749 W
 Block C012	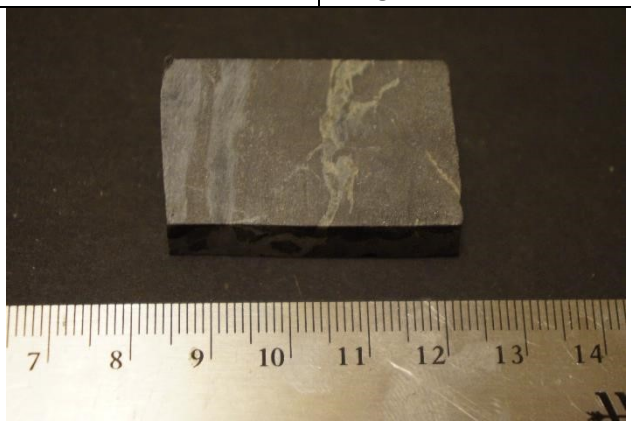 Cut section of C012	
Facies represented: black chert, magnetite		
Description: Sample C012 was taken from the C-series of blocks in the northern Sherman Mine. The sample comprises 5 cm thick magnetite beds and 1-3 cm thick black chert beds. Minor syndepositional faults deform the otherwise laminated bedding.		

Sample: C060	Lat: 47.06999 N	Long: 79.8727 W
 Block C060	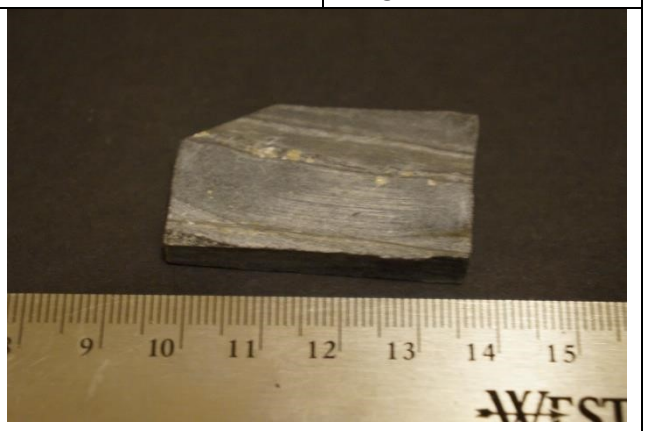 Cut section of C060	
Facies represented: black chert, magnetite		
Description: Sample C060 was taken from the C-series of blocks in the northern Sherman Mine. The sample comprises 2 cm thick magnetite beds and 4-5 cm thick black chert beds. Pyrite mineralization occurs along bedding surfaces.		

Sample: D001	Lat: 47.06405 N	Long: 79.8979 W
 Block D001	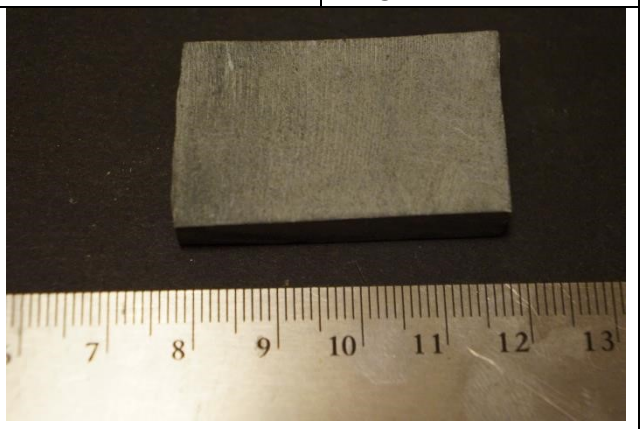 Cut section of D001	
Facies represented: Chlorite		
Description: Sample D001 was taken from the D-series of blocks in the northern Sherman Mine. The sample is a mafic volcaniclastic and is not bedded.		

Sample: D015	Lat: 47.06452 N	Long: 79.8922 W
 Block D015	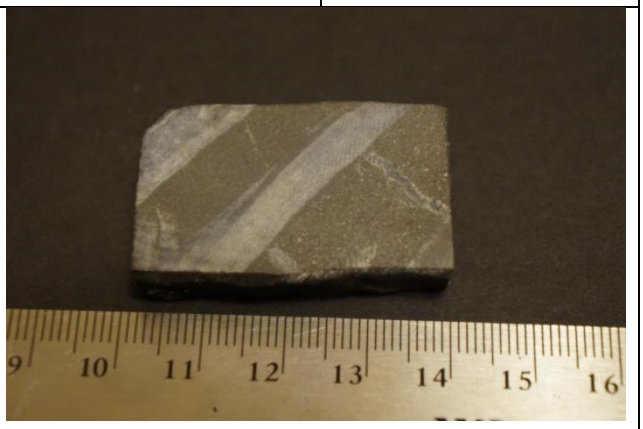 Cut section of D015	
Facies represented: magnetite, white chert		
Description: Sample D015 was taken from the D-series of blocks in the northern Sherman Mine. The sample contains 1, 3 and 5 cm thick magnetite beds and 0.7-1 cm white chert beds. Quartz veins in the magnetite beds do not cross-cut bedding and are confined to magnetite beds.		

Sample: D020	Lat: 47.06513 N	Long: 79.8885 W
 Block D020	 Cut section of D020	
Facies represented: magnetite, black chert		
Description: Sample D020 was taken from the D-series of blocks in the northern Sherman Mine. The sample contains 5-6 cm thick black chert beds and 1-2 cm thick magnetite beds. Quartz veins are ubiquitous and generally are perpendicular to bedding. Analytical samples D020-1 (a 5 cm thick black chert bed) and D020-2 (a 2 cm thick magnetite bed) were cut from sample D020.		

Sample: SM011	Lat: 47.06886 N	Long: 79.8747 W
 Sample SM011	 Cut section of SM011	
Facies represented: jasper, magnetite		
Description: Sample SM011 was found in the C-series of blocks in the northern part of the Sherman mine. The sample contains 0.5-3 cm thick jasper beds and 0.2-2 cm thick magnetite beds. Jasper beds are microbanded with <1 mm magnetite laminae, and magnetite beds include <0.1 mm jasper clasts.		

SM011 is a ‘float’, it was found on the ground in the Sherman Mine, not sampled from a block. The sample was collected to examine the paragenetic relationship between magnetite and jasper at the bed-scale, as well as to make a more complete data set of jasper geochemistry.

SM052	Lat: 47.06999 N	Long: 79.8726 W
 Sample SM052	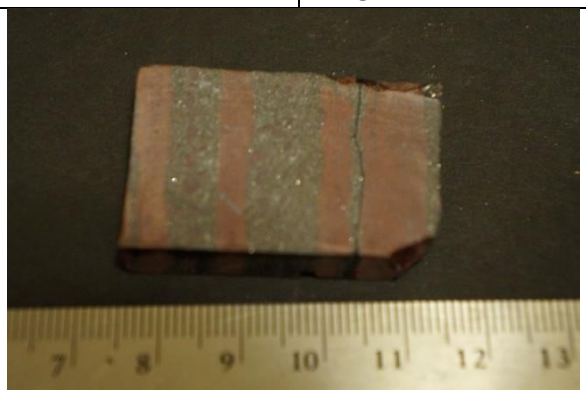 Cut section of SM052	
Facies represented: jasper, magnetite		
Description: Sample SM052 was found in the C-series of blocks in the northern part of the Sherman mine. The sample contains 0.5-2 cm thick jasper beds and 0.2-2 cm thick magnetite beds. Jasper beds are microbanded with <1 mm magnetite laminae, and magnetite beds include <0.1 mm jasper clasts. SM052 is a ‘float’, it was found on the ground in the Sherman Mine, not sampled from a block. The sample was collected to examine the paragenetic relationship between magnetite and jasper at the bed-scale, as well as to make a more complete data set of jasper geochemistry.		

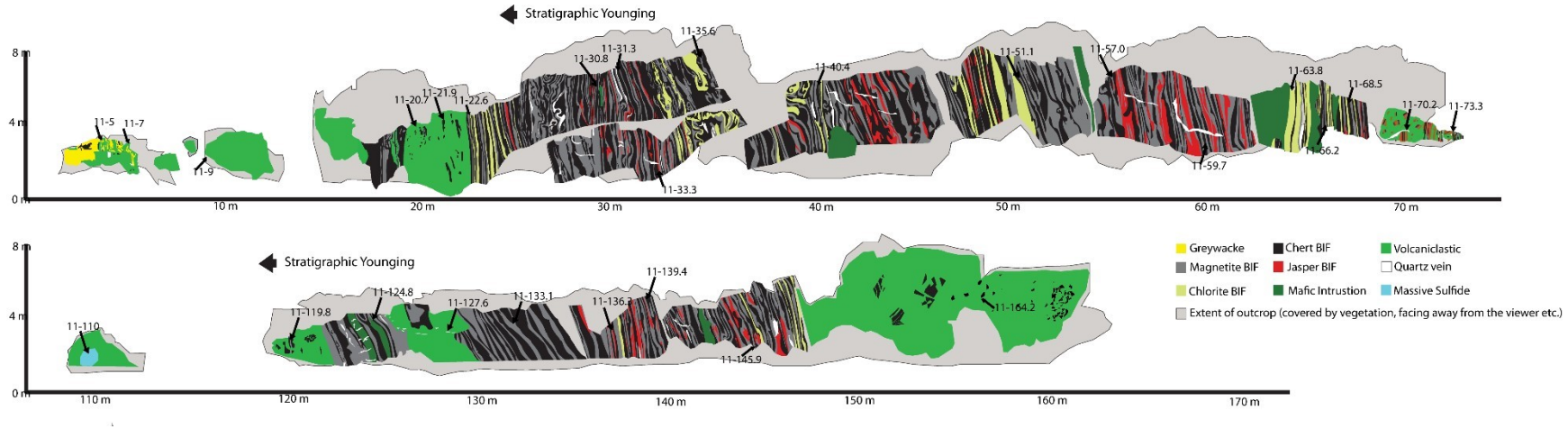

Figure A.1 Sketch of the Highway 11 outcrop, Type section for the Temagami BIF. Sampling locations for H11 samples are indicated. Samples were taken at ~5 m spacing to provide a mineralogical and geochemical profile of the outcrop.

Appendix 2: Thin Section Description

The following is a description of each thin section used in this thesis. Included are the facies from which the thin section was cut, modal mineralogy determined by point counting, and a photoscan of each thin section. Minerals are abbreviated: mgt (magnetite), hmt (hematite), qtz (quartz), chl (chlorite), carb (carbonate), apt (apatite), lcx (leucoxene), bt (biotite), ser (sericite) and ilm (ilmenite).

Sample	Facies																
		Mgt 1	Mgt 2	Mgt 3	Hmt 1	Hmt 2	Coarse qtz	Fine qtz	Chl	Sulphide	Carb	Apt	Lcx	Bt	Ser	Ilm	Photo
H11-5	Chlorite			10			5	15	40						20	10	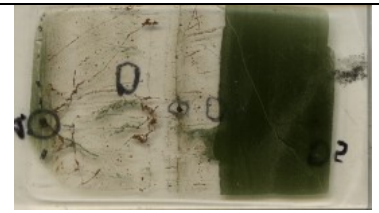
H11-7a	Chlorite																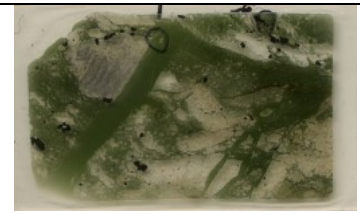
H11-7b	Chlorite			10				10	50	5		10	5			10	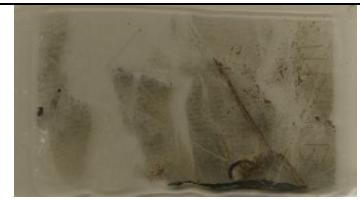

		Mgt 1	Mgt 2	Mgt 3	Hmt 1	Hmt 2	Coarse qtz	Fine qtz	Chl	Sulphide	Carb	Apt	Lcx	Bt	Ser	Ilm	Photo
H11-9a	Chlorite, black chert	20	10					20	35						10	5	
H11-9b	Chlorite, white chert		10				20	20	40	5					5		
H11-20.7	Chlorite			20				20	40						20	10	
H11-21.9a	black chert, white chert		10	20					30	5					15	10	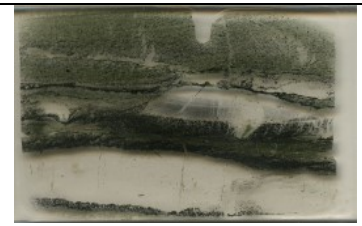
H11-21.9b	black chert, magnetite, white chert	10	10	50			10	5			5	5		5			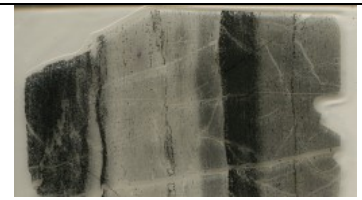

		Mgt 1	Mgt 2	Mgt 3	Hmt 1	Hmt 2	Coarse qtz	Fine qtz	Chl	Sulphide	Carb	Apt	Lcx	Bt	Ser	Ilm	Photo
H11-22.6	Chlorite		10	10			10		60	10							
H11-30.8	white chert, magnetite, black chert		10	20			50			10	10						
H11-31.3	black chert, magnetite, white chert	20	10	15			15	20	10		5	5					
H11-33.3	magnetite, white chert, jasper	5		70	10	5		10									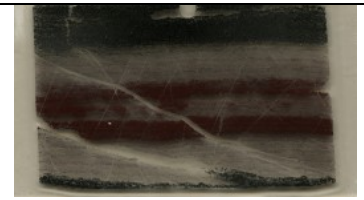
H11-35.6	magnetite, white chert, jasper		10	50	20		10	10									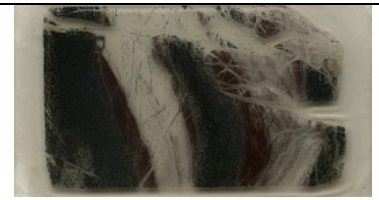

		Mgt 1	Mgt 2	Mgt 3	Hmt 1	Hmt 2	Coarse qtz	Fine qtz	Chl	Sulphide	Carb	Apt	Lcx	Bt	Ser	Ilm	Photo
H11-65.8	white chert		5	10			80				5						
H11-66.2	chlorite		20				15		50		10	5					
H11-68.5	white chert, magnetite			30			40		10		10	5	5				
H11-70.4a	black chert, magnetite, white chert	20		20			20	20	5		5		5	5			
H11-70.4b	white chert, black chert	20	10	20			10	20		5	5		5	5			
H11-73.3	white chert, magnetite		20	20			40				5			15			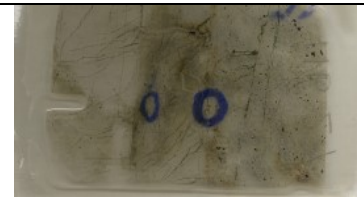

		Mgt 1	Mgt 2	Mgt 3	Hmt 1	Hmt 2	Coarse qtz	Fine qtz	Chl	Sulphide	Carb	Apt	Lcx	Bt	Ser	Ilm	Photo
H11-119.8	magnetite, white chert, black chert	10	10	30			20	10	5		5	5	5				
H11-124.8	magnetite, white chert, black chert	10	10	30			20	10	5		5	5	5				
H11-125.6a	chlorite, white chert		10				40		30		10						
H11-128.1	magnetite, black chert	20	5	30		5		20	10			5	5				
H11-130.2	chlorite, white chert, black chert	10		5		5	30	10	30		5	5					

		Mgt 1	Mgt 2	Mgt 3	Hmt 1	Hmt 2	Coarse qtz	Fine qtz	Chl	Sulphide	Carb	Apt	Lcx	Bt	Ser	Ilm	Photo
H11-133.1	magnetite, black chert	20		40				20	5		5	5	5				
H11-136.3	magnetite, white chert, jasper	10	5	30	10		15	10	10			5	5				
H11-139.4	magnetite, white chert		10	30			30		5		5	5	5				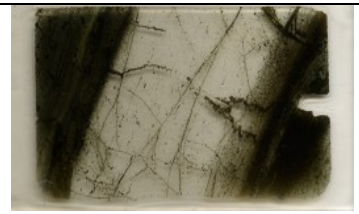
H11-145.9a	white chert, black chert, magnetite	10	10	30			30	10			5	5					
H11-145.9b	white chert, black chert, magnetite	10	10	30			30	10			5	5					

		Mgt 1	Mgt 2	Mgt 3	Hmt 1	Hmt 2	Coarse qtz	Fine qtz	Chl	Sulphide	Carb	Apt	Lcx	Bt	Ser	Ilm	Photo
H11-164.2	Chlorite, black chert	20	10			5		20	20	5	5	5	5	5			
A027	white chert				10		80		5		5						
A028a	chlorite, white chert		15				70		10	5							
A028b	chlorite, white chert		15				70		10	5							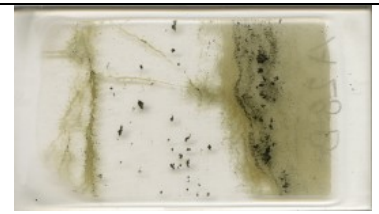
A030	white chert, magnetite			30			70				5	5					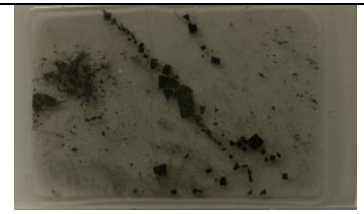

		Mgt 1	Mgt 2	Mgt 3	Hmt 1	Hmt 2	Coarse qtz	Fine qtz	Chl	Sulphide	Carb	Apt	Lcx	Bt	Ser	Ilm	Photo
B013a	black chert, magnetite, white chert	10	10	20			25	10		15	10						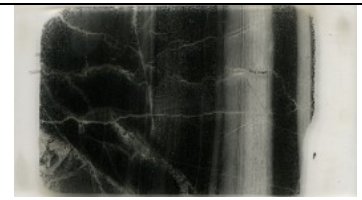
B013b	white chert	10					50	10			20	5		5			
B013c	chlorite		10	20			20		30		5	5	5	5			
C003	chlorite, white chert						30		20								
C012	magnetite, white chert, black chert	10	10	20		5	20	10			5	5	5				

		Mgt 1	Mgt 2	Mgt 3	Hmt 1	Hmt 2	Coarse qtz	Fine qtz	Chl	Sulphide	Carb	Apt	Lcx	Bt	Ser	Ilm	Photo
C060	black chert, jasper, white chert	20			10		30	30			5			5			
D001	magnetite, chlorite, black chert white chert	10	15	30			10	10	10		2	2				10	
D015	black chert, magnetite, white chert	20	10	10			30	20			3	3	3				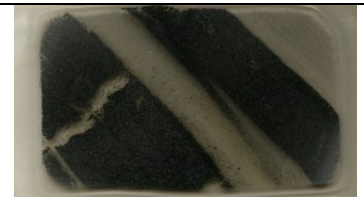
D020	white chert, magnetite	10	10	30		5	20	10			5	5	5				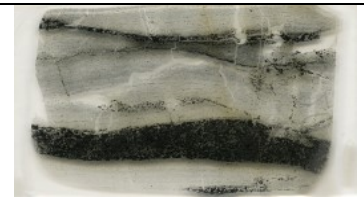
SM11	black chert, magnetite, white chert, jasper	10	10	20	10	5		20	5		5	5	5	5			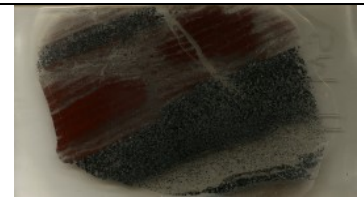

		Mgt 1	Mgt 2	Mgt 3	Hmt 1	Hmt 2	Coarse qtz	Fine qtz	Chl	Sulphide	Carb	Apt	Lcx	Bt	Ser	Ilm	Photo
SM052	black chert, magnetite, white chert, jasper	10	10	10	15	5	10	25			5	5	5				

Appendix 3: Sherman Mine Block Description

Block	UTM_X (m)	UTM_Y(m)	W (m)	H(m)	D(m)	Bedding (m)	%Ch	Beds (cm)	%Mt	Habit	Cracks	Layering (cm)	%Chl	Habit	Mag	Sulfides	Layering (cm)	%Jas	Transitions	Microbanded	Layyering (cm)	Ductile	Brittle
A001	585501	5212785.1	2	1.1	1.4	1.35	50	1,3	35	massive	no	1,3	12	layered	weakly	none	10	3	to black chert	no	1,3		
A002	585501	5212786.3	1.7	0.9	1.2	1.5	40	3,5	40	massive	no	1,3	20	layered	no	none	1,3				3,5		
A003	585501	5212789.7	1.8	1.3	1.5	1	39.5		45	massive	no		15	layered	no	finely disseminated sulfides	5	0.5	to black chert	no	1,3		
A004	585494	5212790	1.7	1.1	1.3	1.35	65	0.2, 4	35	massive	no										0.2, 4		
A005	585493	5212792.2	2.2	1.6	1.1	1.45	65		30	massive	no	0.1,1						5	to black chert	no	1,3	folding	
A006	585488	5212793.5	2.1	0.8	0.9	0.8	80		20	massive	no												breccia
A007	585485	5212797.1	1.7	0.9	1.1	1.45	50	1,3	35	massive	no	1,3	15	intruded	no	none	5				1,3		
A008	585481	5212799.5	1.5	1.7	1.7	1.45	45	7,10	45	euhedral	no	0.5,1						10	to black chert	yes	7,10		
A009	585478	5212798.1	1.7	1.3	1.3	1.25	55		44	euhedral	no	0.5,1	1	layered	no	none	3						boudinage (ductile?)
A010	585473	5212799.7	1	1.3	0.7	0.45	60	1,2	15	massive	no	0.5,1						15	to black chert	yes	1,2		
A011	585473	5212799.1	1.9	0.7	0.8	0.8	75	0.5,1	25	massive	no	0.5,1											brittle offset
A012	585467	5212797.3	1.6	1.2	1.3	1.35	95	1,3					5	intruded	weakly	large/secondary sulfides	3				1,3	undulation	
A013	585464	5212804.3	2.6	1.1	1.4	1	70	1,4	30	massive	no	1,2											
A014	585464	5212809	2.3	2.2	1.1	1.1	80	1,3	20	massive	no	0.2,1											
A015	585457	5212806.8	1.8	1.3	1.2	1.5	50	2,4	50	euhedral	no	1,4											brittle offset
A016	585454	5212809.3	1.7	1.2	2.2	1.6	50	1,3.5	30	massive	no	0.5,2	20	intruded	no	large/secondary sulfides	15					folding	
A017	585449	5212811.7	1.7	1	1.9	1.7	70	1,3	30	euhedral	no	0.1,1											
A018	585445	5212812.3	1.6	1.6	1.4	1.6	70	1,3	30	euhedral	no	0.5,2											brittle offset
A019	585438	5212814.3	1.1	1.1	1.2	1.15	23	0.5,2	50	massive	no	0.5,2	1	layered	no	none	0.5,2	25	to black chert	yes	0.5,2		
A020	585438	5212814.2	0.7	1.3	1.5	1.55	30	1,3	70	euhedral	no	0.5,2										folding	brittle offset
A021	585439	5212813.6	1.7	1.3	1.9	1.8	40	1,3	40	euhedral	no	0.2,1						20	to black chert	no	1,3		brittle offset
A022	585435	5212814.2	1.9	1.4	1.1	1.2	70	1,2	30	massive and euhedral	no	0.5,1.5										folding	
A023	585430	5212813.7	1.4	1.2	1.4	1.3	50	1,3	25	euhedral	no	0.7,2	25	layered	no	finely disseminated sulfides	5						

A024	585430	5212813.5	1.2	0.8	1.1	1.2	95	2,5	4	massive	no	0.5,2	1	lenses	weakly	none						bed pinching	
A025	585429	5212814	2.1	1.4	1.3	2.1	50	1,3	30	massive	no	0.1,0.7	20	layered	weakly	none	0.1,0.7						
A026	585384	5212830.1	2	2.9	2.4	2.2	50	1,3	30	massive	no	0.5,1.5						20	none	yes	0.1,0.5		
A027	585382	5212830.1	2.6	2.3	2	2.3	50	0.5,3	35	massive	no	0.1,0.7	15	intruded	weakly	large/secondary sulfides	4						
A028	585382	5212828.3	2.5	2.8	2.3	2.6	80	1,3	15	massive	no	0.2,1	5	layered	no	large/secondary sulfides	4						
A029	585376	5212826.5	1.8	1.8	2.7	1.9	60	0.5,1	40	massive	no	0.3,1											
A030	585364	5212830.5	1.7	2.2	2.7	2	89		1	massive	no		10	lenses	weakly	none							breccia
B001	585359	5213165.7	1.4	0.8	1.6	1.42	70	0.7,3	30	massive	no	0.3,1											
B002	585360	5213166.4	2.3	1.7	2	1.7	60	1,2	40	massive	no	0.3,1											
B003	585361	5213168.3	1.6	1.7	1.7	0.9	70	2,3	30	massive	no	0.3,1											
B004	585360	5213167.7	1.3	1.2	1.5	1.9	70	1,3	30	massive	yes	0.5,2											boudinage (ductile?)
B005	585361	5213171.2	1.9	1.3	1.9	1.3	50	2,4	50	massive	no	0.3,1											
B006	585362	5213170.7	1.3	1.5	2.1	2.1	60	2,5	40	massive	no	0.3,1											
B007	585363	5213173.6	1	1	1.4	1	65	1,4	30	massive	no	0.1,2	5	lenses	no	none						folding	
B008	585362	5213174.2	1.1	0.8	2.5	1.9	40	2,3	60	massive	no	0.5,1											
B009	585363	5213174.8	1.3	1	1	1.1	60	0.2,3	40	massive and euhedral	no	0.1,1											
B010	585363	5213177.3	2.3	1.9	2.3	1.4	60	0.5,3	40	massive	no	0.1,1.5											
B011	585363	5213177.1	3.3	1.5	2.1	1.5	60	2,4	40	massive	no	0.5,1											
B012	585362	5213179.4	2.9	2.2	1.5	1.9	60	0.3,2	40	euhedral	no	0.1,1											
B013	585363	5213181.6	2.3	1.4	3	2.5	55	0.5,4	35	euhedral	no	0.5,2						10	to black chert	yes	0.5,4	folding	
B014	585361	5213188.3	2.1	0.8	1.7	0.8	60	0.5,1.5	40	euhedral	no	0.5,1.5											
B015	585363	5213187.1	1.8	1.5	1.6	1.9	50	1,4	40	massive with jasper	yes	0.2,1						10	to black chert	no	1,4		boudinage (ductile?)
B016	585362	5213189.9	1.5	1.8	1.6	1.8	35	0.5,4	30	euhedral	no	0.2,1	20	layered	no	large/secondary sulfides	4,5	10	to magnetite	no	0.5,4	folding	breccia
B017	585362	5213193.6	2.2	1.1	1.5	1.4	60	0.3,3	25	massive	no	0.1,0.9	15	layered	no	large/secondary sulfides	5					folding	
B018	585363	5213194.9	1.5	1.4	2.1	1.4	60	0.5,1	35	massive and euhedral	no	0.5,1						5	to black chert	no	0.5,1	undulation	
B019	585364	5213196.5	1	1.1	1.3	1.1	80	2,4	20	massive	yes	0.5,1										bed thickening	brittle offset
B020	585364	5213197.5	2.3	1.6	1.3	1.5	100	2,5														folding	
B021	585363	5213199.9	1.9	1.7	1.6	1.7	80	0.2,4	20	massive	no	0.2,4										undulation	
B022	585365	5213202.3	3.8	1.4	1.8	2.7	100	0.5,20														undulation	

B023	585366	5213204.1	1.9	1.7	1.2	1.9	80	0.2,2	20	massive	no	0.2,1												brittle offset
B025	585366	5213205.4	1.6	1	1.6	1.6	20	0.1,0.5	60	euhedral with jasper	yes	0.1,0.3						20	none	yes	0.1,0.5			brittle offset
B026	585369	5213208.7	2.4	1.5	2.2	1.8							100	0	weakly	finely disseminated sulfides								
B027	585369	5213210.9	2.3	1.7	2	1.8	39	1,3	61	euhedral	yes	0.5,2												
B028	585370	5213210.2	2.4	1.1	1.5	1.6	36	0.5,3	55	massive	no	0.2,1	2	lenses	weakly	large/secondary sulfides	2	8	to black chert	yes	0.5,3	bed thickening		
B029	585370	5213213.1	1.5	1.8	1.3	1.5	60	0.2,2	30	euhedral with jasper	no	0.2,2						10	to black chert	yes	0.2,2			
B030	585373	5213216.5	2.2	1.6	1.7	1.6	100	0.5,11																
B031	585373	5213212.7	1.8	1.6	1.6	1.7	100	0.5,15																
B032	585377	5213215.3	3.3	2	2.8	3	70	0.5,4	30	massive	yes	0.5,1										undulation		
B033	585380	5213216.9	1.7	1.7	1.6	1.7	70		30	massive	yes													breccia
B034	585382	5213222.2	3.1	2.1	2.4	2.2	100	0.5,10														undulation		
B035	585384	5213221.7	3.3	2.2	3.1	2.3	60	0.1,3	35	euhedral with jasper	no	0.1,1						5	to black chert	no	0.1,3			
C001	585398	5213390.6	2.1	1.6	1.6	1.6	68	0.5,2	30	massive and euhedral	no	0.5,1						2	to black chert	yes	0.5,2	bed thickening		autobreccia
C002	585402	5213387.2	1.3	1.6	3.4	1.2	80	0.5,1	20	massive	yes	0.2,7												
C003	585406	5213386.9	1.6	1.4	1.5	1.5	43	1,3	55	massive with jasper	yes	0.5,1						2	to black chert	no	1,3	undulation		
C004	585409	5213395	2.6	1.8	2.1	1.5	55	0.5,3	40	massive	no	0.5,1						5	none	yes	0.5,3	faulting		
C005	585408	5213400	1.6	1.3	2.1	2.1	60	1,2	30	massive	no	0.5,2	5	layered	strongly	large/secondary sulfides	2	5	to black chert	yes	1,2			autobreccia
C006	585412	5213408.8	1.6	1.5	2.8	1.5	70	0.2,2	30	massive	no	0.2,1												
C007	585412	5213410	2.1	1.8	1.4	1.6	80		20	euhedral	no													breccia
C008	585414	5213412.4	2.1	1.2	1.6	1.2	55	1,2	20	massive	yes	0.5,2	15	layered	weakly	none	1,10							
C009	585421	5213424.1	2.6	1.7	1.6	2.6	70	1,3	25	euhedral with jasper	no	0.5,2						5	to black chert	yes	1,3	folding		
C010	585426	5213426.9	2	1.6	1.9	2.1	60	1,2	40	euhedral	no	0.2,1										undulation		autobreccia
C011	585426	5213429	1.2	0.9	1.5	1.2	34	1,3	40	massive with jasper	yes	0.5,1	15	lenses	no	large/secondary sulfides	2,7	1	to black chert	no		undulation		
C012	585427	5213430.8	1.1	1	1.7	1	50	1,2	35	massive	no	0.2,0.8	15	layered	weakly	none	1,18							
C013	585429	5213432.5	1.7	1.6	2	1.6	20	1,2	50	massive	yes	0.2,1						30	none	yes	1,2			autobreccia

C014	585429	5213432.5	1.5	1.6	1.9	1.6	59	1,3	40	massive	no	0.2,1						1	to black chert	no	1,3		
C015	585431	5213432.6	2.3	1.5	1.3	1.2	55	0.5,3	44	massive and euhedral	yes	0.5,1	1	lenses	weakly	none	3						
C016	585434	5213433.8	2.5	2	2.9	1.9	50	1,3	30	euhedral with jasper	no	0.2,1						10	to black chert	yes	1,3		
C017	585437	5213434.1	1.9	1.6	1.7	1.6	60	0.5,2	30	euhedral with jasper	no	0.2,1						10	to black chert	yes	0.5,2	folding	brittle offset
C018	585439	5213438.5	2.3	1.7	1.5	1.5	75	0.5,4	25		no	0.2,2											
C019	585441	5213440.4	2	1.7	1.6	1.7	80	0.5,3	25	massive and euhedral	yes	0.5,1						5	to magnetite	no	0.5,2		
C020	585446	5213443.4	2.6	1.3	1.4	2.6	70	0.5,5	30	massive and euhedral	no	0.2,1.2										folding	autobreccia
C021	585453	5213449.1	1.6	1.2	1.3	2.6	15	0.5,3	65	massive	yes	0.5,1	10	layered	no	large/secondary sulfides	2,7	10	to black chert	no	0.5,2		
C022	585454	5213448.3	2.4	1.5	1.3	1.3	70	0.2,2	30	massive and euhedral	no	0.2,1										bed pinching	
C023	585456	5213452.7	2.3	1.8	1.2	1.2	65	1,3	30	massive and euhedral	no	0.2,1.3						5	to black chert	no	2	bed thickening	
C024	585459	5213455.7	1.9	1.8	1.7	1.8	60	1,3	40	massive	no	1,1.5										folding	
C025	585465	5213458.8	2.1	1.3	1.4	1.4	60	3,15	10	massive	yes	1,3										bed thickening	
C026	585467	5213462.4	2.4	1	1.3	2.4	85	1,3	15	euhedral	no	0.5,1											breccia
C027	585469	5213464.2	1.6	1.6	2.2	1.6	60	0.5,4	40	euhedral	no	0.5,1											breccia
C028	585472	5213465.9	1.3	1.2	1.6	1.6	60	0.5,1	30	euhedral	no	0.2,0.7	8	layered	weakly	finely disseminated sulfides	2,4	2	to black chert		0.5,1		
C029	585473	5213469	1.3	1.4	1.8	1.8	59.5	0.5,3	35			0.2,1	5	layered	no	large/secondary sulfides	2,4	0.5	to black chert	no	0.5,3		
C030	585478	5213469.6	2.6	1.8	2.3	1.3	50	0.5,2	35			0.5,2	10	lenses	weakly	large/secondary sulfides	3	5	to black chert	no	0.5,2		
C031	585483	5213471.5	2	1.6	1.7	2	65	0.5,3	35	euhedral	no	0.5,2										undulation	
C032	585485	5213471.9	1.6	1.4	1.2	1.4	50	0.5,3	20	euhedral	no	0.5,2	25	layered	no	large/secondary sulfides	2,5	5	to black chert	yes	0.5,3		
C033	585487	5213475	2.1	1.5	1.5	1.6	54	1,3	45	euhedral	no	1,2						1	to black chert	no	0.7,1		
C034	585493	5213479.2	2.2	1.6	2	1.3	30	0.5,4	50	euhedral	yes	0.5,2	15	layered	no	finely disseminated sulfides	1,3	5	to magnetite	yes	2,4		
C035	585497	5213480.8	2.7	0.9	1.7	1.1	40	0.5,2					60	layered	weakly	finely disseminated sulfides	2,15					undulation	

C036	585496	5213484.8	1.7	1.3	1.5	1.7	30	0.5,4	15			0.3,1	40	layered	weakly	finely disseminated sulfides	1,20	15	to black chert	yes	0.5,4	undulation	
C037	585500	5213488.1	3.2	1.6	1.3	3	50	1,2	35			0.2,1	10	layered	weakly	finely disseminated sulfides	2,4	5	to black chert	no	1,2	undulation	
C038	585502	5213492.7	2.6	1.6	2.1	1.5	65	0.5,5	35	massive and euhedral	no	0.2,1											brittle offset
C039	585507	5213500.5	2.2	1.3	1.4	2.2	35	1,4	50									15	to black chert	yes	1,4	folding	autobreccia
C040	585512	5213505.9	2.9	1.6	1.6	1.6	70	1,3	30	euhedral	no	0.3,1											
C041	585515	5213511.7	1.5	2.2	1.1	1.2	70	2,9	30			0.5,1											
C042	585519	5213513.4	1.3	1.4	1.4	1.5	80	0.5,4	20			0.5,1										folding	breccia
C043	585521	5213513.8	1.2	1.2	2	1.2	60	1,5	40			0.5,1										folding	autobreccia
C044	585524	5213516	1.7	1.4	2.3	1.6	95	1,10	5			1											boudinage (ductile?)
C045	585526	5213518	1.7	1.7	1.4	1.1	50	1,2	35	massive and euhedral	no	0.1,1						15	to black chert	yes	1,2		
C046	585531	5213519.4	2.3	1.8	1.6	1.4	70	1,10	30	euhedral	no	0.2,3										bed thickening	
C047	585533	5213519.7	2.8	1.7	1.8	1.5	70	2,12	30			2,5										bed thickening	
C048	585535	5213522.5	2.2	1.5	2.4	1.6	80	2,20	20			0.2,1										bed thickening	
C049	585539	5213524.8	2.1	1.3	1.8	2.1	75	2,4	25	massive and euhedral	no	0.2,2											
C050	585543	5213526.7	2.2	1.3	1.3	1.5	60	0.5,2	40	euhedral	no	0.5,1											breccia
C051	585550	5213528.2	2.8	1.4	2.1	2.1	75	0.1,3	25	euhedral	no	0.2,1										undulation	
C052	585553	5213531.5	2.8	2	2	2.6	60	1,2	40	euhedral	no	0.1,1											
C053	585553	5213531	2	1.8	2.5	2.5	75	2,6	25	euhedral	no	0.5,1										undulation	
C054	585557	5213532.4	2.6	1.3	1.3	1.3	75	1,3	25	massive and euhedral	no	0.2,1											
C055	585558	5213532.9	1.7	1.8	2	1.7	50	0.1,2	20	massive and euhedral	no	0.1,1						30	to black chert	yes	0.1,1		
C056	585568	5213541	2.5	1.3	2.9	1.6	50	0.2,2	40	euhedral	no	0.2,2						10	to black chert	no	0.2,2	undulation	
C057	585579	5213547.6	2.1	1.5	1.4	1.6	50	0.2,3	30	euhedral	no	0.2,2						20	to black chert	yes	0.2,3	bed pinching	
C058	585585	5213551.6	1.7	1.5	1.8	1.7	70	0.2,3	30	euhedral	no	0.2,3										folding	
C059	585586	5213552.6	2.3	1.1	2.3	2.3	70	0.2,2	30	euhedral	no	0.2,2										undulation	autobreccia
C060	585590	5213558.1	3.2	2.7	2.4	3.2	75	1,5	25	euhedral	no	0.2,1											

C061	585592	5213558.7	2.8	1.5	2.8	2.9	58	0.1,4	40	euhedral	no	0.2,1						2	to black chert	no	0.1,2	undulation	
C062	585598	5213563	3.1	1.8	2.3	2.2	70	0.5,2	28	euhedral	no	0.5,2						2	to black chert	no	0.5,2	undulation	
C063	585602	5213564.3	1.8	1.9	1.9	2.3	65	1,7	35	euhedral	no	0.2,1										folding	autobreccia
C064	585607	5213566.5	2.2	1.3	1.9	1.9							100	layered	no	none							
C065	585612	5213566.8	3.2	1.6	2.6	2.3	75	0.2,5	25	euhedral	no	0.2,2											
C066	585612	5213568.3	1.8	1.1	2.2	1.8	70	0.2,2	25	euhedral	no	0.2,2						5	to black chert	yes	0.2,2		
C067	585618	5213567.4	1.8	1.2	1.8	1.8	55	0.2,4	45	euhedral	no	0.2,2											boudinage (ductile?)
C068	585622	5213572.4	2.2	1.5	1.6	2.2	55		30	euhedral with jasper	no	0.5,1						15	to black chert	yes	0.5,2		
C069	585624	5213572.8	2.2	1.8	1.7	1.6	60	0.2,3	40			0.2,3										undulation	
C070	585628	5213575.5	2.7	1.9	2.3	1.9	65	0.2,3	35	massive	yes												brittle offset
C071	585632	5213579.1	2.3	1.6	2.2	1.8	65	0.2,2	35	euhedral	no	0.2,2											
C072	585635	5213578.9	2.8	1.6	1.4	2.8	70	0.5,3	25	euhedral	no	0.5,2						5	to black chert	no	0.5,3		
C073	585636	5213581.7	2	1.6	2.2	1.4	75	0.1,5	25	euhedral	no	0.1,2											brittle offset
C074	585640	5213582.9	1.9	1.6	1.7	1.8	75	0.2,3	20	euhedral	no	0.2,2						5	to black chert	yes	0.2,3	bed pinching	
C075	585642	5213585.7	2.9	1.6	2.1	1.5	65	0.2,2	35	euhedral	no	0.2,2											
C076	585657	5213592.1	2.5	1.3	2.5	2.5	55	0.5,1	45	euhedral	no	0.5,1											
C077	585658	5213593.5	2.7	1.7	1.4	1.7	45	0.5,3	55	euhedral	no	1,3											
C078	585660	5213593	1.9	1.9	2.1	1.7	60	0.5,3	40	euhedral	no	0.5,1											
C079	585663	5213595.5	2.9	1.6	2.4	2.5	70	1,20	30	euhedral	no	1,2										folding	boudinage (ductile?)
C080	585665	5213600.9	1.5	1.8	2.2	1.9	60	0.5,4	40	euhedral	no	0.5,2										bed thickening	boudinage (ductile?)
C081	585672	5213604.4	0.9	1.6	1.5	1.5	60	0.5,4	40	euhedral	no	0.3,1.5											
C082	585676	5213608	2.1	1.6	1.8	1.6	65	1,3	30	massive and euhedral	no	0.5,2	5	lenses	weakly	none	4					bed pinching	
C083	585679	5213608.8	1.2	1.3	2.4	1.2	80	0.5,4	20	euhedral	no	0.3,1.5										bed pinching	boudinage (ductile?)
C084	585686	5213612.8	1.4	1.4	2.2	2.2	70	0.5,5	30	euhedral	no	0.5,1											
C085	585686	5213614.3	2.1	2.2	3	2.2	60	1,4	40	euhedral	no	1,2											
C086	585692	5213616.3	2.2	1.6	1.8	2.2	60	1,6	40	euhedral	no	1.5,2											
C087	585694	5213615.3	2	1.7	2	1.7	60	2,6	40	euhedral	no	0.3,2											
C088	585697	5213616.5	1	1.9	2.5	2	70	0.7,3	30	euhedral	no	0.2,3											
C089	585702	5213615.6	1.5	1.4	1.9	1.5	70	1,4	30	euhedral	no	1,2											

C090	585703	5213616.8	1.5	1.8	2.4	1.9	55	0.5,4	45	euhedral	no	0.5,1												
C091	585707	5213616.7	1.7	1.4	1.1	1	60	1,4	40	euhedral	no	0.5,1.5												brittle offset
C092	585709	5213616.5	1.9	1.5	2.1	1.9	70	0.5,3	30	euhedral	no	0.5,2											folding	
C093	585713	5213615.4	1.5	1.9	1.7	1.5	65	1,2	35	massive	no													breccia
C094	585716	5213618.1	2.3	1.8	3.5	1.9	75	0.5,3	25	massive	no	0.3,3												
C095	585720	5213619.7	2	1.6	1.2	1.3	70	0.2,2	45	euhedral	no	0.2,2												
C096	585723	5213619.9	2.2	2.3	1.6	2.2	55	0.2,2	45	euhedral	no	0.2,2												brittle offset
C097	585724	5213621.4	3	1.5	1.9	1.4	60	1,3	40	massive	no	1,2												
C098	585731	5213620.5	1.7	1.4	2.5	1.5	65	0.2,2	35	euhedral	no	0.2,2											undulation	
C099	585733	5213620.3	3	1.8	3.8	3	70	1,3	30	massive	no	0.2,2											folding	
C100	585738	5213620.6	2.9	2	3.7	3.7	75	0.5,3	25	massive	no	0.5,3												
C101	585749	5213620.7	1.1	1.3	2.1	1.1	75	0.5,3	25	euhedral	no	0.2,2												
C102	585752	5213622.8	1.5	1.6	1.9	1.3	40	0.5,15	60	euhedral	no	0.5,3											bed thickening	
C103	585755	5213623.1	1.6	1.4	1.8	1.6	70	1,3	30	euhedral	no	0.5,2											undulation	
C104	585757	5213624.4	2.1	1.5	2.2	1.7	60	1,3	40	euhedral	no	0.5,2											bed pinching	
C105	585759	5213625.3	2.4	1.7	1.5	1.4	58	1,3	40	massive	no	0.5,2	5	lenses	weakly		2							
C106	585760	5213627.8	1.2	2.7	1.1	2.6	65	2,4	33	euhedral	no	0.5,1	2	lenses	no	none	4						bed thickening	boudinage (ductile?)
C107	585770	5213634.7	1.6	1.8	2.1	1.6	68	1,5	30	euhedral	no	0.5,1						2	to black chert	no	1,3			
C108	585774	5213638.3	2.5	2.2	2.3		90																	breccia
C109	585778	5213638.1	1.9	1.2	1.7	1.2	80	2,20	20	euhedral	no													
C110	585781	5213641.9	0.9	1.7	2.1	1.9	70	2,3	30	euhedral	no	0.5,1												autobreccia
C111	585789	5213642	2.7	1.6	1.7	2.7	60	1.5,2	40		no	1,3											6	brittle offset
C112	585791	5213643.3	3	1.9	1.9	3	75	2,5	25	euhedral	no	1,3											folding	
C113	585794	5213645.4	1.7	1.6	1.5	1.3	60	0.5,4	40	massive and euhedral	no	0.3,2											bed pinching	
C114	585799	5213647.8	2.5	1.9	2.4	2.5	70	1,4	30	euhedral	no	0.5,1											bed pinching	boudinage (ductile?)
C115	585801	5213648.3	3.3	1.5	2.9	1.5	70	0.5,3	30	euhedral	no	0.3,1											bed thickening	
C116	585807	5213651.4	2.8	2.5	3.7	2.8	60	1,5	40	euhedral	no	0.5,2												
C117	585809	5213652.4	2.2	1.3	2.8	1.3	70	0.5,4	40	euhedral	no	0.3,2												
C118	585813	5213654.8	1.6	2.2	1.6	1.6	55	0.5,2	45	massive and euhedral	no	0.5,2											undulation	
C119	585817	5213655.4	2.8	1.9	2.4	2.6	55	0.3,3	45	euhedral	no	0.3,2												

C120	585820	5213656.2	2.3	2	2.5	2.3	70	1,4	30	massive and euhedral	no	1,4										bed pinching	brittle offset
C121	585825	5213660.9	2.2	2.1	1.7	1.7	75	1,3	25	euhedral	no	0.5,2											
C122	585831	5213660.8	2.5	1.7	2.4	1.8	65	0.5,3	35	massive	no	0.2,1											
C123	585842	5213667.5	3.2	2	3.2	2	74	0.5,5	25	massive	no	0.3,3						1	to black chert	no	3		autobreccia
C124	585863	5213671.3	3.3	2.5	2.7	2.5	68	0.1,3	30	euhedral	no	0.1,1						2	to black chert	no	2		
D001	583686	5212871.7	2.1	1.3	1.4								100		weakly	finely disseminated sulfides							
D002	583688	5212873.9	2	1	2.1	1.6	75	0.5,4	25	euhedral	no	0.3,1.5											
D003	583692	5212872.6	1.6	1.9	3.2	3.2							100										
D004	583691	5212872.6	1.2	1.4	2.1	2.1	63	0.5,3	35	massive and euhedral	no	0.5,3						2	to black chert	no	2	bed pinching	
D005	583696	5212872.5	2.1	1.6	1.7	1.7	70	1,4	20	euhedral	no	1,2						10	to black chert	yes	1,4	bed pinching	
D006	583697	5212874.8	1.6	1.5	2.4	2.4	70	1,3	30		yes	0.5,2											
D007	583695	5212875.4	1.8	1.3	1.9	1.8	68	0.3,3	30	massive and euhedral	no	0.3,2	2	lenses	no	large/secondary sulfides	2						
D008	583701	5212875.8	2.7	1.9	1.9	2.9	85	0.3,3	15	euhedral	no	0.5,1										folding	
D009	583703	5212875.1	3.1	2	2.2	3.1	70	1,3	20	euhedral	yes	0.4,1						10	to black chert	yes	1,3		
D010	584100	5212925.5	2.1	1.6	1.8	1.6	69	1,3	30	euhedral	no	0.5,3	1	lenses	no	large/secondary sulfides	3					bed pinching	boudinage (ductile?)
D011	584103	5212925.8	2	1.3	1.4	1.4	45	0.5,3	30	euhedral with jasper	no	0.5,3	5	intruded	strongly	finely disseminated sulfides	4	20	none	yes	0.5,3	folding	
D012	584107	5212928.5	2.1	2.1	2	2.1	65	0.2,3	35	euhedral with jasper	no	0.2,1										undulation	
D013	584107	5212927.8	4.7	1.9	2	2.6	50	0.5,2	35	euhedral with jasper	no	0.2,1						5	to black chert	yes	0.5,2	folding	
D014	584115	5212929.6	2.9	2.2	2.6	2	67	0.5,3	30	euhedral	no	0.2,2						3	to black chert	no	0.5,3	undulation	
D015	584120	5212929.1	2.9	2.1	1.8	2.1	70	1,5	30	massive and euhedral	yes	0.2,2.5										undulation	
D016	584126	5212930.2	2.6	2.2	2.1	2	75	0.5,5	25		yes	0.2,1										bed pinching	boudinage (ductile?)
D017	584125	5212930.2	3	2	2.5	2.5	70	0.5,3	30		no	0.1,2											
D018	584137	5212933.2	3.3	1.3	1.5	2.2	64	0.5,3	35	euhedral	no	0.2,2						2	to black chert	no	0.5,3	bed pinching	brittle offset
D019	584385	5212998.3	2.5	1.5	1.5	1.8	55	0.2,3	30	euhedral with jasper	no	0.2,2	10	intruded	no	none		5	to black chert	yes	0.2,3		

D020	584399	5213001.2	1.6	1.6	1.7	1.2	69	0.5,4	20	massive and euhedral	no	0.3,2	10	intruded	strongly	finely disseminated sulfides		1	to black chert	no	2		
D021	584414	5213001.8	1.6	1.7	2.8	2.8	55	0.5,4	45	massive	yes	0.3,3											
D022	584417	5213002.9	2.8	1.3	1.6	1.5	60	1,4	35	massive and euhedral	no	0.2,2.5						5	to black chert	yes	2		
D023	584420	5213004.7	2.1	1.4	1.1	1.5	65	1,3	35			0.5,2										bed pinching	
D024	584421	5213006.1	0.9	1.5	1.4	1.4	75	0.5,3	25	euhedral	no	0.2,1										bed thickening	
D025	584477	5213011.3	1.8	1.3	1.4	1.5	60	0.5,6	30	euhedral with jasper	no	0.2,3						10	to black chert	yes	0.5,6		
D026	584490	5213008.1	1.5	1.5	2.1	1.4	63	0.5,3	35	euhedral	no	0.2,2						2	to black chert	no	0.5,3		
D027	584493	5213006.1	1.7	0.9	1.6	0.9	60	0.5,3	40	euhedral	no	0.2,1										bed pinching	
E001	587200	5212052	1.3	1.4	1.6	1.1	65	1,4	20	euhedral	no	0.3,2	10	lenses	no	large/secondary sulfides		5	to black chert	yes	0.3,2		
E002	587199	5212047.7	1.7	1.1	1	1.7	63	0.5,3	25	massive and euhedral	no	0.3,2	2	lenses	no	large/secondary sulfides	1,2	10	to black chert	yes	0.5,3		
E003	587195	5212048.2	1.9	0.9	1.5	0.9	80	0.5,3	15	euhedral	no	0.2,0.5						5	to black chert	no	0.5,3		
E004	587191	5212047.2	1.8	1.4	1.9	1.6	33		50	euhedral	no		33	intruded	strongly	none							breccia
E005	587190	5212046.8	2.3	1	2	1	50	0.5,3	30	euhedral	no	0.2,3						20	none		0.5,2		
E006	587189	5212045.7	2.3	1.8	2.2	1.7	60	0.5,3	30	euhedral	no	0.5,2	10	layered	no	none	5					bed thickening	
E007	587183	5212042.2	2.4	1.8	2.4	2.4	70	0.5,3	20	euhedral	no	0.5,3	5	lenses	weakly	large/secondary sulfides	4	5	to black chert	no	0.5,3	bed pinching	boudinage (ductile?)
E008	587180	5212040.9	1.8	0.9	2.4	1.8	30	0.2,2	25	euhedral	no	0.2,2	5	lenses	no	finely disseminated sulfides	3	40	none	yes	0.2,2	undulation	
E009	587177	5212037.1	1.9	0.7	1.8	0.7	30	0.5,2	40	massive	no	0.5,4						30	to black chert	no	0.5,2		
E010	587176	5212039.3	2.8	2.1	2.3	2.5	60	0.2,3	40	euhedral	no	0.2,3										bed pinching	brittle offset
E011	587174	5212037.9	2.1	0.7	1.6	0.7	70	0.1,2	30	massive	no	0.1,1											
E012	587172	5212037.1	2.7	1	1.5	1	80	0.5,3	20	euhedral	no	0.1,1										undulation	
E013	587169	5212035.8	2.2	1.4	1.6	1.2	60	0.5,2	25	euhedral	no	0.2,1	5	lenses	weakly	none	3	10	none	no	0.5,2		
E014	587167	5212034.5	3.2	1.6	1.6	1.2	25	0.2,2	50	euhedral	no	0.5,3						25	none	no	0.2,2		
E015	587164	5212031	3.6	0.8	1.7	0.8	50	0.3,2	30	massive	no	0.3,2						20	none	no	0.3,2		brittle offset
E016	587159	5212028.5	1.8	1.3	1.9	1.4	33		33	euhedral	no		33					1					breccia
E017	587156	5212026.2	2.8	1.3	1.3	1.3	40	0.3,3	30	euhedral	no	0.2,2						30	none	no	0.3,3		autobreccia
E018	587154	5212024.3	2.1	1.4	1.8	1.8	50	0.3,2	40	massive	no	0.3,2						10	none	yes	0.3,2		

E019	587153	5212021.9	2.1	0.9	2.2	2.2	50	1,8	15	euhedral	no	0.2,1	35	layered	no	large/secondary sulfides	1,8							
E020	587147	5212022.7	2.3	2.1	2.7	2.1	60	0.7,3	40	massive	no	0.2,2										undulation		
E021	587142	5212016.4	2.1	2.2	2.5	2.2	58	1,5	25	euhedral	no	1,5	15	lenses	strongly	finely disseminated sulfides	5	2	to black chert	yes	1,3	folding		
E022	587141	5212018.2	2.1	1.5	1.7	1.4	65	1,4	25	massive	no	1,2	1	layered	no	large/secondary sulfides	2	5	none	yes	1,4			
E023	587138	5212018.2	2.5	1.7	2.1	1.8	68	0.2,3	30	euhedral	no	0.2,3	2	lenses	no	none	2.5							autobreccia
E024	587138	5212014.8	2.1	1.6	2	2	30	0.3,6	40	massive	no	0.5,3	5	layered	no	none	2	25	to black chert	no	0.3,5			
E025	587129	5212016.5	2.5	1.2	1.4	1.2	25	0.2,2	40	euhedral with jasper	no	0.5,2	20	layered	weakly	none	4,12	15	none	no	0.2,2			
E026	587127	5212012.6	2.4	1.5	1	1	60	0.2,6	24	euhedral	no	0.2,1	1	layered	no	large/secondary sulfides	2	15	none	no	0.2,2			
E027	587126	5212010.7	1.6	1.2	2.1	0.7	70	0.3,4	24	massive and euhedral	no	0.2,2	1	lenses	no	large/secondary sulfides	2	5	to black chert	no	0.3,2	folding	brittle offset	
E028	587122	5212009	2.3	1.3	1.6	1.6	70	0.1,3	24	massive and euhedral	no	0.1,1	5	layered	weakly	none	2.5	1	to black chert	no	0.1,3			
E029	587120	5212008.4	2.1	1.6	1.8	1.6	19	1,3	1		no		80	layered	weakly	finely disseminated sulfides	20,60							
E030	587118	5212008.6	2.1	1.1	1.3	1.1	55	0.2,3	40		no	0.2,2	2	lenses	no	large/secondary sulfides	4	3	to black chert	no	0.2,3	folding	autobreccia	
E031	587116	5212007.6	1.3	1.6	1.2	1.3	45	1,4	5	massive	no	0.1,0.5	50	layered	weakly	finely disseminated sulfides	3,13	1	to black chert	no	0.1,3			
E032	587112	5212005.2	2.2	1.3	1.2	1.2	20	0.3,1.5	50		no	0.5,2	5	lenses	no	none	3	25	none	yes	0.3,1.5	folding	autobreccia	
E033	587108	5212004.7	2.2	1.1	1.8	1	40	0.3,2	25		no	0.3,2	15	intruded	no	large/secondary sulfides	4,5	20	to black chert	no	0.3,2			
E034	587108	5212001.1	2.1	1	1.3	1.2	20	0.3,2	50		no	0.3,2	10	layered	no	large/secondary sulfides	3,5	20	to black chert	yes	0.3,2	folding		
E035	587105	5212002.1	1.6	1.7	2.1	1.5	59	0.3,4	30	euhedral	no	0.5,1	10	layered	weakly	large/secondary sulfides	3,4	1	to black chert	no	0.3,4	bed pinching	boudinage (ductile?)	
E036	587102	5212001.7	2.4	1	1.4	1	40	0.3,2	40		no	0.3,2						20	none	no	0.3,2			
E037	587099	5212002	2.4	1.6	1.8	1.4	5	0.5,1	40	massive and euhedral	no	0.2,2	55	layered	weakly	large/secondary sulfides	1,5						breccia	
E038	587100	5211999.9	2.1	1.7	2.1	1.6	58	0.5,5	25	euhedral	no	1,8	15	layered	no	finely disseminated sulfides	3,5	2	to black chert	no	0.5,3	bed thickening		
E039	587091	5211998.1	2.1	1.8	1.5	1.5	45	0.5,3	30	massive and euhedral	no	0.5,4	10	layered	weakly	none	5	15	to black chert	no	0.5,3	bed pinching		

E040	587088	5211997.5	0.8	1.6	2.2	1.3	30	0.5,4	40	euhedral	no	0.2,1.5	20	layered	weakly	finely disseminated sulfides	0.5,4	10	to black chert	no	0.5,4	bed pinching	
E041	587082	5211997	2.3	1	1.6	1	50	0.2,2	20		no	0.2,2	30	layered	strongly	large/secondary sulfides	0.2,2						brittle offset
E042	587079	5211994.3	1.8	1.5	1.8	1.5	50	0.5,3	20	euhedral	no	0.5,3	30	layered	weakly	large/secondary sulfides	2,8						
E043	587076	5211994.2	1.9	1.6	2.7	1.9	48	0.5,2	35		no	0.5,2	15	layered	weakly	none	4,5	2	to black chert	no	0.5,2		
E044	587072	5211994.7	2.5	1.7	3	1.7	40	0.2,3	30	euhedral	no	0.2,3	20	layered	no	finely disseminated sulfides	0.2,3	10	none	no	0.3,2		
E045	587068	5211994.9	1.9	1.6	1.9	1.8	40	0.5,2	20	euhedral	no	0.5,2	35	layered	weakly	finely disseminated sulfides	1,7	5	to black chert	no	0.5,2	faulting	boudinage (ductile?)
E046	587067	5211993.2	2.9	0.6	1.4	0.6	70	0.3,2	15	massive and euhedral	no	0.3,2	10	layered	no	none	3,5	5	to black chert	yes	0.3,2		
E047	587060	5211990.2	2.1	0.9	2.2	0.9	65	0.5,3	25	euhedral	no	0.5,2	10	layered	no	large/secondary sulfides	3,4					folding	
E048	587055	5211990.8	2.5	1.2	1.6	1.6	60	0.2,3	20	euhedral	no	0.2,3	15	lenses	weakly	large/secondary sulfides	3,4	5	to black chert	no	0.2,3	folding	autobreccia
E049	587052	5211990	3.2	2.2	2.1	1.9	45	0.3,2	19	massive and euhedral	no	0.3,2	35	layered	no	finely disseminated sulfides	1,5	1	to black chert	no	0.3,2		brittle offset
E050	587050	5211990.3	2.3	1.7	1.2	1.5	10	0.2,2	35	euhedral	no	0.2,2	30	layered	no	large/secondary sulfides	0.3,3	25	to black chert	yes	0.2,2		
E051	587045	5211990.6	2.8	1.1	1.7	1.8	70	0.5,6	20		no	0.4,1	10	layered	weakly	none	2,4					bed pinching	
E052	587042	5211990.5	1.8	1.4	2.1	1.6	48	0.5,4	35		no	0.2,3	15	layered	strongly	finely disseminated sulfides	2,5	2	to black chert	no	0.5,4	bed thickening	
E053	587038	5211990.3	3	1.5	2								100	intruded	no	none							
E054	587036	5211990.9	2.3	1.7	2.2	1.9	38	1,4	30	euhedral	no	1,3	30	layered	weakly	finely disseminated sulfides	2,8	2	to black chert	no	1,3	undulation	brittle offset
E055	587031	5211988.9	1.9	2.8	2.2	2.1	50	0.5,3	40		no	0.3,2						10	to black chert	no	0.5,3	folding	
E056	587030	5211989.7	2.2	0.8	1.2	1.5	50	0.5,3	15		no	0.2,3	35	layered	weakly	large/secondary sulfides	1,4					folding	
E057	587029	5211991	3	1.1	2.1	3	40	0.5,7	50		no	0.3,4						10	none	no	0.5,1	bed pinching	brittle offset
E058	587025	5211988	1.9	1.1	1.7	1	35	0.2,5	50		no	0.2,3						15	none	yes	0.5,1	bed thickening	
E059	587023	5211987.6	1.8	0.6	1.6	0.6	40	0.5,3	30		no	0.1,1	20	layered	weakly	none	0.5,2	10	to black chert	no	0.5,3		
E060	587020	5211986.7	1.1	0.9	1.2	0.9	90	1,3	10	euhedral	no	0.2,1											
E061	587018	5211985.8	2.6	1.5	2.1	1.6	40	0.5,3	20	euhedral	no	0.1,3	30	layered	weakly	finely disseminated sulfides	1,8	10	none	no	0.5,3		

E062	587011	5211985.7	2.2	1.6	1.7	1.4	60	2,6	40	massive and euhedral	no	0.2,1												
E063	587007	5211985.4	2	1.1	1.7	1.1	69	0.5,3	10	massive	no	0.3,3	20	layered	weakly	large/secondary sulfides	2,3	1	to black chert	no	0.1,0.5			
E064	587007	5211985.5	2	0.7	2.2	2.1	30	0.5,2	25	massive	no	0.5,1	40	layered	weakly	none	8,10	5	to black chert	no	0.5,2	folding		
E065	587002	5211986.2	2.6	2.2	2.1	2.1	30	1,3	30	euhedral	no	0.5,1.5	45	layered	weakly	large/secondary sulfides	1,8	5	to black chert	no	1,3	folding		autobreccia
F001	585369	5211372.4	2.4	1.5	2.5	2.4	40	0.2,2	40	massive	no	0.2,1	15	layered	no	large/secondary sulfides	5,8	5	to black chert	no	0.2,2			
F002	585374	5211374.9	2.2	1.8	2.1	1.8	48	0.5,3	20	massive	no	0.2,1	30	layered	weakly	large/secondary sulfides	2,3	2	to black chert	yes	0.5,2			
F003	585377	5211375.6	1.9	1.6	1.4	1.4	58	0.2,5	20	euhedral	no	0.5,3	20	layered	weakly	none	8,10	2	to black chert	yes	0.2,4	bed thickening		
F004	585379	5211377.9	1.6	1.5	1.5	1.5	25	0.5,4	40	euhedral	yes	0.3,2						35	none	no	0.5,3			
F005	585382	5211378.5	2.1	1.5	1.7	1.7	25	0.5,3	30	euhedral	no	0.5,2	40	layered	weakly	large/secondary sulfides	5,9	5	to black chert	no	0.5,2	bed pinching		
F006	585384	5211381.5	2.7	1.9	2	2	30	0.2,2	50	euhedral	no	0.2,2										folding	breccia	
F007	585387	5211382.7	2.4	1.7	2	1.7	35	0.2,2	45	massive	no	0.2,2						20	to black chert	yes	0.2,2			
F008	585387	5211383.7	2.7	1.5	1.2	1.5	58	0.2,5	40	euhedral	no	0.5,3						5	to black chert	no	0.2,3			
F009	585390	5211382.9	2.3	1.2	1.9	1.2	55	0.7,2	38	euhedral	no	0.2,2	2	layered	no	none	3	5	to black chert	no	0.7,2			
F010	585395	5211389.9	1.2	1.2	1.4	1.4	83	1,3.7	15	euhedral	no	0.5,2						2	to black chert	no	1,3			autobreccia
F011	585397	5211390.4	1.5	1.2	1.6	1.2	70	0.5,3	20	massive	no	0.2,1												
F012	585398	5211392.1	1.7	1.5	1.3	1.5	60	1,5	40	massive	no	0.3,3												
F013	585401	5211391.4	2.1	2.2	2.9	2	40	0.3,3	35	massive and euhedral	no	0.5,2						25	to black chert	yes	0.3,3			
F014	585402	5211393.6	2.7	1.5	1.3	2.5	70	0.5,4	13	massive and euhedral	no	0.5,4						2	to black chert	no	0.3,1	folding		autobreccia
F015	585402	5211396	2.5	1.7	1.5	1.7	33	0.5,3	50	massive and euhedral	no	0.5,5	2	lenses	no	none	3	15	to black chert	yes	0.5,3			
F016	585405	5211396.7	1.5	1.7	1.9	1.7	55	0.2,3	30	euhedral	no	0.2,2						15	to black chert	yes	0.2,3			
F017	585409	5211395.8	1.9	1.7	1.5	1.5	25	0.3,2	50	massive and euhedral	yes	0.5,1						25	none	yes	0.3,2			brittle offset
F018	585407	5211399	1.9	1.7	1.5	1.7	30	0.3,3	50	euhedral	no	0.3,2	10	layered	no	finely disseminated sulfides	2,3	20	none	no	0.3,2			
F019	585411	5211402.2	1.9	1.5	1.5	1.9	35	0.3,1.5	60	euhedral	no	0.5,1						15	to black chert	no	0.3,1.5	bed pinching		
F020	585414	5211401.4	1.7	1.1	1.8	1.7	10	0.5,2	60	massive	no	0.3,2						30	to black chert	yes	0.5,1			
F021	585414	5211402.3	1.9	1.5	1.1	1.1	60	0.5,4	40	euhedral	no	0.5,3												

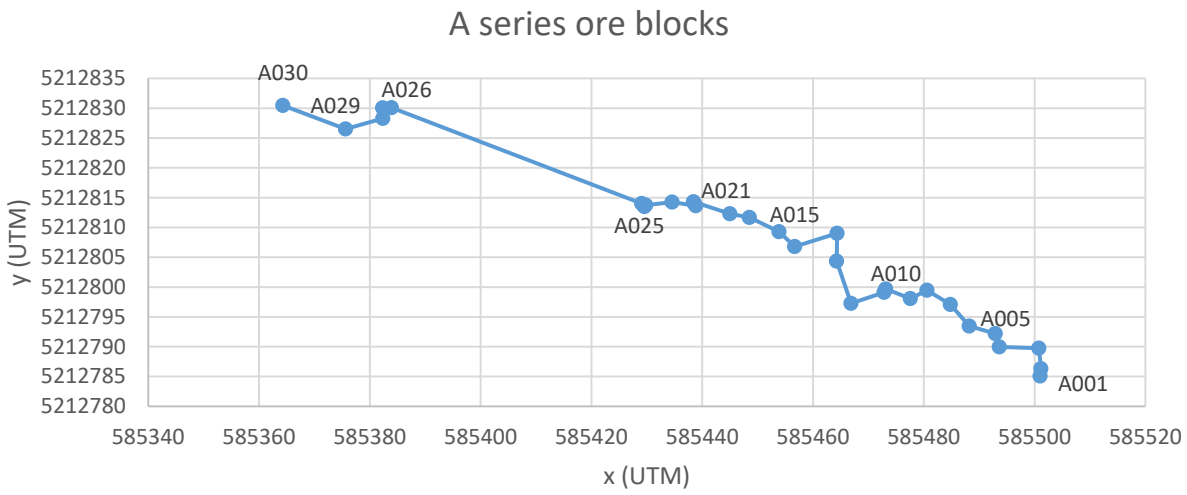
A series ore blocks
A030
A029
A026
A025
A021
A015
A010
A005
A001
y (UTM)
x (UTM)
5212835
5212830
5212825
5212820
5212815
5212810
5212805
5212800
5212795
5212790
5212785
5212780
585340
585360
585380
585400
585420
585440
585460
585480
585500
585520

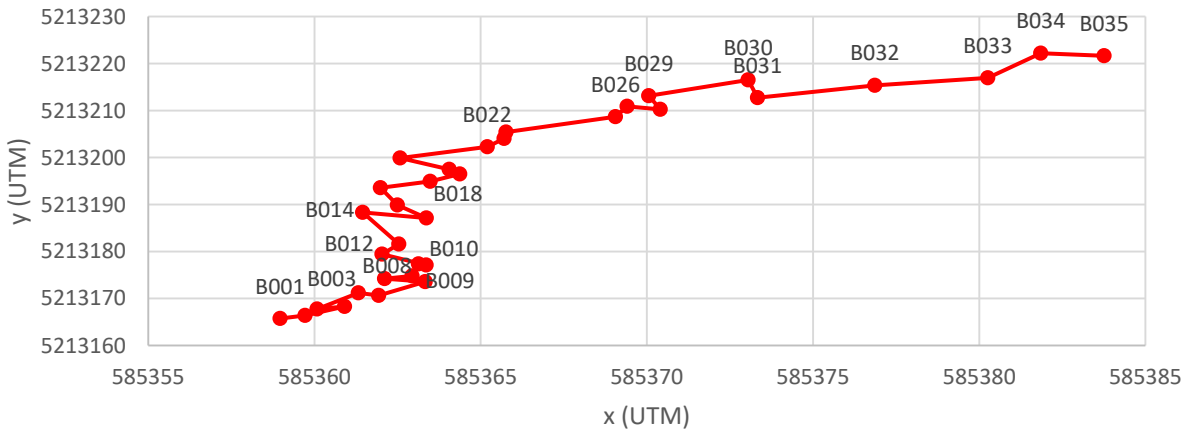
B series ore blocks
B034
B035
B030
B031
B032
B033
B029
B026
B022
B018
B014
B012
B010
B008
B009
B001
B003
y (UTM)
x (UTM)
5213230
5213220
5213210
5213200
5213190
5213180
5213170
5213160
585355
585360
585365
585370
585375
585380
585385

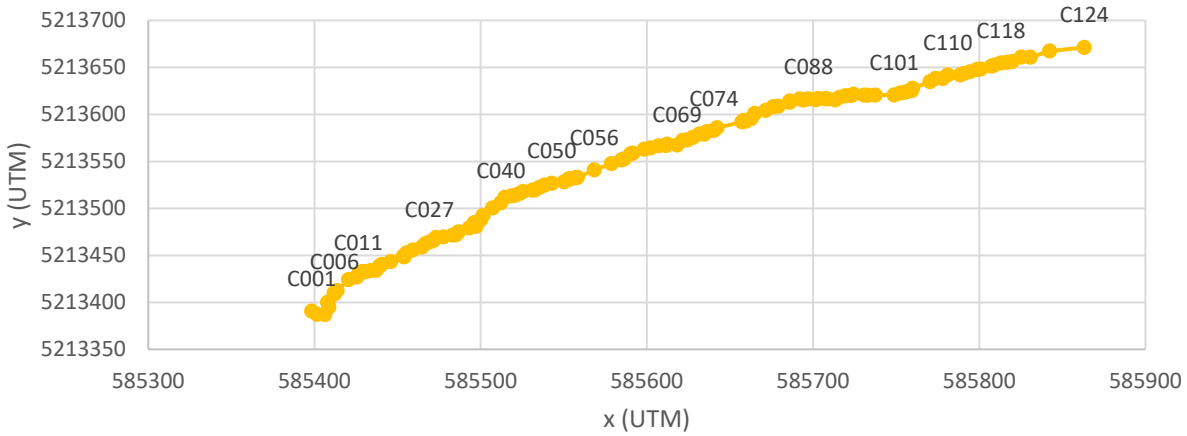
C series ore blocks
C124
C118
C110
C101
C088
C074
C069
C056
C050
C040
C027
C011
C006
C001
y (UTM)
x (UTM)
5213700
5213650
5213600
5213550
5213500
5213450
5213400
5213350
585300
585400
585500
585600
585700
585800
585900

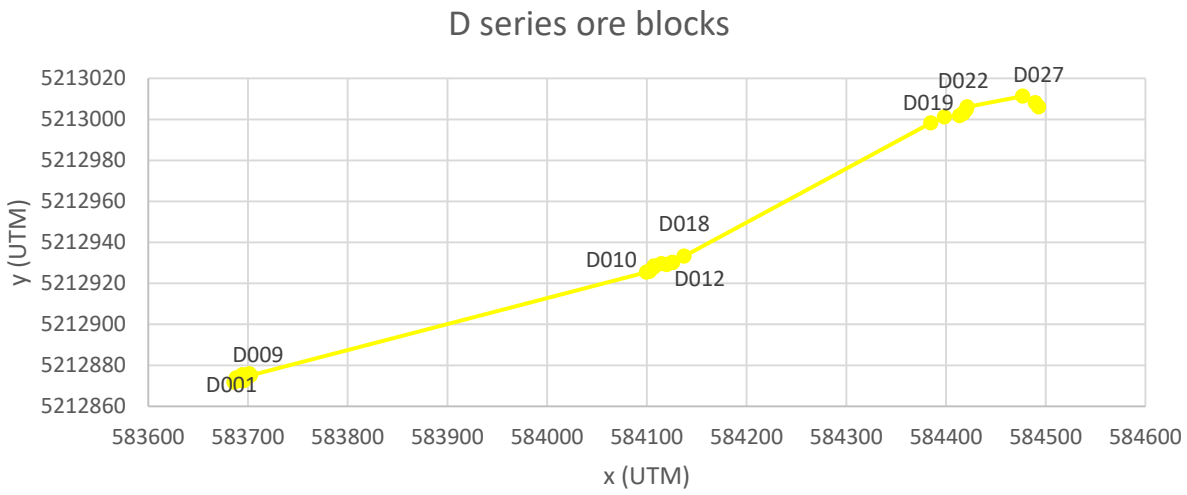
D series ore blocks
5213020
5213000
5212980
5212960
5212940
5212920
5212900
5212880
5212860
y (UTM)
583600
583700
583800
583900
584000
584100
584200
584300
584400
584500
584600
x (UTM)
D001
D009
D010
D012
D018
D019
D022
D027

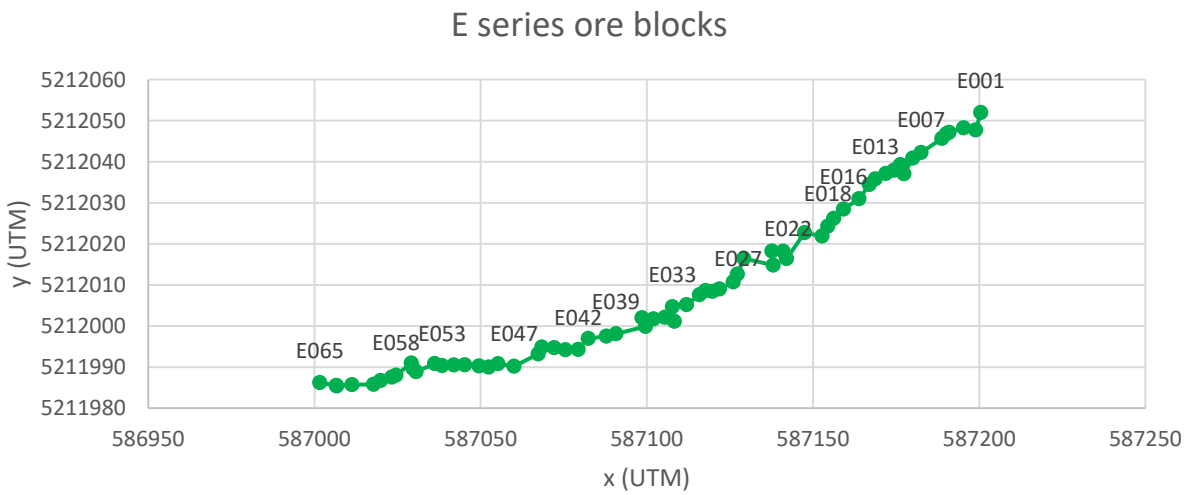
E series ore blocks
5212060
5212050
5212040
5212030
5212020
5212010
5212000
5211990
5211980
y (UTM)
586950
587000
587050
587100
587150
587200
587250
x (UTM)
E001
E007
E013
E016
E018
E022
E027
E033
E039
E042
E047
E053
E058
E065

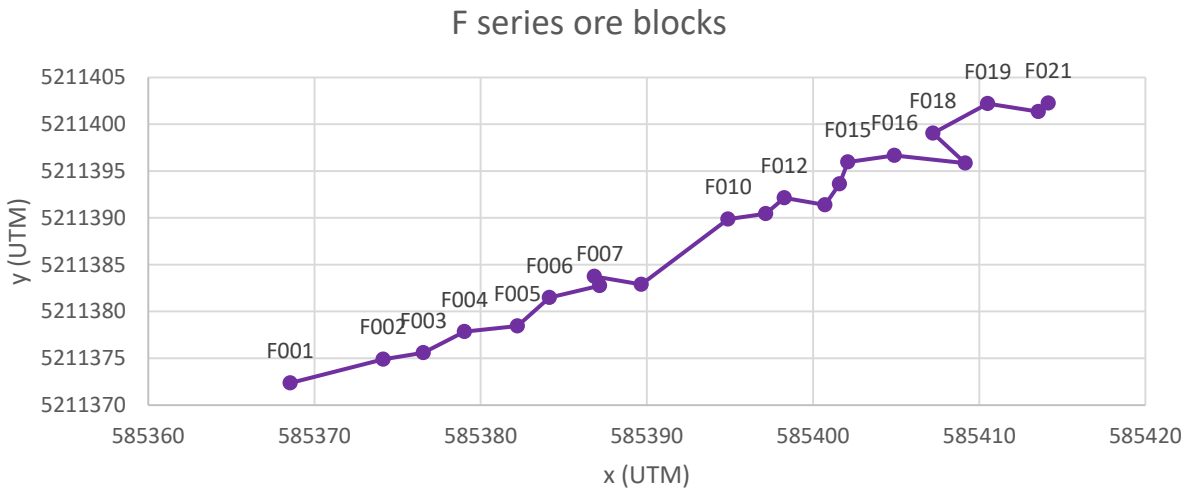
F series ore blocks
5211405
5211400
5211395
5211390
5211385
5211380
5211375
5211370
y (UTM)
585360
585370
585380
585390
585400
585410
585420
x (UTM)
F001
F002
F003
F004
F005
F006
F007
F010
F012
F015
F016
F018
F019
F021

Figure A.2 Distribution of ore blocks in the Sherman Mine. The plots show the coordinates of every block in a particular series (A, B, C, D, E or F) in UTM. Coordinates are in Zone 17N. Individual blocks are labelled to show the progression of each series.

Appendix 4: Summary statistics of geochemistry data set

		Temagami BIF (n=54)*						
		Min	Max	Q1	Q3	Mean	Median	Standard Deviation
Si	%	1.29	46.0	18.3	41.0	28.0	28.6	12.7
Al	%	0.021	7.95	0.093	0.639	1.28	0.198	2.26
Fe	%	0.881	63.2	5.96	33.4	22.0	19.6	17.9
Ca	%	0.014	4.37	0.105	0.511	0.559	0.229	0.868
Mg	%	0.024	4.99	0.152	1.97	1.14	0.455	1.33
Na	%	0.001	5.00	0.001	0.017	0.108	0.004	0.651
K	%	0.001	1.94	0.007	0.051	0.090	0.019	0.269
P	%	0.002	0.19	0.013	0.052	0.040	0.035	0.037
LOI	%	-2.60	33.55	-0.108	4.16	2.65	1.40	5.28
C_{tot}	%	0.01	2.85	0.050	0.485	0.426	0.120	0.650
S_{tot}	%	0.00	1.13	0.0100	0.048	0.114	0.020	0.236
Ti	ppm	3.00	6515	12.0	301	540	39.0	1187
Mn	ppm	16.1	5680	153	926	894	324	1326
Zn	ppm	1.29	185	5.56	42.3	30.1	15.2	35.1
Cu	ppm	0.020	668	0.945	8.19	22.0	2.35	88.0
Pb	ppm	0.050	9.10	0.500	1.85	1.62	1.10	1.89
Au**	ppm	<0.001	<0.001	<0.001	<0.001	<0.001	<0.001	<0.001
Ag	ppm	0.005	1.46	0.010	0.090	0.091	0.030	0.198
As	ppm	0.010	918.00	0.533	2.28	20.05	0.990	119.42
Sb	ppm	0.010	2.45	0.143	0.628	0.526	0.355	0.586
Hg	ppm	0.001	0.33	0.001	0.008	0.022	0.002	0.057
Tl	ppm	0.005	0.52	0.005	0.005	0.036	0.005	0.095
Cd	ppm	0.010	0.20	0.010	0.058	0.048	0.030	0.051
Co	ppm	0.050	49.0	0.553	4.93	5.73	1.92	9.64
Ni	ppm	0.050	520	4.20	26.3	28.3	14.5	68.2
Se	ppm	0.010	22.9	0.103	0.658	0.903	0.290	2.98
Mo	ppm	0.005	12.4	0.053	3.44	2.41	0.955	3.07
Te	ppm	0.010	1.44	0.010	0.060	0.069	0.030	0.187
Sn	ppm	0.100	2.00	0.100	0.200	0.236	0.100	0.318
Ge	ppm	0.600	14.3	2.95	5.88	4.97	4.65	2.86
Bi	ppm	0.002	1.42	0.002	0.041	0.059	0.012	0.189
In	ppm	0.010	0.06	0.010	0.010	0.016	0.010	0.012
Re	ppm	0.0001	0.0085	0.0003	0.0017	0.0012	0.0009	0.0013
W	ppm	0.070	72.1	0.238	1.16	4.38	0.515	12.5
Cr	ppm	2.90	1130	6.20	40.7	48.5	23.7	146
V	ppm	0.100	152	1.63	12.4	15.3	4.20	28.6
Ga	ppm	0.080	31.9	0.380	3.36	4.44	0.860	7.57
Zr	ppm	0.100	149	0.825	11.9	22.0	2.35	40.6

Ba	ppm	0.500	553	1.70	25.85	34.12	4.45	85.1
Cs	ppm	0.005	46.0	0.080	0.560	2.01	0.185	6.96
Li	ppm	0.050	49.5	0.200	2.58	5.76	0.650	12.2
Be	ppm	0.010	2.36	0.143	0.920	0.626	0.430	0.565
B	ppm	0.100	63.8	2.65	53.5	30.2	32.2	23.3
Hf	ppm	0.050	3.90	0.050	0.475	0.615	0.100	1.05
Nb	ppm	0.100	12.8	0.100	0.975	1.28	0.100	2.41
Ta	ppm	0.005	1.15	0.030	0.113	0.137	0.050	0.216
Rb	ppm	0.050	78.5	0.275	1.80	5.46	0.545	15.0
Sr	ppm	0.920	168	5.45	28.3	22.5	9.84	30.5
U	ppm	0.020	3.10	0.060	0.265	0.339	0.120	0.573
Th	ppm	0.025	11.4	0.025	0.790	1.11	0.135	2.23
Y	ppm	0.250	48.2	1.68	8.25	6.69	5.00	7.61
La	ppm	0.120	34.2	0.745	5.54	5.52	1.76	8.20
Ce	ppm	0.270	60.4	1.18	10.2	10.7	3.18	16.4
Pr	ppm	0.030	6.76	0.130	1.12	1.23	0.380	1.89
Nd	ppm	0.110	25.1	0.563	4.27	4.75	1.59	7.16
Sm	ppm	0.020	5.85	0.115	0.845	0.941	0.375	1.40
Eu	ppm	0.022	1.94	0.118	0.498	0.401	0.262	0.399
Gd	ppm	0.050	5.73	0.160	0.870	0.865	0.530	1.13
Tb	ppm	0.005	1.10	0.030	0.148	0.141	0.090	0.190
Dy	ppm	0.050	6.83	0.180	0.873	0.849	0.580	1.14
Ho	ppm	0.005	1.38	0.040	0.188	0.177	0.120	0.228
Er	ppm	0.030	3.89	0.120	0.605	0.536	0.350	0.661
Tm	ppm	0.003	0.576	0.022	0.091	0.083	0.051	0.099
Yb	ppm	0.030	3.64	0.140	0.608	0.546	0.335	0.646
Lu	ppm	0.004	0.567	0.021	0.103	0.089	0.058	0.102
Sc	ppm	0.500	21.0	0.500	1.00	2.12	0.500	4.00
ΣREE	ppm	0.755	146	3.9	28.62	28.5	12.2	40.2

*The complete dataset is presented as supplemental material to Diekrup et al., in preparation

** Au was measured by INAA in the BIF standards FeR-3 and FeR-4. Neither standard reported Au concentrations above the detection limit, so Au analysis was removed from the analytical methods.

Black chert (n=13)

		Min	Max	Q1	Q3	Mean	Median	Standard Deviation
Si	%	23.1	46.0	35.5	42.4	37.7	40.7	7.17
Al	%	0.021	6.05	0.148	0.254	1.05	0.196	2.08
Fe	%	1.31	30.0	4.18	8.80	8.94	5.92	7.88
Ca	%	0.043	1.51	0.086	0.172	0.264	0.143	0.380
Mg	%	0.024	3.93	0.109	0.730	0.825	0.283	1.11
Na	%	0.001	0.479	0.001	0.010	0.043	0.004	0.126
K	%	0.007	1.94	0.010	0.028	0.171	0.016	0.511
P	%	0.002	0.061	0.013	0.039	0.025	0.022	0.019
LOI	%	-1.07	7.57	0.260	3.16	1.91	1.44	2.21
C_{tot}	%	0.010	1.01	0.035	0.333	0.226	0.075	0.304
S_{tot}	%	<0.001	0.280	0.010	0.093	0.077	0.030	0.099
Ti	ppm	5.99	83.9	7.49	28.5	23.4	15.0	22.5
Mn	ppm	52.9	883	142	336	295	225	235
Zn	ppm	1.29	103	2.80	24.6	24.3	5.19	32.9
Cu	ppm	0.020	114	1.47	8.43	16.3	6.79	29.9
Pb	ppm	0.100	6.60	0.200	1.10	1.12	0.700	1.64
Au	ppm	0	0	0	0	0	0	0
Ag	ppm	0.005	0.230	0.010	0.070	0.067	0.050	0.073
As	ppm	0.010	6.06	0.340	1.44	1.35	0.880	1.61
Sb	ppm	0.050	1.24	0.090	0.410	0.301	0.170	0.328
Hg	ppm	0.001	0.24	0.001	0.080	0.043	0.002	0.069
Tl	ppm	0.005	0.250	0.005	0.005	0.027	0.005	0.065
Cd	ppm	0.010	0.140	0.010	0.050	0.044	0.020	0.047
Co	ppm	0.140	14.60	0.700	8.020	5.113	2.570	5.083
Ni	ppm	0.050	88.0	10.600	43.60	29.82	21.40	24.08
Se	ppm	0.010	1.15	0.080	0.590	0.405	0.270	0.399
Mo	ppm	0.060	10.10	0.970	8.810	4.426	3.220	3.871
Te	ppm	0.010	0.12	0.010	0.050	0.037	0.010	0.036
Sn	ppm	0.100	2.000	0.100	0.300	0.354	0.100	0.514
Ge	ppm	1.500	5.00	2.100	4.900	3.477	3.600	1.286
Bi	ppm	0.002	0.088	0.002	0.035	0.026	0.009	0.031
In	ppm	0.010	0.030	0.010	0.010	0.013	0.010	0.007
Re	ppm	0.0001	0.0030	0.0006	0.0018	0.0013	0.0012	0.0009
W	ppm	0.070	56.6	0.490	3.08	8.34	0.900	15.8
Cr	ppm	3.60	90.3	15.4	80.6	45.0	36.7	32.9
V	ppm	0.400	49.1	0.900	6.90	10.7	2.50	16.4
Ga	ppm	0.120	18.7	0.260	1.21	3.07	0.700	5.79
Zr	ppm	0.400	3.70	0.550	2.30	1.50	1.200	1.13
Ba	ppm	1.30	35.8	1.70	6.40	7.87	2.95	10.7
Cs	ppm	0.040	1.56	0.070	0.190	0.328	0.170	0.431

Li	ppm	0.050	44.0	0.200	0.700	5.93	0.500	13.3
Be	ppm	0.070	2.11	0.080	0.440	0.435	0.150	0.586
B	ppm	1.70	60.7	45.2	59.3	46.8	56.5	18.5
Hf	ppm	0.050	2.70	0.050	0.200	0.465	0.050	0.873
Nb	ppm	0.100	6.90	0.100	0.900	1.285	0.600	2.086
Ta	ppm	0.005	0.590	0.005	0.070	0.114	0.050	0.190
Rb	ppm	0.170	78.5	0.390	1.10	6.70	0.470	20.7
Sr	ppm	2.29	40.5	5.42	9.68	10.2	5.87	10.3
U	ppm	0.020	1.60	0.040	0.200	0.349	0.120	0.530
Th	ppm	0.025	5.47	0.025	0.250	0.842	0.120	1.69
Y	ppm	0.250	16.4	1.20	6.40	4.60	3.00	4.78
La	ppm	0.120	23.4	0.500	4.35	4.95	1.51	7.96
Ce	ppm	0.270	49.2	0.760	7.69	9.89	2.60	16.7
Pr	ppm	0.030	5.50	0.080	0.910	1.12	0.300	1.89
Nd	ppm	0.110	20.7	0.370	3.85	4.20	1.19	6.89
Sm	ppm	0.020	3.69	0.090	0.730	0.791	0.280	1.18
Eu	ppm	0.025	1.01	0.086	0.357	0.295	0.192	0.308
Gd	ppm	0.050	2.72	0.100	0.760	0.697	0.350	0.870
Tb	ppm	0.005	0.410	0.020	0.110	0.104	0.050	0.127
Dy	ppm	0.050	2.49	0.110	0.720	0.626	0.300	0.738
Ho	ppm	0.005	0.510	0.030	0.160	0.130	0.070	0.151
Er	ppm	0.030	1.46	0.090	0.470	0.393	0.210	0.449
Tm	ppm	0.005	0.23	0.012	0.075	0.061	0.031	0.069
Yb	ppm	0.030	1.64	0.070	0.540	0.411	0.200	0.489
Lu	ppm	0.005	0.264	0.015	0.091	0.066	0.032	0.078
Sc	ppm	0.500	8.00	0.500	1.00	1.65	0.500	2.348
ΣREE	ppm	0.755	113	2.42	22.0	23.7	7.38	37.8

White chert (n=9)

		Min	Max	Q1	Q3	Mean	Median	Standard Deviation
Si	%	23.6	45.6	37.2	44.2	39.3	41.3	6.64
Al	%	0.074	1.21	0.140	0.413	0.345	0.254	0.309
Fe	%	0.881	21.0	1.16	10.0	6.49	4.18	6.80
Ca	%	0.014	1.05	0.161	0.529	0.384	0.364	0.282
Mg	%	0.121	1.21	0.223	0.820	0.514	0.277	0.371
Na	%	0.001	0.038	0.001	0.008	0.007	0.002	0.011
K	%	0.003	0.161	0.006	0.031	0.032	0.016	0.044
P	%	0.002	0.074	0.002	0.020	0.017	0.009	0.021
LOI	%	0.480	13.5	1.33	5.25	3.72	1.47	4.14
C_{tot}	%	0.030	2.85	0.370	0.535	0.787	0.475	0.938
S_{tot}	%	0.010	0.530	0.010	0.138	0.128	0.025	0.188
Ti	ppm	5.99	216	7.49	27.0	40.2	15.0	62
Mn	ppm	25.5	2290	259	1370	884	678	726
Zn	ppm	2.14	30.5	4.80	15.7	11.7	7.60	9.22
Cu	ppm	0.670	13.6	2.33	7.61	5.18	2.78	3.96
Pb	ppm	0.050	2.60	0.200	1.40	0.859	0.500	0.915
Au	ppm	0	0	0	0	0	0	0
Ag	ppm	0.005	0.050	0.010	0.035	0.023	0.020	0.016
As	ppm	0.230	35.5	0.440	2.78	4.39	0.640	9.91
Sb	ppm	0.030	0.500	0.065	0.250	0.205	0.180	0.158
Hg	ppm	0.001	0.333	0.001	0.015	0.044	0.001	0.097
Tl	ppm	0.005	0.030	0.005	0.005	0.007	0.005	0.007
Cd	ppm	0.010	0.050	0.010	0.025	0.020	0.020	0.012
Co	ppm	0.500	11.9	0.570	2.82	2.67	1.06	3.22
Ni	ppm	0.300	23.8	3.25	18.10	11.51	12.20	7.92
Se	ppm	0.030	0.680	0.085	0.345	0.241	0.180	0.200
Mo	ppm	0.005	4.190	0.065	3.635	1.860	2.010	1.752
Te	ppm	0.010	0.100	0.010	0.045	0.035	0.020	0.029
Sn	ppm	0.100	0.100	0.100	0.100	0.100	0.100	0.000
Ge	ppm	1.50	4.00	2.25	3.10	2.63	2.40	0.696
Bi	ppm	0.002	0.149	0.004	0.032	0.029	0.010	0.044
In	ppm	0.010	0.020	0.010	0.010	0.011	0.010	0.003
Re	ppm	0.0001	0.0027	0.0004	0.0009	0.0008	0.0005	0.0008
W	ppm	0.110	5.81	0.140	0.330	0.867	0.290	1.75
Cr	ppm	3.00	47.1	5.65	32.5	20.6	19.3	15.7
V	ppm	0.100	13.3	0.650	3.65	3.64	1.70	4.58
Ga	ppm	0.080	3.40	0.205	1.15	0.918	0.710	0.965
Zr	ppm	0.200	24.0	0.600	2.55	4.073	1.100	6.824
Ba	ppm	0.500	25.1	0.800	3.23	4.00	1.35	7.12
Cs	ppm	0.030	1.05	0.065	0.215	0.257	0.120	0.326

Li	ppm	0.050	2.60	0.100	0.750	0.650	0.300	0.810
Be	ppm	0.030	0.54	0.055	0.215	0.165	0.120	0.151
B	ppm	2.00	59.3	32.2	55.6	42.5	53.0	17.9
Hf	ppm	0.050	0.500	0.050	0.150	0.127	0.050	0.130
Nb	ppm	0.100	0.100	0.100	0.100	0.100	0.100	0.000
Ta	ppm	0.005	0.120	0.020	0.060	0.048	0.030	0.038
Rb	ppm	0.050	5.700	0.200	1.020	1.042	0.380	1.581
Sr	ppm	0.920	168	3.05	9.24	21.6	6.23	46.7
U	ppm	0.020	0.320	0.045	0.120	0.098	0.070	0.081
Th	ppm	0.025	1.16	0.025	0.140	0.196	0.025	0.332
Y	ppm	0.500	8.30	0.950	3.70	2.67	1.30	2.64
La	ppm	0.160	6.86	0.270	2.36	1.93	0.95	2.39
Ce	ppm	0.280	12.7	0.395	4.56	3.42	1.270	4.40
Pr	ppm	0.040	1.36	0.050	0.530	0.378	0.120	0.476
Nd	ppm	0.150	5.01	0.225	2.220	1.510	0.680	1.810
Sm	ppm	0.030	0.92	0.080	0.460	0.299	0.130	0.334
Eu	ppm	0.041	0.515	0.070	0.277	0.184	0.093	0.169
Gd	ppm	0.080	0.930	0.115	0.460	0.326	0.130	0.319
Tb	ppm	0.010	0.150	0.020	0.070	0.051	0.020	0.051
Dy	ppm	0.060	0.890	0.115	0.410	0.301	0.150	0.289
Ho	ppm	0.010	0.190	0.020	0.095	0.064	0.030	0.062
Er	ppm	0.030	0.560	0.065	0.285	0.190	0.110	0.186
Tm	ppm	0.003	0.078	0.011	0.044	0.029	0.018	0.027
Yb	ppm	0.030	0.500	0.075	0.280	0.195	0.120	0.173
Lu	ppm	0.004	0.093	0.012	0.047	0.032	0.017	0.031
Sc	ppm	0.500	2.000	0.500	0.500	0.682	0.500	0.441
ΣREE	ppm	1.11	29.9	1.51	12.2	8.91	3.97	10.6

Magnetite (n=19)

		Min	Max	Q1	Q3	Mean	Median	Standard Deviation
Si	%	5.60	38.2	10.2	21.9	16.6	13.9	8.51
Al	%	0.021	2.92	0.079	0.466	0.433	0.175	0.652
Fe	%	11.492	63.2	30.4	50.8	41.5	42.2	14.3
Ca	%	0.021	4.37	0.111	0.715	0.833	0.272	1.22
Mg	%	0.054	3.70	0.169	1.94	1.09	0.338	1.17
Na	%	0.001	0.112	0.002	0.054	0.027	0.004	0.035
K	%	0.003	0.518	0.020	0.138	0.130	0.055	0.169
P	%	0.002	0.170	0.035	0.059	0.053	0.044	0.036
LOI	%	-2.60	7.88	-1.70	2.07	0.556	-0.350	3.04
C_{tot}	%	0.020	2.30	0.050	0.670	0.477	0.130	0.675
S_{tot}	%	<0.001	1.13	0.010	0.045	0.169	0.020	0.340
Ti	ppm	12.0	737	30.0	160	150	87	186
Mn	ppm	36.4	5680	146	1485	1252	271	1774
Zn	ppm	4.010	76.8	9.210	38.5	27.2	19.4	21.4
Cu	ppm	0.020	54.6	0.055	4.730	8.772	1.690	16.6
Pb	ppm	0.300	5.500	0.800	2.55	1.70	1.30	1.35
Au	ppm	0	0	0	0	0	0	0
Ag	ppm	0.005	0.260	0.020	0.050	0.045	0.020	0.057
As	ppm	0.300	24.5	0.610	2.28	3.70	1.10	6.32
Sb	ppm	0.240	2.45	0.505	1.32	0.980	0.630	0.724
Hg	ppm	0.001	0.045	0.001	0.005	0.005	0.001	0.010
Tl	ppm	0.005	0.520	0.005	0.040	0.081	0.005	0.147
Cd	ppm	0.010	0.180	0.010	0.040	0.040	0.030	0.043
Co	ppm	0.230	16.0	0.555	3.29	3.13	1.77	4.46
Ni	ppm	0.200	79.2	2.20	23.5	17.0	11.1	21.2
Se	ppm	0.040	2.3	0.195	0.5	0.6	0.3	0.6
Mo	ppm	0.005	6.880	0.045	2.99	2.02	1.66	2.19
Te	ppm	0.010	0.24	0.020	0.06	0.05	0.03	0.06
Sn	ppm	0.100	0.500	0.100	0.200	0.174	0.100	0.125
Ge	ppm	2.90	14.3	5.35	9.70	7.62	7.80	2.95
Bi	ppm	0.002	0.280	0.003	0.048	0.052	0.023	0.079
In	ppm	0.010	0.060	0.010	0.010	0.013	0.010	0.011
Re	ppm	0.0001	0.0085	0.0004	0.0015	0.0013	0.0009	0.0019
W	ppm	0.220	12.1	0.365	0.845	1.19	0.510	2.59
Cr	ppm	3.20	69.3	8.65	35.9	23.1	20.7	17.35
V	ppm	1.50	38.6	3.10	8.35	8.55	6.00	9.15
Ga	ppm	0.440	7.54	0.730	2.95	2.03	1.61	1.75
Zr	ppm	0.800	59.6	2.00	7.75	9.07	4.50	13.9
Ba	ppm	0.900	144	5.40	31.1	30.8	16.6	40.7
Cs	ppm	0.040	46.0	0.26	4.05	5.63	0.570	11.3

Li	ppm	0.200	5.70	0.350	2.15	1.48	0.900	1.50
Be	ppm	0.230	2.36	0.745	1.35	1.07	0.920	0.548
B	ppm	0.100	52.2	1.50	33.9	19.1	8.00	19.0
Hf	ppm	0.050	1.40	0.050	0.200	0.232	0.100	0.311
Nb	ppm	0.100	1.40	0.100	0.650	0.453	0.300	0.433
Ta	ppm	0.030	0.250	0.040	0.075	0.069	0.050	0.052
Rb	ppm	0.140	61.1	0.830	9.01	11.0	1.12	18.1
Sr	ppm	2.21	90.8	8.14	41.0	28.5	14.2	26.4
U	ppm	0.040	0.660	0.075	0.185	0.163	0.130	0.141
Th	ppm	0.025	2.910	0.065	0.605	0.481	0.200	0.671
Y	ppm	1.60	16.3	3.75	7.90	6.25	6.70	3.26
La	ppm	0.530	34.2	1.40	4.74	4.87	3.20	7.27
Ce	ppm	0.930	47.8	2.28	8.34	7.98	5.48	10.4
Pr	ppm	0.100	5.31	0.275	0.905	0.886	0.600	1.14
Nd	ppm	0.330	19.2	1.18	3.70	3.41	2.52	4.10
Sm	ppm	0.090	3.26	0.270	0.800	0.644	0.480	0.689
Eu	ppm	0.103	1.94	0.220	0.502	0.443	0.357	0.392
Gd	ppm	0.130	2.74	0.410	0.750	0.678	0.600	0.549
Tb	ppm	0.030	0.36	0.065	0.120	0.109	0.110	0.071
Dy	ppm	0.180	2.040	0.415	0.785	0.674	0.650	0.397
Ho	ppm	0.040	0.380	0.090	0.170	0.144	0.140	0.076
Er	ppm	0.120	1.220	0.275	0.525	0.454	0.430	0.241
Tm	ppm	0.020	0.191	0.044	0.084	0.072	0.073	0.038
Yb	ppm	0.130	1.32	0.295	0.575	0.477	0.460	0.267
Lu	ppm	0.015	0.231	0.048	0.099	0.080	0.079	0.048
Sc	ppm	0.500	4.00	0.500	0.500	0.868	0.500	0.930
ΣREE	ppm	3.32	120	8.09	21.8	20.9	14.6	25.4

Jasper (n=5)

		Min	Max	Q1	Q3	Mean	Median	Standard Deviation
Si	%	30.9	41.8	32.6	39.6	35.6	33.6	4.38
Al	%	0.064	0.180	0.075	0.089	0.095	0.082	0.039
Fe	%	6.68	21.4	9.93	19.6	15.4	18.7	6.07
Ca	%	0.050	0.522	0.168	0.325	0.250	0.204	0.153
Mg	%	0.030	0.555	0.047	0.342	0.208	0.109	0.201
Na	%	0.001	0.037	0.001	0.001	0.007	0.001	0.013
K	%	0.001	0.030	0.003	0.017	0.011	0.005	0.011
P	%	0.013	0.074	0.036	0.060	0.045	0.041	0.020
LOI	%	-0.510	0.240	-0.188	-0.103	-0.142	-0.145	0.219
C_{tot}	%	0.050	0.050	0.050	0.050	0.050	0.050	0.000
S_{tot}	%	0.010	0.010	0.010	0.010	0.010	0.010	0.000
Ti	ppm	3.00	47.9	5.99	5.99	12.5	5.99	15.9
Mn	ppm	38.6	290	41.1	239	129	53	106
Zn	ppm	2.57	33.1	4.77	10.1	10.9	7.64	10.3
Cu	ppm	0.020	2.71	0.105	1.11	0.832	0.480	0.942
Pb	ppm	0.050	3.60	1.03	1.28	1.38	1.15	1.08
Au	ppm	0	0	0	0	0	0	0
Ag	ppm	0.005	0.100	0.005	0.031	0.027	0.005	0.035
As	ppm	0.330	1.85	0.830	1.57	1.12	1.02	0.525
Sb	ppm	0.370	0.930	0.410	0.628	0.568	0.545	0.190
Hg	ppm	0.001	0.051	0.005	0.009	0.013	0.007	0.017
Tl	ppm	0.005	0.010	0.005	0.005	0.006	0.005	0.002
Cd	ppm	0.010	0.050	0.010	0.030	0.023	0.020	0.015
Co	ppm	0.050	1.910	0.360	0.795	0.683	0.450	0.603
Ni	ppm	0.200	58.4	1.250	20.5	15.717	5.00	20.8
Se	ppm	0.010	0.170	0.015	0.108	0.072	0.065	0.060
Mo	ppm	0.005	12.4	0.059	4.63	3.24	0.565	4.59
Te	ppm	0.010	0.030	0.010	0.018	0.015	0.010	0.008
Sn	ppm	0.100	0.100	0.100	0.100	0.100	0.100	0
Ge	ppm	3.80	6.40	4.15	5.08	4.82	4.80	0.853
Bi	ppm	0.00	0.013	0.003	0.011	0.007	0.006	0.004
In	ppm	0.010	0.010	0.010	0.010	0.010	0.010	0
Re	ppm	0.000	0.002	0.000	0.001	0.001	0.000	0.001
W	ppm	0.170	2.59	1.17	1.83	1.47	1.17	0.798
Cr	ppm	2.90	116	4.23	48.9	32.7	4.95	43.1
V	ppm	0.400	4.50	0.550	1.75	1.48	0.700	1.46
Ga	ppm	0.180	0.860	0.220	0.480	0.400	0.320	0.235
Zr	ppm	0.100	1.800	0.400	0.675	0.667	0.500	0.541
Ba	ppm	0.500	128	1.78	35.6	30.5	3.25	46.5
Cs	ppm	0.030	0.53	0.050	0.160	0.153	0.060	0.176

Li	ppm	0.050	1.00	0.100	0.950	0.508	0.450	0.431
Be	ppm	0.250	0.57	0.333	0.413	0.380	0.350	0.100
B	ppm	4.20	63.8	14.7	56.2	36.5	42.4	23.5
Hf	ppm	0.050	0.700	0.050	0.100	0.175	0.075	0.236
Nb	ppm	0.100	1.70	0.100	0.700	0.500	0.100	0.611
Ta	ppm	0.020	0.070	0.023	0.055	0.040	0.035	0.019
Rb	ppm	0.050	2.37	0.108	0.283	0.537	0.210	0.824
Sr	ppm	1.80	56.8	14.5	38.5	25.0	15.7	19.5
U	ppm	0.040	0.200	0.048	0.078	0.083	0.070	0.054
Th	ppm	0.025	0.080	0.025	0.025	0.034	0.025	0.020
Y	ppm	2.10	5.80	2.88	4.90	4.00	4.30	1.32
La	ppm	0.660	2.72	0.785	1.24	1.22	0.945	0.702
Ce	ppm	1.10	4.28	1.23	2.19	2.01	1.59	1.10
Pr	ppm	0.130	0.520	0.145	0.250	0.242	0.205	0.133
Nd	ppm	0.450	1.93	0.660	1.07	0.998	0.980	0.478
Sm	ppm	0.050	0.460	0.165	0.260	0.225	0.205	0.125
Eu	ppm	0.115	0.372	0.152	0.244	0.219	0.225	0.085
Gd	ppm	0.150	0.500	0.228	0.385	0.320	0.340	0.119
Tb	ppm	0.030	0.090	0.038	0.070	0.058	0.065	0.022
Dy	ppm	0.180	0.590	0.255	0.453	0.363	0.350	0.140
Ho	ppm	0.050	0.120	0.063	0.110	0.083	0.075	0.027
Er	ppm	0.160	0.360	0.210	0.318	0.255	0.230	0.072
Tm	ppm	0.023	0.054	0.030	0.046	0.039	0.040	0.011
Yb	ppm	0.140	0.350	0.198	0.283	0.245	0.255	0.069
Lu	ppm	0.024	0.064	0.031	0.043	0.039	0.037	0.013
Sc	ppm	0.500	0.500	0.500	0.500	0.500	0.500	0
ΣREE	ppm	3.30	12.0	4.27	6.69	6.32	5.98	2.84

Banded Chlorite (n=4)

		Min	Max	Q1	Q3	Mean	Median	Standard Deviation
Si	%	15.7	24.2	17.6	21.6	19.7	19.5	3.13
Al	%	3.15	7.89	4.19	6.98	5.56	5.60	1.84
Fe	%	21.5	33.8	21.8	26.4	25.3	22.9	5.00
Ca	%	0.121	1.17	0.213	0.507	0.456	0.264	0.418
Mg	%	2.34	3.61	2.53	3.13	2.87	2.78	0.478
Na	%	0.001	0.031	0.001	0.019	0.012	0.008	0.012
K	%	0.003	0.018	0.011	0.017	0.013	0.015	0.006
P	%	0.022	0.092	0.028	0.062	0.049	0.041	0.027
LOI	%	3.28	5.80	3.96	5.34	4.61	4.69	0.960
C_{tot}	%	0.110	0.110	0.110	0.110	0.110	0.110	0.000
S_{tot}	%	0	0	0	0	0	0	0
Ti	ppm	719	4010	818	3066	2083	1801	1373
Mn	ppm	273	610	337	470	416	391	124
Zn	ppm	48.8	185	70.6	112	99.9	83.0	51.2
Cu	ppm	1.89	10.8	2.04	4.34	4.24	2.14	3.79
Pb	ppm	0.800	8.70	0.875	4.13	3.25	1.75	3.23
Au	ppm	0	0	0	0	0	0	0
Ag	ppm	0.140	0.260	0.155	0.185	0.180	0.160	0.047
As	ppm	0.850	1.30	0.948	1.23	1.09	1.10	0.179
Sb	ppm	0.050	0.180	0.118	0.165	0.133	0.150	0.050
Hg	ppm	0.001	0.006	0.001	0.004	0.003	0.002	0.002
Tl	ppm	0.005	0.010	0.005	0.006	0.006	0.005	0.002
Cd	ppm	0.060	0.140	0.090	0.118	0.103	0.105	0.029
Co	ppm	2.900	11.800	4.370	6.625	6.115	4.880	3.380
Ni	ppm	5.10	35.0	6.60	23.68	16.78	13.50	11.96
Se	ppm	0.27	1.3	0.43	1.0	0.7	0.7	0.4
Mo	ppm	0.005	0.94	0.016	0.340	0.276	0.080	0.387
Te	ppm	0.040	0.070	0.048	0.063	0.055	0.055	0.011
Sn	ppm	0.100	0.600	0.400	0.525	0.425	0.500	0.192
Ge	ppm	4.100	8.900	5.450	7.325	6.425	6.350	1.728
Bi	ppm	0.00	0.04	0.01	0.02	0.01	0.01	0.01
In	ppm	0.020	0.040	0.028	0.033	0.030	0.030	0.007
Re	ppm	0.001	0.003	0.002	0.003	0.002	0.002	0.001
W	ppm	0.070	0.590	0.123	0.485	0.313	0.295	0.215
Cr	ppm	10.2	64.6	10.2	45.9	31.2	25.0	22.7
V	ppm	16.3	104.0	17.5	69.0	48.9	37.6	35.8
Ga	ppm	10.1	32	14.7	20.9	18.9	16.7	8.0
Zr	ppm	45.4	149.0	69.3	96.4	87.7	78.1	37.86
Ba	ppm	0.700	44.1	1.98	14.1	12.8	3.25	18.1
Cs	ppm	0.005	0.340	0.084	0.228	0.161	0.150	0.122

Li	ppm	4.10	41.6	17.9	35.8	25.5	28.2	14.1
Be	ppm	0.410	0.970	0.508	0.895	0.698	0.705	0.230
B	ppm	0.100	40.7	0.100	10.3	10.3	0.100	17.6
Hf	ppm	1.30	3.40	2.20	3.25	2.60	2.85	0.822
Nb	ppm	1.80	7.00	4.05	6.18	4.88	5.35	1.94
Ta	ppm	0.300	0.650	0.465	0.643	0.528	0.580	0.141
Rb	ppm	0.150	2.260	0.180	1.180	0.855	0.505	0.854
Sr	ppm	3.96	14.6	7.81	11.6	9.56	9.85	3.81
U	ppm	0.530	2.16	0.823	1.55	1.24	1.14	0.605
Th	ppm	2.53	7.89	5.01	7.04	5.76	6.30	2.00
Y	ppm	7.50	19.5	8.78	16.5	12.9	12.4	4.83
La	ppm	2.74	29.1	5.28	28.1	16.4	17.0	12.08
Ce	ppm	6.04	60.4	11.9	58.8	34.6	36.1	24.8
Pr	ppm	0.720	6.76	1.46	6.45	3.89	4.03	2.70
Nd	ppm	3.02	24.7	5.44	23.7	14.3	14.8	9.76
Sm	ppm	0.770	4.44	1.09	4.21	2.64	2.67	1.66
Eu	ppm	0.325	1.17	0.371	1.15	0.755	0.763	0.400
Gd	ppm	0.840	2.99	0.990	2.84	1.915	1.915	0.980
Tb	ppm	0.150	0.490	0.173	0.423	0.305	0.290	0.144
Dy	ppm	0.930	2.860	1.125	2.343	1.788	1.680	0.773
Ho	ppm	0.210	0.600	0.263	0.480	0.383	0.360	0.151
Er	ppm	0.650	1.750	0.830	1.435	1.155	1.110	0.421
Tm	ppm	0.102	0.278	0.138	0.220	0.183	0.176	0.065
Yb	ppm	0.660	1.84	0.983	1.49	1.24	1.23	0.429
Lu	ppm	0.113	0.286	0.169	0.242	0.204	0.208	0.063
Sc	ppm	3.00	11.0	3.00	8.00	6.00	5.00	3.32
ΣREE	ppm	17.3	136	30.2	132	79.8	82.9	54.3

Massive Chlorite (n=4)

		Min	Max	Q1	Q3	Mean	Median	Standard Deviation
Si	%	19.7	26.4	21.2	24.2	22.8	22.6	2.44
Al	%	5.65	7.95	5.70	6.89	6.46	6.12	0.927
Fe	%	5.42	20.3	13.2	19.7	15.3	17.7	5.93
Ca	%	0.100	2.71	0.331	2.47	1.40	1.40	1.16
Mg	%	3.44	4.99	3.58	4.17	3.99	3.76	0.601
Na	%	0.005	5.00	0.006	1.26	1.26	0.009	2.16
K	%	0.003	0.027	0.004	0.011	0.010	0.005	0.010
P	%	0.004	0.192	0.047	0.113	0.086	0.074	0.068
LOI	%	5.43	8.75	5.46	6.97	6.51	5.93	1.35
C_{tot}	%	0.390	0.390	0.390	0.390	0.390	0.390	<0.001
S_{tot}	%	0.010	0.010	0.010	0.010	0.010	0.010	<0.001
Ti	ppm	1157	6515	1844	4263	3314	2793	2030
Mn	ppm	523	940	530	654	639	546	175
Zn	ppm	67.6	89.8	75.4	83.5	79.2	79.7	7.96
Cu	ppm	1.97	80.9	18.6	54.5	38.2	35.0	29.1
Pb	ppm	1.20	3.40	1.20	1.83	1.78	1.25	0.939
Au	ppm	0	0	0	0	0	0	0
Ag	ppm	0.190	0.260	0.228	0.253	0.235	0.245	0.027
As	ppm	0.490	16.6	5.40	13.5	9.13	10.3	6.63
Sb	ppm	0.010	0.140	0.048	0.118	0.080	0.085	0.049
Hg	ppm	0.001	0.005	0.001	0.002	0.002	0.001	0.002
Tl	ppm	0.005	0.005	0.005	0.005	0.005	0.005	0.000
Cd	ppm	0.130	0.200	0.138	0.178	0.160	0.155	0.027
Co	ppm	6.72	49.0	17.4	32.2	25.8	23.8	15.2
Ni	ppm	12.7	57.1	20.2	42.4	32.5	27.7	18.4
Se	ppm	1.29	3.30	1.40	2.00	1.90	1.51	0.814
Mo	ppm	0.005	2.28	0.005	1.19	0.780	0.418	0.929
Te	ppm	0.060	0.170	0.083	0.125	0.108	0.100	0.040
Sn	ppm	0.100	1.200	0.175	0.900	0.575	0.500	0.449
Ge	ppm	1.30	5.00	2.88	4.78	3.60	4.05	1.46
Bi	ppm	0.002	0.171	0.033	0.078	0.066	0.045	0.063
In	ppm	0.030	0.060	0.038	0.053	0.045	0.045	0.011
Re	ppm	0.000	0.002	0.001	0.002	0.002	0.002	0.001
W	ppm	0.070	0.580	0.190	0.453	0.323	0.320	0.191
Cr	ppm	18.6	60.1	23.3	44.1	35.6	28.0	17.8
V	ppm	26.6	152	53.4	114	85.5	81.7	46.6
Ga	ppm	20.8	24.7	22.0	23.4	22.7	22.7	1.40
Zr	ppm	76.8	136	110	128	115	123	22.6
Ba	ppm	0.800	29.9	1.55	9.65	8.85	2.35	12.2
Cs	ppm	0.150	0.250	0.188	0.220	0.203	0.205	0.036

Li	ppm	11.4	49.5	15.8	41.1	29.1	27.8	15.4
Be	ppm	0.420	1.270	0.750	1.000	0.865	0.885	0.302
B	ppm	0.100	31.1	0.250	8.08	7.98	0.350	13.4
Hf	ppm	2.30	3.90	2.68	3.45	3.08	3.05	0.593
Nb	ppm	1.20	12.8	3.23	8.60	6.28	5.55	4.33
Ta	ppm	0.250	1.15	0.303	0.693	0.565	0.430	0.354
Rb	ppm	0.180	0.36	0.225	0.323	0.273	0.275	0.068
Sr	ppm	4.96	113	25.5	67.6	50.7	42.4	39.7
U	ppm	0.510	3.10	0.615	1.67	1.36	0.920	1.03
Th	ppm	1.80	11.4	2.43	5.23	4.75	2.91	3.87
Y	ppm	12.7	48.2	16.9	30.4	25.9	21.4	13.5
La	ppm	9.85	23.9	14.5	20.3	17.2	17.6	5.10
Ce	ppm	19.0	50.9	31.8	47.5	38.1	41.2	12.3
Pr	ppm	2.09	6.14	4.14	5.88	4.71	5.31	1.59
Nd	ppm	7.94	25.1	16.0	24.4	19.0	21.4	6.81
Sm	ppm	1.65	5.85	3.55	5.34	4.21	4.68	1.59
Eu	ppm	0.791	1.44	1.03	1.33	1.16	1.20	0.24
Gd	ppm	1.43	5.73	3.11	4.55	3.75	3.92	1.54
Tb	ppm	0.260	1.10	0.478	0.785	0.648	0.615	0.302
Dy	ppm	1.53	6.83	2.56	4.91	3.88	3.59	1.96
Ho	ppm	0.330	1.38	0.503	0.968	0.775	0.695	0.392
Er	ppm	0.980	3.89	1.48	2.86	2.26	2.08	1.09
Tm	ppm	0.159	0.576	0.218	0.422	0.336	0.304	0.158
Yb	ppm	1.06	3.64	1.43	2.70	2.16	1.97	0.977
Lu	ppm	0.169	0.567	0.234	0.409	0.337	0.306	0.148
Sc	ppm	4.00	21.0	5.50	19.5	12.5	12.5	7.57
ΣREE	ppm	47.2	126	84.2	124	98.4	110	31.8

Appendix 5: Analytical Methods

EPMA and SEM Imaging Techniques

All analytical techniques discussed in Chapter 9 rely on the interaction of a focused electron beam with the surface of sample materials. The electron beam is drawn from a tungsten filament, accelerated by a certain acceleration voltage (typically 1520 kV), focused by electromagnetic lenses and pointed on the surface of the sample.
The more the beam gets focused, the smaller the spot size (SS, no unit, typically 5557). A smaller spot size allows for an increased resolution, but also produces more noise in the image and lowers the intensity of the electron beam. On the SEM, the electron beam current cannot be directly controlled, but results directly from the spot size. On the EPMA, the current can be controlled directly by changing the electrical current through the filament. The distance between the tip of the electron gun aperture and the surface of the sample is expressed as working distance (WD, typically between 8-10 mm).

The SEM can produce backscattered (BSE) – and secondary electron images (SEI). The intensity (expressed as brightness) of backscattered electrons depends on the average atomic number of the material, and therefore allows a differentiation of mineral phases, but not the identification of those. The intensity of the SEI depends less on the chemistry of the sample, but expresses the surface topography of the sample.
Working with polished thin sections, the emphasis will here be on BSE images.
Besides the production backscattered and secondary electrons, the electrons on the

sample surface can be raised to an excited state by interaction with high-energy electrons from the beam. Falling back to the unexcited state, energy is released in the form of x-rays (or by other pathways, e.g. photons). The produced x-rays have a certain energy, depending on the relation between the electron orbitals and the element core. The energy level and intensity of x-rays with the specific energy can be detected and used like fingerprints to identify the presence of certain elements. On the SEM, an energy dispersive detector can produce a spectrum (EDS) and calculate quick, semiquantitative abundances of the elements. Results from the EDS detector can be used to identify minerals, but are not suitable to quantify trace elements or minute variations in mineral chemistry. The EPMA is equipped with five wavelength-dispersive detectors (WDS). Each of those detectors contains a diffraction crystal that allows the fine tuning to a certain wavelength of x-rays. The intensity of the x-rays is being compared to the intensity of standard materials of certified composition and allows for the quantitative determination of major and trace elements down to typically <100 ppm levels. Other than x-rays, energy can be released in the form of photons, and the resulting brightness can be detected using a cathodoluminescence detector on the SEM.

Whole Rock Analytical Methods

Two different analytical methods were used in tandem to address analytical challenges presented by BIF samples. First, magnetite cannot be fully dissolved by the four acid method used in TD-ICP, so elements hosted in magnetite (Fe, Si etc.) should be measured by FUS-ICP. However, an average combined concentration of ~55% for Si

and Fe in Algoma-Type BIF (see Table 12.1) means that the concentration of trace elements is extremely low. Trace element analyses of BIF from Govidnaraju, (1994), Slack et al., (2007) and Thurston et. al (2012), reported concentrations below the detection limit measurable by FUS-ICP. These shortcomings of TD-ICP and FUS-ICP are especially relevant for trace elements hosted in magnetite. The low detection limits provided by TD-ICP analysis was more vital to a comprehensive, accurate data set than fully dissolving magnetite except in the case of Ge, hosted in magnetite and was likely above the FUS-ICP detection limit based on LA-ICP-MS analyses of magnetite (Dare et. al, 2014). Na and K were measured by TD-ICP because the metaborate used in the fusion process contains these elements in higher concentration than the average Algoma-Type BIF (0.4% and 0.2%, respectively: see Table 12.1).

Previous studies of two standard samples of BIF from Temagami (FeR-3 and FeR-4) were reported by Bau and Alexander (2009). In this study the samples were dissolved in ultrapure HF and $HClO_4$, then samples were either diluted by 0.5M HCl for trace element analysis by ICP-MS or analysed by ICP-OES to determine major element concentrations.

In this study, FeR-3 and FeR-4 were analysed both by FUS-ICP and TD-ICP to compare results from each method. The results for FeR-3 and FeR-4 from Bau and Alexander (2009), Dulski (2001) and Govindaraju (1994) are compared to our results from both methods in Table 6.3.

Quality Control

For ICP-OES, the fused samples were analysed with 18 certified reference materials, all prepared by the same fusion process. Every 30th sample was prepared and analysed in duplicate; one blank was prepared and analysed. Calibration was achieved using a variety of international reference materials: NIST 694, DNC-1, GBW07113, LKSD-3, TDB-1, W-2a, DTS-2b, Sy-4, CTA-AC-1, BIR-1a, NCS DC86312, ZWC, NCS DC70009, OREAS 100a, OREAS 101A, OREAS 101B, JR-1. Independent control standards were also analysed. For ICP-MS, the fused blank was run in triplicate every 15-20 samples. Controls and standards, which were fused with the samples, were also run after each group of samples. Fused duplicates were run every 30 samples. In routine analyses by this method, the instrument is recalibrated every 40 samples. For the 4-acid digestion and ICP-MS, a blank is run every 40 samples, replicates are performed every 15 samples, and international standards run approximately every 30 samples.

Iron formations standards (FeR-3 and FeR-4) were also analyzed and compared with both certified values and data from other published analyses (Bau and Alexander, 2009; Govindaraju, 1994; Dulski, 2001). These results are presented in Table 6.3. FeR-3 is from the lower Temagami BIF and consists of chert, magnetite and jasper with minor chlorite. FeR-4 is from the upper Temagami BIF and consists of chert, magnetite and chlorite (Abbey et. al, 1983). FeR-4 has a larger volcaniclastic component than FeR-3, as indicated by higher concentrations of Rb, Zr, Th and LREE in FeR-4 (Bau and Alexander, 2009).

Appendix 6: Uncropped Field Photographs

Several figures in this thesis present field photographs to illustrate textural and structural features of the Temagami BIF. In order to highlight specific features, photographs were cropped to show only the relevant feature. This appendix presents uncropped versions of each photograph presented in figures in the body of the thesis. The header on each photograph indicates where it appears in the body of the thesis.


Figure 4.2A


Figure 4.2B


Figure 4.2C


Figure 4.2D


Figure 6.2A


Figure 6.2B

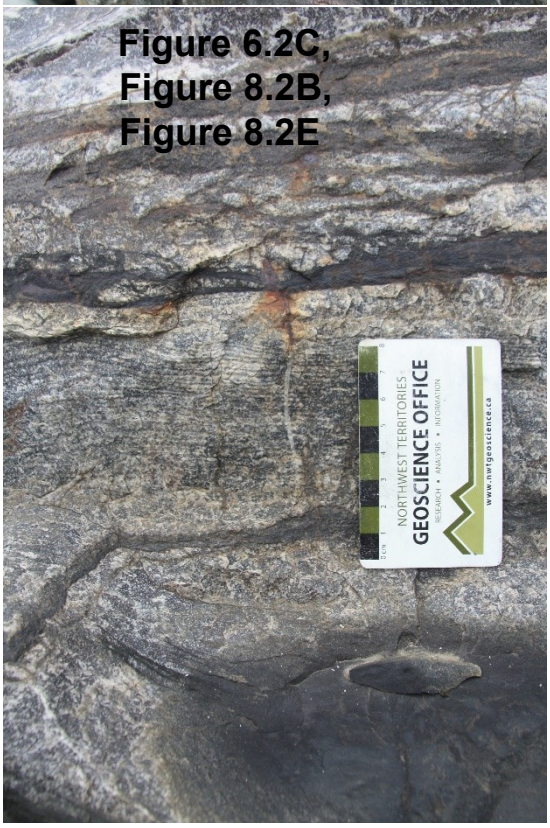
Figure 6.2C,
Figure 8.2B,
Figure 8.2E
NORTHWEST TERRITORIES
GEOSCIENCE OFFICE
www.nwtgeoscience.ca


Figure 6.2D


Figure 6.3A


Figure 6.3B


Figure 6.3C


Figure 6.3D,
Figure 6.4D


Figure 6.3E


Figure 6.4A

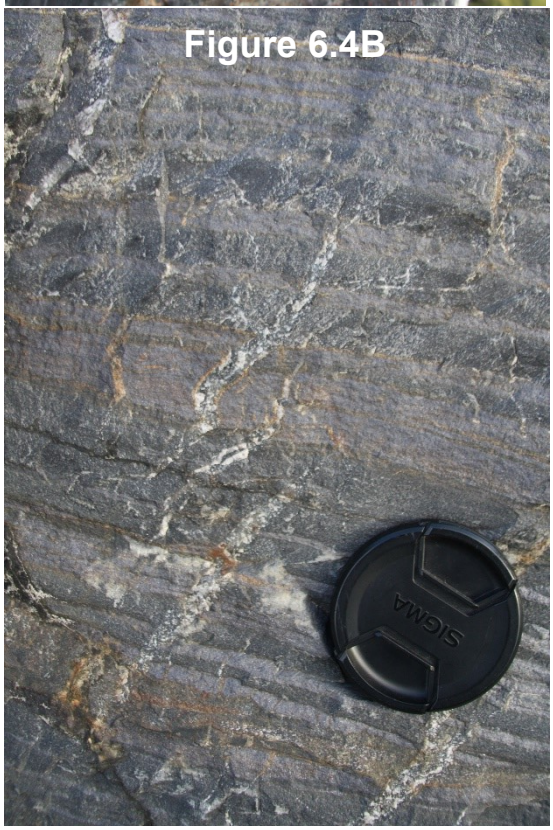
Figure 6.4B
SIGMA


Figure 6.4C

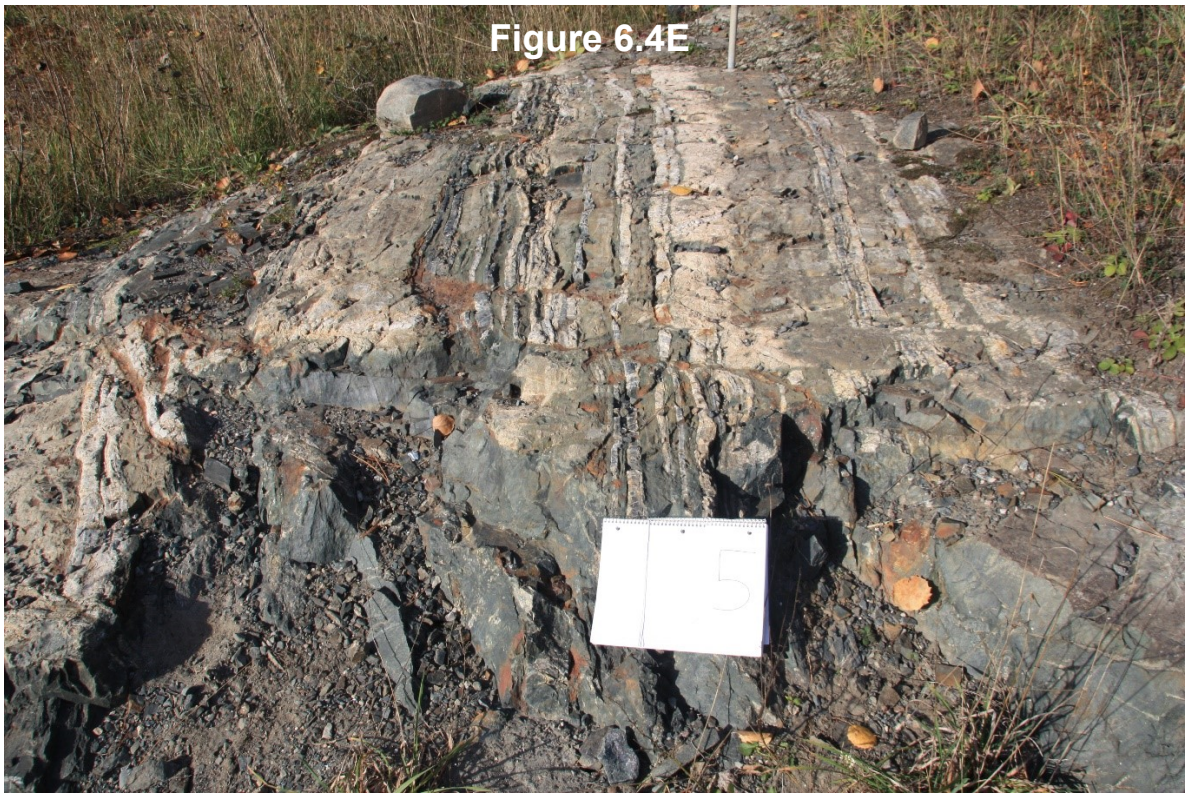

Figure 6.4E

Figure 6.4F